ANNALS OF THE UNIVERSITY OF CRAIOVA
ANNALES DE L'UNIVERSITÉ DE CRAIOVA

ANALELE UNIVERSITĂȚII DIN CRAIOVA

SERIA: INGINERIE ELECTRICĂ
SERIE: ELECTRICAL ENGINEERING
SÉRIE: INGÉNIERIE ÉLECTRIQUE
Anul/Year/Année 45
No. 45, Vol. 45, Issue 1, 2021

December 2021

ISSN 1842 - 4805

EDITURA UNIVERSITARIA

ANNALS OF THE UNIVERSITY OF CRAIOVA

13, A.I. Cuza Str., CRAIOVA 200585
ROMANIA

We exchange publications with similar institutions of country and from abroad

ANNALES DE L'UNIVERSITÉ DE CRAIOVA

Rue A.I. Cuza, No. 13, CRAIOVA 200585
ROUMANIE

On fait des échanges des publications avec les institutions similaires du pays et de l'étranger

This journal is published by the Faculty of Electrical Engineering from the University of Craiova.
The authors are fully responsible for the originality of their papers and for accuracy of their notes.

REVIEWERS COMMITTEE

Lia-Elena ACIU – *Transilvania University of Braşov,* Romania
Maricel ADAM – *"Gh. Asachi" Technical University of Iaşi,* Romania
Mihaela ALBU – *University "Politehnica" of Bucharest,* Romania
Slavoljub ALEKSIC – *University of Nis,* Serbia
Horia BĂLAN – *Technical University of Cluj-Napoca,* Romania
Gheorghe BĂLUŢĂ – *"Gh. Asachi" Technical University of Iaşi*, Romania
Alexandru BITOLEANU – *University of Craiova, Romania*
Maria BROJBOIU – *University of Craiova,* Romania
Emil CAZACU – *University "Politehnica" of Bucharest,* Romania
Aurel CÂMPEANU – *University of Craiova,* Romania
Mihai CERNAT – *Transilvania University of Braşov,* Romania
Marian CIONTU – *University of Craiova,* Romania
Daniel Cristian CISMARU – *University of Craiova,* Romania
Grigore CIVIDJIAN – *University of Craiova,* Romania
Zlata CVETCOVIC – *University of Nis,* Serbia
Leszek CZARNECKI – *Louisiana State University*, USA
Daniela DANCIU – *University of Craiova,* Romania
Sonia DEGERATU – *University of Craiova,* Romania
Iuliu DELEŞEGA – *University "Politehnica" of Timişoara,* Romania
Silvia-Maria DIGĂ – *University of Craiova,* Romania
Peter DINEFF – *Technical University of Sofia,* Bulgaria
Radu DOBRESCU – *University "Politehnica" of Bucharest,* Romania
Mircea-Adrian DRIGHICIU – *University of Craiova,* Romania
Laurentiu Marius DUMITRAN – *University "Politehnica" of Bucharest,* Romania
Sorin ENACHE – *University of Craiova,* Romania
Virgiliu FIRETEANU – *University "Politehnica" of Bucharest,* Romania
Dan FLORICĂU – *University "Politehnica" of Bucharest,* Romania
Cristian FOŞALĂU – *"Gh. Asachi" Technical University of Iaşi*, Romania
Teodor Lucian GRIGORIE – *Military Technical Academy "Ferdinand I",* Romania
Mircea-Dan GUSA – *"Gh. Asachi" Technical University of Iaşi*, Romania
Stefan HĂRĂGUŞ – *University "Politehnica" of Timişoara,* Romania
Elena HELEREA – *Transilvania University of Braşov,* Romania
Eugen HNATIUC – *"Gh. Asachi" Technical University of Iaşi,* Romania
Kemal HOT – *Polytechnic of Zagreb,* Croaţia
Eugen IANCU – *University of Craiova,* Romania
Nathan IDA – *University of Akron,* USA
Maria IOANNIDES – *National Technical University of Athens,* Greece
Valentin IONIŢĂ – *University "Politehnica" of Bucharest,* Romania
Mihai IORDACHE – *University "Politehnica" of Bucharest,* Romania
Marcel ISTRATE – *"Gh. Asachi" Technical University of Iaşi*, Romania
Sergiu IVANOV – *University of Craiova,* Romania
Wilhelm KAPPEL – *National Research and Development Institute for Electrical Engineering (ICPE – CA) Bucharest,* Romania
Liviu KREINDLER – *University "Politehnica" of Bucharest,* Romania
Gheorghe LIVINŢ – *"Gh. Asachi" Technical University of Iaşi*, Romania
Dumitru Dorin LUCHACHE – *"Gh. Asachi" Technical University of Iaşi*, Romania
Lucian MANDACHE – *University of Craiova,* Romania
Gheorghe MANOLEA – *University of Craiova,* Romania
Andrei MARINESCU – *Romanian Academy of Technical Science, Craiova Branch,* Romania
Iliana MARINOVA – *Technical University of Sofia,* Bulgaria

Claudia MARTIŞ – *Technical University of Cluj-Napoca,* Romania
Ernest MATAGNE – *Université Catholique de Louvain,* Belgium
Leonardo-Geo MĂNESCU – *University of Craiova,* Romania
Dan MIHAI – *University of Craiova,* Romania
Alexandru MOREGA – *University "Politehnica" of Bucharest,* Romania
Mihaela MOREGA – *University "Politehnica" of Bucharest,* Romania
Nazih MOUBAYED – *Lebanese University,* Lebanon
Călin MUNTEANU – *Technical University of Cluj-Napoca,* Romania
Florin MUNTEANU – *"Gh. Asachi" Technical University of Iaşi,* Romania
Valentin NĂVRĂPESCU – *University "Politehnica" of Bucharest,* Romania
Mitică Iustinian NEACĂ – *University of Craiova,* Romania
Ciprian NEMEŞ – *"Gh. Asachi" Technical University of Iaşi*, Romania
Petre-Marian NICOLAE – *University of Craiova,* Romania
Dragoş NICULAE – *University "Politehnica" of Bucharest,* Romania
Petru NOTINGHER – *University "Politehnica" of Bucharest,* Romania
Teodor PANĂ – *Technical University of Cluj-Napoca,* Romania
Camelia PETRESCU – *"Gh. Asachi" Technical University of Iaşi*, Romania
Ioan POPA – *University of Craiova,* Romania
Dan POPESCU – *University of Craiova,* Romania
Daniela POPESCU – *University of Craiova,* Romania
Mihaela POPESCU – *University of Craiova,* Romania
Miroslav PRSA – *University of Novi-Sad,* Serbia
Mircea M. RĂDULESCU – *Technical University of Cluj Napoca,* Romania
Victoriţa RĂDULESCU – *University "Politehnica" of Bucharest,* Romania
Benoit ROBYNS – *Ecole des Hautes Etude d'Ingénieur de Lille,* France
Constantin ROTARU – *Military Technical Academy "Ferdinand I",* Romania
Alex RUDERMAN – *Elmo Motion Control Ltd,* USA
Sergey RYVKIN – *Trapeznikov Institute of Control Sciences,* Russia
Alexandru SĂLCEANU – *"Gh. Asachi" Technical University of Iaşi*, Romania
Cristina Gabriela SĂRĂCIN – *University "Politehnica" of Bucharest,* Romania
Constantin SĂRMAŞANU – *"Gh. Asachi" Technical University of Iaşi,* Romania
Dan SELIŞTEANU – *University of Craiova,* Romania
Victor ŞONTEA – *Technical University of Moldova,* Moldova
Alexandru STANCU – *"A.I. Cuza" University of Iaşi,* Romania
Viorel STOIAN – *University of Craiova,* Romania
Ryszard STRZELECKI – *University of Technology Gdansk,* Poland
Flavius-Dan ŞURIANU – *University "Politehnica" of Timişoara,* Romania
Lorand SZABO – *Technical University of Cluj-Napoca,* Romania
Radu-Adrian TÎRNOVAN – *Technical University of Cluj-Napoca,* Romania
Raina TZENEVA – *Technical University of Sofia*, Bulgaria
Ioan VADAN – *Technical University of Cluj-Napoca*, Romania
Viorel VARVARA – *"Gh. Asachi" Technical University of Iaşi*, Romania
Ion VLAD – *University of Craiova*, Romania
Ivan YATCHEV – *Technical University of Sofia*, Bulgaria

CONTENTS

Wireless Transfer of Electric Power - a Disruptive Technology

Andrei Marinescu
Romanian Academy of Technical Sciences, Craiova Branch Craiova, Romania
University of Craiova, Romania
ancor2005@gmail.com

DOI: 10.52846/AUCEE.2021.1.01

***Abstract*—Wireless (contactless) transfer of electric power is a disruptive technology because it abandons wired transmission technology, the only technology used in electrical and electronic engineering until recently, just like in the past animal traction and film photography were replaced by mechanical traction and digital photography. Although revealed at the end of the nineteenth century through Tesla's inventions, it could be applied in practice only in the '80s of the twentieth century, with the development of power electronics and microprocessors. After an introduction and an overview of the operating principles, the paper presents the readiness level reached by this technology, the stage of standardization, Romanian achievements and future prospects for high power applications.**

Cuvinte cheie—*transmiterea puterii fără contact, tehnologie diruptivă, nivel tehnologic,expunere umană la câmp magnetic, aplicații*

Keywords—*wireless power transfer, disruptive technology, readiness level, magnetic field human exposure, applications*

I. Introduction

A disruptive technology, as defined by CM Christensen [1] is a technological innovation, a product or service, fundamentally different from the dominant technology on the market. One of the characteristics of disruptive technologies is that they coexist with existing technologies and are initially considered inferior by most consumers [2,3].

This category has included over time: the replacement of animal traction by mechanical traction and then by electrical traction, vacuum tubes replaced by transistors and then by integrated circuits, incandescent filament light bulbs replaced by the LEDs, HDDs by SSDs, 2D printers by 3D, 4D etc.

A similar paradigm shift in which the traditional transmission of electricity by conduction is replaced by the contactless transmission is a typical disruptive technology [4]. It is best known as Wireless Power Transfer (WPT) and has many important advantages in modern technology due to the absence of contacts and their wear, ease of use in aggressive or explosive environments, in air or water, with applications for both electric drives and for charging storage batteries in the most various fields such as: medicine, robotics, electric mobility, etc. The transfer of energy is carried out in the near field (magnetic or electric) on small and medium distances, with efficiency comparable to the transmission by galvanic contact and with the possibility of simultaneous transmission of power and data. Due to the different operating principle, both the theoretical bases and the simulation of circuits and fields through numerical methods are essential to the design and practical achievement of these systems in order to ensure interoperability, and increase the efficiency and the transferred power [5]. In [6] it is stated that: "*Wireless Power Transfer is now recognized as one of the 'Hottest' Research Areas in Electrical Engineering combining the EE Foundation Studies of Electricity and Magnetism with Power Electronics and Microprocessor Control*". This statement best summarizes the special endeavors in the field. The research into the IEEE Xplore database shows that in the field of inductive WPT alone during the period 2010-2020 [7] more than 1800 papers were published with an annual increase rate of 100%, plus over 6000 patents registered since Tesla patents until today, as evidenced by a search in the USPTO (U.S. Patent and Trademark Office) [8]. The papers on WPT listed above are featured not only in journals and conferences dedicated to power electronics applications but also in publications in related fields such as medicine, electromagnetic compatibility, etc. These figures are exceeded in number only by publications in the field of microelectronics. The IEEE Xplore database contains 32 papers in the field of Romanian authors, published after 2012 [7]. When the necessary high powers are transmitted, for example, to charge the batteries of an electric vehicle (EV) in static or dynamic charging systems, the limitation of human exposure to the stray magnetic field [9] requires electromagnetic shielding measures [10]. The autonomous driving systems of EVs on highways and in urban areas currently represent an important argument for the application of the contactless transfer of electric power. The paper analyzes the principles of designing inductive power couplers, the technological readiness level of these systems in contrast to plug-in charging, the evaluation and optimization of their parameters, the standards and regulations in force, the Romanian achievements for EVs and prospects for application in the near future.

II. Construction of Inductive Power Transfer Systems

A. Realization and evaluation of power transfer through an inductive coupler

The inductive coupler is an essential element of a WPT system. The simplest inductive coupler is shown in Fig. 1. It is in fact a two-port circuit with an input port and an output port usually consisting of two air core planar (circular or solenoidal) coils, loosely coupled, with self-inductances L_1 and L_2 and R_1 and R_2 with their AC value at operating frequency,. The primary coil is the transmitter (Tx) and the secondary coil is the receiver (Rx). Their position in the xyz coordinate system can be random, in the most general case; therefore the variable mutual inductance M largely determines the power transfer efficiency between the two ports. The gap between the coils (h) on z axis is the

separation gap of the coupler which can be constant or variable depending on the application.

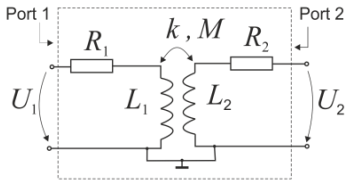

Fig. 1. Schematic diagram of the two-port inductive coupler.

M is calculated according to the known relation:

$$M = k(L_1 L_2)^{1/2} \quad (1)$$

where k is the coupling factor of the two coils. In current practice, the value of k is small (0.1 – 0.2), which is why the circuit is considered loosely coupled.

The weak coupling is determined on the one hand by achieving a transfer distance as long as possible on z axis and on the other hand by the decrease of the power transfer sensitivity in the applications where the horizontal position of Tx against Rx (x, y axes) is variable (EV case) [6].

The value of $k(M)$ is usually increased by using magnetic flux concentrators made of ferrite material with different geometries [11].

For the calculation of the maximum power which can be transfered in the case of the inductive coupler in Fig.1, we start from the relation for the apparent power transmitted from port 1 to port 2:

$$S_2 = |U_{20}.I_{sc}| \quad (2)$$

where U_{20} is the voltage at the terminals of port 2 at no-load and I_{sc} is the short-circuit current generated at port 2.

After simple calculations using (1), we obtain:

$$S_2 = \omega.k^2.L_1.I_1^2 \quad (3)$$

or

$$S_2 = k^2.S_1 \quad (4)$$

where S_1 is the apparent power available in the primary Tx of the coupler.

Under these conditions, unlike the power transformer for which k~1, the Tx-Rx energy transfer indicated by S_2 is very low mainly due to the very high leakage inductances specific to the air core coils of the inductive coupler.

To increase the power transfer in WPT systems, the leakage inductances of the Tx and Rx coils are compensated by series or parallel capacitors.

Classical compensation topologies use simple LC-type networks, i.e. S-S, S-P, P-S and P-P (Fig. 2) in which the resonant frequencies of the primary and secondary are equal.

Under these conditions, regardless of the method of achieving the primary compensation, the relation (4) becomes:

$$S_2 = k^2.S_1.Q_2 \quad (5)$$

where Q_2 is the loaded quality factor of the circuit Rx at the operating frequency ω.

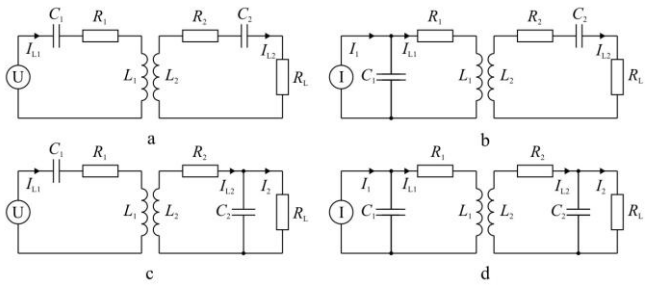

Fig. 2. The main inductive coupler compensation topologies. a-S-S, b-P-S, c-S-P, d-P-P.

Therefore the topologies in Fig.2 allow the practical realization of inductive WPT couplers with transfer outputs between 85 and 90 % when Tx and Rx are coaxial.

In order to be used in practice and compared in terms of efficiency, the S-S and S-P topologies are powered by voltage inverters and the P-S and P-P topologies are powered by current inverters as shown in Figs. 2.

There are a large number of parameters involved in the behavior of the inductive coupler, including: coil geometry, operating frequency, heat losses depending on the conductor used (solid or litz wire), winding step [12], magnetic field concentrators, loaded quality factor at operating frequency, etc.

Although they are simple and economical and therefore theoretically treated in many papers, the practical application of these topologies under variable load, short circuit, coupler coils offset, etc. affects both the operation of the primary inverter and the overall efficiency of the WPT system.

For these reasons, at high powers, when the stability and efficiency of the system is decisive, the application of hybrid compensation topologies with several energy accumulators has become widespread. The most common networks are the LCL and LCC topologies, symmetrical in the primary or secondary, or mixed (Fig. 3).

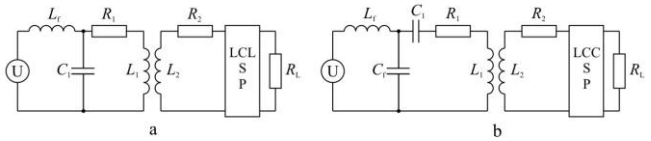

Fig. 3. Hybrid compensation topologies. a-LCL, b-LCC.

In the case of LCL topology [13] with a single resonant frequency, the series inductance L_f (usually equal to L_1) transforms the voltage inverter into a constant current inverter, the operation of which is load independent with a unit power factor.

In the case of LCC topology [14], the difference from LCL consists in inserting a capacity C_1 in series with L_1, which leads to the decrease of the inductive reactance of L_1 and, as a result, now $L_f < L_1$. The new circuit may have also a single resonant frequency given by $L_f.C_f = (L_1 - L_f).C_1$. Interoperability with other WPT systems is improved and the influence of the variation of the coupling factor produced by the coils offset (misalignment) as well as the Tx - Rx air gap is smaller.

To make a comparison of the performance of inductive couplers, their factor of merit (FOM) [15], a dimensionless

parameter determining the transfer efficiency is defined and can be determined based on the relation:

$$FOM = kQ = \omega M/R \quad (6)$$

where Q and R represent the geometric averages of the quality factors, respectively of the AC resistances of the two coils.

The transfer efficiency can be expressed as:

$$\eta_{max} \approx 1 - 2/kQ \quad (7)$$

The maximization of product kQ is a necessary measure, but the reduction of k (unjustifiably increased gap between the coupler coils) must be carefully controlled in practical applications because it greatly influences the operating mode of the inverter used.

The process of evaluation of a prototype coupler begins by analyzing the constructive variants achieved by simulation with 2D or 3D finite element; the physical optimized model is achieved and finally the values of the characteristic parameters (L, R, M, k, Q) obtained by simulation are compared with those experimentally determined; the experimental method described in [16] using a vector network analyzer (VNA) with impedance meter function is useful (Fig.4).

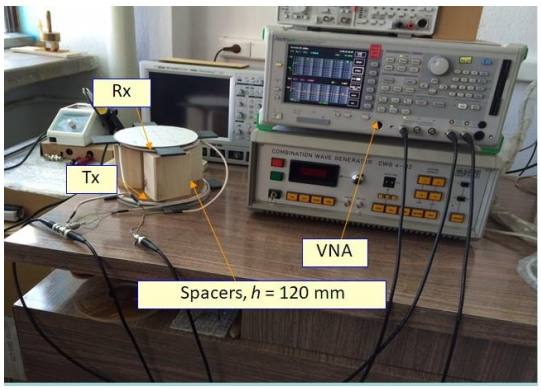

Fig. 4. Lab evaluation of the parameters of an inductive coupler with VNA.

Currently, inductive couplers are designed for transferred powers of 3.7 - 22 kW for EVs or 100 - 300 kW for electric buses and even 1MW for Maglev trains and ferries [17].

At transfer powers of over 50 kW, the inductive coupler has either a structure consisting of three coils powered by single or three-phase inverters [18], or has a modular construction consisting of four or six coplanar coils powered by single-phase inverters with synchronized operation [19].

Fig. 5 shows the laboratory test of the complete prototype of a inductive WPT system consisting of: frequency converter, Tx - Rx resonant circuits, microcontrollers, rectifier, filter and artificial load resistor which in this case replaces the charging battery.

The main qualification tests which must be performed on a WPT system are at least the following: efficiency test, PFC and power test, air gap and offset flexibility, magnetic field emissions according to the standards in the following paragraph.

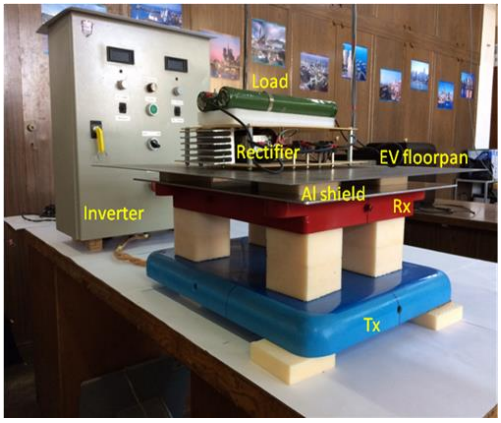

Fig. 5. Testing an EV WPT system for 3.7 kW in the laboratory. At the upper part (above Rx) there is the Al shield (2 mm thick) over which a steel plate (3 mm thick) simulates the EV chassis.

B. Standardization of WPT systems

The standards cited below are the result of extensive international collaboration. The IEC standards marked as CD (Committee Draft) are versions in the stage of final approval. The American standard, SAE J2954 [20] is the first WPT standard published as final version in 2020.

Although the standards are not mandatory, they are still fundamental elements of conduct for designers but also for researchers when approaching a new concept and especially when this concept, although original, must be compatible with other existing systems.

As proof, the success of Qi wireless mobile charging system developed by Witricity [21], currently produced on a large scale by companies worldwide is based on the publication of the company standards by IEC [22].

The main standards related to the WPT are:

- IEC 61980-1:2020, Electric Vehicle Wireless Power Transfer (WPT) Systems – Part 1: General requirements;

- IEC 61980-2, Ed. 1, (CD), Electric Vehicle Wireless Power Transfer (WPT) Systems – Part 2: Specific requirements for communication between electric road Vehicle (EV) and infrastructure with respect to wireless power transfer (WPT) systems;

- IEC 61980-3, Ed. 1, (CD), Electric Vehicle Wireless Power Transfer (WPT) Systems – Part 3: Specific requirements for the magnetic field wireless power transfer systems;

- ISO 19363:2020 Electrically propelled road vehicles – Magnetic field wireless power transfer - Safety and interoperability requirements;

- SAE J2954:2020 Surface Vehicle Standard – Wireless Power Transfer for Light-Duty Plug-in Electric Vehicles and Alignment Methodology.

The SAE standard J2954 [20] has adopted the LCC topology [14] and considers the whole set of problems that ensure the industrialization of WPT transfer systems, i.e. interoperability, frequency band, electromagnetic compatibility, protection of living beings from the magnetic stray field and last but not least the optimization of the design of the inductive coupler, which is the result of tests

performed on actual systems in the laboratory and in operation for powers between 3.7 and 11 kW.

C. *Operating frequency of wireless power transfer systems*

The general rule governing any WPT system, whether it is intended for data or power transfer is its non-conflicting co-existence with radio communication systems, which is why the ITU (International Telecommunication Union) established the so-called ISM frequency band for industrial, scientific and medical equipment [23], which includes fixed frequencies from 6.78, 13.56, 27 MHz to 2.4 GHz and above. Some of these frequencies are used for magnetic resonance-based power transfer systems [24].

Furthermore in [23], by an international agreement, the use a non - ISM frequency band in the range 10 - 100 kHz is allowed for WPTs charging, namely:

1. 42 – 48 kHz and 52 – 58 kHz for light EVs;
2. 19–21 kHz and 59 – 61 kHz for heavy electric vehicles (buses) with charging powers of 75 - 300 kW;
3. 85 ± 0.5% kHz proposed by SAE J2954 [20] for light EVs with charging powers of 3.7 – 11 kW using low voltage AC grid.

The main reason that led to this choice is related to the fact that WPT systems have interference emissions in very confined areas around the equipment/vehicle because in the near field the magnetic component decreases proportionally by $1/d^3$ and, as a result, they are considered localized sources of magnetic field or Short Range Devices (SRDs) [25].

The frequency range 1 (42–48 kHz) was used for the prototype built so far in Romania [26], solely due to the available litz wire (elementary wire with a diameter of 0.2 mm). Currently there are litz wires with an elementary wire of 0.05 - 0.071 mm which can be used to approach operating frequencies up to 200 kHz The transition to range 3 (85 kHz) is in progress for the second generation WPT of the same EV.

D. *Block diagram of a WPT system*

Fig. 6 shows this block diagram vs. the similar diagram used for plug-in charging [27]. The most important difference is the replacement of the isolation transformer with an inductive coupler and its compensation circuits that form a critical area with a significant share in the overall efficiency in the absence of a careful planning of its parameters.

Both systems must contain active filters on the supply side so as not to generate harmonics in the supply network, taking into consideration the high powers flowing through them. It can be noted that, in the case of WPT systems, the onboard part includes fewer components. As a result, the energy transfer efficiency of the two systems can be comparable under a suitable design.

When using modern semiconductor components with SiC [28], the current overall efficiency of the WPT exceeds 90 % when the offset of the coupler coils is within the limits allowed by the system.

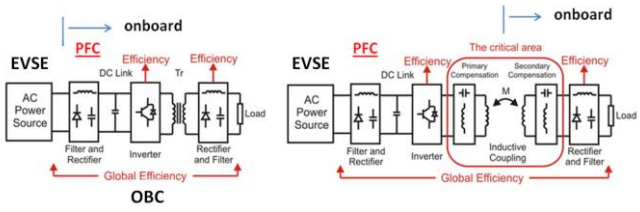

Fig. 6. Comparison between the block diagrams of plug-in equipment (a) and WPT (b). EVSE-Electric Vehicle Service Equipment, OBC-OnBoard Charger, PFC-Power Factor Correction.

E. *Storage batteries as a load for the inverter used for the WPT system*

In most cases, the WPT systems are used to charge storage batteries, the charging mode of which is a combination of constant current (CC) charging followed by a final constant voltage (CV) charging as shown in Fig. 7.

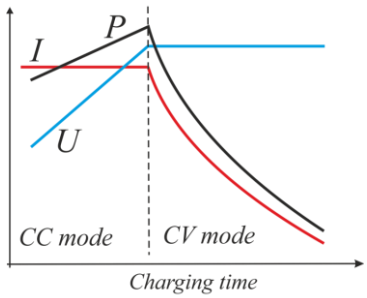

Fig. 7. Typical quantities in the storage battery charging process.

During this process, the inverter operates at variable power (P) in both CC and CV mode, noting that its peak power is generated at the end of the constant current area, and then it decreases 5 - 7 times in the constant voltage area.

This operating mode must be taken into account when designing the system by using current and voltage sensors in the automatic control loop so that the efficiency of the inverter is not affected. In the case of EVs, the charging/discharging mode is governed by the specific "C" parameter which represents the battery charging/discharging rate (C-Rate). It represents the numerical value of the ratio (A/Ah) of the charging/discharging current in A to the battery capacity in Ah. A normal charge is to 0.15 C which means, for example, for a 60 Ah battery, a 10A charging current for about 6 hours. Traction Li-Ion batteries are sized for 1 or 2 C mode. Fast or ultra-fast charging of certain EV batteries can be performed to 3 C (180 A in 20 minutes in the above case) or even to 4 C, under continuous temperature monitoring and forced cooling, a process performed on this systems [29]. Improving the control algorithms of the state of charging (SOC) and state of health (SOH) of the battery is one of the current endeavors of the research in the field so that the concerned regime will neither affect the operating safety, nor the battery life [30].

In the case of WPT charging, it should be noted that this is a typical intermittent charging system: the battery is charged automatically, without operator intervention, every time the EV reaches a public charging station and parks there even for a few minutes. This operating mode results in lower power consumption and increased battery life. In the case of urban electric buses, the system is widely practiced on the

route or at the end of the line where it is called "opportunity charging".

III. Technological Readiness Level of WPT Systems

There are technical influencers who consider that the technologies based on the wireless transmission of information and more recently of power are inefficient and dangerous to health although all studies conducted so far do not lead to this conclusion [31].

In the case of the WPT there is still an opinion that the power and transfer efficiency are low as opposed to plug-in transmission. The actual situation is as follows: on the one hand WPT equipment with powers up to 300 kW was built and used in practice on buses [19] and, on the other hand, for the plug-in charging system, losses were not considered: in the transformer from the charging station, in the connection cables, in the connectors, in the charger on board the EV which provides the AC/DC conversion. The overall efficiency of any equipment is the product of the partial efficiencies of the blocks in the system. If equal efficiencies of 97% are considered in theory in the case of four blocks, an overall efficiency of 89% will be reached! For a current WPT system, the efficiency is comparable to the plug-in system, i.e. 85 - 90% [32].

In both cases, the transition from Si semiconductors used in current power electronics to SiC or GaN semiconductors will increase the overall efficiency by at least 95%.

Since it is a disruptive technology, the number of WPT pieces of equipment in operation so far is relatively small, because the "technological readiness level" or TRL is lower. Regardless of the field of activity, TRL [33] defines 1 - 9 stages of maturity and TRL 4-6 is considered the bridge between scientific research and engineering application.

In the case of WPT, the highest level (9) has been reached (meaning "Technology proven through successful operations") by some companies: KAIST (Korea), Conductix – Wampfler (Germany), Plugless Power (US) etc mentioned in the FP 7 "FABRIC" project [34], but there are many other companies with level 7 – 8 achievements.

In Romania, the activity in the WPT field started almost 10 years ago in several university centers and research institutes is mostly focused on theoretical and experimental research included in doctoral theses, bachelor's theses and scientific publications and less on functional models or prototypes which have reached in some cases the TLR level 3, i.e. "demonstrating the functionality of the concept, in relation to the critical functionalities of the system, through analytical and experimental studies". The explanation for this situation consists, to a certain extent, in the almost non-existent funding offered by the Romanian Research Authority for this disruptive technology.

In Romania the highest known level is level 6 [35] in which the real-scale prototype, capable of fulfilling all the functions required by the operating system was tested in an environment relevant to the real operating conditions.

IV. WPT Charging System for Dacia Electron EV and Other Applications

The DACIA Electron automobile based on the mechanical structure of the Dacia Sandero automobile was built by CCIA (R&D Center for the Automobile Industry) at the University of Pitesti with the support of Renault RTR Romania in 2016 and publicly presented in 2017 at the EV Show 2017 [27]. It has a "combined charging system" consisting of the classic plug-in system and a WPT Charging system built by ACER Romania [36] in collaboration with INDA-Eltrac SRL, Craiova [37] (Fig. 8).

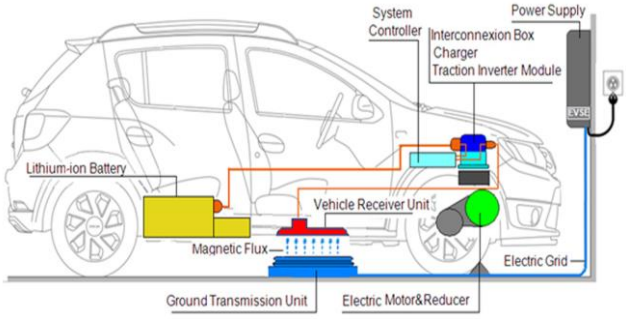

Fig. 8. WPT charging system mounted on DACIA Electron EV [27].

This is an industrial prototype (TRL 6) with a standardized load power of 3.7 kW for a ground clearance ranging between 80 and 110 mm (currently increased to 140 mm). It performs the CC-CV charging cycle for a modern cobalt-free LPF (LiFePO4) battery [35] of 12.3 kWh, with the voltage of 205 V and weight of 160 kg. The range of this EV is at least 100 km.

The prototype is our starting point for R&D on WPT power transfer systems with powers over 1 kW, such as:

- urban rail vehicles (catenary-free trams);
- buses, minibuses, vans and commercial vehicles;
- unmanned aerial vehicles (UAV);
- unmanned underwater vehicles (UUV);
- factory transportation equipment including autonomous (AGV);
- robotics and radar rotating platforms

ASSESSMENT OF HUMAN EXPOSURE TO THE MAGNETIC FIELD GENERATED BY THE WPT

Although basically there is no person inside the EV during battery charging, the limits set by ICNIRP [9] for the protection of persons who are for various reasons in the vicinity or passing by must be observed and certified by measurements performed by accredited laboratories. Fig. 9 presents a comparison of the evolution of the permissible level of exposure during 1998 – 2010 [9].

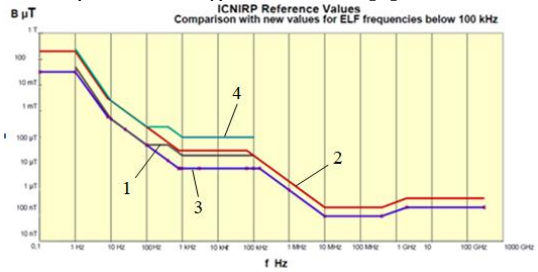

Fig. 9. Evolution of the ICNIRP [9] exposure level during 1998 - 2010: 1-occupational 1998, 2-public 2010, 3-public 1998, 4-occupational 2010.

In the 10 - 100 kHz frequency range of interest for inductive WPT systems, a relaxation took place: the level of magnetic field allowed for the public has increased from 6.25 μT to 27 μT and for workers from 50 μT to 100 μT. This increase is the result of applying the precautionary

principle on which international standards for exposure to electromagnetic radiation are generally based.

The distance at which the measurement is taken is 500 mm from the edge of the inductive coupler or 300 mm from the side edge of the EV at a height of 0.7 m from the ground. An example of 42 kHz operating frequency measurements for DACIA Electron is shown in Fig. 10 a, b, highlighting the asymmetrical position of the Rx receiver required by the design of this vehicle chassis (Sandero) to maintain the ground clearance. The level of 27 µT is exceeded only in that area (34 µT) To decrease the *B* value below 34 µT (red) to 22 µT, additional shielding of Rx was required.

a)

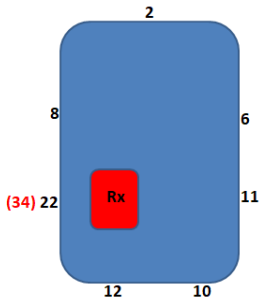

b)

Fig.10. Magnetic B field in µT around EV DACIA Electron. a) Rx location, b) Three-dimensional measured B values for 3.7 kW transferred power (top view).

V. WPT Perspectives and Associated Problems

At present it is clear that, regardless of the current opinion of users of automobiles with internal combustion engines, EVs are already winning due to the measures to limit the manufacture and use of Diesel engines in some EU countries. In the very near future EVs will become autonomous and connected vehicles and then it will not be possible to design an autonomous EV without an automatic battery charging based on WPT.

Discussions that the use of EVs aggravates pollution caused by fossil fuels used to increase the electricity generation in conventional power plants are unjustified for two reasons: first, environmental pollution is especially dangerous in large urban areas and then, the renewable sources associated with energy storage systems will totally or partially compensate for the increase in electricity consumption [38]. In addition, as the number of EVs increases, they will be able to provide, if necessary, the electricity needed in certain critical situations by using bidirectional inverters (conversion of G2V to V2G system).

It should be noted that the change of the current paradigm in urban electric mobility is also under discussion, by building small EVs (less than 2 m in length), with a range limited to 30-50 km, parked perpendicular to the road and charged right there by WPT according to the expression: "Smaller, lighter, greener". Such examples already exist in the mass production [39], while EVs with the current dimensions to be intended for long-distance travel.

Here are some of the concerns of the near future related to electric mobility and wireless power transfer:

- Accelerated generalization of electric public transport in urban areas (buses, commercial vehicles, etc.);

- Increasing the public acceptability of the WPT [40];

- The improvement of the WPT energy transfer efficiency up to 95%, by using modern switching circuits with SiC or GaN;

- The transition from the plug-in system to the WPT system with a transitory coexistence period;

- The recycling used Li-Ion batteries taking into account the limited global reserves of Li, Co, etc.;

- The achievement of virtual power plants (static storage from renewable energy sources) and the expansion of individual prosumer systems [38];

- Realization of fast and ultra-fast EV charging stations and coordination of energy consumption through Smart Grid technique;

- Generation of EVs artificial noise to warn cyclists and pedestrians (the probability of an accident caused by EVs is twice as high as opposed to vehicles fitted with internal combustion engines) [41];

- Promoting Romanian WPT R & D projects within the national cluster network "WPT Rom Net" [42] open to all research institutions and production companies, local public administration authorities, employers' associations or professional associations, legal entities and individuals interested in contributing to the development and practical application of WPT knowledge.

- Publishing in English, to increase the visibility of Romanian research in the field, using also the special dedicated issues of the "Annals of the University of Craiova - Electrical Engineering Series" [43].

VI. Conclusions

The paper aims to draw the attention of potential users and funders to the applications and benefits of wireless power transfer (WPT).

The WPT has many advantages for the most diverse applications of modern technology due to the absence of contacts and their wear, ease of use in aggressive or explosive environments, conductive liquids (marine environment), the possibility of simultaneous power transfer and data communication and its efficiency comparable to plug-in systems on short and medium distances, at power levels reaching tens or hundreds of kW.

The paper provides a brief overview of the technical solutions, applications and perspectives offered by the WPT in light of the growing interest in reducing pollution in large

cities and the prospect of large-scale use of autonomous and connected EVs.

A practical example is the 3.7 kW industrial WPT prototype built for charging the battery fitted on EV DACIA Electron.

The integration in the Smart Grid of EVs fast/ultra-fast charging stations, including renewable energy sources, energy storage systems and proper management of energy sources and energy demand will result in energy efficient solutions.

ACKNOWLEDGMENT

The paper is part of the scientific activities of the National Network WPT Rom Net [42].

Received on July 20,2021
Editorial Approval on November2, 2021

REFERENCES

[1] CM Christensen, *The Innovator's Dilemma, when new technologies cause great firms to fail*, Harvard Business School Press, Boston, Ch 10, pp159-171, ISBN 0-87584-585-1, 1997.

[2] Innovation Society, https://innovatingsociety.com/

[3] Susan Adams, Clayton Christensen, *On What He Got Wrong About Disruptive Innovation*, Available: https://www.forbes.com/sites/forbestreptalks/2016/10/03/clayton-christensen-on-what-he-got-wrong-about-disruptive-innovation /? sh = 76472bd4391b .[Accessed: 15-May-2021]

[4] The Disruptive Potential of Wireless EV Charging, Available: https://www.navigantresearch.com/reports/the-disruptive-potential-of-wireless-ev-charging . [Accessed: 13-Apr-2021]

[5] A. Marinescu, Georgiana. Rosu, L. Mandache, O. Baltag, "Achievements and Perspectives in Contactless Power Transmission", *EPE 2018 Conference*, Iasi, October 2018.

[6] JT Boys, GA Covic, "The Inductive Power Transfer Story at the University of Auckland", *IEEE Circuits & Systems Magazine*, Vol.15, Issue 2, May 2015, pp: 6-27.

[7] Search for Inductive WPT Electric Vehicles Publications in IEEE Xplore Archive, Available on: https://ieeexplore.ieee.org/search/searchresult.jsp?queryText=inductive%20power%20transfer% 20for% 20Electric% 20Vehicles & highlight = true & returnFacets = ALL & returnType = SEARCH & matchPubs = true & ranges = 2010 2020 Year , [Accesed: 07.20.2021].

[8] USPTO-US *Patent and Trademark Office*, Available on: https://www.uspto.gov/ , [Accesed: 07.20.2021]

[9] ICNIRP Guidelines for Limiting Exposure to Time - varying Electric and Magnetic Fields (1 Hz - 100 kHz), Health Physics 99 (6), pp. 818-836, 2010.

[10] K. Jiseong, K. Jonghoon, K. Sunkyu, K. Hongseok, S. In-Soo, S. Nam Pyo, et al., "Coil Design and Shielding Methods for a Magnetic Resonant Wireless Power Transfer System", *Proc. IEEE*, vol. 101, No. 6, pp. 1332-1342, 2013.

[11] TH Kim, S. Yoon, JG Yook, GH Yun, WY Lee, "Evaluation of power transfer efficiency with ferrite sheets in WPT system," *2017 IEEE Wireless Power Transfer Conference (WPTC)*, 2017, pp. 1 -4, two: 10.1109 / WPT.2017.7953894.

[12] A. Marinescu, I. Dumbravă, "AC Resistance of Inductive Coupler with Pitch Coils for Contactless Power Transfer", *International Conference on Applied and Theoretical Electricity (ICATE)* , October 4 - 6, 2018, Craiova, Romania.

[13] L. Tan, S. Pan, C. Xu, C. Yan, H. Liu, X. Huang, "Study of Constant Current-Constant Voltage Output Wireless Charging System Based on Compound Topologies", *Journal of Power Electronics*, Vol. 17, No. 4, pp. 1109-1116, July 2017.

[14] J. Deng *et al*., "Frequency and Parameter Combined Tuning Method of LCC-LCC Compensated Resonant Converter with Wide Coupling Variation for EV Wireless Charger", in *IEEE Journal of Emerging and Selected Topics in Power Electronics*, two: 10.1109 / JESTPE.2021.3077459.

[15] T. Ohira, "The kQ Product as Viewed by an Analog Circuit Engineer", *IEEE Circuits and Systems Magazine*, First Quarter 2017, pp.27-32.

[16] A. Marinescu , I. Dumbravă , "Using VNA for IPT Coupling Factor Measurement", *2016 IEEE International Power Electronics and Motion Control Conference* (PEMC) .

[17] G. Guidi, JA Suul, F. Jenset and I. Sorfonn, "Wireless Charging for Ships: High-Power Inductive Charging for Battery Electric and Plug-In Hybrid Vessels", in *IEEE Electrification Magazine*, vol. 5, no. 3, pp. 22-32, Sept. 2017, two: 10.1109 / MELE.2017.2718829.

[18] K. Kusaka, R. Kusui, J. Itoh, D. Sato, S. Obayashi, and M. Ishida, "A 22 kW-85 kHz Three-phase Wireless Power Transfer System with 12 coils", *IEEE Energy Conversion Congress and Exposition (ECCE*), Baltimore, MD, USA, 2019, pp. 3340-3347.

[19] A. Calabro, B. Cohen, A. Daga, J. Miller and F. McMahon, "Performance of 200-kW Inductive Charging System for Range Extension of Electric Transit Buses", *2019 IEEE Transportation Electrification Conference and Expo (ITEC*), 2019, pp. 1-5, doi: 10.1109 / ITEC.2019.8790490.

[20] SAE J2954: - SAE J2954: *2020 Surface Vehicle Standard-Wireless PowerTransfer for Light-Duty Plug-in / Electric Vehicles and Alignment Methodology*

[21] Witricity, Qi Interface, Available on: http://www.wirelesspowerconsortium.com/ [Accesed: 6.10.2021] Available: http://www.wirelesspowerconsortium.com/

[22] IEC PAS 63095-1.2: 2017, "Interface definitions" and "Reference Designs".

[23] ITU-R Report SM.2303-2, 2017, *Wireless Power Transmission using Technologies other than Radio Frequency Beam*, pp.29-33.

[24] M.Kesler, *Highly Resonant Wireless Power Transfer: Safe, Efficient, and over Distance*, Witricity White paper, 2017.

[25] M. Feliziani and S. Cruciani, "Mitigation of the magnetic field generated by a wireless power transfer (WPT) system without reducing the WPT efficiency", *Proc. INT Symp. Electromagn. Compat. (EMC - EUROPE)*, 2013, pp. 610-615.

[26] DG Marinescu, V. Nicolae, F. Serban, I. Vieru, N. Mierloiu, N. Boicea, A. Marinescu, A.Vintila, „An Electric Crossover Concept Car", *EVS30 Symposium* Stuttgart, Germany, October 9 - 11, 2017.

[27] A.Marinescu, I.Dumbrava, A.Vintilă, DG Marinescu, D.Neagu, V.Nicolae, A.Radu, „The Way to Engineering EV Wireless Charging: DACIA Electron", *EV 2017* (Electric Vehicles International Conference & Show), Bucharest, 2017.

[28] B. Basille, J. Rangaraju, „Wich new semiconductor technologies will speed electric vehicle charging adoption", *AN SLIY005*, pp 1-7, Texas Instruments Inc, 2017.

[29] C. Suarez, W. Martinez, "Fast and Ultra-Fast Charging for Battery Electric Vehicles - A Review," *2019 IEEE Energy Conversion Congress and Exposition (ECCE)*, 2019, pp. 569-575, doi: 10.1109 / ECCE.2019.8912594.

[30] S. Zhang, H. Sun, C. Lyu, "A method of SOC estimation for power Li-ion batteries based on equivalent circuit model and extended Kalman filter", *2018 13th IEEE Conference on Industrial Electronics and Applications (ICIEA*), 2018, pp. 2683-2687, doi: 10.1109 / ICIEA.2018.8398164.

[31] R. Bosshard, JW Kolar, "Inductive power transfer for electric vehicle charging: Technical challenges and tradeoffs", *IEEE Power Electronics Magazine*, vol. 3, no. 3, pp. 22-30, Sept. 2016.

[32] Gereon Meyer (Ed), *Advanced Microsystems for Automotive Applications*, Springer, 2012, Ch.5, pp. 49-52

[33] Horizon 2020, Work Program 2016-2017, General Annexes, pp. 35-44, Available on: https://ec.europa.eu/programmes/ horizon2020 / en / what-work-program , [Accesed on 5.20.2021]

[34] M. Emre, P. Vermaat, D. Naberezhnykh, Y. Damousuis, T. Theodoropoulos, V. Cirimele, A. Doni, "D 3.3.1 - Review of existing power transfer solutions", *Public Deliverable EU FABRIC project (605405)*, 2014.

[35] A. Marinescu, A. Vintila, DG Marinescu, V. Nicolae, "Development of a wireless battery charger for Dacia Electron EV," *10th*

International Symposium on Advanced Topics in Electrical Engineering (ATEE), pp. 241-247, 2017

[36] ACER (Romanian EMC Association), Available on: www.acero.ro/ , Accessed: 14.07.2021

[37] INDAELTRAC SRL, Available on: https://www.indaeltrac.com/ , Accessed: 20.07.2021

[38] N. Golovanov, A. Marinescu, „Power Supply of EV Charging Stations in a Smart Grid (in Romanian)", *The 13th edition of the Conference "ASTR Days"* October 17-19, 2018, Ploiești, Romania.

[39] WJ Mitchell, Ch. E. Borroni-Bird, LD Burns, *Reinventing the Automobile-Personal Urban Mobility for the 21st Century*, 227 pp. , The MIT Press, Cambridge, Massachusetts, 2010

[40] Sylvia Heyvaert, O. Hegazy, Th. Coosemans, J. Van Mierlo, „Social Acceptance of Wireless Battery Charging Systems: Belgium Case Study", *2014 IEEE International Electric Vehicle Conference* (IEVC), 2014, pp. 1-6, doi: 10.1109 / IEVC.2014.7056075 .

[41] *Silent Revolution: Engine Sound Design for EVs*, Available on: https://interestingengineering.com/silent-revolution-engine-sound-design-for-evs , Accessed: 20.06.2021

[42] A. Marinescu, „The Romanian Wireless Power Transfer Network", *JESI Journal of Engineering Sciences and Innovation*, Electrical and 149-156, 2020

[43] "Wireless Power Transfer" Special issue of *Annals of the University of Craiova*, Vol. 42, Issue 1, pp. 47, 2018

Application of the Rotor Field-Oriented Control for an Induction Motor Used in Electric Traction

Mihaela Popescu*, Alexandru Bitoleanu* and Constantin Vlad Suru*
* University of Craiova, Faculty of Electrical Engineering, Craiova, Romania, mpopescu@em.ucv.ro

DOI: 10.52846/AUCEE.2021.1.02

***Abstract* – In this paper, the rotor field-oriented control is applied for a three-phase induction motor used in electric traction of an autonomous locomotive powered by a battery. First, the operating equations in the rotor field-oriented system are introduced. Then, the control scheme based on the structural scheme and operational equations are presented. After referring to the design of the controllers, the performances of the control system during the start-up process by prescribing a ramp speed and step rotor flux are addressed and analyzed. Four values of the prescribed speed are taken into consideration. Through the presented results, the synthesis of the control system and control algorithm are validated.**

Cuvinte cheie: *control cu orientare după fluxul rotoric, tracțiune electrică, locomotivă autonomă, motor trifazat de inducție, regulator cu histerezis, regulator PI.*

Keywords: *rotor field-oriented control, electric traction, autonomous locomotive, three-phase induction motor, hysteresis controller, PI controller.*

I. Introduction

In the 1970s, Haase [1] and Blaschke [2] introduced the so-called field-orientation technique applied to the induction motor, which involves decoupling the torque and magnetic flux as with the direct current motor. In a reference frame that rotates simultaneously with the rotor flux, the torque can be controlled by the q-axis component of the stator current vector.

The best known implementation of the rotor field-oriented control is the indirect control. According to this, the rotor flux is estimated and not measured, based on the associated equations [3].

When the voltage control is taken into consideration, two control paths exist in the structure of the rotor field-oriented control [4]-[6]. Within the first path, the external loop is of the speed and the subordinate loop is of the active current. In the second path, the external loop is of the rotor flux and the subordinate loop is of the reactive current.

The difficulty in the implementation of the voltage control consists of the need to design four controllers. But, if a control structure with current control is adopted, only two controllers remain in the system to be designed and the inverter control is performed by a hysteresis controller [6].

Among the challenges of implementing the rotor field-oriented control, the accurate estimation of the motor parameters and ensuring the most precise control of the current's components are highlighted [7]-[14]. In [11], the proposed strategy involves the use of the rotor field-oriented model equations to estimate the electromagnetic torque and rotor resistance.

To estimate the rotor resistance, the authors of [10] designed a scheme based on the rotor flux model and fuzzy controller. In [14], a sensorless fuzzy logic based indirect vector control with an adaptation scheme for the rotor resistance using neural learning algorithm was taken into consideration.

An adaptive sliding-mode observer was proposed in [8], and the online adaptation of the rotor resistance was achieved. A sliding mode observer based on rotor-flux was presented in [12] and a predictive field-oriented controller was used.

To keep the speed and torque of the induction motor oriented on the rotor field during the supply voltage drop, a new control technique was analyzed in [13], in which the d-axis and q-axis current control is based on solving the voltage, current, and torque constraints in the current plane.

The results presented in this paper were obtained by carrying out the PACETSINEFEN project in the frame of POC program, European Regional Development Fund. The implementation of the proposed control system will be done on an electric traction physical model of a locomotive powered by a battery.

The next part of this paper is organized as follows. In section II, the operating equations and control scheme are presented. Next, the attention is directed to the synthesis of speed and rotor flux controllers. Then, section IV presents the performance of the system, in which, the start-up process by prescribing a ramp speed and a step rotor flux, for four prescribed speeds, are taken into consideration. The paper ends with some conclusions and future research directions.

II. Operating Equations and Control Scheme

The equation of operation are expressed in the (d, q) reference frame with the d-axis oriented in the direction of the rotor flux (Fig. 1). As shown, the q-axis component of the rotor flux is zero. λ is the angle between the rotating (d, q) reference frame and the fixed reference frame (α, β).

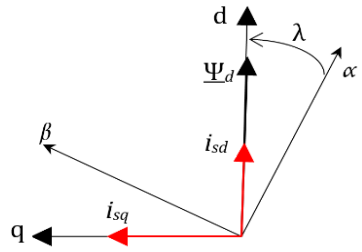

Fig. 1. Orientation of the rotating (d, q) reference frame.

The following expression of the electromagnetic torque shows that, if the rotor flux is constant, the electromagnetic torque can be controlled only through the q-axis component of the rotor current.

$$m = -\frac{3}{2} p \Psi_{rd} i_{rq}. \quad (1)$$

The equations of the rotor circuit are [15]:

$$0 = R_r i_{rd} + \frac{d}{dt}\Psi_{rd}; \quad (2)$$

$$0 = R_r i_{rq} + (\omega_1 - p\omega)\Psi_{rd}, \quad (3)$$

where the expressions of the rotor flux on the two axes are:

$$\Psi_{rd} = L_r i_{rd} + L_m i_{sd}; \quad (4)$$

$$0 = L_r i_{rq} + L_m i_{sq}. \quad (5)$$

The equation of motion is added to the system of equations.

$$J\frac{d\omega}{dt} = -\frac{3}{2} p \Psi_{rd} i_{rq} - m_s. \quad (6)$$

The following quantities are used in equations (1) - (6):

$\underline{i}_r$, $\underline{\Psi}_r$ - the spatial phasors of the rotor currents and rotor flux referred to the system (d, q);
m, m_s – the electromagnetic and static torque respectively;
R_s, R_r – the stator and rotor resistances referred to the stator;
L_r – the inductance on a rotor phase referred to the stator;
L_m – the magnetization inductance;
p – the number of pole pairs;
ω – the angular velocity of the rotor;
ω_1 – the electrical speed of the rotating coordinate system.

The adopted control structure shown in Fig. 2 involves the current control, which is easier to implement compared to the voltage control. As shown, to synthesize the control signals for transistors, a three-phase hysteresis controller (Hys) is used. The existence of two controllers (Rω for speed and Rψ for the rotor flux), the transformation blocks for the reference frame ((d,q) →(α,β) and (α,β)→(a,b,c)) and the speed transducer (Tω) is highlighted. The rotor flux is calculated based on the stator current and the motor speed and the position angle λ of the rotating reference frame is calculated based on the sine and cosine functions, as follows [6], [15]:

$$cos\lambda = \frac{\Psi_{s\alpha}}{|\underline{\Psi}_r|}; \quad sin\lambda = \frac{\Psi_{s\beta}}{|\underline{\Psi}_r|}. \quad (7)$$

As illustrated in Fig. 2, there are two independent control paths, for speed and active current control and for rotor flux and reactive current respectively.

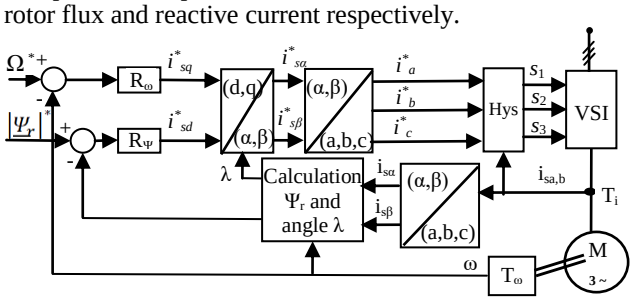

Fig. 2. Structure of the control system with current control.

In the first path, the prescribed active current is obtained at the output of the speed controller, whereas, in the second path, the prescribed reactive current is obtained at the output of the flux controller.

III. Synthesis of Speed and Rotor Flux Controllers

To express the involved transfer functions of the two controllers, the operational equations in the Laplace domain were used [6].

The parameters of the PI speed controller ($\theta_{1\Omega}$ and θ_{Ω}) which intervene in its transfer function,

$$G_{R\omega}(s) = \frac{1+s\theta_{1\Omega}}{s\theta_{\Omega}}, \quad (8)$$

were determined using the symmetry criterion [6].

$$\theta_{1\Omega} = 4T_{\Sigma}; \quad \theta_{\Omega} = \frac{8K_f T_{\Sigma}^2}{T_m}, \quad (9)$$

where T_{Σ} is the dead time of the active current control loop (the sum of the speed transducer time constant and the sampling time T_s), the amplification factor K_f is:

$$K_f = \frac{3pL_m}{2L_r}\frac{\psi_{rN}}{T_N}\frac{\Omega_N}{}, \quad (10)$$

and the mechanical time constant (T_m) is:

$$T_m = \frac{2JL_r\Omega_N}{3pL_m I_N \Psi_{rN}}. \quad (11)$$

The parameters of the PI flux controller ($\theta_{1\psi}$ and θ_{ψ}) in the transfer function,

$$G_{R\Psi}(s) = \frac{1+s\theta_{1}\Psi}{s\theta_{\Psi}}, \quad (12)$$

were provided by using the Modulus criterion in Kesller variant [6].

IV. Control System Performance

The performance of the control system was assessed by using a specific Matlab-Simulink model developed for the experimental test platform. Table I summarizes the main parameters of the voltage source inverter and traction motor and Table II contains the parameters of the two controllers.

TABLE I.
Main Parameters of the Voltage Source Inverter and Traction Motor

Inverter parameters							
U_{in} (V)	**U_{Nout} (V)**	**P_N (kVA)**	**f_N (Hz)**	**f (Hz)**	**C_d (μF)**	**U_{CdN} (V)**	**IGBTs**
750	500	190	50	0-135	1400	1800	CM2400HC-34H
Traction motor rated parameters							
U_N (V)	**P_{2N} (kW)**	**f_{1N} [(Hz)**	**I_N (A)**	**cosφ$_N$**	**η_N**	**s_N**	**n_N (rpm)**	**M_N (Nm)**
500	155	45	218	0.888	0.924	0.02518	1316	1125
R_1 (Ω)	**X_{1N} (Ω)**	**$L_{σ1}$ (mH)**	**R_2 (Ω)**	**X_{2N} (Ω)**	**$L_{σ2}$ (mH)**	**R_m (Ω)**	**X_m (Ω)**	**L_m (mH)**
0.035	0.0621	0.2197	0.0358	0.067	0.2387	89.38	3.2507	11.497

TABLE II.
Parameters of the Speed and Flux Controllers

$K_{pΩ}$	**$T_{iΩ}$**	**$K_{pΩ}$**	**$T_{iΩ}$**	**$K_{pψ}$**	**$T_{iψ}$**
$\Omega_p \geq \Omega_N/2$		$\Omega_p < \Omega_N/2$		36	0.32
100	0.003	200	0.004		

The ramp prescription of four speed values ($\Omega_N/10$, $\Omega_N/2$, Ω_N and $2\Omega_N$) and step rotor flux, at nominal resistive torque is considered.

The time evolution of speed, rotor flux, rotor flux components, electromagnetic torque, phase current and current components on the two axes are determined and analyzed. The main quantities during the steady-state operation are summarized for each case. To illustrate the performance of the control system, the following quantities were determined: rise time, settling time, maximum current and torque, overshoot, stator current distortion factor, efficiency and power factor.

A. Performance in the case of prescribed speed of $0.1\Omega_N$

The time evolutions of the main quantities for the prescribed speed of $0.1\Omega_N$ are shown in Fig. 3 - Fig. 9.

Also, the main quantities during the steady-state operation are illustrated in Table III and the quantities that characterize control system performance are summarized in Table IV.

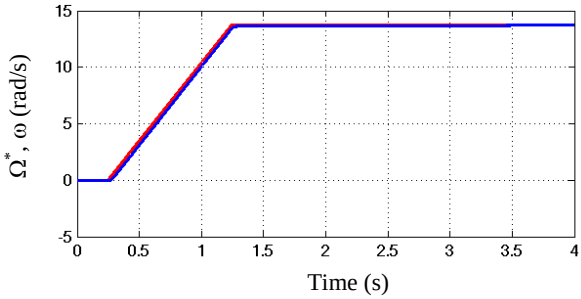

Fig. 3. Time evolution of the speed: prescribed speed ($\Omega_N/10$) –in red; actual speed – in blue.

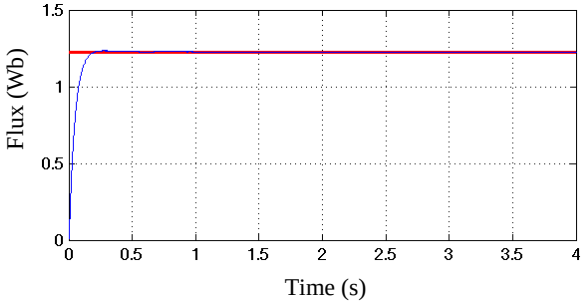

Fig. 4. Time evolution of the rotor flux for prescribed speed $\Omega_N/10$: prescribed value– in red; actual value – in blue.

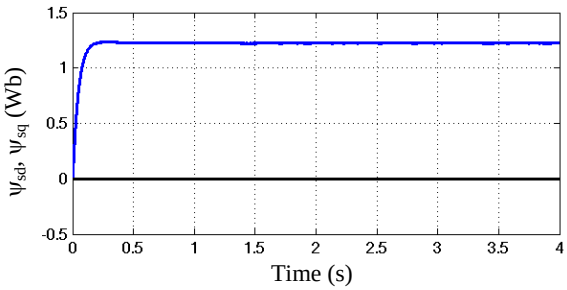

Fig. 5. Time evolution of the rotor flux components for prescribed speed $\Omega_N/10$: on the d axis – in blue; on the q axis – in black.

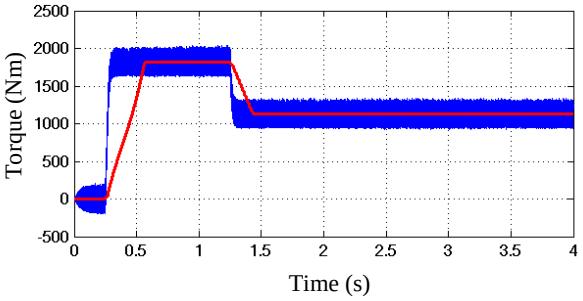

Fig. 6. Time evolution of the electromagnetic torque for prescribed speed $\Omega_N/10$: average torque – in red; actual torque – in blue.

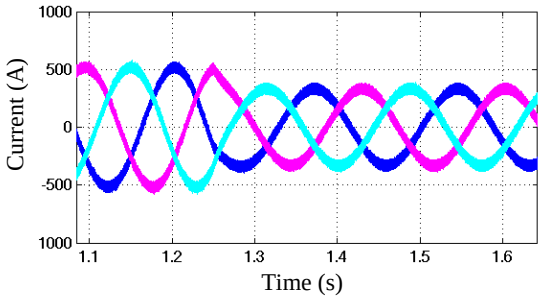

Fig. 7. Time evolution of the stator currents for prescribed speed $\Omega_N/10$.

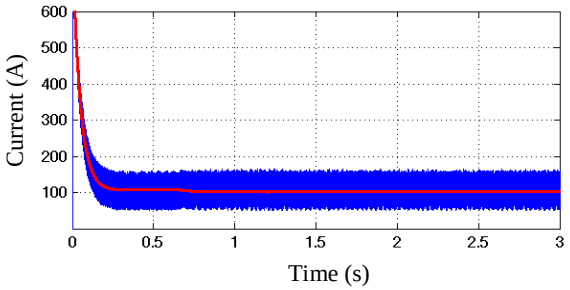

Fig. 8. Time evolution of the stator current component on the d axis for prescribed speed $\Omega_N/10$: prescribed value– in red; actual value– in blue.

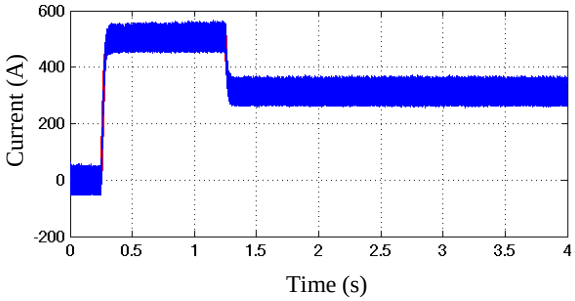

Fig. 9. Time evolution of the stator current component on the q axis for prescribed speed $\Omega_N/10$: prescribed value – in red; actual value – in blue.

TABLE III.
MAIN QUANTITIES IN STEADY STATE FOR PRESCRIBED SPEED $\Omega_N/10$

U (V)	U_1 (V)	I (A)	I_1 (A)	P (kW)	S (kVA)	P_m (kW)
377	40	235	234	17	266	15.4

TABLE IV.
CONTROL PERFORMANCE FOR PRESCRIBED SPEED $\Omega_N/10$

t_c (s)	t_r (s)	I_M/I_N	T_M/T_N	THD_I (%)	η	PF
1	4	1.8	1.6	12.33	0.9	0.064

B. *Performance in the case of prescribed speed of $0.5\Omega_N$*

In the case of prescribed speed of $0.5\Omega_N$, the time evolutions of the main quantities are presented in Fig. 10 - Fig. 17. Table V shows the quantities specific to the steady-state operation and Table VI contains the indicators of the control system performance.

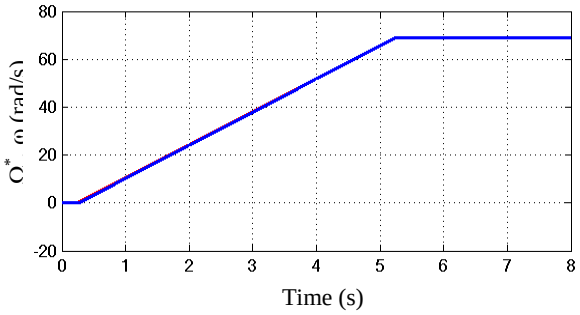

Fig. 10. Time evolution of the speed: prescribed speed ($\Omega_N/2$) –in red; actual speed – in blue.

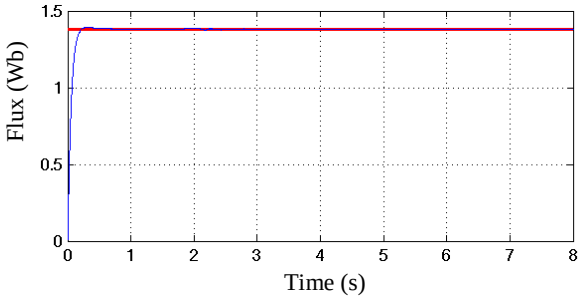

Fig. 11. Time evolution of the rotor flux for prescribed speed $\Omega_N/2$: prescribed value– in red; actual value – in blue.

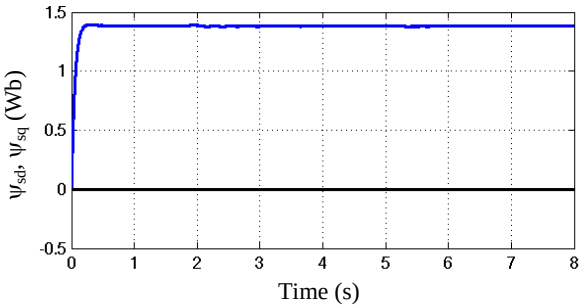

Fig. 12. Time evolution of the rotor flux components for prescribed speed $\Omega_N/2$: on the d axis – in blue; on the q axis – in black.

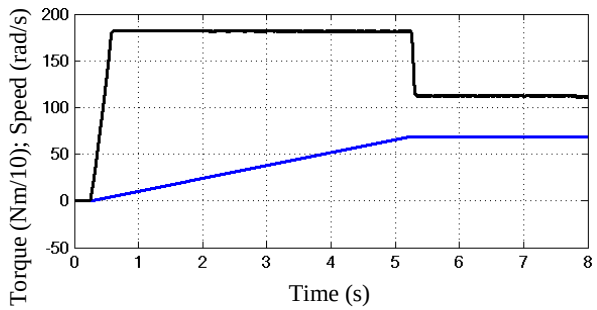

Fig. 13. Time evolution of the average electromagnetic torque (in black) and actual speed (in blue) for prescribed speed $\Omega_N/2$.

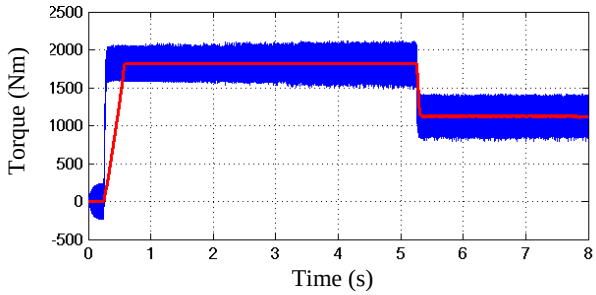

Fig. 14. Time evolution of the electromagnetic torque for prescribed speed $\Omega_N/2$: average torque – in red; actual torque – in blue.

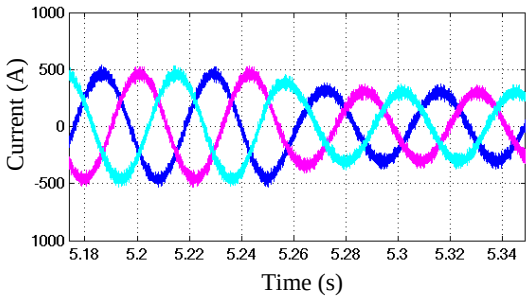

Fig. 15. Time evolution of the stator currents for prescribed speed $\Omega_N/2$.

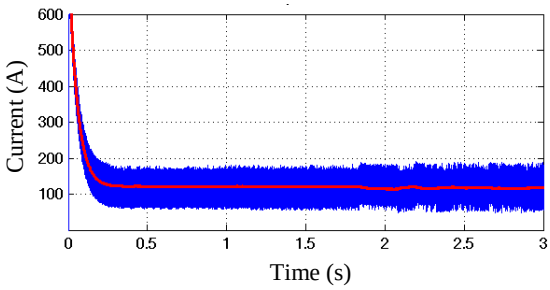

Fig. 16. Time evolution of the stator current component on the d axis for prescribed speed $\Omega_N/2$: prescribed value– in red; actual value– in blue.

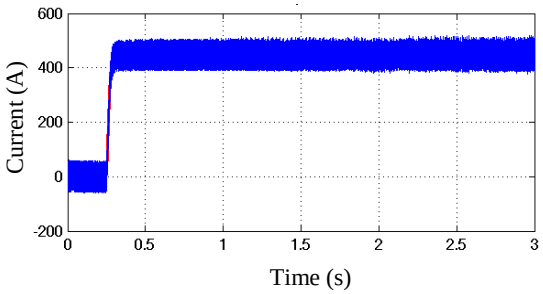

Fig. 17. Time evolution of the stator current component on the q axis for prescribed speed $\Omega_N/2$: prescribed value – in red; actual value – in blue.

TABLE V.
MAIN QUANTITIES IN STEADY STATE FOR PRESCRIBED SPEED $\Omega_N/2$

U (V)	U_1 (V)	I (A)	I_1 (A)	P (kW)	S (kVA)	P_m (kW)
376	138	233	231	80	263	71

TABLE VI.
CONTROL PERFORMANCE FOR PRESCRIBED SPEED $\Omega_N/2$

t_c (s)	t_r (s)	I_M/I_N	T_M/T_N	THD_I (%)	η	PF
5.6	5.6	1.8	1.8	12.42	0.94	0.31

C. *Performance in the case of prescribed speed of Ω_N*

For the case of prescribing the nominal speed, Table VII illustrates the main quantities which characterize the steady state regime and the time evolution of the quantities of interest is shown in Fig. 18 – Fig. 25. The control performance for the prescribed nominal speed is contained in Table VIII.

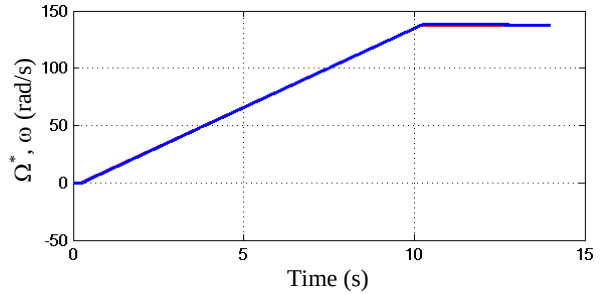

Fig. 18. Time evolution of the speed: prescribed speed (Ω_N) –in red; actual speed – in blue.

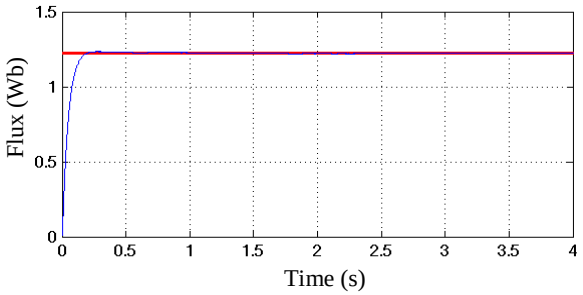

Fig. 19. Time evolution of the rotor flux for prescribed speed Ω_N: prescribed value– in red; actual value – in blue.

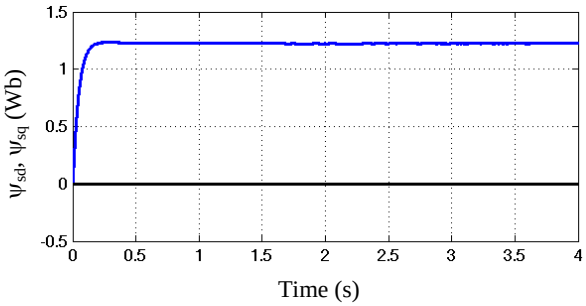

Fig. 20. Time evolution of the rotor flux components for prescribed speed Ω_N: on the d axis – in blue; on the q axis – in black.

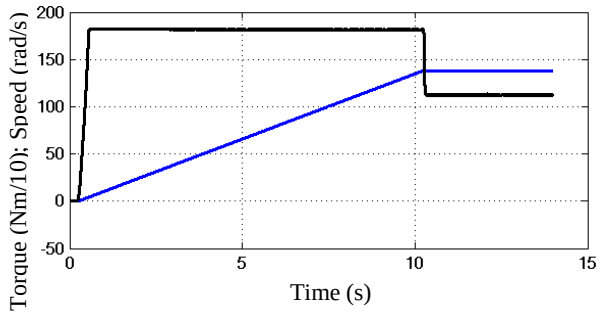

Fig. 21. Time evolution of the average electromagnetic torque (in black) and actual speed (in blue) for prescribed speed Ω_N.

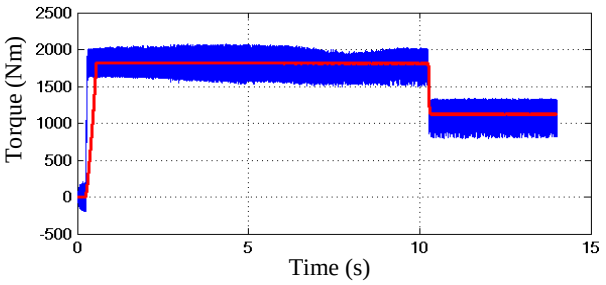

Fig. 22. Time evolution of the electromagnetic torque for prescribed speed Ω_N: average torque – in red; actual torque – in blue.

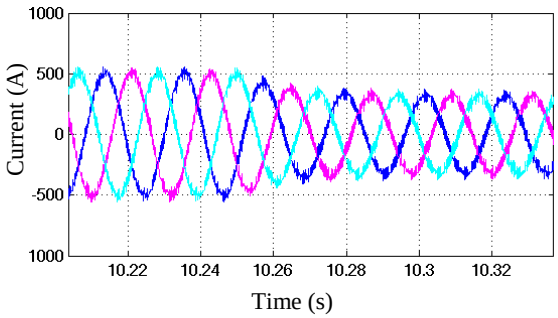

Fig. 23. Time evolution of the stator currents for prescribed speed Ω_N.

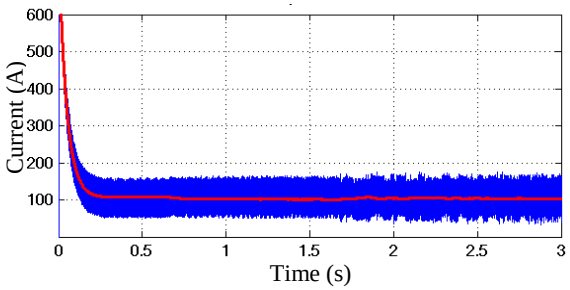

Fig. 24. Time evolution of the stator current component on the d axis for prescribed speed Ω_N: prescribed value– in red; actual value– in blue.

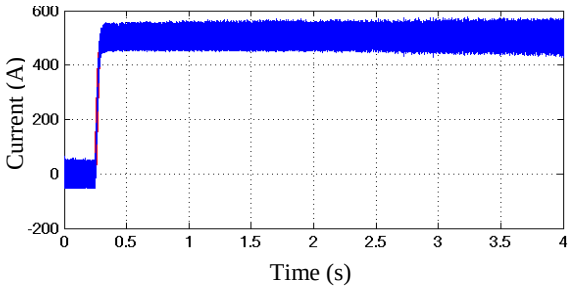

Fig. 25. Time evolution of the stator current component on the q axis for prescribed speed Ω_N: prescribed value – in red; actual value – in blue.

TABLE VII.
MAIN QUANTITIES IN STEADY STATE FOR PRESCRIBED SPEED Ω_N

U (V)	U_1 (V)	I (A)	I_1 (A)	P (kW)	S (kVA)	P_m (kW)
378	264	225	223	160	254	155

TABLE VIII.
CONTROL PERFORMANCE FOR PRESCRIBED SPEED Ω_N

t_c (s)	t_r (s)	I_M/I_N	T_M/T_N	THD_I (%)	η	PF
10	10	1.8	1.6	11.4	0.94	0.63

D. *Performance in the case of prescribed speed of $2\Omega_N$*

When $2\Omega_N$ is prescribed, the steady-state regime is characterized by the quantities illustrated in Table IX. How the quantities of interest evolve over time is presented in Fig. 26 – Fig. 32.

The system performance for the prescribed speed of $2\Omega_N$ is summarized in Table X.

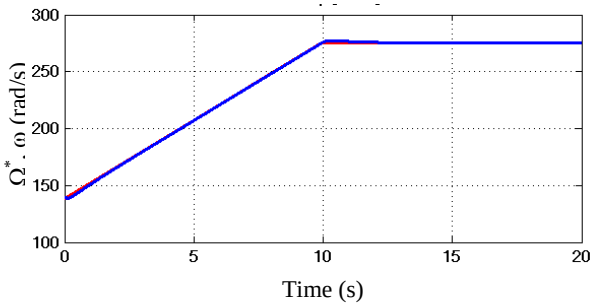

Fig. 26. Time evolution of the speed: prescribed speed ($2\Omega_N$) –in red; actual speed – in blue.

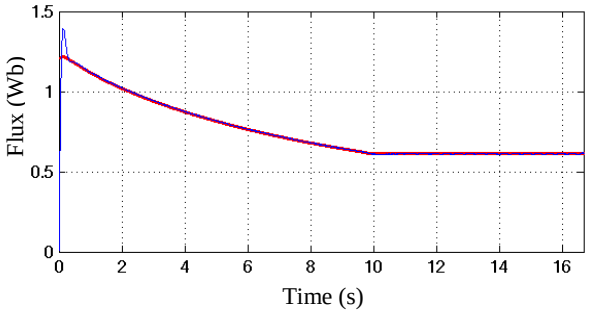

Fig. 27. Time evolution of the rotor flux for prescribed speed $2\Omega_N$: prescribed value– in red; actual value – in blue.

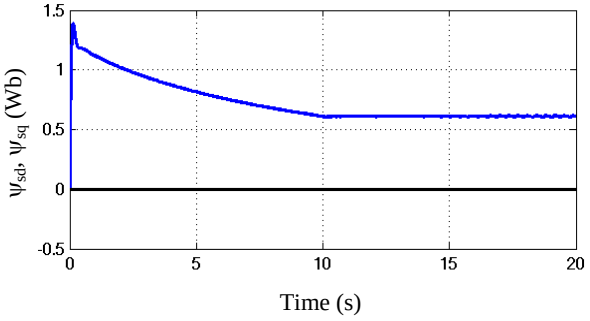

Fig. 28. Time evolution of the rotor flux components for prescribed speed $2\Omega_N$: on the d axis – in blue; on the q axis – in black.

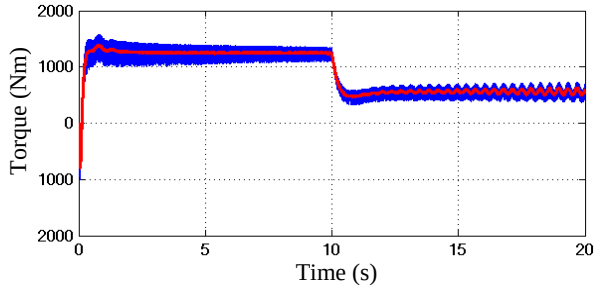

Fig. 29. Time evolution of the electromagnetic torque for prescribed speed $2\Omega_N$: average torque – in red; actual torque – in blue.

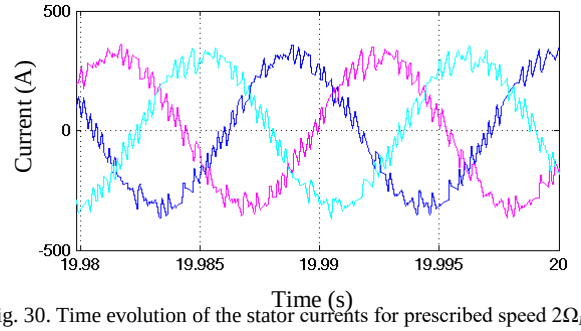

Fig. 30. Time evolution of the stator currents for prescribed speed $2\Omega_N$.

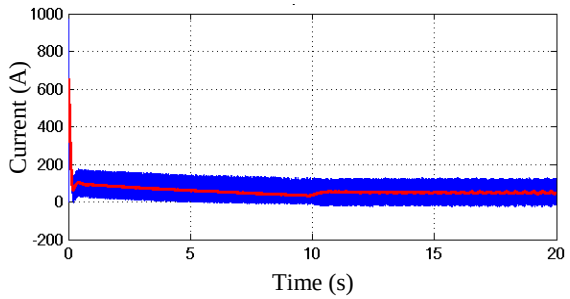

Fig. 31. Time evolution of the stator current component on the d axis for prescribed speed $2\Omega_N$: prescribed value– in red; actual value– in blue.

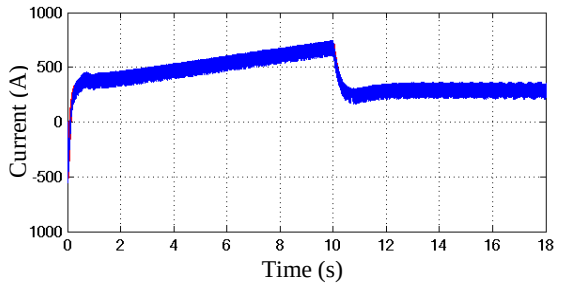

Fig. 32. Time evolution of the stator current component on the q axis for prescribed speed $2\Omega_N$: prescribed value – in red; actual value – in blue.

TABLE IX.
MAIN QUANTITIES IN STEADY STATE FOR PRESCRIBED SPEED $2\Omega_N$

U (V)	U_1 (V)	I (A)	I_1 (A)	P (kW)	S (kVA)	P_m (kW)
371	269	225	224	168	250	155

TABLE X.
CONTROL PERFORMANCE FOR PRESCRIBED SPEED $2\Omega_N$

t_c (s)	t_r (s)	I_M/I_N	T_M/T_N	THD_I (%)	η	PF
20	20	2.98	1.42	11.14	0.94	0.667

E. *Results analysis*

The time evolution of the speed shown in Fig. 2, Fig. 10, Fig. 18 and Fig. 26 illustrates that the actual speed accurately follows the prescribed speed and there is only a very small overshoot. This overshoot is higher at high speed, but it does not exceed 0.04 %.

It can be seen that the rotor flux has a fast increase (Fig. 3, Fig. 11, Fig. 19 and Fig. 27) and a higher short-term overshoot occurs at high speed (for speed over the nominal value). Then, the prescribed value is very well followed.

The component of the rotor flux on the q axis is always zero (Fig. 4, Fig. 12, Fig. 20 and Fig. 28), which confirms the good orientation of the system according to the rotor flux.

As shown in Fig. 6, Fig. 14, Fig. 22 and Fig. 29, the electromagnetic torque has a fast increase too. Its maximum value is of $1.8T_N$ for $0.5\Omega_N$ and of $1.42T_N$ for $2\Omega_N$ (Table XI). Also, high ripple of the electromagnetic torque is highlighted even during the steady-state operation.

The stator current increases rapidly to a maximum value of about $1.8I_N$ for prescribed speeds below the nominal value and of about $3I_N$ for high prescribed speed (Fig. 7, Fig. 15, Fig. 23, Fig. 31 and Table XI). There are ripples in the current waveform due to the variable switching frequency (2.5 - 4 kHz).

In terms of performance indicators during the steady-state operation, the power factor has a very low value (about 0.064) at the lowest speed and increasing values with increasing prescribed speed (about 0.667 for the highest speed), as shown in Table XI. The efficiency value is 0.9 for the lowest prescribed speed and 0.94 for higher speeds (Table XI). The total harmonic distortion factor of the stator current is quite high (about 12 % at low speeds and 11 % at high speeds) - Table XI.

TABLE XI.
SYNTHESIS OF CONTROL PERFORMANCE INDICATORS FOR ALL PRESCRIBED SPEEDS

	t_c (s)	t_r (s)	I_M/I_N	T_M/T_N	THD_I (%)	η	*PF*
$0.1\Omega_N$	1	4	1.8	1.6	12.33	0.9	0.064
$0.5\Omega_N$	5.6	5.6	1.8	1.8	12.42	0.94	0.31
Ω_N	10	10	1.8	1.6	11.4	0.94	0.63
$2\Omega_N$	20	20	2.98	1.42	11.14	0.94	0.667

V. CONCLUSIONS

The good results presented in this paper validate both the proposed control algorithm and the synthesis of the control system.

Starting from the observation that the switching frequency is not constant during the system operation (it varies from about 2.5 kHz in steady-state regime to about 4 kHz in transient regime), the adoption of a variable hysteresis band for the current controller would be necessary.

In order for the prescribed speed ramp to be tracked, it is necessary to adapt the speed controller parameters according to the prescribed speed range. By using the designed parameters of the speed controller for prescribed speed over $\Omega_N/2$, good performance in speed tracking is obtained. At lower prescribed speeds, however, keeping the same speed controller parameters leads to the inability for the prescribed speed ramp to be accurately followed, but the performance in steady state regime remains good.

The next stage of the research will be directed towards the use of an adaptive speed controller and the implementation the proposed control system on an experimental setup, which is being worked on.

ACKNOWLEDGMENT

This work was performed through Competitiveness Operational Program, project PACETSINEFEN, ID: P_40_196/105687, (2016–2021), European Regional Development Fund.

Source of research funding in this article: POC Program, project PACETSINEFEN.

Contribution of authors:
First author – 50%
First coauthor – 30%
Second coauthor – 20%

Received on July 29, 2021
Editorial Approval on November 30, 2021

REFERENCES

[1] K. Hasse, "Zur Dynamik drehzahlgeregelter Antriebe mit Stromrichtergespeisten Asynchronkurzschlufermotoren," *Ph.D. dissertation*, T. U. Darmstadt, 1969.

[2] F. Blaschke, "The principle of field orientation as applied to the new transvector closed loop control system for rotating field machines," *Siemens Rev*, vol. 39, no. 5, pp. 217–220, May 1972.

[3] P. C. Valencia-Manrique and R. Jesus Coaquira-Castillo, "Speed performance comparative of indirect field oriented control based on current model for induction motors in educational equipment," in *Proc. 2020 IEEE XXVII International Conference on Electronics, Electrical Engineering and Computing*, 2020, pp. 1-4.

[4] D. G. Holmes, B. P. McGrath and S. G. Parker, "Current regulation strategies for vector-controlled induction motor drives," *IEEE Transactions on Industrial Electronics*, vol. 59, no. 10, pp. 3680-3689, Oct. 2012.

[5] A. Pal, S. Das and A.K. Chattopadhyay, "An improved rotor flux space vector based mras for field-oriented control of induction motor drives," *IEEE Transactions on Power Electronics*, vol. 33, no. 6, pp. 5131-5141, June 2018.

[6] M. Popescu, A. Bitoleanu and C. V. Suru, "Synthesis of rotor field-orientation control for induction traction motor," in *Proc. 2021 International Conference on Applied and Theoretical Electricity (ICATE)*, 2021, pp. 1-6.

[7] G. Jo and J. Choi, "Rotor field-oriented V/f drive system implementation with oscillation suppression compensator in induction motors," *IEEE Journal of Emerging and Selected Topics in Power Electronics*, 2020.

[8] S. Yang, R. Sun, P. Cao, Z. Xie and X. Zhang, "Sliding-mode observer based rotor resistance updating method for indirect vector controlled induction motor," in *Proc. 2017 IEEE Transportation Electrification Conference and Expo*, Asia-Pacific (ITEC Asia-Pacific), Harbin, China, 2017, pp. 1-5.

[9] A. Gogea, O. Stoicuta, T. Pana and A. Paramon, Comparative study a two adaptive observers of speed and rotor flux of the induction motor," in *Proc. 2019 8th International Conference on Modern Power Systems* (MPS), Cluj-Napoca, Cluj, Romania, 2019, pp. 1-8.

[10] S. Chacko and S. Jain, "TS -Fuzzy controller based rotor resistance estimation for indirect field oriented controlled IM drive utilizing rotor flux," in *Proc. 2014 Annual IEEE India Conference* (INDICON), Pune, India, 2014, pp. 1-6.

[11] D. Troncon, M. Carbonieri, L. Alberti and N. Bianchi, "Measurements and simulation of induction machines flux linkage characteristics adopting rotor field orientation," in *Proc. 2020 International Conference on Electrical Machines* (ICEM), Gothenburg, Sweden, 2020, pp. 225-231.

[12] H. Xie, F. Wang, W. Zhang, C. Garcia, J. Rodríguez and R. Kennel, "Sliding mode flux observer based predictive field oriented control for induction machine drives," in *Proc. 2020 IEEE 9th International Power Electronics and Motion Control Conference* (IPEMC2020-ECCE Asia), 2020, pp. 3021-3025.

[13] M. J. Cheerangal, A. K. Jain and A. Das, "Control of rotor field-oriented induction motor drive during input supply voltage sag," *IEEE Journal of Emerging and Selected Topics in Power Electronics*, vol. 9, no. 3, pp. 2789-2796, June 2021.

[14] S. Chandran, "Neural learning algorithm based rotor resistance estimation for fuzzy logic based sensorlless IFOC of induction motor," in *Proc. 2014 International Conference on Power Signals Control and Computations*, Thrissur, India, 2014, pp. 1-6.

[15] T. Pană, O. C. Stoicuța, *Stabilitatea sistemelor de acționare vectoriala cu motoare de inducție*, Ed. Mediamira, 2016.

Impact of Experimental Measurements Accuracy on Validation Process of Crimped Connections

Alin-Iulian Dolan* and Constantin-Florin Ocoleanu*
* University of Craiova, Electrical Engineering Faculty, Craiova, Romania, adolan@elth.ucv.ro
* University of Craiova, Electrical Engineering Faculty, Craiova, Romania, focoleanu@elth.ucv.ro

DOI: 10.52846/AUCEE.2021.1.03

Abstract **- In the process of validation of crimped connections, the determination of the connector resistance factor and of the initial scatter coefficient has a decisive role. In this paper is studied the impact of the experimental measurements accuracy on the calculation of initial scatter, cumulating data from various types of crimped connections. This coefficient provides information on the behavior of the crimped connection immediately after installation before any aging effect begins. The standards establish that 6 samples are sufficient to be tested to estimate the identification of a "family" of connectors. The measurements were performed on crimped connections of barrel of terminal lug type for three cross sections of cables and on crimped connections of bimetallic through connector type for two pairs of cross sections. The initial scatter is influenced by 6 representative measured quantities as voltage drops, currents and conductor lengths. First, it was imposed a variation by one unit of hundredths digit of initial scatter and was recorded the variation of each quantity, the others 5 quantities being kept constant. Then simultaneous variations of the 6 quantities caused by device reading errors were imposed, determining the quantities with the greatest influence on initial scatter. Useful recommendations for experimenter are made.**

Cuvinte cheie: *conexiuni sertizate, resistenţă electrică, rezultate experimentale, valori statistice, maşini electrice.*

Keywords: *crimped connectors, electrical resistance, experimental results, statistical values, electrical machines.*

I. INTRODUCTION

The crimped connections are permanent electrical contacts widely used in the construction of electrical machines, having a great influence on their reliability [1]. The crimping process is a mechanical one and the crimping quality depends on several factors, from the preparation of the cables and choosing of connectors, to the crimping itself, often made by hydraulic presses.

Much research has been done over time to improve the performances of crimped connections, developing verification methods using ultrasonic inspection [2], [3] and thermography [4], analyzing the behavior at thermal shocks [5] or other factors that affect the contact resistance [6], modeling electric conduction [7] or temperature investigation for different types of crimping [8] with thermal modeling of heat transfer [9], [10]. For a quality pre-control of crimp contact, two solutions were proposed in [11] consisting in experimental determination of specific losses by calculating the initial rate of temperature or checking reaching a critical temperature using on-level thermal indicator. To reduce of contact resistance and increase the reliability of crimped connections, useful solution were proposed in [12] by using two adjacent crimp indents in opposite sides instead of one crimp indents. In a recent work [13] is studied the influence of an improper crimped connection execution on crimping validation, analyzing the limits of variation of parameters so that it will not be compromised.

Checking the quality of a crimped connection is regulated by standards such as [14] and [15], imposing electrical, thermal and mechanical tests.

The electrical test involves measuring the contact resistances of a set of 6 samples, followed by the calculation of connector resistance factors and of a summative coefficient δ called "initial scatter" which must not exceed 0.3. The measurement process is simple but involves high precision measuring devices, necessary for determining resistances of μOhm level.

In [16], a study of the influence of experimental measurements accuracy on this coefficient was performed, cumulating data from 3 sets of crimped connections of barrel of terminal lug type, with different cross sections of cables. From the whole measurement process, 6 independent representative quantities were chosen, with direct influence on the value of δ. First, it was imposed a variation by one unit of hundredths digit of initial scatter and was recorded the variation of each quantity, the others 5 quantities being kept constant. Then simultaneous variations of the 6 quantities caused by device reading errors were imposed, determining the quantities with the greatest influence.

This paper extends the researches on crimped connections of bimetallic through connector type by analyzing two pairs of cross sections.The obtained results are added to those in paper [16] and can help the experimenter to pay more attention to measuring more influential quantities.

II. CONNECTOR RESISTANCE FACTOR AND INITIAL SCATTER

The standard [14] establishes formulas for determining the connector resistance factor for different types of crimping: through connector, bimetallic through connector, branch connector, barrel of terminal lug, palm of terminal lug etc. For the experimental determinations are used sets of 6 samples and reference conductors of each type involved in crimping. The measurements are made in direct current.

For barrel of terminal lug type (Fig. 1) the connector resistance factor (k) is obtained by dividing the connector resistance R_{con} adjusted to its length l_{con} (noted r_{con}), by reference conductor resistance R_r adjusted to its length l_r (noted r_r) [14], [16]:

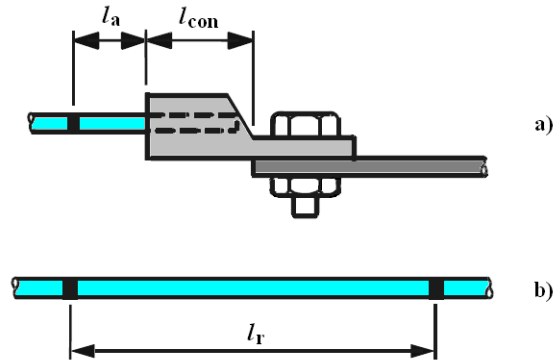

Fig.1. Barrel of terminal lug (a) and reference conductor (b) [16].

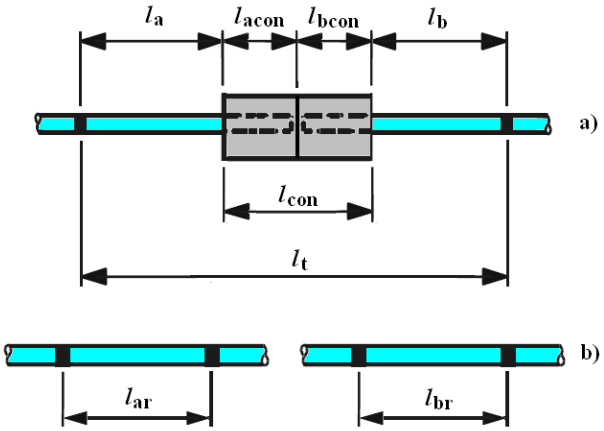

Fig.2. Bimetallic through connector (a) and reference conductors (b).

$$k = \frac{\frac{R_{con}}{l_{con}}}{\frac{R_r}{l_r}} = \frac{r_{con}}{r_r} \quad (1)$$

$$R_{con} = R_1 - R_r \cdot \frac{l_a}{l_r} = R_1 - r_r \cdot l_a \quad (2)$$

$$R_1 = \frac{U_1}{I_1} \cdot \frac{1}{1+\alpha \cdot (\theta_a - 20°C)} \quad (3)$$

$$R_r = \frac{U_r}{I_r} \cdot \frac{1}{1+\alpha \cdot (\theta_a - 20°C)} \quad (4)$$

where R_1 and R_r are referred to 20°C from the ambient temperature θ_a with temperature coefficient of resistance α = 0.004 K^{-1}, U_1 and U_r are the voltage drops on the lengths l_a + l_{con}, respectively, l_r , carrying the direct currents I_1 and I_r.

The length l_a is chosen according to the specifications of the standard.

For bimetallic through connector type (Fig. 2) the connector resistance factor (k) is obtained by dividing the connector resistance R_{con} by sum of both conductor resistances (R_{acon} and R_{bcon}) on the lengths l_{acon} and l_{bcon} that make up the connector [14]:

$$k = \frac{R_{con}}{R_{acon} + R_{bcon}} = \frac{R_{con}}{\frac{R_{ar}}{l_{ar}} \cdot l_{acon} + \frac{R_{br}}{l_{br}} \cdot l_{bcon}} = \frac{R_{con}}{r_{ar} \cdot l_{acon} + r_{br} \cdot l_{bcon}} \quad (5)$$

$$R_{con} = R_t - R_{acon} - R_{bcon} = R_t - r_{ar} \cdot l_{acon} - r_{br} \cdot l_{bcon} \quad (6)$$

$$R_t = \frac{U_t}{I_t} \cdot \frac{1}{1+\alpha \cdot (\theta_a - 20°C)} \quad (7)$$

$$R_{ar} = \frac{U_{ar}}{I_{ar}} \cdot \frac{1}{1+\alpha \cdot (\theta_a - 20°C)} \quad (8)$$

$$R_{br} = \frac{U_{br}}{I_{br}} \cdot \frac{1}{1+\alpha \cdot (\theta_a - 20°C)} \quad (9)$$

where R_t , R_{ar} and R_{br} are referred to 20°C , U_t , U_{ar} and U_{br} are the voltage drops on the lengths l_a + l_{con}+ l_b, respectively, l_{ar} and l_{br} carrying the direct currents I_t, I_{ar} and I_{br}. The lengths l_a and l_b are chosen according to the specifications of the standard.

The initial scatter coefficient (δ) provides information on the behavior of the crimped connection immediately after installation before any aging effect begins. It is considered that 6 samples are sufficient to be tested to estimate the identification of a "family" of connectors. If the resistance factors for the type of connector tested are almost equal, it can be assumed that the same design and assembly technology will lead to the same result on a conductor of the same type. The resistance factors calculated above are considered to follow a normal distribution with unknown mean and unknown variance.

The empirical mean of the resistance factors before the standardized heat cycle 1 is an estimator for the unknown statistical mean:

$$\bar{k}_0 = \frac{1}{6} \cdot \sum_{i=1}^{6} k_i \quad (10)$$

The empirical standard deviation of the resistance factors of the six connectors before heat cycle 1 is an estimator for the unknown statistical standard deviation:

$$s_0 = \sqrt{\frac{1}{5} \cdot \sum_{i=1}^{6} \left(k_i - \bar{k}_0\right)^2} \quad (11)$$

The relative initial scatter of the mean of the connector resistance factors of the six connectors before heat cycle 1 standardized by the mean is:

$$\delta = \frac{1}{\sqrt{6}} \cdot \frac{s_0}{\bar{k}_0} \cdot t_s \quad (12)$$

where t_s is 99.5% quantile of Student distribution with 5 degree of freedom (t_s = 4.032).

This dimensionless parameter represents the percentage deviation from the estimated mean resistance factor and indicates that, for a given probability, a resistance factor is not expected to exceed. It is based on a 99% confidence interval for the unknown true mean. The quantile t_s indicates here that the confidence interval will cover the unknown true mean of the resistance factors with a 99% probability before the heat cycle 1.

III. Experimental Measurements

The measurements were performed on two types of crimped connections:

1) barrel of terminal lug type for three cables with cross sections: S_1 = 95 mm^2, S_2 = 185 mm^2, S_3 = 300 mm^2 [16];

2) bimetallic through connector type for two pairs of cables with cross sections S_{a4} = 70 mm^2, S_{b4} = 56.11 mm^2 and S_{a5} = 60.21 mm^2, S_{b5} = 120 mm^2.

For testing the first type, the samples were made in pairs, two at the ends of the same cable, so that for each cross section we have 3 cables with two crimps, counting 6 samples. In Fig. 3 are shown a pair of crimp connections. In these conditions the reference conductor resistance adjusted to length was deduced by (4) for each cable, identifying $l_{ai} = l_{ri}$ and averaging the results (Fig. 3):

$$r_r = \left(\frac{1}{3}\cdot\sum_{i=1}^{3}\frac{U_{ai}}{I_{ai}\cdot l_{ai}}\right)\cdot\frac{1}{1+\alpha\cdot(\theta_a-20°C)} \quad (13)$$

The connector resistances results by (2) and (3) (Fig. 3):

$$R_{con1i} = R_{1i} - r_r\cdot l_{ai} \quad (14)$$

For the second type, the samples were independent and the measured quantities are indicated in Fig. 4. The reference conductor resistances were deduced for each cable, identifying $l_{ai} = l_{ari}$ and $l_{bi} = l_{bri}$ and averaging the results (Fig. 4):

$$r_{ar} = \left(\frac{1}{6}\cdot\sum_{i=1}^{6}\frac{U_{ai}}{I_{ai}\cdot l_{ai}}\right)\cdot\frac{1}{1+\alpha\cdot(\theta_a-20°C)} \quad (15)$$

$$r_{br} = \left(\frac{1}{6}\cdot\sum_{i=1}^{6}\frac{U_{bi}}{I_{bi}\cdot l_{bi}}\right)\cdot\frac{1}{1+\alpha\cdot(\theta_a-20°C)} \quad (16)$$

The connector resistances results by (6)-(9) (Fig. 4):

$$R_{coni} = R_{ti} - r_{ar}\cdot l_{aconi} - r_{br}\cdot l_{bconi} \quad (17)$$

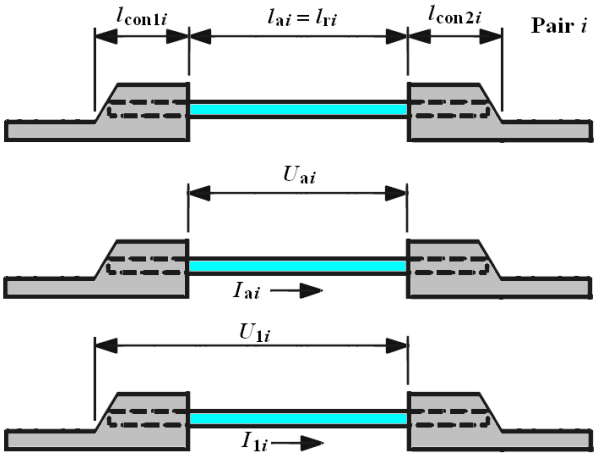

Fig. 3. Pair i with 2 samples and quantities taken into account for determining the reference conductor resistance and connector resistance for barrel of terminal lug [16].

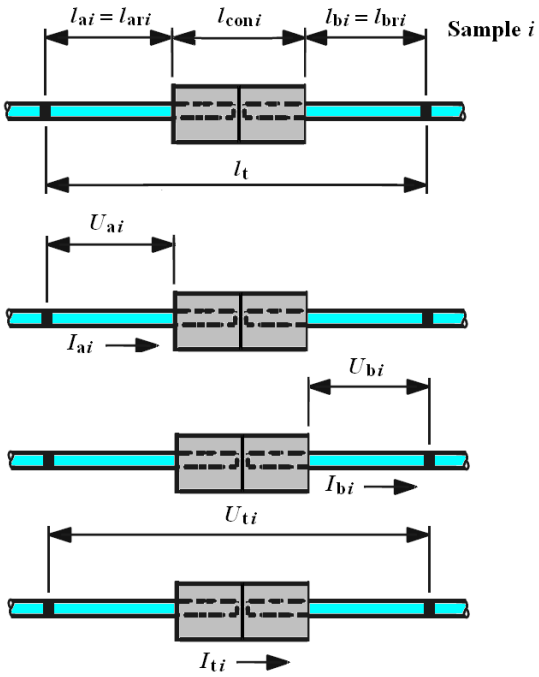

Fig. 4. Sample i and quantities taken into account for determining the reference conductor resistances and connector resistance for bimetallic through connector.

Measurement results on connector resistance factor (k), empirical mean of the resistance factors ($\bar{k}_0$), empirical standard deviation of the resistance factors (s_0) and initial scatter of the mean of the resistance factors (δ) are presented in Tables I-V for the two types of crimped connections. Graphical representations are shown in Figs. 5-9.

TABLE I.
Measurement Results for Crimped Connections of Barrel of Terminal Lug Type with Cross Section S_1 = 95 mm^2 [16]

Sample	1	2	3	4	5	6
k	1,080	1,181	1,171	1,080	1,181	1,193
$\bar{k}_0$	1,147					
s_0	0,053					
δ	0,076					

TABLE II.
Measurement Results for Crimped Connections of Barrel of Terminal Lug Type with Cross Section S_2 = 185 mm^2 [16]

Sample	1	2	3	4	5	6
k	0,923	0,686	0,812	0,797	0,652	0,822
$\bar{k}_0$	0,782					
s_0	0,099					
δ	0,208					

TABLE III.
MEASUREMENT RESULTS FOR CRIMPED CONNECTIONS OF BARREL OF TERMINAL LUG TYPE WITH CROSS SECTION S_2 = 300 mm^2 [16]

Sample	**1**	**2**	**3**	**4**	**5**	**6**
k	1,007	0,987	1,048	1,007	0,904	0,982
$\bar{k}_0$	0,989					
s_0	0,048					
δ	0,080					

TABLE IV.
MEASUREMENT RESULTS FOR CRIMPED CONNECTIONS OF BARREL OF TERMINAL LUG TYPE WITH CROSS SECTIONS S_{a4} = 70 mm^2, S_{b4} = 56.11 mm^2

Sample	**1**	**2**	**3**	**4**	**5**	**6**
k	1,122	1,288	1,473	1,439	1,272	1,151
$\bar{k}_0$	1,291					
s_0	0,144					
δ	0,183					

TABLE V.
MEASUREMENT RESULTS FOR CRIMPED CONNECTIONS OF BARREL OF TERMINAL LUG TYPE WITH CROSS SECTIONS S_{a4} = 60.21 mm^2, S_{b4} = 120 mm^2

Sample	**1**	**2**	**3**	**4**	**5**	**6**
k	0,800	0,594	0,551	0,492	0,596	0,639
$\bar{k}_0$	0,612					
s_0	0,105					
δ	0,282					

IV. ANALYSIS OF THE RESULT VARIATIONS

The used measuring instruments are analog: a voltmeter with a 30 scale-divisions, marked every 0.1 div, used in the 25mV/div range and an ammeter with a 150 scale-divisions, marked every 0.1 div, used in the 100A/150div range. The lengths of the conductors were measured with the measuring tape, marked every 1 mm (1 div).

The measurement process involves reading many quantities (Q) such as voltage drops, currents or conductor lengths, on which the final result depends

For crimped connections of barrel of terminal lug type [16] there are 6 sets of quantities of the same type: U_{ai}, I_{ai}, l_{ai}, U_{1i} and U_{2i}, I_{1i} and I_{2i}, l_{1i} and l_{2i}, $i = \overline{1 \div 3}$. From each set, only one quantity was chosen to study its influence on the final result. Therefore it can be written:

$$\delta = \delta(U_{aj}, I_{aj}, l_{aj}, U_{kj}, I_{kj}, l_{kj}) \qquad (18)$$

where the chosen indexes k and j correspond to the value farthest from the average of connector resistance factor k:

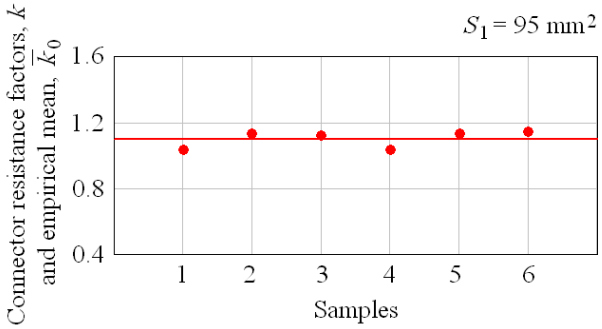

Fig. 5. Connector resistance factors and empirical mean for crimped connection of barrel of terminal lug type, S_1 = 95 mm^2 [16].

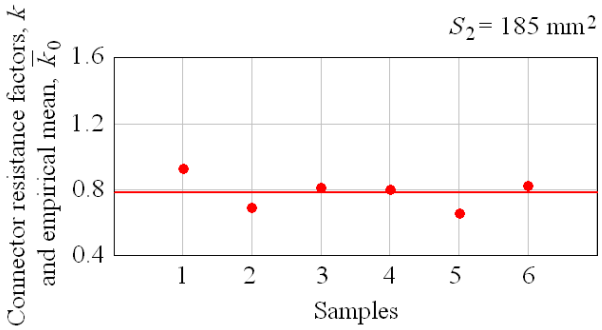

Fig. 6. Connector resistance factors and empirical mean for crimped connection of barrel of terminal lug type, S_2 = 185 mm^2 [16].

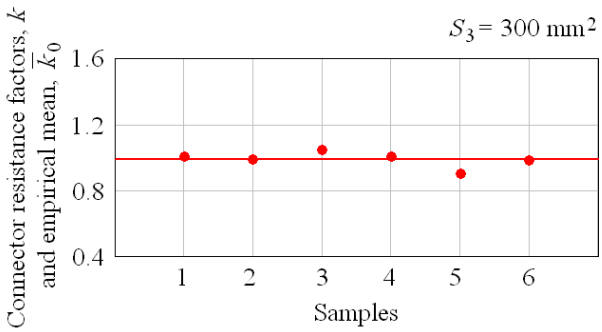

Fig. 7. Connector resistance factors and empirical mean for crimped connection of barrel of terminal lug type, S_3 = 300 mm^2 [16].

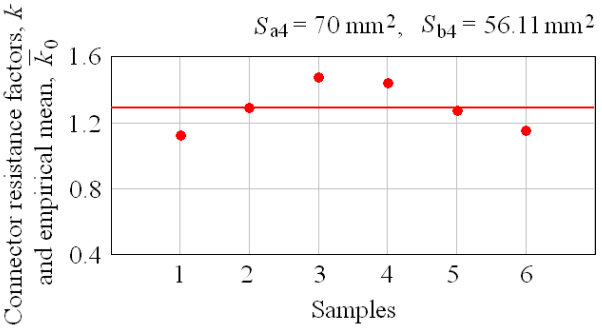

Fig. 8. Connector resistance factors and empirical mean for crimped connection of bimetallic through connector type, S_{a4} = 70 mm^2, S_{b4} = 56.11 mm^2.

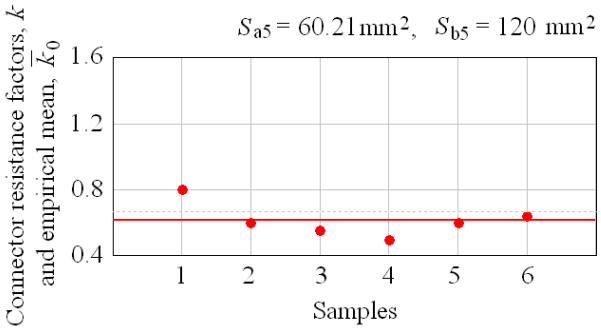

Fig. 9. Connector resistance factors and empirical mean for crimped connection of bimetallic through connector type, S_{a5} = 60.21 mm^2, S_{b5} = 120 mm^2.

$$\delta_{S1} = \delta_{S1}(U_{a1}, I_{a1}, l_{a1}, U_{11}, I_{11}, l_{11}) \quad (19)$$

$$\delta_{S2} = \delta_{S1}(U_{a1}, I_{a1}, l_{a1}, U_{11}, I_{11}, l_{11}) \quad (20)$$

$$\delta_{S3} = \delta_{S3}(U_{a2}, I_{a2}, l_{a2}, U_{22}, I_{22}, l_{22}) \quad (21)$$

For crimped connection of bimetallic through connector type the read quantities form also 6 sets of quantities of the same type: U_{ai} and U_{bi}, I_{ai} and I_{bi}, l_{ai} and l_{bi}, U_{ti}, I_{ti}, l_{ti}, $i = \overline{1 \div 6}$. As the same, from each set, only one quantity was chosen to study its influence on the final result. Therefore it can be written:

$$\delta = \delta(U_{aj}, I_{aj}, l_{aj}, U_{tj}, I_{tj}, l_{tj}) \quad (22)$$

where the chosen index j correspond to the value farthest from the average of the connector resistance factor k:

$$\delta_{S4} = \delta_{S4}(U_{a3}, I_{a3}, l_{a3}, U_{t3}, I_{t3}, l_{t3}) \quad (23)$$

$$\delta_{S5} = \delta_{S5}(U_{a1}, I_{a1}, l_{a1}, U_{t1}, I_{t1}, l_{t1}) \quad (24)$$

Based on this information, a study of the impact of the variations of these quantities on the initial scatter coefficient was performed.

In the first stage, it was imposed a variation $\Delta\delta_{lim}$ of initial scatter coefficient δ corresponding to the change by one unit of its hundredths digit:

$$\Delta\delta_{lim} = \frac{0.01}{\delta} \quad (25)$$

and the range of variation of each of the 6 quantities was exclusively determined (ΔQ_{lim}) and compared with the measuring instruments reading errors:

$$\Delta U = \frac{0.05 \cdot \text{div}}{U_{read}[\text{div}]}, \quad \Delta I = \frac{0.05 \cdot \text{div}}{I_{read}[\text{div}]}, \quad \Delta l = \frac{0.5 \cdot \text{div}}{l_{read}[\text{div}]} \quad (26)$$

This means that the variation limits of initial scatter for the five cases are $\Delta\delta_1$ = 12.790%, $\Delta\delta_2$ = 4.809%, $\Delta\delta_3$ = = 12.488% [16], $\Delta\delta_4$ = 5.457%, $\Delta\delta_5$ = 3.543%. The results are presented in Table VI.

It is observed that for crimped connections of barrel of terminal lug type the variations allowed for each voltage drops U_{kj} for the modification by one unit of the hundredths digit of initial scatter are lower than reading error of the voltmeter. Therefore an increased attention is indicated to these measurements, which are more sensitive. There is a general increase in the sensitivity of measurements ($\Delta Q/\Delta Q_{lim}$) to smaller sections of conductors.

TABLE VI. EXCLUSIVE VARIATION OF EACH QUANTITY THAT LEADS TO CHANGE BY ONE UNIT OF THE HUNDREDTHS DIGIT OF INITIAL SCATTER

Cross sections, S / Initial scatter, δ / $\Delta\delta_{lim}$	**ΔU_{aj_lim} / ΔU_{aj} [%]**	**ΔI_{aj_lim} / ΔI_{aj} [%]**	**ΔL_{aj_lim} / ΔL_{aj} [%]**	**ΔU_{kj_lim} / ΔU_{kj} [%]**	**ΔI_{kj_lim} / ΔI_{kj} [%]**	**ΔL_{kj_lim} / ΔL_{kj} [%]**
S_1 = 95 mm^2	ΔU_{a1_lim}	ΔI_{a1_lim}	ΔL_{a1_lim}	ΔU_{11_lim}	ΔI_{11_lim}	ΔL_{11_lim}
δ_1 = 0.078	0.289	0.289	0.263	0.185	0.185	0.178
$\Delta\delta_{lim1}$ = 12.79%	ΔU_{a1}	ΔI_{a1}	ΔL_{a1}	ΔU_{11}	ΔI_{11}	ΔL_{11}
	0.230	0.062	0.103	**0.213**	0.062	0.095
S_2 = 185 mm^2	ΔU_{a1_lim}	ΔI_{a1_lim}	ΔL_{a1_lim}	ΔU_{11_lim}	ΔI_{11_lim}	ΔL_{11_lim}
δ_2 = 0.208	0.675	0.675	0.896	0.208	0.208	0.223
$\Delta\delta_{lim2}$ = 4.809%	ΔU_{a1}	ΔI_{a1}	ΔL_{a1}	ΔU_{11}	ΔI_{11}	ΔL_{11}
	0.450	0.060	0.119	**0.403**	0.060	0.105
S_3 = 300 mm^2	ΔU_{a2_lim}	ΔI_{a2_lim}	ΔL_{a2_lim}	ΔU_{22_lim}	ΔI_{22_lim}	ΔL_{22_lim}
δ_3 = 0.080	0.561	0.562	0.790	0.175	0.175	0.192
$\Delta\delta_{lim3}$ = 12.488%	ΔU_{a2}	ΔI_{a2}	ΔL_{a2}	ΔU_{22}	ΔI_{22}	ΔL_{22}
	0.317	0.033	0.091	**0.287**	0.033	0.082
S_{a4} = 70 mm^2	ΔU_{a3_lim}	ΔI_{a3_lim}	ΔL_{a3_lim}	ΔU_{t3_lim}	ΔI_{t3_lim}	ΔL_{t3_lim}
S_{b4} = 56.11 mm^2	9.765	9.958	1.929	0.334	0.334	0.239
δ_4 = 0.183	ΔU_{a3}	ΔI_{a3}	ΔL_{a3}	ΔU_{t3}	ΔI_{t3}	ΔL_{t3}
$\Delta\delta_{lim4}$ = 5.457%	0.455	0.082	0.325	0.180	0.083	0.140
S_{a5} = 60.21 mm^2	ΔU_{a1_lim}	ΔI_{a1_lim}	ΔL_{a1_lim}	ΔU_{t1_lim}	ΔI_{t1_lim}	ΔL_{t1_lim}
S_{b5} = 120 mm^2	5.13	5.163	0.943	0.229	0.229	0.273
δ_5 = 0.080	ΔU_{a1}	ΔI_{a1}	ΔL_{a1}	ΔU_{t1}	ΔI_{t1}	ΔL_{t1}
$\Delta\delta_{lim5}$ = 3.543%	0.440	0.038	0.347	0.207	0.034	0.137

For crimped connection of bimetallic through connector type a greater sensitivity of measurements can be associated to the greater rate of cross sections (S_{max}/S_{min}).

In the second stage, a variation identical to the reading errors of the measuring instruments was imposed exclusively for each quantity and the effect on the initial scatter variation was recorded. The results are presented in Table VII.

Once again, there is a greater sensitivity in measuring U_{kj} voltage drops ($\Delta\delta/\Delta\delta_{lim}$) compared to other quantities in the case of barrel of terminal lug. The same trend can be found in measuring U_{ti} voltage drops for bimetallic through connector, especially for greater rate of cross sections (S_{max}/S_{min}).

In the last stage, the impact of the simultaneous variations of the 6 quantities on the initial scatter coefficient was evaluated, using the theory of experimental design [17], [18], [19]. For this, the matrix of experiments X in normalized form having $2^6 \times 2^6$ elements was used, in which the variation limits of quantities were replaced by –1 and +1 and the vector of the response function Y carries the corresponding initial scatter values.

TABLE VII. EFFECT OF EXCLUSIVE VARIATION IDENTICAL TO READING ERROR OF EACH QUANTITY ON INITIAL SCATTER

Cross section, S / Initial scatter, δ / $\Delta\delta_{lim}$	**ΔU_{aj} / $\Delta\delta$ [%]**	**ΔI_{aj} / $\Delta\delta$ [%]**	**ΔL_{aj} / $\Delta\delta$ [%]**	**ΔU_{kj} / $\Delta\delta$ [%]**	**ΔI_{kj} / $\Delta\delta$ [%]**	**ΔL_{kj} / $\Delta\delta$ [%]**
$S_1 = 95$ mm^2	ΔU_{a1}	ΔI_{a1}	ΔL_{a1}	ΔU_{11}	ΔI_{11}	ΔL_{11}
$\delta_1 = 0.078$	0.230	0.062	0.103	0.213	0.062	0.095
$\Delta\delta_{lim1} = 12.79\%$	10.190	2.743	5.002	**15.008**	4.418	7.015
$S_2 = 185$ mm^2	ΔU_{a1}	ΔI_{a1}	ΔL_{a1}	ΔU_{11}	ΔI_{11}	ΔL_{11}
$\delta_2 = 0.208$	0.450	0.060	0.119	0.403	0.060	0.105
$\Delta\delta_{lim2} = 4.809\%$	3.231	0.432	0.646	**9.307**	1.396	0.280
$S_3 = 300$ mm^2	ΔU_{a2}	ΔI_{a2}	ΔL_{a2}	ΔU_{22}	ΔI_{22}	ΔL_{22}
$\delta_3 = 0.080$	0.317	0.033	0.091	0.287	0.033	0.082
$\Delta\delta_{lim3} = 12.488\%$	7.167	0.752	1.494	**20.357**	2.375	5.337
$S_{a4} = 70$ mm^2 $S_{b4} = 56.11$ mm^2 $\delta_4 = 0.183$ $\Delta\delta_{lim4} = 5.457\%$	ΔU_{a3} 0.455 0.255	ΔI_{a3} 0.082 0.046	ΔL_{a3} 0.325 0.977	ΔU_{t3} 0.180 2.958	ΔI_{t3} 0.083 1.366	ΔL_{t3} 0.140 3.243
$S_{a5} = 60.21$ mm^2 $S_{b5} = 120$ mm^2 $\delta_5 = 0.080$ $\Delta\delta_{lim5} = 3.543\%$	ΔU_{a1} 0.440 0.304	ΔI_{a1} 0.038 0.026	ΔL_{a1} 0.347 1.305	ΔU_{t1} 0.207 3.214	ΔI_{t1} 0.034 0.520	ΔL_{t1} 0.137 1.777

$$X = \begin{pmatrix} 1 & -1 & -1 & -1 & -1 & \dots & 1 \\ 1 & 1 & -1 & -1 & -1 & \dots & -1 \\ 1 & -1 & 1 & -1 & -1 & \dots & -1 \\ 1 & 1 & 1 & -1 & -1 & \dots & 1 \\ 1 & -1 & -1 & 1 & -1 & \dots & -1 \\ \vdots & \vdots & \vdots & \vdots & \vdots & \ddots & \vdots \\ 1 & 1 & 1 & 1 & 1 & 1 & 1 \end{pmatrix}, \quad Y = \begin{pmatrix} Y_1 \\ Y_2 \\ Y_3 \\ Y_4 \\ Y_5 \\ \\ Y_{64} \end{pmatrix} \qquad (27)$$

The effect of the variation of the quantity Q_m on the initial scatter is obtained with the formula:

$$E(Q_m) = \frac{1}{64} \cdot \sum_{s=1}^{64} \left(Y_s \cdot X_{s,m+1} \right), \quad m = \overline{1 \div 6} \qquad (28)$$

Based on this study were drawn the histograms of effects shown in Figs. 10-14.

As expected, for barrel of terminal lug the most influential quantities are U_{kj} voltage drops on connector + conductor, all the more so as the quality of the crimps is worse (case of S_2).

The least influence has I_{aj} currents measured in order to calculate the resistance of the reference conductor.

For bimetallic through connector the most influential quantities are the total lengths l_{ti} of assembly conductor a + connector + conductor b, but quite influential is also the total voltage drops U_{ti}.

However, the sensitivities for bimetallic through connector type are lower than for barrel of terminal lug type.

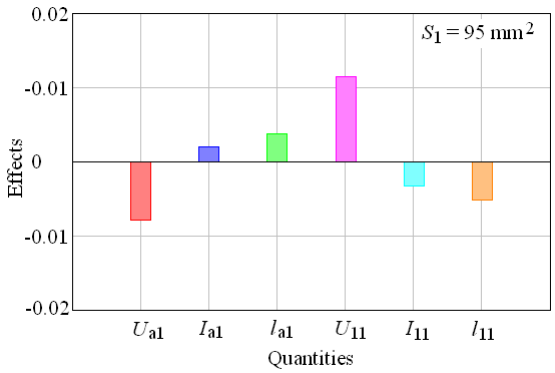

Fig. 10. Histogram of effects for $S_1 = 95$ mm^2 [16].

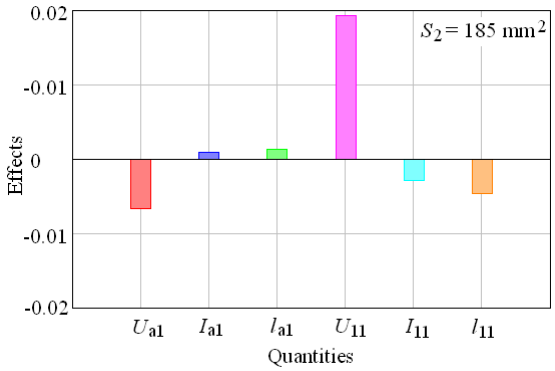

Fig. 11. Histogram of effects for $S_2 = 185$ mm^2 [16].

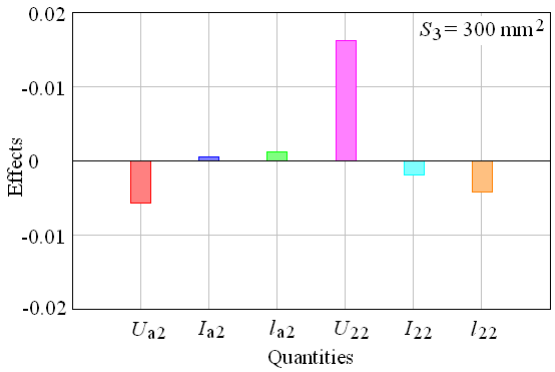

Fig. 12. Histogram of effects for $S_3 = 300$ mm^2 [16].

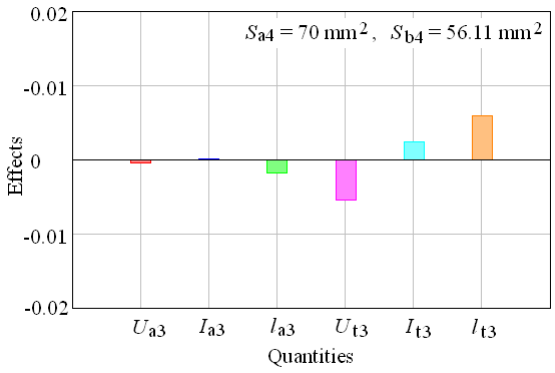

Fig. 13. Histogram of effects for $S_{a4} = 70$ mm^2, $S_{b4} = 56.11$ mm^2.

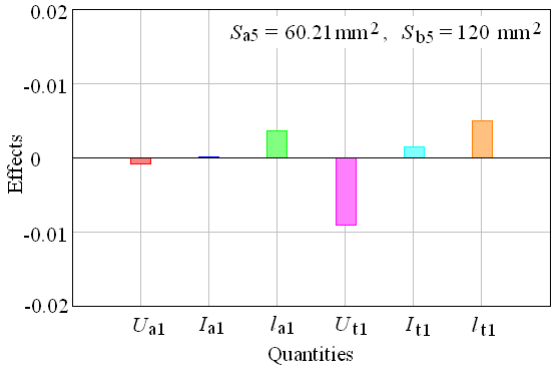

Fig. 14. Histogram of effects for S_{a5} = 60.21 mm^2, S_{b5} = 120 mm^2.

V. Conclusions

The impact of the experimental measurements accuracy on validation process of crimped connections was studied, cumulating data for two constructive types: barrel of terminal lug and bimetallic through connector. For this study, three sets of samples of the first type and two sets of the second type were used, for which the connector resistance factor and the summative coefficient initial scatter were determined.

Choosing 6 independent representative quantities with direct influence on the initial scatter it was found that for crimped connections of the first type, the measurement of voltage drops on both conductor + connector is very sensitive, being able to induce errors that affect the hundredths digit of this coefficient by more than one unit. As a result, the entire validation process can be compromised if initial scatter exceed to 0.3. It was also observed a general increase in the sensitivity of measurements to smaller sections of cables.

For the second type, a greater sensitivity can be associated to the greater rate of cross sections of cables involved in crimping.

Cumulating the variations of the quantities caused by the reading errors of the measuring instruments, the same conclusions are reached, which recommends an increased attention of the experimenter to measuring of voltage drops on both conductor + connector, for barrel of terminal lug type and to measuring the total lengths of assembly conductor a + connector + conductor b and also the total voltage drops, for bimetallic through connector type.

Acknowledgment

Source of research funding in this article: Research program of the Electrical Engineering Department financed by the University of Craiova.

Contribution of authors:
First author – 50%
First coauthor – 50%

Received on July 17, 2021
Editorial Approval on November 15, 2021

References

[1] BS EN 60352-2:2006, Solderless connections, Part 2: crimped connections – general requirements, test methods and practical guidance, 2006.

[2] E. Cramer, F. Daniel Perey, and T. William Yost, "Wire crimp connectors verification using ultrasonic inspection," IV Conferencia Panameri-cana de END Buenos Aires, Octobre, 2007.

[3] K. Elliott Cramer, F. Daniel Perey, and T. William Yost, "Wire crimp connectors verification using ultrasonic inspection," IV Conferencia Panamericana de END, Buenos Aires, pp. 1-11, 2007.

[4] M. Finc, T. Kek, and J. Grum, "Use of thermography and ultrasonic inspection for evaluation of crimped wire connection quality," 18thWorld Conference on nondestructive testing, Durban, South Africa, 2012.

[5] D.R. Liu, T. Bracket, and S. McCarthy, "Contact resistance comparison of good and bad crimp joints with tinned wires under thermal shock", Electrical Contacts, Proceedings of the Forty-Seventh IEEE Holm Conference, pp. 35-43, 2001.

[6] M. Mohd Ruzlin, A. H. Huzainie Shafi, and A.G. Ahmad Basri, "Study of cable crimping factors affecting contact resistance of medium voltage cable ferrule and lug," 22nd International Conference of electricity distribution, Stockholm, Suedia, 2013.

[7] G. Rosazza Prin, T. Courtin, and L. Boyer, "A new method to investigate electrical conduction in crimp joints. Influence of the compaction ratio and electrical model," Electrical Contacts, Proceedings of the Forty-Eighth IEEE Holm Conference, pp. 246 – 251, 2002.

[8] C.-F. Ocoleanu, A.-I. Dolan, G.A. Cividjian, and S. Teodorescu, "Temperature investigations in two type of crimped connection using experimental determinations," International Journal of Mechanical, Aerospace, Industrial and Mechatronics Engineering, Vol. 8, No. 10, pp. 1633-1636, 2014, International Conference on Thermal Engineering, Barcelona, Spain, 2014.

[9] C.-F. Ocoleanu, I. Popa, A.-I. Dolan, and V. Ivanov, "Magneto-Thermal Model for Crimped Connections," Annals of the University of Craiova, Series: Electrical Engineering, No. 38, pp. 56-61, Universitaria Publishing House, 2014.

[10] C.-F. Ocoleanu, I. Popa, A.-I. Dolan, and V. Ivanov, "Crimped Connections Heat Transfer Coefficient Law Determination Using Experimental and Numerical Results," Proceedings of the XII-th IEEE International Conference on Applied and Theoretical Electricity - ICATE 2014, pp. 1-4, Craiova, Romania, October 23-25, 2014.

[11] C.-F. Ocoleanu, G.A. Cividjian, and Gh. Manolea, "Solutions for quality pre-control of crimp contacts used in electric power systems and electrical machines," 3nd International Symposium On Environment Friendly Energies And Applications, pp. 1-6, 2014.

[12] C.-F. Ocoleanu, G.A. Cividjian, and Gh. Manolea, "Technological solution for increasing the quality of crimped connections," 2015 IEEE 1st International Forum on Research and Technologies for Society and Industry Leveraging a better tomorrow (RTSI), Sept. 16-18, pp. 1-6, 2015.

[13] C.-F. Ocoleanu, and A.-I. Dolan, "Experimental and Statistical Study of Connector Resistance Factor Influence on Crimping Validation Process," 7-th International Conference on Renewable Energy Research and Applications - ICRERA 2018, Paris, France, Oct 14-17, pp.174-178, 2018.

[14] BS EN 61238-1:2003, Compression and mechanical connectors for power cables for rated voltages up to 36 kV – Part 1: test methods and requirements, 2003.

[15] B945-05, Standard Guide for Specification and Quality Assurance for the Electrical Contact of Crimped Wire Terminations.

[16] A.-I. Dolan, and C.-F. Ocoleanu, "Influence of Experimental Measurements Accuracy on Connector Resistance Factor for Crimped Connections," XVI-th IEEE International Conference on Applied and Theoretical Electricity – ICATE 2021, Craiova, Romania, May 27-29, 2021, pp. 1-5, 2021.

[17] D. Montgomery, Design and analysis of experiment, 5-th Edition, Arizona State University, 2000.

[18] S. Vivier, "Strategies d'optimisation par la methode des plans d'experiences et applications aux dispositives electrotechniques modelise par elements finis," Ph-D Thesis, Lille, 2002.

[19] A.-I. Dolan, "Optimization of DC electromagnet using design of experiments and FEM," XIII-th IEEE International Conference on Applied and Theoretical Electricity – ICATE 2016, Craiova, Romania, October 06-08, pp. 1-6, 2016.

Real-Time Sensorless Control of the PMSM based on Genetic Algorithm, Sliding Mode Observer, and SCADA Integration

Claudiu-Ionel NICOLA, Marcel NICOLA, Maria-Cristina NIŢU,
Dumitru SACERDOŢIANU, Ancuţa-Mihaela ACIU
National Institute for Research, Development and Testing in Electrical Engineering - ICMET/Research Department, Craiova, Romania, nicolaclaudiu@icmet.ro, marcel_nicola@yahoo.com, cristinamarianitu@yahoo.com, dumitru_sacerdotianu@yahoo.com, ancutu13@yahoo.com

DOI: 10.52846/AUCEE.2021.1.04

Abstract **- This paper presents an application for real-time implementation of the Permanent Magnet Synchronous Motor (PMSM) sensorless control system and its integration into Supervisory Control And Data Acquisition (SCADA). Starting from the operating equations of the PMSM and by implementing the global Field Oriented Control (FOC) control strategy, in which the saturation of the integral component of the PI controller is prevented by using an anti-windup technique, the numerical simulations performed in Matlab/Simulink lead to good performance, which recommends the real-time implementation. For the optimal tuning of the PI speed controller of the PMSM the genetic algorithm (GA) is used. Numerical simulations are performed in order to choose the type of Digital Signal Processing (DSP) used for the real-time implementation, considering that a global criterion of successful implementation is the performance/cost ratio. Besides, the integration into SCADA provides flexibility of the control system but also the possibility of online/offline processing from the point of view of other specific requirements. Among them we mention the energy quality analysis, whose first exponent calculated also in real-time is Total Harmonic Distortion (THD). Real-time implementations are performed in Matlab/Simulink and LabVIEW programming environments. According to the trend of the last years, the use of an Internet of Things (IoT) platform for viewing the variables of the control process on the Internet plays an important role.**

Cuvinte cheie: *PMSM, FOC, algoritm genetic, observer în regim alunecător, sisteme încorporate, SCADA.*

Keywords: *PMSM, FOC, genetic algorithm, sliding mode observer, embedded systems, SCADA.*

I. INTRODUCTION

The extent of research on PMSM control with or without speed/position encoder is well-known, considering that PMSMs have a number of constructive advantages that meet the requirements of precision electrical actuators, robotics, and computer peripherals [1-5].

Among the many types of control we can mention from the PI controllers, to the adaptive, predictive and intelligent control type of controllers [6-9].

The computational intelligence has lately been providing a series of optimization algorithms which are characterized by the fact that they can be applied to the control problems under the conditions where the uncertainties are not known, and there are also unmodeled parts of the system, but the results provided by these algorithms are very good [10, 11]. Starting from the classic FOC-type control structure of a PMSM, the article presents the problem of optimally tuning the PI-type speed controller. In this respect, we start from the performance of a controller tuned in the classic manner using the Ziegler-Nichols method together with the trial and error method, and preceded by the optimization of the adjustment parameters of the PI speed controller.

Further, one of the most widely used speed observers is the SMO-type observer. The Matlab/Simulink environment is commonly used to compare the performance of these control systems. The advantages and disadvantages of various types of controllers can be thus revealed through high-precision numerical simulations. This analysis is inherently followed by the real-time implementation of the control system in embedded systems. The designer of these systems must weigh in the balance both the performance of the control systems studied by numerical simulations, and the cost of their real-time implementations in embedded systems. The real-time implementations of the PMSM sensorless control system are performed in Matlab/Simulink and LabVIEW programming environments [12-14].

Moreover, there is an inherent problem of creating a local control interface, as well as the problem of integration in the local SCADA. Thus, the control can be performed via secure communications from the Intranet/Internet. The integration into SCADA provides the transmission of signals of interest to other client systems. Thus, on the one hand, the computer server is no longer forced to perform a series of processing tasks, and on the other hand, there is the possibility of running such tasks online or offline, followed by the efficient management of global computing resources. In this sense, a separate task can run online on a client computer to monitor the quality electrical parameters of the controlled PMSM. The main parameter analyzed, but not the only one is the THD. For increased flexibility, according to the trend of the last years, the use of an IoT platform for viewing the variables of the PMSM control process on the Internet plays an important role [15-17].

The presented article is based on [20] and can be considered as a follow-up on a series of articles presented by the same authors regarding the numerical simulations of the PMSM control using various types of controllers. The

tuning of the parameters of the PI controller of the outer speed loop is optimized using an optimization method based on genetic algorithm. Thus, the article presents the real-time implementation of the PMSM control and its integration into SCADA.

The rest of the paper is structured as follows: the mathematical model and the numerical simulation for the sensorless control of the PMSM is described in Section II. Section III presents the real-time implementation of the sensorless control of the PMSM and its integration into SCADA. The experimental results of the control system are presented in Section IV. Some conclusions and some ideas for the next papers are presented in the final section presents.

II. Mathematical Model Description of the PMSM Sensorless Control System

Fig. 1 presents the proposed general diagram for the PMSM sensorless control. The control system is based on the global FOC-type strategy. It can be noted that the anti-windup PI controller is fed at the input with the error between the reference speed and the speed estimated by the SMO-type observer and generates i_{qref} at the output. For the optimal tuning of the PI speed controller of the PMSM, namely parameters K_p and K_i, the genetic algorithm is used. The stator currents are acquired from the PMSM windings, and currents i_d and i_q are obtained by applying the transformation in the *d-q* reference frame. The errors between these currents and their reference values i_{qref} and i_{dref}, and i_{dref} is set to zero according to the FOC strategy, are inputs for two PI controllers which in turn generate the voltages u_d and u_q. Fig. 2 show the block diagram of the PI anti-windup speed controller.

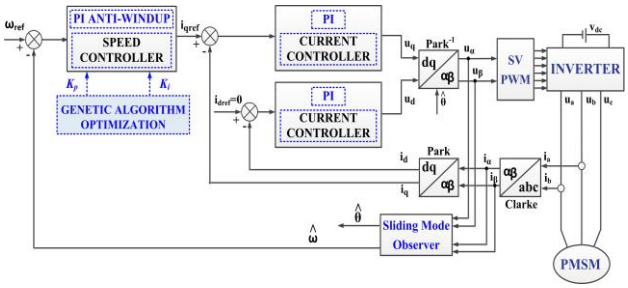

Fig. 1. The block diagram of the PMSM sensorless control system.

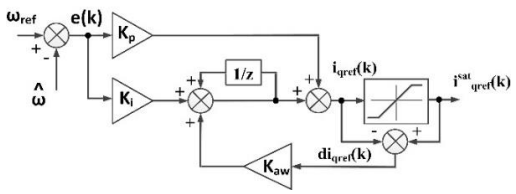

Fig. 2. The block diagram of the PI anti-windup speed controller.

The mathematical model of the PMSM in the *d-q* reference frame is the following [1], [6-8]:

$$\begin{bmatrix} u_q \\ u_d \end{bmatrix} = \begin{bmatrix} R_q + \rho L_q & \omega_e L_d \\ -\omega_e L_q & R_d + \rho L_d \end{bmatrix} \begin{bmatrix} i_q \\ i_d \end{bmatrix} + \begin{bmatrix} \omega_e \lambda_0 \\ \rho \lambda_0 \end{bmatrix} \quad (1)$$

where: u_d, u_q - stator voltages; R_d, R_q - *d*-axis and *q*-axis stator resistances; L_d, L_q - *d*-axis and *q*-axis stator inductances; i_d, i_q - *d*-axis and *q*-axis currents; ω_e - electrical angular velocity of the PMSM rotor; λ_0 - flux linkage; ρ - differential operator.

The magnetic flux of PMSM engine is expressed by the following relations:

$$\begin{aligned} \lambda_q &= L_q i_q \\ \lambda_d &= L_d i_d + \lambda_0 \end{aligned} \quad (2)$$

The following relations are obtained by using the notation T_e for the electromagnetic torque developed by the PMSM:

$$\begin{aligned} T_e &= \frac{3}{2} n_p \left(\lambda_d i_q - \lambda_q i_d \right) \\ T_e &= K_t i_q \\ T_e &= T_L + B\omega + J \frac{d\omega}{dt} \end{aligned} \quad (3)$$

where: $K_t = (3/2)(n_p \lambda_0)$ is the torque constant, B is the viscous friction coefficient, J is the moment of rotor inertia, n_p is the number of pole pairs, and T_L is the load torque.

For $L_d = L_q = L$, $R_d = R_q = R_s$, and $\omega_e = n_p \cdot \omega$, where ω is the rotor speed, the following PMSM model can be obtained:

$$\begin{pmatrix} \dot{i}_d \\ \dot{i}_q \\ \dot{\omega} \end{pmatrix} = \begin{pmatrix} -\frac{R_s}{L} & n_p \omega & 0 \\ -n_p \omega & -\frac{R_s}{L} & -\frac{n_p \lambda_0}{L} \\ 0 & \frac{K_t}{J} & -\frac{B}{J} \end{pmatrix} \begin{pmatrix} i_d \\ i_q \\ \omega \end{pmatrix} + \begin{pmatrix} \frac{u_d}{L} \\ \frac{u_q}{L} \\ -\frac{T_L}{J} \end{pmatrix} \quad (4)$$

A. Genetic Algorithm

It starts from a population of individuals (chromosomes) and creates a hierarchy of them. The number of chromosomes is usually 50, and the ranking is done according to the value of the objective function, which must be minimized. Depending on this value, but also on the values of the objective functions of the other individuals, each chromosome receives a probability of selection for reproduction. The following relation is thereby defined [10, 11]:

$$Adequate(P_{ind}) = 2 - PS + 2(PS - 1)\frac{P_{ind} - 1}{N_{ind}} \quad (5)$$

where: P_{ind} is the position of the individual, N_{ind} is the size of the population, and PS is the selection pressure, $1 \leq PS \leq 2$.

For the fittest individual, $P_{ind} = N_{ind}$ and it has the highest value of the fitness function, and, for the unfittest individual, $P_{ind} = 1$ and it has the lowest value of the fitness function.

For the tournament selection, where each individual in the current population is represented by a space proportional to the value of its evaluation function, the successive random sampling of this space of chromosome representation ensures that the best chromosomes have greater chances to be selected in a certain step than the weaker

ones. Within the algorithm for the mutation function, which has the role of generating new individuals based on the random modification of the individuals in the current population, the adaptive type is selected. For replacement, which is a way of generating the new population, the fitness function will be used: number of offspring > number of parents, only the best offspring will replace parents. The structure of the GA type algorithm is shown as a graph in Fig. 3.

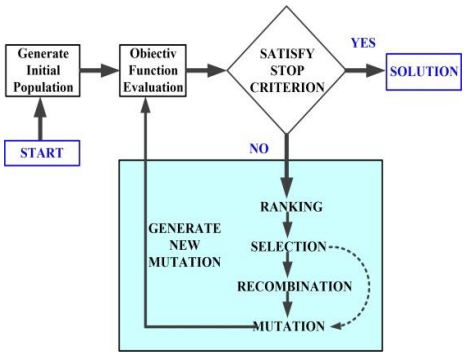

Fig. 3. The general structure of the genetic algorithm.

For each member of the population, the genetic algorithm calculates the speed error (e_ω) and the change in speed error ($s_{e\omega}$). The controller output variable is the change in the reference current (Δi_{qref}). e_ω and $s_{e\omega}$ are defined in step k as follows [10, 11]:

$$e_\omega(k) = \omega_{ref} - \omega(k) \tag{6}$$

$$se_\omega(k) = e_\omega(k) - e_\omega(k-1) \tag{7}$$

where: ω_{ref} is the reference speed.

The steps for the PMSM speed control are summarized as follows:

- The PMSM speed signal is stored in the Matlab workspace;
- The speed error is calculated and its value is updated step by step;
- The numerical representation of each parameter K_p and K_i of the PI-type speed controller is chosen;
- The crossover probability (p_c) and the mutation probability (p_m) is chosen.
- An initial population of parameters K_p and K_i is generated (yielding a random selection result);
- Δi_{qref} is generated for each member of the population C_i, i = 1,2, ...,n using the conventional PI control laws ($\Delta i_{qref}(k) = K_p e_\omega(k) + K_i se_\omega(k)T$);
- The value of the *fitness* function is assigned to each element of the population C_i, i = 1,2, ...,n.

$$p_1 = e_\omega(k) \tag{8}$$

$$p_2 = se_\omega(k) \tag{9}$$

$$F = \frac{1}{\alpha_1 p_1^2 + \alpha_2 p_2^2} \tag{10}$$

The maximum fit of the population C_i becomes C^* and the change in the control action is sent ($i_{qref}^*(k)$) to control the PMSM:

$$i_{qref}^*(k+1) = i_{qref}^*(k) + \Delta i_{qref}^*(k) \tag{11}$$

The criterion according to which the algorithm is performed is based on the integral of timed-weighted absolute error (ITAE) and has the following form:

$$f(t) = \int_0^t t|e(t)|dt \tag{12}$$

B. *Sliding Mode Observer*

By using the inverse Park transform, as can be noted in Fig. 1, the currents in the α-β reference frame are obtained and expressed in the following form [1], [6]:

$$\begin{aligned} \frac{di_\alpha}{dt} &= -\frac{R_s}{L} i_\alpha - \frac{1}{L} e_\alpha + \frac{1}{L} u_\alpha \\ \frac{di_\beta}{dt} &= -\frac{R_s}{L} i_\beta - \frac{1}{L} e_\beta + \frac{1}{L} u_\beta \end{aligned} \tag{13}$$

The equations of the SMO-type observer for the estimation of the PMSM rotor speed and position are based on the estimation of the back-EMF e_α and e_β.

$$\begin{aligned} \frac{d\hat{i}_\alpha}{dt} &= -\frac{R_s}{L} \hat{i}_\alpha + \frac{1}{L} u_\alpha - \frac{1}{L} kH(\hat{i}_\alpha - i_\alpha) \\ \frac{d\hat{i}_\beta}{dt} &= -\frac{R_s}{L} \hat{i}_\beta + \frac{1}{L} u_\beta - \frac{1}{L} kH(\hat{i}_\beta - i_\beta) \end{aligned} \tag{14}$$

Where the k parameter represents the observer gain, and function H is of *sigmoid* type:

$$H(x-y) = \frac{2}{1+e^{-a(x-y)}} - 1 \tag{15}$$

where: a represents a positive constant, and the *sigmoid* function indicated in relation (15) will be assigned values between -1 and 1 for a = 4.

Based on these, the estimates of the back-EMF are obtained in the following form [6]:

$$\begin{aligned} \hat{e}_\alpha &= kH(\bar{i}_\alpha) = -\lambda_0 \hat{\omega}_e \sin\theta_e \\ \hat{e}_\beta &= kH(\bar{i}_\beta) = \lambda_0 \hat{\omega}_e \cos\theta_e \end{aligned} \tag{16}$$

The PMSM rotor speed and position estimates expressed in relations (17) and (18) are obtained from the relation (16).

$$\hat{\omega}_e = \frac{\sqrt{\hat{e}_\alpha^2 + \hat{e}_\beta^2}}{\lambda_0} \tag{17}$$

$$\hat{\theta}_e(t) = \int_{t_0}^t \hat{\omega}_e(t)dt + \theta_0 \tag{18}$$

where: θ_0 is the initial electrical position of the rotor

III. NUMERICAL SIMULATION

Fig. 4 shows the block diagram for implementation in Matlab/Simulink of the PMSM sensorless control system. The sensorless character of the PMSM is given by the implementation of a SMO-type observer described in previous section. The PMSM nominal parameters are presented in Table I. Fig. 5 shows the comparative time evolution of the estimated speed of the PMSM based on PI controller and PI-GA-type controller. Other quantities presented in Fig. are the load torque and electromagnetic torque, of the stator currents, and currents i_d and i_q obtained based on the numerical simulation performed in Matlab/Simulink. It can be observed that by using the genetic algorithm to optimize the tuning parameters of the PI speed controller, when applying some speed reference step signals, the system response does not show overshooting and the response time is reduced.

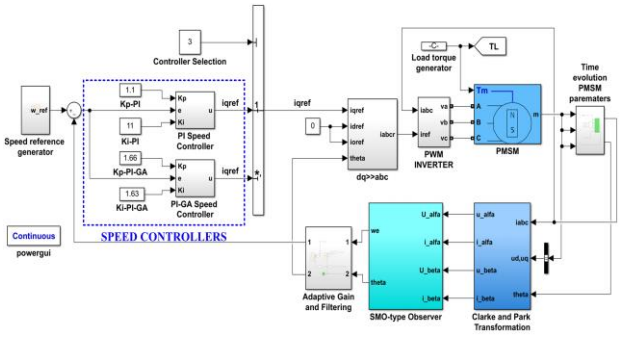

Fig. 4. The block diagram for implementation in Matlab/Simulink of the PMSM sensorless control system.

TABLE I. NOMINAL PARAMETERS OF THE PMSM

Parameter	Value	Unit
Rated voltage	24	V
Rated power	55	W
Rated speed	4000	rpm
Stator winding resistance - R_s	0.405	Ω
Stator winding inductance - L_s	0.63e-3	H
Moment of rotor inertia - J	4.6e-6	kg·m^2
Rotor friction - B	1.13e-6	N·m·s/rad
Permanent magnet flux linkage - λ_0	0.175	Wb
Pole pairs number - P	4	-

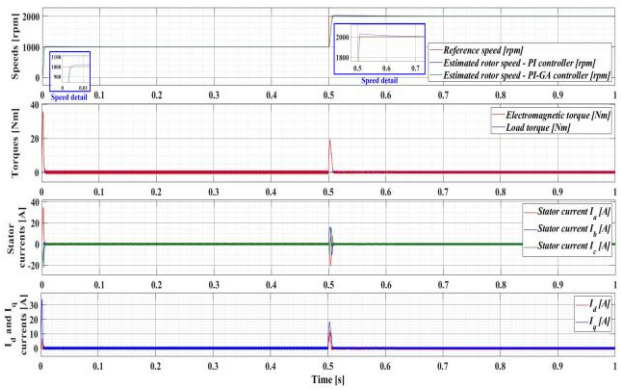

Fig. 5. Time evolution for the numerical simulation of the PMSM sensorless control system.

IV. THE ARCHITECTURE FOR THE REAL-TIME SENSORLESS CONTROL OF PMSM AND SCADA INTEGRATION

Fig. 6 shows the proposed architecture for the integration into SCADA of the real-time control system of a PMSM. The characteristics and operating equations of the PMSM, together with the control possibilities are presented in the previous section by means of numerical simulations in Matlab/Simulink.

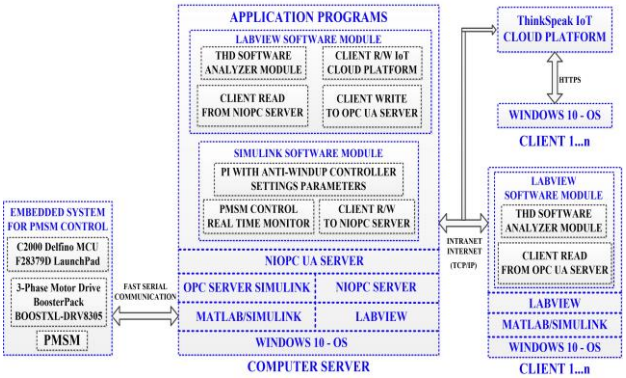

Fig. 6. The proposed general diagram for SCADA integration of the PMSM sensorless control system.

For the real-time implementation, we will use a development platform consisting of LAUNCHXL-F28379D and three-phase drive stage BOOSTXL DRV8305EVM. LAUNCHXL-F28379D use USB connected isolated XDS100v2 JTAG debug probe for real-time debug and flash programming; and contain TMS320F28379D MCU type controller with the following hardware characteristics: 200 MHz dual C28xCPUs type processor and dual CLAs, 1 MB Flash memory, 16-bit/12-bit ADCs type converter; 12-bit DACs type converter, comparators module, filters module, HRPWMs module, eCAPs module, eQEPs module, and CANs communication module. The BOOSTXL-DRV8305EVM platform is based on the DRV8305 motor gate driver and CSD18540Q5B power MOSFET. This type of module has individual DC bus and phase voltage sense as individual low-side current shunt sense for sensorless algorithms used for the control of the PMSM [17].

The block diagram of the software application for the real-time control of the PMSM is implemented in Simulink and is shown in Fig. 7. By analogy to Fig. 1, we note the implementation of the FOC type strategy, of which we mention the outer control loop for the control of speed (see Fig. 8), the inner control loop for the control of currents i_d and i_q (see Fig. 9), and the communication loop which will be required later in the software application for monitoring the control process (see Fig. 10). The running time of the two control loops is 0.05ms for the current loop, and for the speed loop it is 0.5ms.

The usual software blocks for real-time implementation are provided by the Motor Control Blockset Toolbox (Park and Clarke transforms, the sensorless observers, the anti-windup IP, etc.). By means of the Embedded Coder Support Package for TI C2000 Processors, the application program is translated into C language or machine code to be downloaded to the F28379D MCU. A code optimization is also performed, resulting in the translation from fixed point to adjustable point, leading to major improvements in the real-time control performances [17].

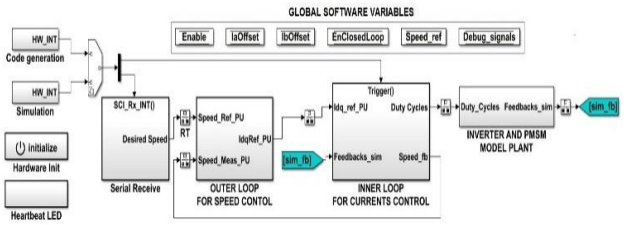

Fig. 7. The block diagram of the software application for real-time implementation in the embedded system.

The discrete time equation of the PI-type controller with anti-windup is the following:

$$i_{qref}(k) = \left\lfloor K_p + \left(K_i + di_{qref}(k) K_{aw}\right) \frac{T_s z}{z-1} \right\rfloor e(k) \quad (19)$$

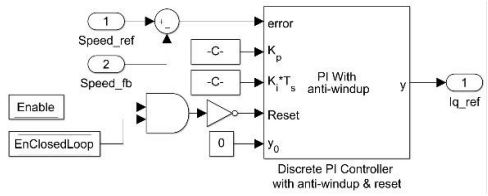

Fig. 8. The block diagram for implementation in Matlab/Simulink of the speed controller.

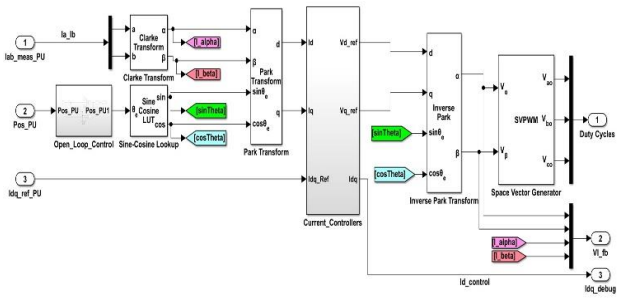

Fig. 9. The block diagram for implementation in Matlab/Simulink of the current controllers and PWM generation signals.

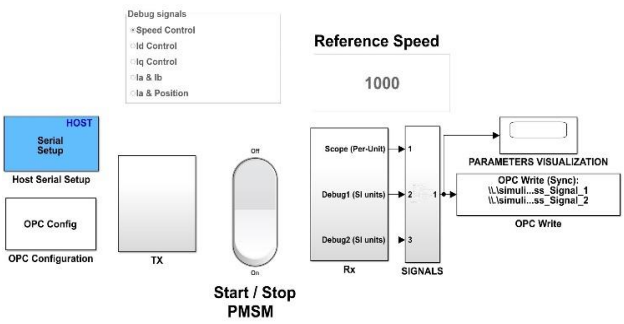

Fig. 10. The block diagram of the software application for monitoring the control process of the PMSM.

The connection between the OPC servers embedded in these software development environments provides the data stream for supervising the PMSM control between Matlab/Simulink and LabVIEW. For this purpose, we define the network-published shared variable, by which the data in the Intranet network based on Ethernet TCP/IP can be written and read. The Shared Variable Engine (EVS) mechanism uses the NI Publish-Subscribe Protocol (NI-PSP) to transfer data corresponding to the variables distributed in the data network [15, 18].

Fig. 11 shows the connection achieved between the OPC server embedded in Simulink and the "*localhost/National Instruments.Variable Engine.1*" server embedded in LabVIEW using blocks from the OPC Toolbox Simulink. The OPC Write block in SVE presented in Fig. 12 is used to perform the actual writing of the PMSM control process variables. These variables are accessible in software programs developed in LabVIEW on the computer server, but are also accessible to the embedded OPC UA server to achieve the communication with client computers connected to the Intranet/Internet.

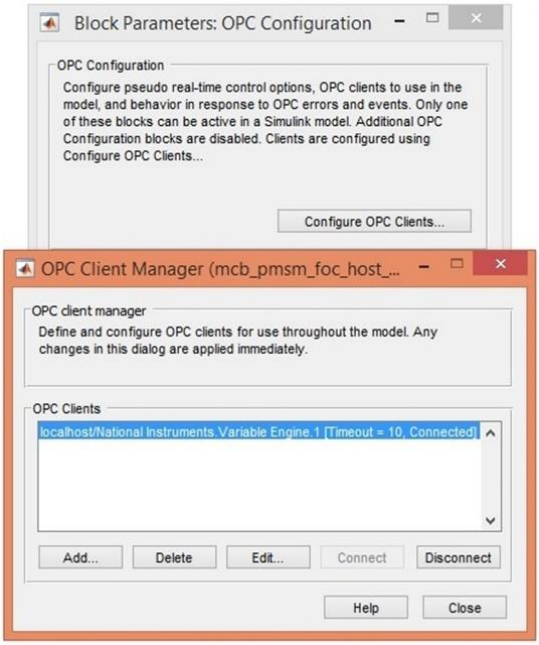

Fig. 11. Simulink OPC Server configuration.

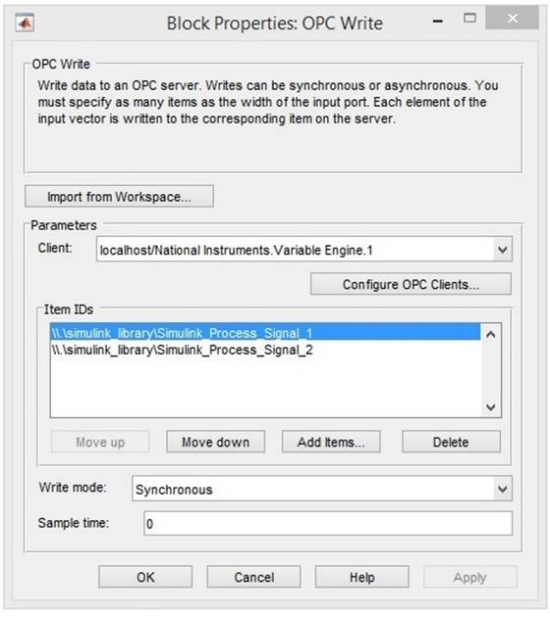

Fig. 12. Simulink OPC Server write variables of the control process.

Fig. 13 shows the LabVIEW project tree with the software applications developed on the computer server and the SVE library.

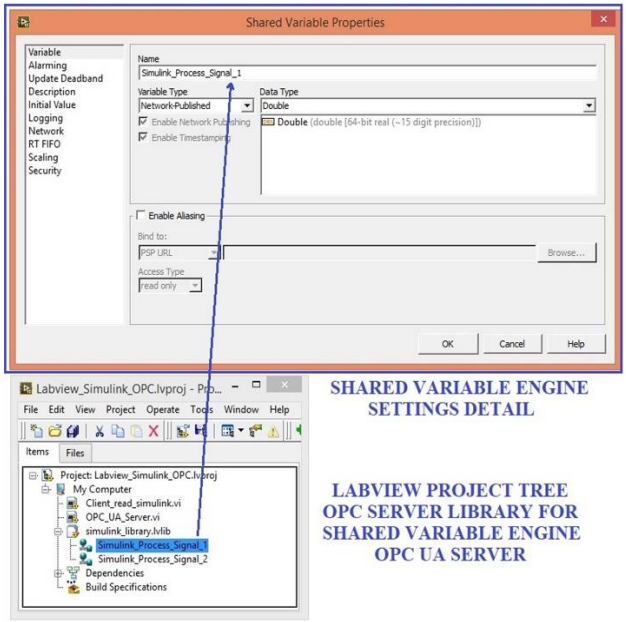

Fig. 13. LabVIEW project tree for the software applications on the computer server.

Fig. 14, Fig. 15, and Fig. 16 show the OPC UA server configuration tasks and the read/write tasks which ensure communication between the OPC UA servers on the computer server and the client software applications on the computers connected to the Internet.

Besides, a separate task can run online on a client computer to monitor the quality electrical parameters of the controlled PMSM [16].

Fig. 17 shows the implementation in a client/LabVIEW for THD analysis software module.

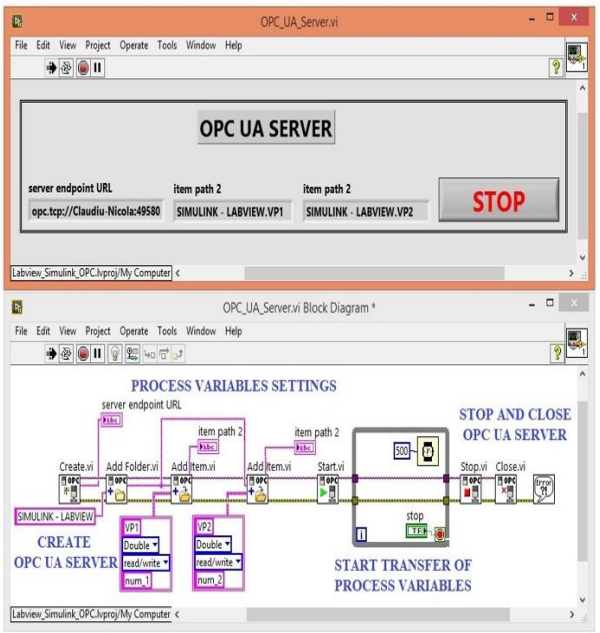

Fig. 14. OPC UA server configuration and implementation in LabVIEW.

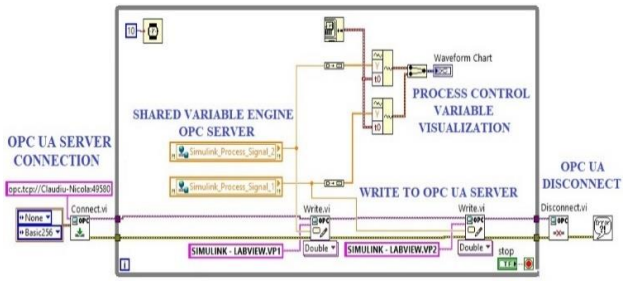

Fig. 15. Implementation in LabVIEW of the OPC UA client write.

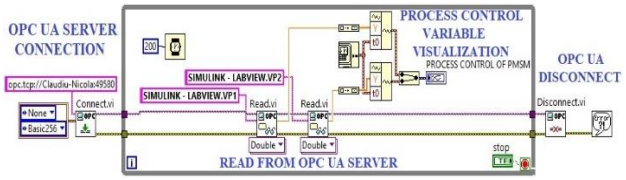

Fig. 16. Implementation in LabVIEW of the OPC UA client read.

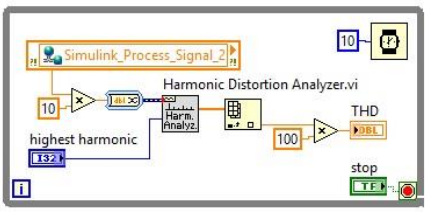

Fig. 17. Implementation in a client/LabVIEW of the task for the THD analysis.

Data from the PMSM control process can be shared in a more flexible way by using an IoT platform, which allows the data in the cloud to be viewed, analyzed and processed. The platform can be accessed from both Matlab/Simulink and LabVIEW using specific GET, POST, PUT, and DELETE commands. These commands create, write, read, or delete communication channels. These commands are HTTP requests and responses and fit into the representational state transfer (REST) architecture [19]. The configuration of a communication channel used in the presented application can be done at the address "*https://thingspeak.com/channels/1306529*" and is presented schematically as in Fig. 18.

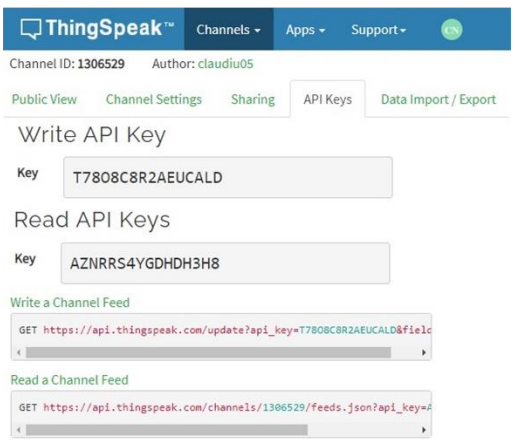

Fig. 18. Configuration settings of the IoT server for read / write channel.

A separate task implemented in LabVIEW on the computer server (see Fig. 19) writes data to this channel.

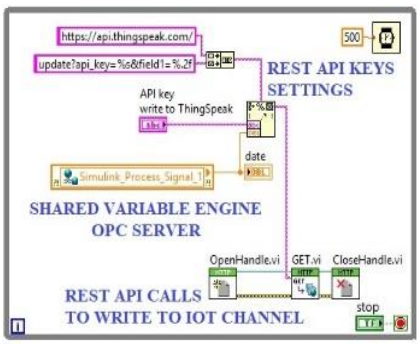

Fig. 19. Configuration settings of the IoT server for read / write channel.

V. Experimental Results

The PMSM sensorless control system was tested in real- time in two stages. The values of the speed and the parameters of interest (currents and torque) are presented in the first stage using the interface on the host computer/computer server (see Fig.s 20-24). In the second stage, the integration into SCADA and the communication with IoT cloud platform were tested (see Fig. 25 and Fig. 26).

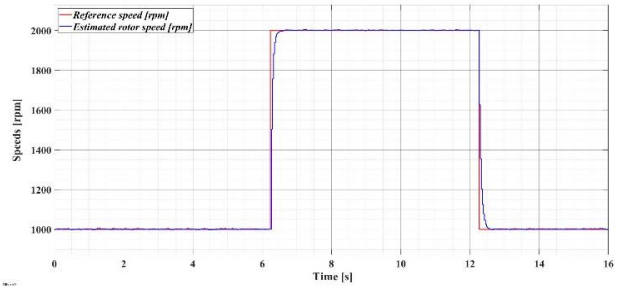

Fig. 20. Time evolution of the estimated PMSM rotor speed.

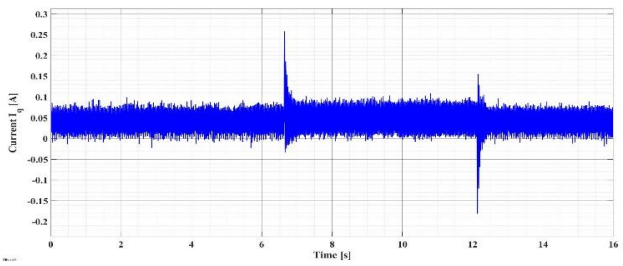

Fig. 21. Time evolution of current I_q.

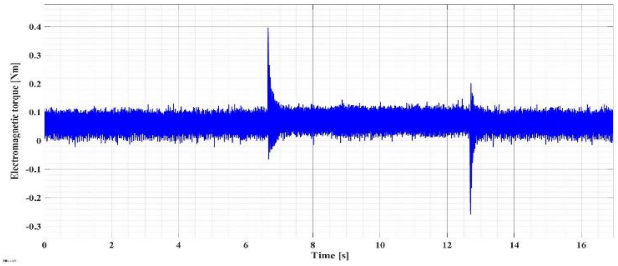

Fig. 22. Time evolution of the electromagnetic torque T_e.

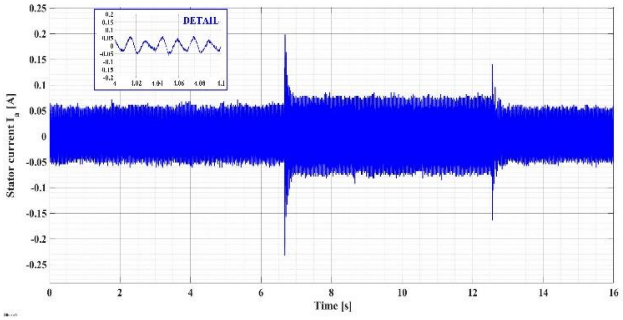

Fig. 23. Time evolution of the stator current I_a.

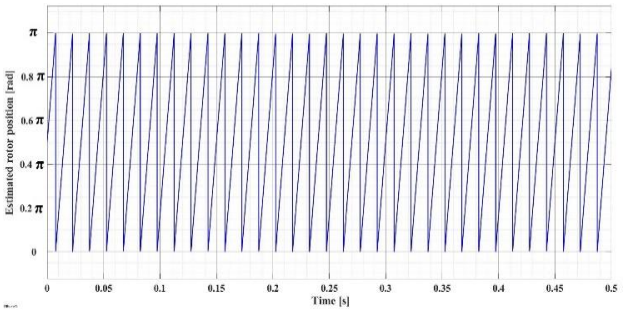

Fig. 24. Time evolution of the PMSM rotor position.

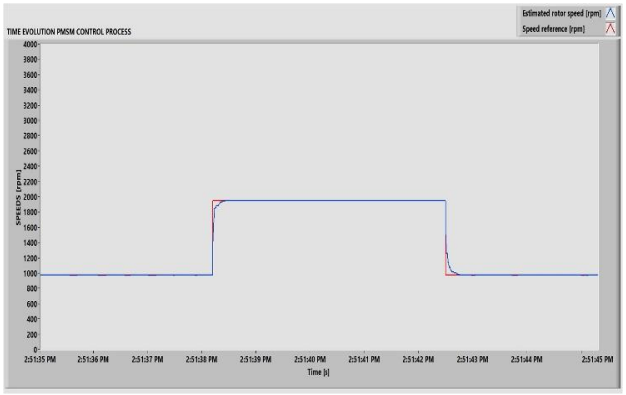

Fig. 25. Time evolution of the estimated PMSM rotor speed on OPC UA client read.

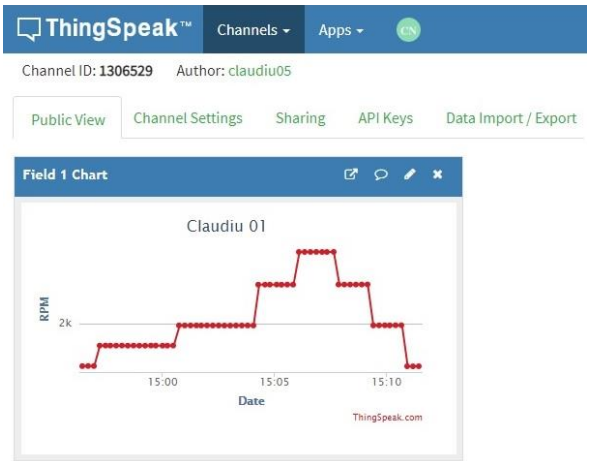

Fig. 26. Time evolution of the estimated PMSM rotor speed on IoT cloud platform.

VI. CONCLUSIONS

The article presents the mathematical models of a PMSM, of the FOC-type sensorless control, using a PI-type control with anti-windup and an SMO-type rotor speed and position observer. The tuning of the parameters of the PI-type with anti-windup speed controller is optimized by using a genetic algorithm. The article presents both the numerical simulations and the real-time implementation of the control system using a LAUNCHXL-F28379D-type development and control platform and three-phase drive stage DRV8305EVM from Texas Instruments.

OPC-type servers are used to achieve the integration into SCADA. For greater flexibility, an IoT platform is used, in order to use computers with no Simulink or LabVIEW software development modules installed. In future papers we will focus on the real-time implementation of a multi-motor application in which the control of parameters is performed locally or on the Intranet through proper integration into the local SCADA system.

ACKNOWLEDGMENT

The paper was developed with funds from the Ministry of Research and Innovation as part of the NUCLEU Program: PN 19 38 01 03 and PN 19 38 01 04.

Contribution of authors:

First author – 40%

First coauthor – 30%

Second coauthor – 10%

Third coauthor – 10%

Fourth coauthor – 10%

Received on July 31, 2021

Editorial Approval on November 20, 2021

REFERENCES

[1] V. Utkin, J. Guldner, J. Shi, Sliding mode control in electromechanical systems, second edition. Automation and Control Engineering, Taylor & Francis, 2009.

[2] B. K. Bose, Modern power electronics and AC drives, Prentice Hall, Knoxville, Tennessee, USA, 2002.

[3] H. Wang and J. Leng, "Summary on development of permanent magnet synchronous motor," *Chinese Control And Decision Conference (CCDC)*, Shenyang, China, 2018, pp. 689-693.

[4] Z. Liu, Y. Li, and Z. Zheng, "A review of drive techniques for multiphase machines," in CES Transactions on Electrical Machines and Systems, vol. 2, no. 2, pp. 243-251, June 2018.

[5] S. Sakunthala, R. Kiranmayi, and P. N. Mandadi, "A Review on Speed Control of Permanent Magnet Synchronous Motor Drive Using Different Control Techniques," *International Conference on Power, Energy, Control and Transmission Systems (ICPECTS)*, Chennai, China, 2018, pp. 97-102.

[6] M. Nicola and C. I. Nicola, "Sensorless Control for PMSM Using Model Reference Adaptive Control and back -EMF Sliding Mode Observer," *International Conference on Electromechanical and Energy Systems (SIELMEN)*, Craiova, Romania, 2019, pp. 1-7.

[7] M. Nicola and C. I. Nicola, "Sensorless Predictive Control for PMSM Using MRAS Observer," *International Conference on Electromechanical and Energy Systems (SIELMEN)*, Craiova, Romania, 2019, pp. 1-7.

[8] M. Nicola, C. I. Nicola, and M. Duță, "Sensorless Control of PMSM using FOC Strategy Based on Multiple ANN and Load Torque Observer," *International Conference on Development and Application Systems (DAS)*, Suceava, Romania, 2020, pp. 32-37.

[9] M. Mutluer and O. Bilgin, "Design optimization of PMSM by particle swarm optimization and genetic algorithm," *International Symposium on Innovations in Intelligent Systems and Applications*, Trabzon, Turkey, 2012, pp. 1-4.

[10] X. S. Yang, Nature-Inspired Metaheuristic Algorithms, 2nd Edition, Luniver Press, UK, 2010.

[11] A. Enegelbrecht, Computational intelligence an introduction, 2nd Edition, John Wiley&Sons Ltd, Chichester, West Sussex, England, 2007.

[12] C. I. Nicola, M. Nicola, A. Vintilă, and D. Sacerdoțianu, "Identification and Sensorless Control of PMSM Using FOC Strategy and Implementation in Embedded System," *International Conference and Exhibition on Electromechanical and Energy Systems (SIELMEN)*, Craiova, Romania, 10-11 October, 2019, pp. 335-340.

[13] Z. Chen, "Permanent Magnet Synchronous Motor Parameter Test System Based on LabVIEW," *3rd Advanced Information Management, Communicates, Electronic and Automation Control Conference (IMCEC)*, Chongqing, China, 2019, pp. 434-437.

[14] M. Sreejeth, M. Singh, P. Kumar, P. Varshney, and P. Sachdeva, "Implementation of supervisory control system for PMSM drive," *5th India International Conference on Power Electronics (IICPE)*, Delhi, India, 2012, pp. 1-6.

[15] M. Nicola, C. I. Nicola, M. Duță, D. Sacerdoțianu, "SCADA Systems Architecture Based on OPC and Web Servers and Integration of Applications for Industrial Process Control," in International Journal of Control Science and Engineering, vol. 8, no. 1, pp. 13-21, April 2018.

[16] C. I. Nicola *et al*., "Quality analysis of electric energy using an interface developed in LabVIEW environment," *International Conference on Applied and Theoretical Electricity (ICATE)*, Craiova, Romania, 2016, pp. 1-6.

[17] Motor Control Blockset™ User's Guide, Matlab and Simulink, MathWorks, Natick, MA, 2020.

[18] M. S. Mahmoud, M. Sabih, M. Elshafei, "Using OPC technology to support the study of advanced process control," in ISA Transactions, vol. 55, pp. 155-167, March 2015.

[19] The IoT Platform with MATLAB Analytics. Available [online]: https://nl.mathworks.com/help/thingspeak/.

[20] C. I. Nicola, M. Nicola, M. C. Nițu, "Real-Time Sensorless Control of PMSM and SCADA Integration," *International Conference on Applied and Theoretical Electricity (ICATE)*, Craiova, Romania, 2021, pp. 1-6.

The Choice of the Main Power Components in Electric Traction Converters

Lavinius Sorin Goreci*, Mihaela Popescu** and Ion Tilă*
* S.C. INDA SRL, Research&Development Department, Craiova, România, lavinius.goreci@inda.ro, tila.ion@inda.ro
University of Craiova, Faculty of Electrical Engineering, Craiova, Romania, mpopescu@em.ucv.ro

DOI: 10.52846/AUCEE.2021.1.05

***Abstract* – The choice of the power components of the electric traction converters for autonomous vehicles is a very important aspect in their design. The attention in this paper is first focused on the choice of the DC link capacitor, followed by choice of the IGBT modules, their testing and cooling. Then, the choice of power cables is approached. A dedicated test bench for electric traction converters for autonomous vehicles was designed and achieved. In defining the parameters of the test bench, various possible applications on battery-powered vehicles were taken into account, but also their performances, technical characteristics and functional characteristics. An important share belongs to the integrated propulsion/charging system of the Li-Ion battery developed by the company SC INDA SRL. It is already used in automotive on full-electric trucks and in the battery-powered electric locomotives.**

Cuvinte cheie: *vehicul autonomy, IGBT, condensator de current continuu, invertor, radiator, răcire, MELCOSIM.*

Keywords: *autonomous vehicle, IGBT, DC link capacitor, inverter, heat sink, cooling, MELCOSIM.*

I. Introduction

Currently, high voltage and current IGBTs are state-of-the-art power electronics modules for the electric traction converters for autonomous vehicles [1-5]. The IGBT itself is part of a complex power kit which includes besides the transistor, input capacitors, laminated bus bars, the cooling system, gate drives etc. For reliable operation the choice of these components is not an easy task considering the technical characteristics of the traction systems.

The best features of a high power IGBT module are closely related to a reliable and high quality protection for IGBT drivers [1]. The attention in [2] is directed towards the connection between a reliable operation of IGBT modules and three important requirements that they have to fulfill: high junction temperature limit, large safe operating area, high current capacity. Methods for obtaining IGBT switching frequency limits are discussed in [3]. A comparison between switching characteristics and losses of IGBT modules for traction applications is studied experimentally in [4]. Reference [5] describes the equations for the power losses evaluation and passive elements design.

The test bench described below includes the designed inverters in the final purpose of a subsidiary contract to the PACETSINEFEN project within the Competitiveness Operational Program, European Regional Development Fund [6]. A block diagram is presented in Fig. 1, where:

TR – three-phase transformer with control sockets;
R – three-phase rectifier;
INV1, INV2 – three-phase inverters;
Ct – DC link capacitor;
CF – braking chopper;
RF – braking resistor;
MAS1 – asynchronous machine (motor mode);
MAS2 – asynchronous machine (generator mode);
TUi – voltage transducers;
TCi – current transducers;
TG1, TG2 – speed transducers;
TCP – torque transducers;
UCR – electronic control unit.

The testbench consists of two asynchronous machines (MAS1, MAS2) mechanically coupled, the first one operating in motor mode and the second in generator mode. The rated power of each machine is 155 kW and in short-term overload mode they allow 390 kW. This ensures a wide range of tests with power up to 400 kW.The two asynchronous machines are supplied by two inverters INV1 and INV2 with PWM (pulse width modulation) control and variable frequency according to the operating modes. The two inverters have a classic structure and have a common DC link. The energy consumed by MAS1 in the motor mode is taken from MAS2 which operates in generator mode and motor – generator system losses are taken from the power supply

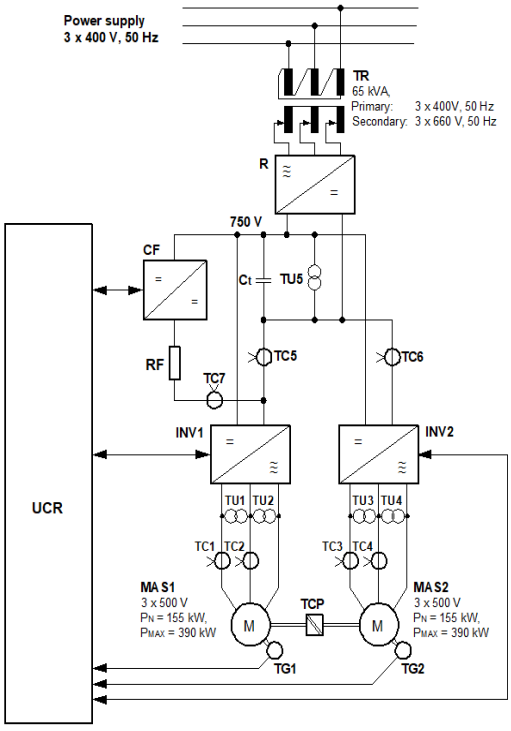

Fig. 1 The block diagram of the test bench.

(3x400 V, 50 Hz) through the transformer TR and rectifier R. For the situation of dynamic regime in the intermediate

circuit, an RF braking resistor is provided, the current through this resistor being controlled by the CF Braking Chopper.

The rest of the paper is organized as follows: Section II describe the choice of DC link capacitor. In section III, the main parameters of leading inverter are defined and his section deals with the choice of IGBT modules. It is followed by the IGBT modules verification in Section IV. Section V and VI are related to the choice of the cooling system and the power cables. Finally, some concluding remarks are drawn.

II. THE CHOICE OF THE DC LINK CAPACITOR

The following relationships are used to calculate the characteristic data for the inverter that supplies MAS1 [7]:

- Rated power,

$$S_{NINV1} = \frac{P_{1NMAS1}}{\cos\varphi_{MAS1}\cdot\eta_{MAS1}} = 188.6\ \text{kVA}\,, \quad (1)$$

where P_{MAS1}, $\cos\varphi_{MAS1}$, η_{MAS1} are the active power, the power factor and respectively the efficiency of machine MAS1.

As can be seen in the block diagram (Fig.1), the direct current intermediate circuit of the inverter INV1 is common with those of the inverter INV2, braking chopper CF and the filter of rectifier R and therefore the total capacitance value in the diagram was taken into account for the calculation of the capacitor bank.

To determine the required capacitance value we will consider the following conditions:

- ripple voltage alowed,

$$U_{RR} = 15\% \cdot U_{CC}\ ; \quad (2)$$

For rated voltage U_{CC} = 750V, it results U_{RR} = 112.5V.

- the inverter efficiency,

$$\eta_{INV1} = 93\ \%\ ;$$

- The input power of the inverter INV1,

$$P_{INV1} = S_{INV1} + p_{INV1} = 202\ \text{kW}, \quad (3)$$

where S_{INV1}, p_{INV1} are the rated power and power losses of the inverter.

To calculate the nedeed capacitance, it can be used the following approached equation [8]:

$$C_{tcalc} = \frac{P_{INV1}}{U_{RR}\left(U_{CC} - \frac{U_{RR}}{2}\right)f_R} = 8600\mu\text{F}\,, \quad (4)$$

where: f_R - the rectifier frequency, f_R=300Hz.

The RMS current through capacitor will be (approached equation) [8]:

$$I_{CRMS} = \frac{U_{RR}}{2\sqrt{2}} \cdot C_{tcalc} \cdot 2 \cdot \pi \cdot f_R = 646\ \text{A}\,. \quad (5)$$

The nedeed capacitance for the inverter INV1:

$$C_{INV1} = C_{tcalc} - (C_{INV2} + C_{CF} + C_R), \quad (6)$$

where:

C_{INV2} = 4380 µF - capacitance value of the inverter INV2;

C_{CF} = 1460 µF - capacitance value of the braking chopper CF;

C_R = 1460 µF - capacitance value of the rectifier R.

We obtain C_{INV1} = 1300 µF.

Two ZEZ SILKO **PVAJP 0 1,8/700** capacitors conected in parallel were selected with the main characteristics:

- rated capacitance C_N = 700 µF ± 10 %;
- rated DC voltage U_N= 1800V;
- insulation voltage U_i= 4800 V;
- maximum rms current I_{max}= 150 A;
- operating temperatures Θ_a = -25/+70 ˚C.

The selection criteria are met as follows:

$$C_t \geq C_{tcalc}; \quad (7)$$

$$U_N > U_{CCmax}; \quad (8)$$

$$I_{CRMS} \geq I_{CRMScalc}. \quad (9)$$

The inequality (9) results from the fact that all the capacitors in the common DC intermediate circuit are connected in parallel (8 capacitors that have the value Imax ≥ 150 A), the value of the total current they can supply will add up, exceeding the value resulting from the calculations.

I. THE CHOISE OF THE IGBT MODULE

The inverter output voltage is equal with the rated voltage of the electric machine [6].

$$U_{NINV1} = U_{NMAS1} = 500\ \text{V}_{\text{AC}}. \quad (10)$$

- The rated current phase of the inverter

Since the windings of the MAS1 electric machine are connected in star, the following results:

$$I_{NMAS1} = \frac{S_{NINV1}}{\sqrt{3}\cdot U_{NMAS1}} = 218\text{A}\,, \quad (11)$$

where: U_{NMAS1} – rated voltage of MAS1.

- Inverter overload power:

$$S_{SINV1} = 1{,}5 \cdot S_{NINV1} = 283\ \text{kVA}; \quad (12)$$

- Inverter overload phase current:

$$I_{SMAS1} = 1{,}5 \cdot I_{NINV1} = 327\ \text{A}; \quad (13)$$

- Inverter supply voltage range:

$$U_{CC} = 600 \div 900\text{V}_{\text{CC}}. \quad (14)$$

The power transistor shall be chosen with respect to the following relationships:

$$I_{TAVN} \cdot k_{SI} \leq I_{ccat}\ ; \quad (15)$$

$$U_b \cdot k_{SU} \leq U_{CEScat}\ ; \quad (16)$$

$$U_b = U_{cc}\ ; \quad (17)$$

$$I_{TAVN} = \frac{\sqrt{2}}{\pi} \cdot I_{SMAS1} = 147.2\ A\ ; \quad (18)$$

where:

I_{TAVN} - the average rated current through the transistor;

$I_{c\,cat}$ - the maximum permissible average current through the transistor;
k_{si} - the current safety factor;
U_b - the voltage that stresses the transistor in off state;
$U_{CES\ cat}$ - the maximum permissible voltage that stresses the transistor in off state;
k_{su} - the voltage safety coefficient;
U_{CC} - the intermediate circuit voltage.

Because the inverter is part of a research test bench where control errors may occur or higher power motors can be tested, the coefficients k_{su}= 1.8, respectively k_{si} = 10 were chosen resulting:

$$U_{CES\ cat} > 1500\ \text{V}; \quad (19)$$

$$I_{C\ cat} > 1500\ \text{A}. \quad (20)$$

The Mitsubishi **CM2400HC - 34H IGBT** module was preliminarily selected, with the main characteristics:

- capsule with a single IGBT - diode switching device;
- collector emitter voltage - V_{CES} = 1700 V;
- direct collector current I_C = 2400A;
- module dimensions : 190 x 140 mm.

An extract from the technical specification of this module is shown in Fig. 2. (a) and (b) [9].

III. Testing of the IGBT Module

Testing was done based on the **MELCOSIM Ver 5.4.0** application, developed by Mitsubishi for the selection of its own IGBT modules, arranged in the most common topologies.

MELCOSIM is designed for the calculation of the stationary and dynamic power losses that occur in modules as well as the temperature variation in the junctions of IGBT transistors and diodes in modules, due to both the direct conduction and switching of these semiconductor devices.

The corresponding data obtained for the specific dynamic thermal resistance of the power modules are used for the design, calculation and dimensioning of the heat sink.

A. *MELCOSIM Program Description*

The converter type (two or three levels) can be selected from the main screen and then, switching in the screens for input and output data is done. The input-output screens consist of four sections: the module code and type, the specified module property, the input field "Common Conditions" for the converter characteristic data and the output field for the calculation results.

MELCOSIM expects nine entries called "Common Conditions" to be able to calculate power losses and temperature in the junction: modulation strategy, output current Io, DC link *Vcc* voltage, switching frequency *Fc*, output frequency *Fo*, modulation factor *M*, load power factor *PFs* and the heat sink temperature measured directly below the *Ts* capsule.

The results field provides the following information: average power losses for IGBT and freewheel diode, divided into static and dynamic parts, total power loss of the module, heat sink temperature, average and maximum temperature in the transistor junction and in the freewheel diode. The graphics output provides the possibility to analyze power losses and temperature in junction by changing one of the application conditions parameters within the specification.

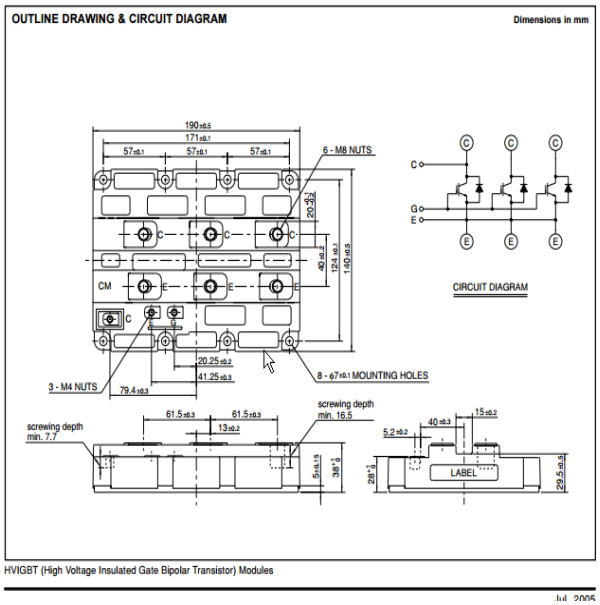

(a)

CM2400HC-34H

HIGH POWER SWITCHING USE INSULATED TYPE

3rd-Version HVIGBT (High Voltage Insulated Gate Bipolar Transistor) Modules

MAXIMUM RATINGS

Symbol	Item	Conditions	Ratings	Unit
V_{CES}	Collector-emitter voltage	V_{GE} = 0V, T_j = 25°C	1700	V
V_{GES}	Gate-emitter voltage	V_{CE} = 0V, T_j = 25°C	±20	V
I_C	Collector current	T_C = 80°C	2400	A
I_{CM}		Pulse (Note 1)	4800	A
I_E (Note 2)	Emitter current		2400	A
I_{EM} (Note 2)		Pulse (Note 1)	4800	A
P_C (Note 3)	Maximum power dissipation	T_C = 25°C, IGBT part	17800	W
T_j	Junction temperature		−40 ~ +150	°C
T_{op}	Operating temperature		−40 ~ +125	°C
T_{stg}	Storage temperature		−40 ~ +125	°C
V_{iso}	Isolation voltage	RMS, sinusoidal, f = 60Hz, t = 1min.	4000	V
t_{psc}	Maximum short circuit pulse width	V_{CC} = 1150V, V_{CES} ≤ 1700V, V_{GE} = 15V, T_j = 125°C	10	µs

ELECTRICAL CHARACTERISTICS

Symbol	Item	Conditions	Limits Min	Limits Typ	Limits Max	Unit
I_{CES}	Collector cut-off current	V_{CE} = V_{CES}, V_{GE} = 0V, T_j = 25°C	—	—	36	mA
$V_{GE(th)}$	Gate-emitter threshold voltage	I_C = 240mA, V_{CE} = 10V, T_j = 25°C	4.5	5.5	6.5	V
I_{GES}	Gate leakage current	V_{GE} = V_{GES}, V_{CE} = 0V, T_j = 25°C	—	—	0.5	µA
$V_{CE(sat)}$	Collector-emitter saturation voltage	I_C = 2400A, V_{GE} = 15V, T_j = 25°C (Note 4)	—	2.60	3.30	V
		I_C = 2400A, V_{GE} = 15V, T_j = 125°C (Note 4)	—	3.10	—	
C_{ies}	Input capacitance	V_{CE} = 10V, f = 100kHz, V_{GE} = 0V, T_j = 25°C	—	210	—	nF
C_{oes}	Output capacitance		—	30.0	—	nF
C_{res}	Reverse transfer capacitance		—	10.1	—	nF
Q_G	Total gate charge	V_{CC} = 850V, I_C = 2400A, V_{GE} = 15V, T_j = 25°C	—	19.8	—	µC
V_{EC} (Note 2)	Emitter-collector voltage	I_E = 2400A, V_{GE} = 0V, T_j = 25°C (Note 4)	—	2.30	3.00	V
		I_E = 2400A, V_{GE} = 0V, T_j = 125°C (Note 4)	—	1.85	—	
$t_{d(on)}$	Turn-on delay time	V_{CC} = 850V, I_C = 2400A, V_{GE} = ±15V	—	—	1.60	µs
t_r	Turn-on rise time	$R_{G(on)}$ = 0.27Ω, T_j = 125°C, L_s = 80nH	—	—	1.30	µs
E_{on}	Turn-on switching energy	Inductive load	—	810	—	mJ/pulse
$t_{d(off)}$	Turn-off delay time	V_{CC} = 850V, I_C = 2400A, V_{GE} = ±15V	—	—	2.70	µs
t_f	Turn-off fall time	$R_{G(off)}$ = 0.27Ω, T_j = 125°C, L_s = 80nH	—	—	0.80	µs
E_{off}	Turn-off switching energy	Inductive load	—	870	—	mJ/pulse
t_{rr} (Note 2)	Reverse recovery time	V_{CC} = 850V, I_C = 2400A, V_{GE} = ±15V	—	—	2.70	µs
Q_{rr} (Note 2)	Reverse recovery charge	$R_{G(on)}$ = 0.27Ω, T_j = 125°C, L_s = 80nH	—	630	—	µC
E_{rec} (Note 2)	Reverse recovery energy	Inductive load	—	330	—	mJ/pulse

Note 1. Pulse width and repetition rate should be such that junction temperature (T_j) does not exceed T_{opmax} rating (125°C).
2. The symbols represent characteristics of the anti-parallel, emitter to collector free-wheel diode (FWDi).
3. Junction temperature (T_j) should not exceed T_{jmax} rating (150°C).
4. Pulse width and repetition rate should be such as to cause negligible temperature rise.

(b)

Fig. 2 Extract from the technical specification of the IGBT module CM2400HC-34H.

All calculation results can be exported to a text file [10].

B. IGBT Module Testing in Overload Conditions

Testing the IGBT module in overload conditions was performed using the MELCOSIM application with the following input data (Fig 3):

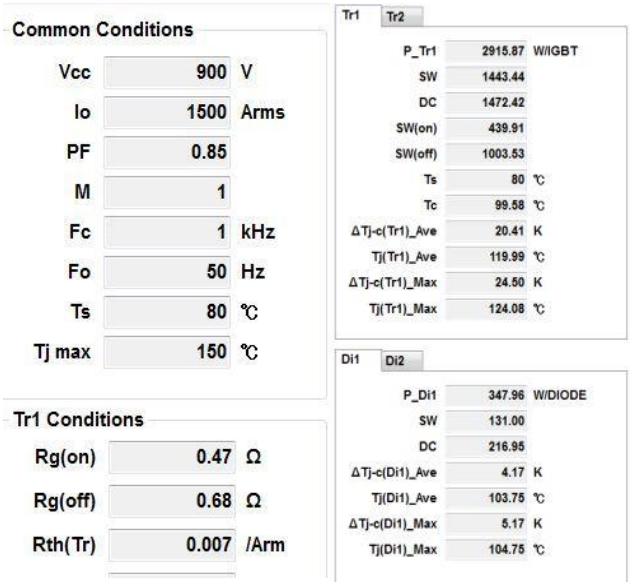

Fig. 3 „Common Condition" and „Result" fields for overload testing.

Vcc - the maximum value for the DC circuit voltage, equal to the voltage that stresses the transistor in off state, respectively equal to the voltage limited by the braking chopper (CF) that is set to the value of 900 Vdc;

Io - The maximum output current of the asynchronous machine adjusted until the program no longer returns invalid messages.

The valid returned parameters correspond to the most unfavorable situation in which the device can operate for the chosen conditions, resulting:

$$I_O \gg I_{SMAS1}\,. \qquad (21)$$

C. IGBT Module Testing for Operation in Rated Conditions (Fig 4):

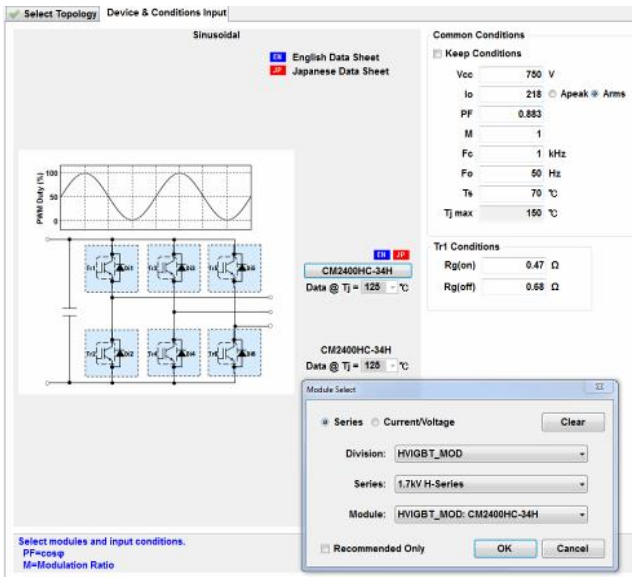

Fig. 4 The „Device & Components" screen for IGBT module testing at the rated condition operation.

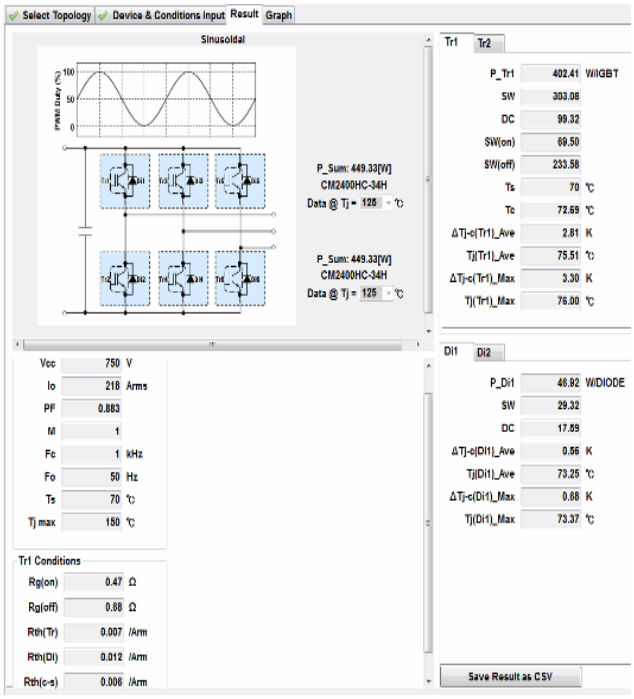

Fig. 5 "Result" screen with the characteristic values for the semiconductor components corresponding to a phase of the inverter.

The following parameters for the operation at rated load values have been introduced (Fig. 4 and Fig. 5):

- Input voltage *Vcc* (U_{ININV1}) = 750 V ;
- Output rated current *Io* (I_{NMAS1}) = 218 A_{RMS};
- Machine power factor *PF* ($\cos\varphi_{NMAS1}$) = 0.883;
- Modulation factor *M* = 1;
- Switching frequency *Fc* = 1 kHz;
- Converter output frequency *Fc* = 50 Hz;
- Heat sink temperature Ts = 70 °C.

The following considerations were considered in order to choose the gate control resistances which are relevant for the turn on and for the turn off process of the IGBT transistors, respectively:

- achieving minimal switching losses in both turn on and turn off by choosing the lowest possible resistance values;
- the peak current of the gate control devices.

The following values have been chosen using the data sheets:

- conduction input resistance $R_{g(ON)}$ = 0.47 Ω/1W;
- blocking resistance $R_{g(Off)}$ = 0.68 Ω/1W.

IV. CHOOSING THE COOLING SYSTEM

The heat transfer diagram (Fig. 6) can be drawn up with the values obtained in the "Result" screen [11].

The "Graph" screen can generate the dissipated power versus time characteristic for two modules belonging to the same phase, giving additional information when multiple capsules are mounted on the same heat sink (Fig. 7).

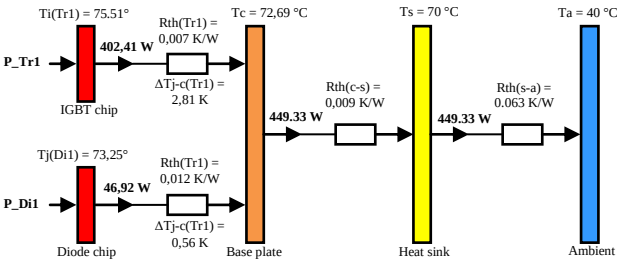

Fig. 6 The heat transfer diagram for the chosen IGBT module.

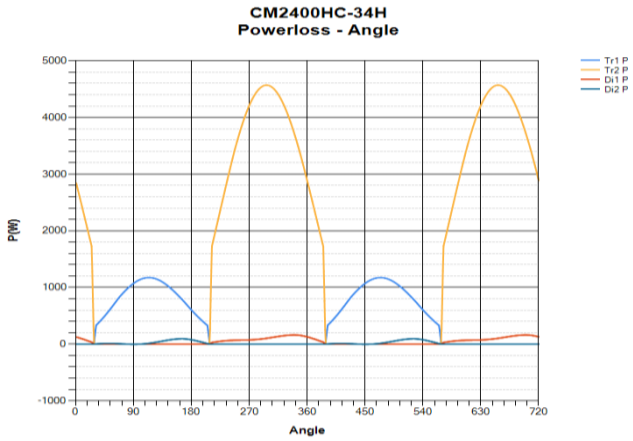

Fig. 7 Power dissipation versus time dependence for modules 1 and 2 of the inverters.

The heat transfer resistance between ambient and heat sink is:

$$Rth_{s-a} = \frac{T_c - T_a}{P\ Sum} - Rth_{c-s} = 0.063\ \text{K/W}, \quad (22)$$

where:

T_c - case temperature;
T_a - ambient temperature;
P_Sum - total power dissipated by the module due to the conduction and commutation losses.

A heat sink is chosen from the catalog in order to meet the condition:

$$Rth_{s\text{-}a}cat < Rth_{s\text{-}a}calc, \quad (23)$$

where:

$Rth_{s\text{-}a}calc$ - calculated thermal resistance heat sink – ambient;
$Rth_{s\text{-}a}cat$ - thermal resistance heat sink – ambient catalog value.

A heat sink with the profile shown in Fig. 8 having a length of 250 mm, manufactured by MECCAL type **P200 83** was chosen [12].

From the thermal transfer curves shown in Fig. 9,it can be seen that, provided an air speed of *Vair* = 7.2 m/s through the heatsink with a length of 250 mm, the following resistance is obtained:

$$Rth_{s\text{-}a}cat = 0.051\ \text{K/W}, \quad (24)$$

which is less than the value in (22), so the cooling system is chosen properly.

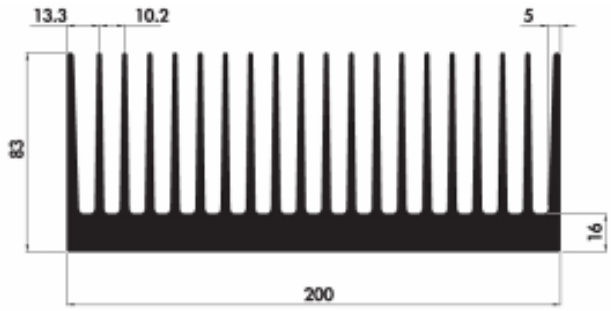

Fig. 8 Transversal section through the heat sink.

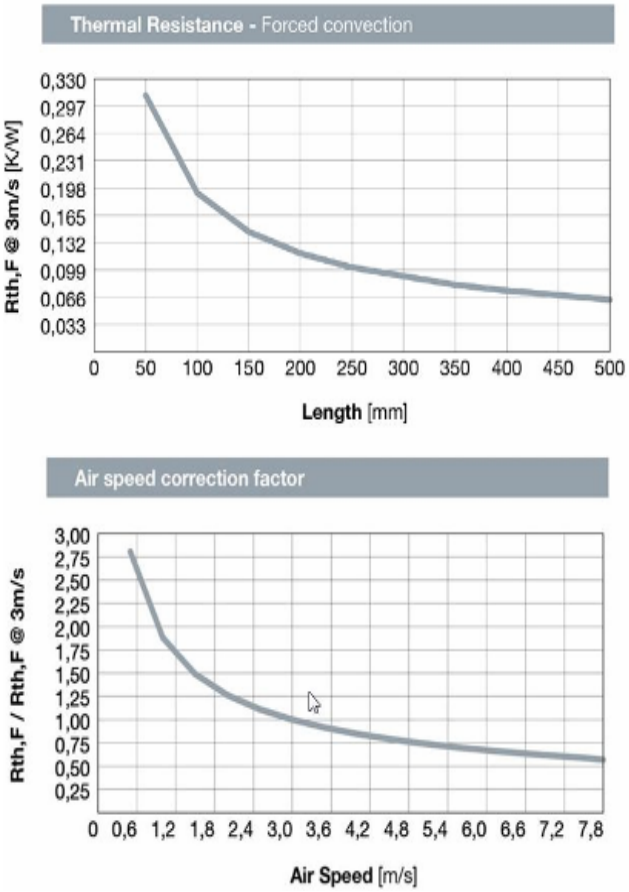

Fig. 9 The thermal transfer curves for the P200 83 heat sink.

V. The Choise of the Power Cables

The following characteristics of the inverters must be taken into account when dimensioning the cables:

- application: railway inverters;
- input voltage: 900 Vdc;
- rated current: 218 A;
- overload current: 327 A.

The cables used for railway rolling stock comply with the standard SR EN 50355:2014 "*Railway applications - Railway rolling stock cables having special fire performance - Guide to use*" [13].

The size of the cable section must be chosen from the standardized cable sections. When choosing the conductor section, the following factors will be taken into account:

- Electrical stresses in insulation, which are due to the operating voltage;

- Electrical stresses due to the intensity of the current flowing through the circuit and which must be lower than those allowed;
- Thermal stresses of the cables due to long-term, overload or short-circuit currents, taking into account the values indicated by the manufacturer and the application of the correction coefficients due to the positioning of the cables during installation as well as the maximum ambient operating temperatures.

The range of HELUTHERM 145 cables produced by HELUKABEL meets the required conditions [14].

Fig. 10 shows the catalog sheet for this type of cables and in Fig. 11 is figured the table of allowed currents and correction coefficients.

According to the catalog sheet, the selection criteria are met as follows:

- Electrical stresses in insulation, which are due to the operating voltage:
  - for cables up to 1 mm^2 U_0/U 300/500 V;
  - for cables from 1.5 mm^2 U_0/U 450/750 V;
  - at fixed and protected installation from 1.5 mm^2 U_0/U 600/1000 V.
- Electrical stresses due to current intensity in the case of outdoor positioning:
  - for outdoor wiring situation 70 mm^2 cable supports a current of 391 A, bigger than overload current – 327A.

Cables with the following codes were chosen:

- 51476 - 70 mm^2 black cable;
- 51340 - 2.5 mm^2 red cable;
- 51338 - 2.5 mm^2 blue cable;
- 51298 - 0.75 mm^2 red cable izolated in SCSI tube;
- 51296 - 0.75 mm^2 blue cable izolated in SCSI tube.

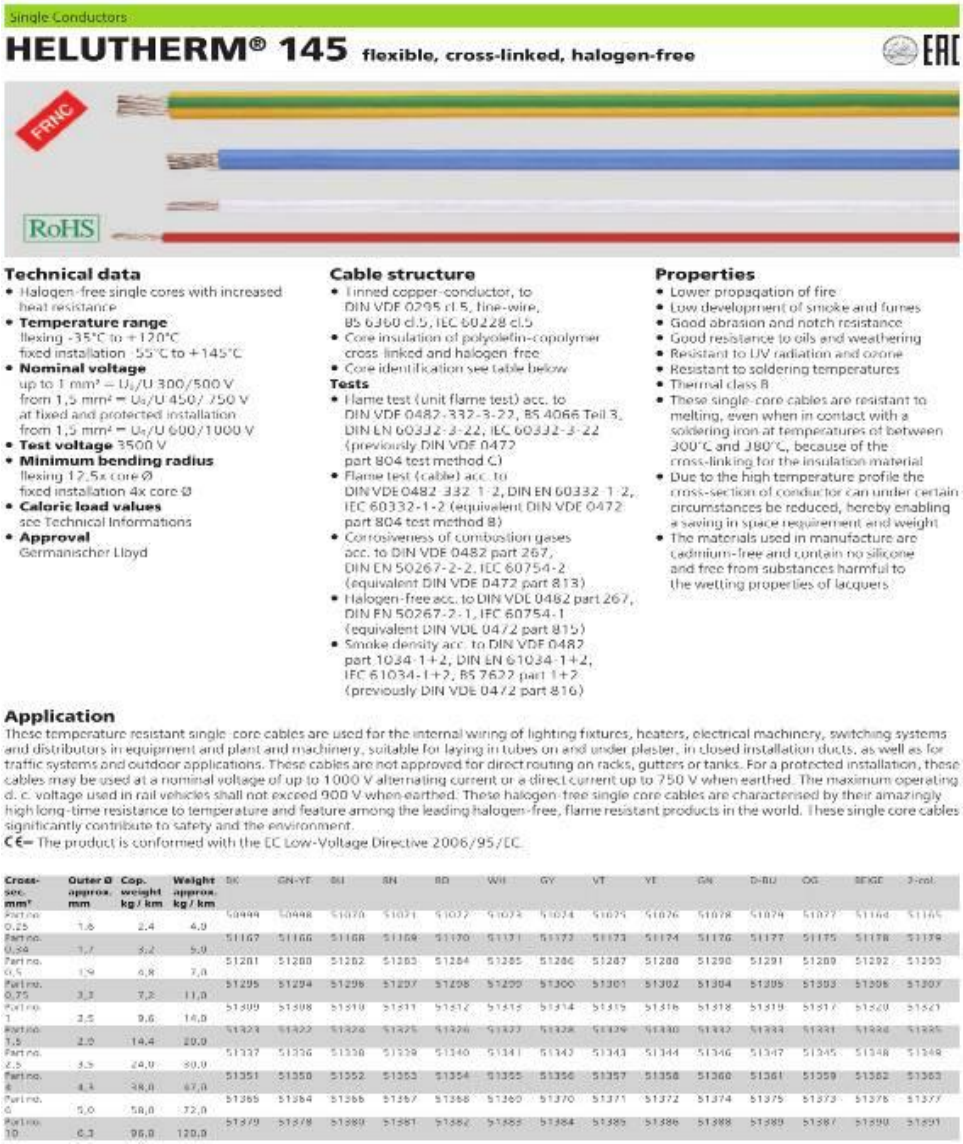

Single Conductors

HELUTHERM® 145 flexible, cross-linked, halogen-free

FRNC

RoHS

Technical data
- Halogen-free single cores with increased heat resistance
- **Temperature range**
  flexing -35°C to +120°C
  fixed installation -55°C to +145°C
- **Nominal voltage**
  up to 1 mm² = U_0/U 300/500 V
  from 1,5 mm² = U_0/U 450/ 750 V
  at fixed and protected installation
  from 1,5 mm² = U_0/U 600/1000 V
- **Test voltage** 3500 V
- **Minimum bending radius**
  flexing 12,5x core Ø
  fixed installation 4x core Ø
- **Caloric load values**
  see Technical Informations
- **Approval**
  Germanischer Lloyd

Cable structure
- Tinned copper-conductor, to DIN VDE 0295 cl.5, fine-wire, BS 6360 cl.5, IEC 60228 cl.5
- Core insulation of polyolefin-copolymer cross-linked and halogen-free
- Core identification see table below

Tests
- Flame test (unit flame test) acc. to DIN VDE 0482-332-3-22, BS 4066 Teil 3, DIN EN 60332-3-22, IEC 60332-3-22 (previously DIN VDE 0472 part 804 test method C)
- Flame test (cable) acc. to DIN VDE 0482-332-1-2, DIN EN 60332-1-2, IEC 60332-1-2 (equivalent DIN VDE 0472 part 804 test method B)
- Corrosiveness of combustion gases acc. to DIN VDE 0482 part 267, DIN EN 50267-2-2, IEC 60754-2 (equivalent DIN VDE 0472 part 813)
- Halogen-free acc. to DIN VDE 0482 part 267, DIN EN 50267-2-1, IEC 60754-1 (equivalent DIN VDE 0472 part 815)
- Smoke density acc. to DIN VDE 0482 part 1034-1+2, DIN EN 61034-1+2, IEC 61034-1+2, BS 7622 part 1+2 (previously DIN VDE 0472 part 816)

Properties
- Lower propagation of fire
- Low development of smoke and fumes
- Good abrasion and notch resistance
- Good resistance to oils and weathering
- Resistant to UV radiation and ozone
- Resistant to soldering temperatures
- Thermal class B
- These single-core cables are resistant to melting, even when in contact with a soldering iron at temperatures of between 300°C and 380°C, because of the cross-linking for the insulation material
- Due to the high temperature profile the cross-section of conductor can under certain circumstances be reduced, hereby enabling a saving in space requirement and weight
- The materials used in manufacture are cadmium-free and contain no silicone and free from substances harmful to the wetting properties of lacquers

Application

These temperature resistant single-core cables are used for the internal wiring of lighting fixtures, heaters, electrical machinery, switching systems and distributors in equipment and plant and machinery, suitable for laying in tubes on and under plaster, in closed installation ducts, as well as for traffic systems and outdoor applications. These cables are not approved for direct routing on racks, gutters or tanks. For a protected installation, these cables may be used at a nominal voltage of up to 1000 V alternating current or a direct current up to 750 V when earthed. The maximum operating d. c. voltage used in rail vehicles shall not exceed 900 V when earthed. These halogen-free single core cables are characterised by their amazingly high long-time resistance to temperature and feature among the leading halogen-free, flame resistant products in the world. These single core cables significantly contribute to safety and the environment.

CE The product is conformed with the EC Low-Voltage Directive 2006/95/EC.

Cross-sec. mm²	Outer Ø approx. mm	Cop. weight kg/km	Weight approx. kg/km	BK	GN-YE	BU	BN	RD	WH	GY	VT	YE	GN	D-BU	OG	BEIGE	3-col.
Part no.				50444	50446	51070	51071	51072	51073	51074	51075	51076	51078	51079	51077	51164	51165
0,25	1,6	2,4	4,0														
Part no.				51167	51166	51168	51169	51170	51171	51172	51173	51174	51176	51177	51175	51178	51179
0,34	1,7	3,2	5,0														
Part no.				51281	51280	51282	51283	51284	51285	51286	51287	51288	51290	51291	51289	51292	51293
0,5	1,9	4,8	7,0														
Part no.				51295	51294	51296	51297	51298	51299	51300	51301	51302	51304	51305	51303	51306	51307
0,75	2,3	7,2	11,0														
Part no.				51309	51308	51310	51311	51312	51315	51314	51315	51316	51318	51319	51317	51320	51321
1	2,5	9,6	14,0														
Part no.				51323	51322	51326	51325	51326	51327	51328	51329	51330	51332	51333	51331	51336	51335
1,5	2,9	14,4	20,0														
Part no.				51337	51336	51338	51339	51340	51341	51342	51343	51344	51346	51347	51345	51348	51349
2,5	3,5	24,0	30,0														
Part no.				51351	51350	51352	51353	51354	51355	51356	51357	51358	51360	51361	51359	51362	51363
4	4,4	38,0	47,0														
Part no.				51365	51364	51366	51367	51368	51369	51370	51371	51372	51374	51375	51373	51376	51377
6	5,0	58,0	72,0														
Part no.				51379	51378	51380	51381	51382	51383	51384	51385	51386	51388	51389	51387	51390	51391
10	6,3	96,0	120,0														

Fig. 10 HELUTHERM 145 cable catalog sheet.

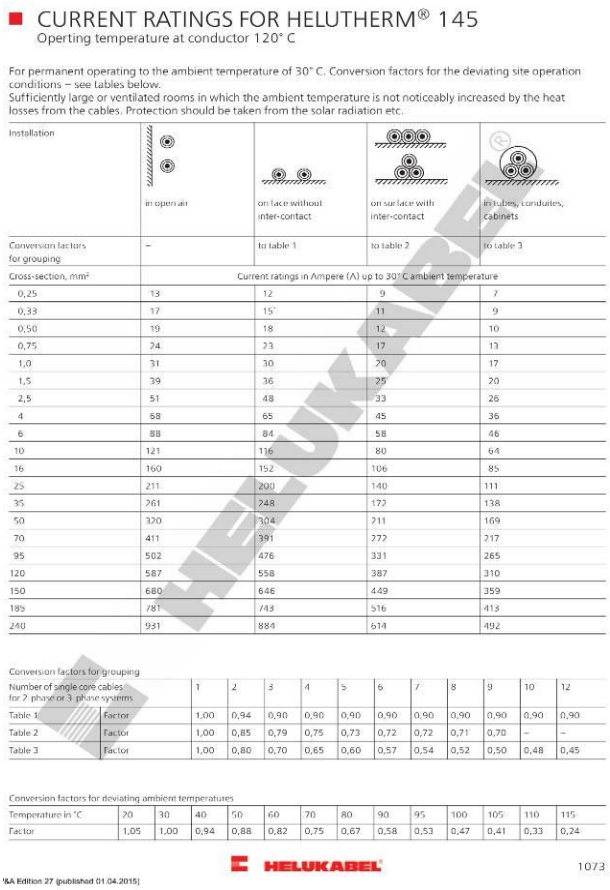

CURRENT RATINGS FOR HELUTHERM® 145
Operting temperature at conductor 120° C

For permanent operating to the ambient temperature of 30° C. Conversion factors for the deviating site operation conditions – see tables below.
Sufficiently large or ventilated rooms in which the ambient temperature is not noticeably increased by the heat losses from the cables. Protection should be taken from the solar radiation etc.

Installation	in open air	on face without inter-contact	on surface with inter-contact	in tubes, conduites, cabinets
Conversion factors for grouping	–	to table 1	to table 2	to table 3
Cross-section, mm²	Current ratings in Ampere (A) up to 30°C ambient temperature			
0,25	13	12	9	7
0,33	17	15	11	9
0,50	19	18	12	10
0,75	24	23	17	13
1,0	31	30	20	17
1,5	39	36	25	20
2,5	51	48	33	26
4	68	65	45	36
6	88	84	58	46
10	121	116	80	64
16	160	152	106	85
25	211	200	140	111
35	261	248	172	138
50	320	304	211	169
70	411	391	272	217
95	502	476	331	265
120	587	558	387	310
150	680	646	449	359
185	781	743	516	413
240	931	884	614	492

Conversion factors for grouping

Number of single core cables for 2 phase or 3 phase systems		1	2	3	4	5	6	7	8	9	10	12
Table 1	Factor	1,00	0,94	0,90	0,90	0,90	0,90	0,90	0,90	0,90	0,90	0,90
Table 2	Factor	1,00	0,85	0,79	0,75	0,73	0,72	0,72	0,71	0,70	–	–
Table 3	Factor	1,00	0,80	0,70	0,65	0,60	0,57	0,54	0,52	0,50	0,48	0,45

Conversion factors for deviating ambient temperatures

Temperature in °C	20	30	40	50	60	70	80	90	95	100	105	110	115
Factor	1,05	1,00	0,94	0,88	0,82	0,75	0,67	0,58	0,53	0,47	0,41	0,33	0,24

HELUKABEL 1073

'kA Edition 27 (published 01.04.2015)

Fig. 11 Current ratings for HELETHERM 145.

VI. Conclusions

The research conducted in this paper highlights the fact that when choosing the force components for a test – experimentation bench designed to test various control strategies for traction converters, it is necessary to consider the addition of bigger safety coefficients than usual at their technical characteristics covering some control errors which may occur. It has also been shown that a forced ventilation cooling system is suitable, cheaper and less complex than a liquid cooling one.

Acknowledgment

This work was supported by the grant POCU380/6/13/123990, co-financed by the European Social Fund within the Sectorial Operational Program Human Capital 2014 – 2020.

Source of research funding in this article: grant POCU380/6/13/123990.

Contribution of authors:
First author – 50%
First coauthor – 30%
Second coauthor – 20%

Received on August 10,2021
Editorial Approval on November 30, 2021

References

[1] X. Huang, W. Chang and T. Q. Zheng, "Study of the protection and driving characteristics for high voltage high power IGBT modules used in traction convertor," 2015 IEEE 10th Conference on Industrial Electronics and Applications (ICIEA), Auckland, New Zealand, 2015, pp. 1330-1334.

[2] M. M. Bakran, H. Eckel, M. Helsper and A. Nagel, "Next Generation of IGBT-Modules Applied to High Power Traction," 2007 European Conference on Power Electronics and Applications, Aalborg, Denmark, 2007, pp. 1-9.

[3] K. Sheng, B.W. Williams, X. He, Z. Qian, S.J. Finney, "Measurement of IGBT switching frequency limits," Power Electronics Specialists Conference, 1999, PESC 99. 30th Annual IEEE.

[4] S. C. Das, A. Tiwari, G. Narayanan and A. K. Kumar, "Experimental investigation on switching characteristics of IGBTs for traction application," 2012 IEEE International Conference onPower Electronics, Drives and Energy Systems (PEDES), Bengaluru, India, 2012, pp. 1-5.

[5] M. B. Inarra, I.B. Zubiaurre, I.L.Bengoetxea, I.Z. Azaceta, "Power Electronic converter. Design Book".

[6] L. S. Goreci, M. Popescu and I. Tilă, "The choice of the IGBTs and their cooling in electric traction converters for autonomous vehicles," 2021 International Conference on Applied and Theoretical Electricity (ICATE), Craiova, Romania, 2021, pp. 1-5.

[7] M. Popescu, A. Bitoleanu, D. Mihai, C. Constantinescu, "Convertoare statice si structuri de comandă performante", Editura Sitech,2000.

[8] AVX: Medium Power Film Capacitors, Application Notes

[9] Mitsubishi HVIGBT Modules CM2400HC-34H, https://www.mitsubishielectric-mesh.com/products/pdf/cm2400hc-34h_e.pdf.

[10] Simulation soft, Mitsubishi Electric Power Module Loss Simulator, http://sem.mitsubishielectric.eu/products/power_semiconductors/melcosim

[11] R. Künzi, "Thermal design of power electronic circuits," CERN Yellow Report CERN-2015-003, pp.311-327.

[12] Air cooled technologies. Heat sinks catalogue, http://www.meccal.com/en/download/catalogo-prodotti-aria.pdf.

[13] SR EN 50355:2014 "*Railway applications - Railway rolling stock cables having special fire performance - Guide to use*"

[14] Helutherm 145 Cable https://helukabel-sea.com/wp-content/uploads/2018/07/HELUTHERM%C2%AE-145.pdf

Optimization of Electromagnetic Devices Using a RSM Enhanced ACO_R Algorithm

Anton Duca* and Bianca Lamba*
* Politehnica University of Bucharest, Bucharest, Romania, anton.duca@upb.ro

DOI: 10.52846/AUCEE.2021.1.06

***Abstract* – The present paper proposes and studies the efficiency of using a RSM enhanced ACO_R algorithm for the optimization of electromagnetic devices. Different RSM methods, such as Box-Behnken, CCD and Doelhert, are applied to find most suitable parameters (optimal set) for the ACO_R in order to solve the corresponding electromagnetic optimization problems. The parameters optimal set is found by building a metaheuristic function. In the same time, the optimal parameter set is searched and determined for each electromagnetic problems for different objective functions, the best and the average global best solution for a tests set. The electromagnetic devices to be optimized are the Loney's solenoid and an energy storage device, as defined by the TEAM22 problem. Both electromagnetic problems are proposed benchmarks from electromagnetic community.**

Cuvinte cheie: *calcul evoluționist optimizare, ACO_R, RSM, Box-Behnken, CCD, Doelhert, electromagnetic, TEAM22, solenoidul lui Loney.*

Keywords: *Evolutionary Computation, Optimization, ACO_R, RSM, Box-Behnken, CCD, Doelhert, Electromagnetic, TEAM22, Loney's solenoid.*

I. Introduction

Proposed in [1] by Dorigo and collaborators, AS (Ant System), like any ant algorithm, is an evolutionary algorithm initially designed for hard non-determinist polynomial problems such as QAP [2] [3], TSP [2] [3] [4] or MKP [5] [6]. The algorithm simulates the search for food behavior by the ant colonies. The process uses the pheromone concept, a substance which is secreted by ants on theirs search paths for food.

To improve the performances of the AS algorithm several solutions have been proposed in the literature, the most effective and known are the ACO (Ant Colony Optimization) [3] and the MMAS (Min-Max Ant System) [2]. Along with algorithms created for combinatorial problems, solutions designed for continuous problems were proposed, like the ACO_R (ACO for real / continuous domains) [7].

Just as any other evolutionary computation algorithm, the ACO_R performance strongly depends by the parameters of the algorithms and, of course, by the optimization problem [8]. To find the ACO_R set of optimal parameters for solving electromagnetic benchmark problems, the present paper studies and proposes the possibility of using the RSM (Response Surface Methodology) [9].

Originally proposed during 1950s in [10] by Box et al. the RSM was targeting statistics and design of experiments. The RSM is a set of mathematical and statistical techniques sequentially applied to map empirical models and / to data, data obtained and provided by experimental designs.

Since proposed, the RSM has been successfully applied independently or embedded in other algorithms to solve various problems from different domains as computer science [4], chemistry [11] or electrical engineering [12] [13] [14].

In the current study, several RSM models, such as Box-Behnken [15], CCD (Central Composite Design) [10] and Doelhert [16] are applied to improve the ACO_R's performances when optimizing electromagnetic devices. The performance tuning is done by searching the optimal set of parameters for the ACO_R. The problems to be solved are TEAM22 (Testing Electromagnetic Analysis Method) [17] and Loney's solenoid [18], two benchmarks proposed by the electromagnetic community.

II. The ACO_R Algorithm

The ACO_R is an ant based algorithm for continuous domains proposed by Socha and Dorigo in [7].

Like any other ACO algorithm, ACO_R is population based but unlike the other algorithms it stores the pheromones table as an archive of solutions (Fig. 1).

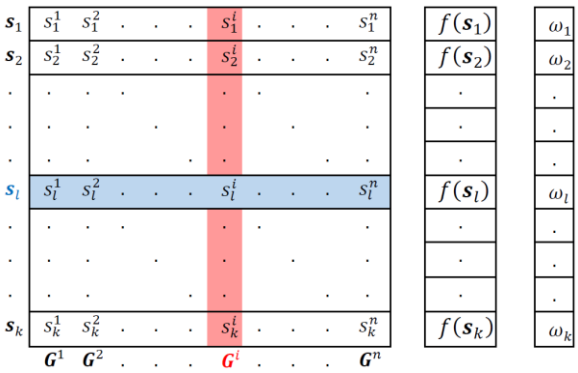

Fig. 1. ACO_R archive (size k): solutions $\boldsymbol{s}_l$, fitness values $f(\boldsymbol{s}_l)$, weights ω_l, search space size n, Gaussian kernels $\boldsymbol{G}^i$ $i = (1, n)$.

The archive is sorted using the fitness values of the solutions ($f(\boldsymbol{s}_l) < f(\boldsymbol{s}_{l+1})$), where f: $\Omega \subset R^n \rightarrow R$ represents the OF (objective function). For each solution there is a weight ω related to its fitness measure $(\omega_l > \omega_{l+1})$.

The weight for a solution s_l is calculated as:

$$\omega_l = \frac{1}{qk\sqrt{2\pi}} e^{-\frac{(l-1)^2}{2q^2k^2}}, \quad (1)$$

where q is a parameter of the ACO_R algorithm called *the locality of the search process* and k is the size of *the archive of solutions*. When q is small the weights for better ranked solutions are bigger, whereas when q is large the weights are more uniform.

If in the case of PSO and GA, where a particle or an individual encapsulates a solution, for ACO algorithms an ant is a solution builder. To construct a new solution an ant starts from a solution l from the archive. The l-th solution is chosen with a wheel probability mechanism:

$$pb_l = \omega_l / \sum_{j=1}^{k} \omega_j \tag{2}$$

The construction of the new solution is performed in n steps. At step i the value for the corresponding variable is calculated using information which only regards the dimension i. The value of the variable is generated randomly by a Gaussian distribution:

$$G_l^i(x) = \frac{1}{\sigma_l^i \sqrt{2\pi}} e^{-\frac{\left(x-\mu_l^i\right)^2}{2\sigma_l^{i\,2}}}, \tag{3}$$

where μ and σ are the mean and the standard deviation of the Gaussian kernel.

For the evaluation of the parameters the archive of solutions is used as follows:

$$\mu_l^i = s_l^i, \tag{4}$$

$$\sigma_l^i = \xi \sum_{e=1}^{k} \left| s_e^i - s_l^i \right| / (k-1), \tag{5}$$

where ξ, the *convergence rate*, is the fourth ACO_R parameter, equivalent with the pheromone evaporation from the ACO algorithm. If ξ is smaller the exploitation is dominant comparing to exploration, so the convergence speed is faster.

After a solution set (size equals the number of ants) is constructed, the solutions are evaluated, added to the archive, and sorted according to their fitness values. Afterwards, the worst solutions are removed in order to keep an imposed value for the archive of solutions. In the end the weights are updated accordingly with the new archive.

The pseudocode of the ACO_R algorithm is [8]:

```
;initialize the archive of solutions
;evaluate the solutions
;calculate the weights

do
        foreach ant of the colony
            ;select a solution l
            ;construct new solution from (l)
            ;evaluate the new solution
        end for
        ;add the new solutions to archive
        ;sort archive according to fitness
        ;remove worst solutions keeping
        a previously imposed archive size
        ;calculate new weights
        noIterations ++
while
        (noIterations < maxNoIterations)
        and
        (optimal solution not found)
```

More explanations and details about ACO_R are available in [7].

III. The RSM enhancement

The main idea behind using RSM to enhance the ACO_R performance is the building of a metaheuristic function g with the purpose of finding the optimal set of ACO_R parameters when solving benchmark electromagnetic problems. The metaheuristic function is quadratic, $g: R^{np} \to R$, a choice which proven to offer good results [12] [20] when approximating functions with unknown landscapes, like in our case:

$$g(p_1, p_2, \dots p_{np}) = c_0 + \sum_{i=1}^{np} (c_i \cdot p_i + c_{ii} \cdot p_i^2) + \sum_{i,j=1\, i \neq j}^{np} c_{ij} \cdot p_i \cdot p_j, \tag{6}$$

where np is the number of ACO_R parameters, $p = [p_1, p_2, \dots p_{np}]$ are the parameters (variables) of the g function, and c the coefficients. The parameters of g are the scaled versions of the ACO parameters (the number of ants, the locality of the search process, the size of the archive and the convergence speed), whereas the return value corresponding to a point (set of parameters) in the definition domain is a measurement of fitness related to the objective function of the problem to be solved.

The optimal set of parameters is found in four steps:

- A number of points in the parameters space are generated using a RSM model, CCD, Box-Behnken or Doelhert.
- The evaluation of the metaheuristic g function is done for each point performing a set of tests, experiments in RSM terms, on the electromagnetic optimization problem (details in the results section).
- The coefficients of the quadratic function are calculated by LMS (Least Mean Square) method thus obtaining the analytical expression of g.
- The optimal set of parameters (considered the point at which g is minimum) is determined by quadratic optimization applied on the analytical expression of g.

The complete algorithm can be summarized as follows:

```
;generate the set of points SP
;    according to the RSM method

foreach point p in SP
    ;perform a set of N tests by solving
    ;    the electromagnetic optimization
    ;    problem N times using ACO_R(p)
    ;evaluate the performance - g(p) -
    ;    using statistics
;calculate the coefficients c by LMS using
;    the set of points SP and
;    the corresponding g(p) values
;find the optimal set of parameters p*,
;    which for g(p*) = g_min,
;    by quadratic optimization

;perform a set of N tests for p* by solving
;    the electromagnetic optimization
;    problem N times using ACO_R(p*)
;evaluate the performance of p*
;    using statistics
```

A. The FFD model

In the Full Factorial Design (FFD) for each variable / parameter of g there are three possible values: minimum, average and maximum. Each parameter value is combined with each value of every other parameter, thus the number

of points in this model is $N = 3^{np}$. Fig. 2 shows the placement of the points in the FFD model for *np* = 3.

The main drawback of the FFD model appears when the number of parameters is high. For such cases, the number of experiments needed is prohibitive, and this design is therefore not suitable when the evaluation of the OF is expensive.

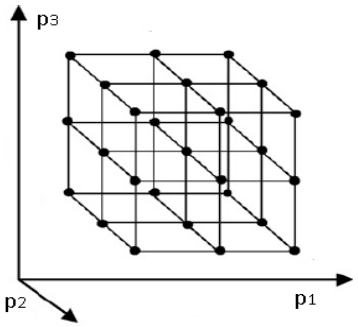

Fig. 2. The points in the FFD model for *np*=3.

B. *The Box-Behnken model*

The Box-Behnken design [15] resides in the FFD model. The points are located inside a hypersphere with the center at the central point of the design space (Fig. 3).

In this design each parameter has three possible values (-1, 0, 1) scaled respectively to the minimum, average and maximum value of the corresponding ACO_R parameter. The number of points for this design in the case of our problems, where *np* = 4, is 25 (Appendix – Table V).

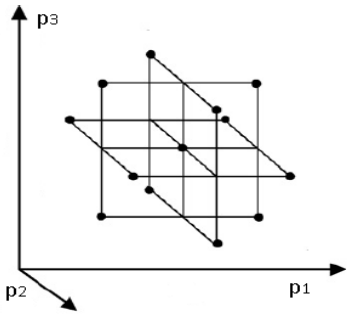

Fig. 3. The points in the Box-Behnken model for *np*=3.

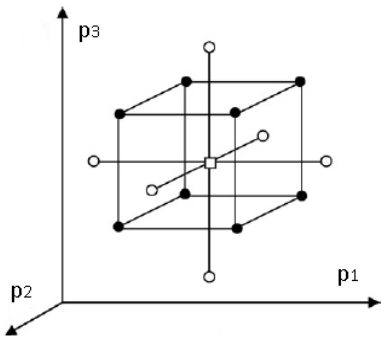

Fig. 4. The points in the CCD model for *np*=3.

C. *The CCD model*

The CCD model [10] consists of a fractional FFD and a star design both centered in the central point of the design space (Fig. 4).

In the star design the points are set a distance α from the center. Each parameter can have five possible levels ($-\alpha$, -1, 0, 1, α). The number of points for this design in the case of our problems is 25 (Appendix – Table VI).

D. *The* DOELHERT *model*

The Doelhert model [16] is the most complex of the RSM models used. Each parameter of the design has a different number of levels, the distance between levels following a uniform distribution. For two parameters the design contains six points and is a hexagon whereas for three parameters contains twelve points and is a cuboctahedron (Fig. 5).

In our case, with four parameters, the design contains 21 points with the coordinates shown in the Appendix – Table VII.

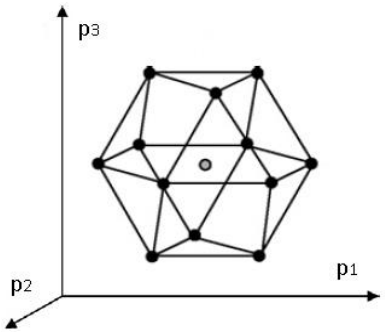

Fig. 5. The points in the Doelhert model for *np*=3.

IV. ELECTROMAGNETIC BENCHMARK PROBLEMS

E. *The TEAM22 problem*

Two coaxial coils carry current with opposite directions (Fig. 6), operate under superconducting conditions and offer the opportunity to store a significant amount of energy in their magnetic fields, while keeping within certain limits the stray field [17].

An optimal design of the device should therefore couple the value of the energy *E* to be stored by the system with a minimum stray field B_{stray}. The two objectives are combined into one objective function:

$$OF = \frac{B_{stray}^2}{B_{norm}^2} + \frac{|E - E_{ref}|}{E_{ref}}, \qquad B_{stray}^2 = \frac{\sum_{i=1}^{22} |B_{stray,i}|^2}{22}, \tag{7}$$

where E_{ref} = 180 MJ, and B_{norm} = 3 μT.

The objective function has as parameters, the radii (R_1, R_2), the heights (h_1, h_2) , the thicknesses (d_1, d_2) and the current densities (J_1, J_2). Besides domain restrictions, the problem must take into account the following conditions: the solenoids do not overlap each other ($R_1 + d_1/2 < R_2 - d_2/2$), and the superconducting material should not violate the quench condition that links together the value of the current density and the maximum value of magnetic flux density

($|J| \leq (-6.4 \cdot |B| + 54.0)\ A/\text{mm}^2$). It is a constrain imposed to the current densities.

The evaluation method of the objective function is based on the Biot-Savart-Laplace formula in which the elliptic integrals are computed by using the King algorithm and numerical integration. Moreover, the optimization problem is reformulated as a one with six parameters, since for a given geometry and a stored energy, the values of the current densities can be computed by deterministic quadratic optimization as in [8] [19].

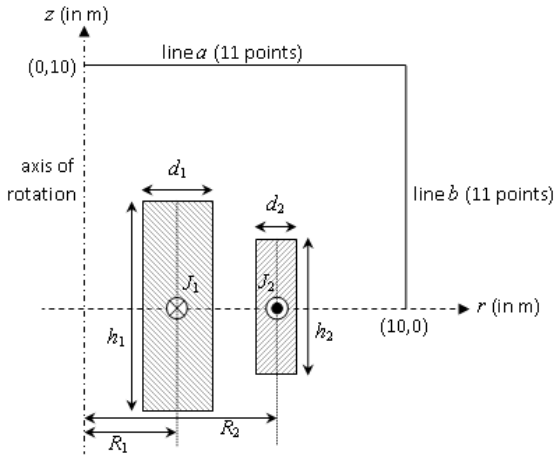

Fig. 6. TEAM22 problem configuration.

F. *The Loney's solenoid*

Defined in [18], the Loney's solenoid electromagnetic problem has one main and two correction coils with the following dimensions (Fig. 7): r_1 = 11 mm, r_2 = 29 mm, h = 120 mm, r_3 = 30 mm, r_4 = 36 mm. The current density through the coils is the same with the goal of having a density of the magnetic flux constant in the center of the main coil.

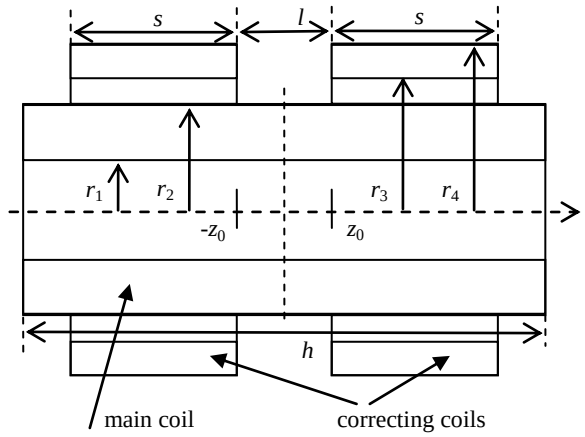

Fig. 7. Loney's solenoid problem configuration.

The objective function to be minimized is (B_{max} - B_{min})/B_0, the difference between the magnetic flux densities along a segment in the middle of the main solenoid divided to the density of the magnetic field in the middle of the main coil (r = 0, z = 0). The maximum / minimum values of the magnetic flux densities are sought along the straight segment [-z_0,z_0], z_0 = 2.5 mm. The optimization problem has two parameters the length s and the distance l between the correction coils.

The implementation details of the Loney's solenoid benchmarks is the same as in the previous papers [8] [19].

V. RESULTS

To test the proposed approach two electromagnetic optimization problems were chosen, namely TEAM 22 [17] and Loney's solenoid [18]. The implementation details of the TEAM 22 and Loney's solenoid benchmarks are the same as in the previous papers [8] [19].

For the construction of the metaheuristic function g the variation intervals for the ACO_R parameters were: the number of ants a, integer values between [2; 8], the archive size k integers between [20; 60], the convergence rate ξ real values between [0.5; 0.99], and the locality of the search process q real values between [1E-4; 1E-2].

To evaluate the performance for a set of parameters (evaluation of the g function) two cases were studied, the min-best OF value and the mean-best OF value over a set of 30 tests, to make a relevant statistical study. The min-best is the minimum of the minimum (best) values, and the mean-best is the average of the minimum values for the mentioned 30 runs. For each test the stopping criteria was a maximum number of 2560 OF evaluations, a number appearing to be sufficient to reach convergence for the chosen benchmark problems [8] [19].

Tables I-IV present results, the obtained optimal set of parameters and the statistical flags for solving the Loney's solenoid and the TEAM22 problems. The statistical flags are calculated once again on a set of 30 independent runs. The best results previously obtained in [8], where the ACO_R performance tuning was roughly performed only on the number of ants, are presented as comparison.

For the Loney's solenoid problem when the objective of g is the min-best OF (Table I) the best solution is obtained with the Box-Behnken design. The optimal parameters provided by the design lean towards exploitation, small convergence rate, small archive size, small locality of search process all in favor of the better ranked solutions. Regarding the value of the OF this is one of the best ever reported in the literature.

When the objective of the metaheuristic function is the mean-best OF (Table II) the best RSM design is Doelhert. The optimal set of parameters are very high number of ants, small archive size and small convergence rate (high converge speed) in favor of exploitation and very high search process locality parameter in favor of exploration. In this case, the set of parameters mentioned in [8] lead to a better mean-best.

For the TEAM 22 problem when the goal of g is min-best OF once again the best approach is Box-Benhken (Table III). The results are once again some of the best in the literature in terms of min-best OF. The optimal set of parameters are quite different from the parameters provided by the same design for the Loney's solenoid. However, the parameter values are rather contradictory, very high number of ants and small archive size clearly in favor of exploitation, very high convergence rate (small convergence speed) and very high locality of the search process in favor of exploration.

Finally, when the objective of the metaheuristic function is the mean-best OF (Table IV) just like in the case of Loney's solenoid the optimal set of parameters for TEAM22 is given by the Doelhert design. The results are almost identical with the ones mentioned in [8], in terms of mean-best OF and also in terms of parameter values, small number of ants, large archive size, high convergence

rate and small locality of the search process, clearly oriented towards exploration.

TABLE I.
RESULTS FOR LONEY'S SOLENOID PROBLEM, WHEN THE METAHEURISTIC OBJECTIVE IS THE MIN-BEST OF

	Method			
	CCD + ACO_R	Box-Behnken + ACO_R	Doelhert + ACO_R	ACO_R [8]
a	2	**4**	3	4
k	34	**26**	60	40
ξ	0.52	**0.50**	0.99	0.85
q	10E-3	**3.4E-3**	9.8E-3	1E-4
Min - best OF value	3.02E-10	**1.24E-10**	5.68E-10	2.22E-9
Max - best OF value	2.8E-6	2.2E-6	2.2E-6	6.10E-8
Mean - best OF value	6.81E-8	9.53E-8	1.17E-7	1.32E-8
Standard deviation	3.09E-7	3.29E-7	3.78E-7	9.78E-9

TABLE II.
RESULTS FOR LONEY'S SOLENOID PROBLEM, WHEN THE METAHEURISTIC OBJECTIVE IS THE MEAN-BEST OF

	Method			
	CCD + ACO_R	Box-Behnken + ACO_R	Doelhert + ACO_R	ACO_R [8]
a	2	2	**8**	**4**
k	20	20	**20**	**40**
ξ	0.99	0.99	**0.53**	**0.85**
q	1E-2	1.3E-3	**1E-2**	**1E-4**
Min - best OF value	1.67E-9	1.21E-9	6.92E-9	2.22E-9
Max - best OF value	5.01E-7	4.00E-7	8.46E-8	6.10E-8
Mean - best OF value	2.17E-8	2.93E-8	**1.61E-8**	**1.32E-8**
Standard deviation	6.19E-8	7.22E-8	8.36E-9	9.78E-9

TABLE III.
RESULTS FOR TEAM22 PROBLEM, WHEN THE METAHEURISTIC OBJECTIVE IS THE MIN-BEST OF

	Method			
	CCD + ACO_R	Box-Behnken + ACO_R	Doelhert + ACO_R	ACO_R [8]
a	2	**8**	2	8
k	50	**20**	50	40
ξ	0.75	**0.99**	0.85	0.85
q	1E-4	**1E-2**	3.2E-4	1E-4
Min - best OF value	2.09E-3	**1.93E-3**	2.01E-3	2.03E-03
Max - best OF value	7.20E-3	1.36E-2	6.05E-3	3.52E+00
Mean - best OF value	2.95E-3	3.33E-3	3.04E-3	1.21E-01
Standard deviation	1.10E-3	2.09E-3	9.56E-4	6.41E-01

TABLE IV.
RESULTS FOR TEAM22 PROBLEM, WHEN THE METAHEURISTIC OBJECTIVE IS THE MEAN-BEST OF

	Method			
	CCD + ACO_R	Box-Behnken + ACO_R	Doelhert + ACO_R	ACO_R [8]
a	2	2	**2**	**4**
k	49	60	**60**	**40**
ξ	0.5	0.52	**0.99**	**0.85**
q	1E-2	1E-2	**1E-4**	**1E-4**
Min - best OF value	2.31E-3	2.02E-3	2.31E-3	2.15E-03
Max - best OF value	3.78E-2	1.14E-2	4.96E-3	5.99E-03
Mean - best OF value	6.37E-3	3.73E-3	**3.03E-3**	**2.97E-03**
Standard deviation	6.63E-3	1.97E-3	5.82E-4	8.03E-04

TABLE V.
PARAMETER VALUES FOR THE BOX-BEHNKEN METHOD

	p_1	p_2	p_3	p_4
1	-1	-1	0	0
2	-1	1	0	0
3	-1	0	0	-1
4	-1	0	0	1
5	-1	0	-1	0
6	-1	0	1	0
7	0	0	-1	-1
8	0	0	-1	1
9	0	0	1	-1
10	0	0	1	1
11	0	-1	-1	0
12	0	-1	1	0
13	0	1	-1	0
14	0	1	1	0
15	0	-1	0	-1
16	0	-1	0	1
17	0	1	0	-1
18	0	1	0	1
19	0	0	0	0
20	1	-1	0	0
21	1	1	0	0
22	1	0	0	-1
23	1	0	0	1
24	1	0	-1	0
25	1	0	1	0

TABLE VI.

PARAMETER VALUES FOR THE CCD METHOD

	p_1	p_2	p_3	p_4
1	-2	0	0	0
2	-1	-1	-1	-1
3	-1	-1	-1	1

4	-1	-1	1	-1
5	-1	-1	1	1
6	-1	1	-1	-1
7	-1	1	-1	1
8	-1	1	1	-1
9	-1	1	1	1
10	0	-2	0	0
11	0	2	0	0
12	0	0	-2	0
13	0	0	2	0
14	0	0	0	-2
15	0	0	0	2
16	0	0	0	0
17	1	-1	-1	-1
18	1	-1	-1	1
19	1	-1	1	-1
20	1	-1	1	1
21	1	1	-1	-1
22	1	1	-1	1
23	1	1	1	-1
24	1	1	1	1
25	2	0	0	0

TABLE VII.

PARAMETER VALUES FOR THE DOELHERT METHOD

	p_1	p_2	p_3	p_4
1	-1	0	0	0
2	-0.5	-0.86603	0	0
3	-0.5	-0.28868	-0.8165	0
4	-0.5	-0.28868	-0.20412	-0.79057
5	-0.5	0.866025	0	0
6	-0.5	0.288675	0.816497	0
7	-0.5	0.288675	0.204124	0.790569
8	0	0	0	0
9	0	0.57735	-0.8165	0
10	0	0.57735	-0.20412	-0.79057
11	0	-0.57735	0.816497	0
12	0	0	0.612372	-0.79057
13	0	-0.57735	0.204124	0.790569
14	0	0	-0.61237	0.790569
15	0.5	0.866025	0	0
16	0.5	0.288675	0.816497	0
17	0.5	0.288675	0.204124	0.790569
18	0.5	-0.86603	0	0
19	0.5	-0.28868	-0.8165	0
20	0.5	-0.28868	-0.20412	-0.79057
21	1	0	0	0

VI. CONCLUSIONS

Following the proposal from [21], the present paper studied the effectiveness of improving the performance of the ACO_R evolutionary algorithm by using RSM strategies for solving electromagnetic benchmark problems. To test and verify the proposed enhancement two electromagnetic benchmarks were chosen, namely TEAM22 and Loney's solenoid.

The enhancement is performed by searching the optimal set of ACO_R parameters. To achieve this goal a metaheuristic quadratic function in the parameters space is constructed using RSM methods, namely CCD, Box-Behnken and Doelhert. For the evaluation of the metaheuristic function two different objectives were studied: the minimum best (min-best) value and the average best (mean-best) value of the original OF over a statistical set of tests.

The results obtained with the proposed approach were compared to previously obtained results from [8], where the ACO_R 's performance was tunned roughly, only on one parameter namely the ants number.

When the objective of the metaheuristic function is the min-best value of the original OF the Box-Behnken design generates the best set of optimal parameters from all the design strategies for both electromagnetic benchmarks. The values obtained for the OF are from author's knowledge some of the best found in the literature for TEAM22 and also Loney's solenoid.

When the objective of the metaheuristic function is the mean-best value of the original OF the Doelhert design is the most suitable for both electromagnetic problems. However, the obtained results are comparable with results obtained in [8] in the case of TEAM22 and a little poorer than the results in [8] in the case of Loney's solenoid.

ACKNOWLEDGMENT

The authors acknowledge the support of our colleague and Professor Gabriela Ciuprina, who has provided the implementation codes for the Loney's solenoid and TEAM22 electromagnetic benchmark problems.

Contribution of authors:
First author – 67%
First coauthor – 33%

Received on July 17,2021
Editorial Approval on November 15, 2021

REFERENCES

[1] M. Dorigo, V. Maniezzo and A. Colorni, Ant system: optimization by a colony of cooperating agents, *IEEE Transactions on Systems, Man, and Cybernetics*, Part B (Cybernetics), 26(1), pp. 29-41, 1996.

[2] T. Stutzle, and H. Hoos, MAX-MIN ant system and local search for the traveling salesman problem, *IEEE Evolutionary Computation*, pp. 309-314, 1997.

[3] M. Dorigo, and G. Di Caro, Ant colony optimization: a new metaheuristic, *Proceedings of the Congress on Evolutionary Computation*, pp. 1470-1477, 1999.

[4] E. Ridge, and D. Kudenko. Tuning the performance of the MMAS heuristic. In *Engineering stochastic local search algorithms. designing, implementing and analyzing effective heuristics*, pp. 46-60. Springer, Berlin, Heidelberg, 2007.

[5] S. Fidanova,, Ant colony optimization and multiple knapsack problem. In *Handbook of Research on Nature-Inspired Computing for Economics and Management*, pp. 498-509. IGI Global, 2007.

[6] L. Ke, Qingfu. Zhang, and R. Battiti, MOEA/D-ACO: A multi-objective evolutionary algorithm using decomposition and antcolony. *IEEE Transactions on Cybernetics*, 43(6), pp. 1845-1859, 2013.

[7] K. Socha, and M. Dorigo, Ant colony optimization for continuous domains, *European journal of operational research*, 185(3), pp.1155-1173, 2008.

[8] Duca, A., Ciuprina, G., Lup, S. and Hameed, I., 2019, March. ACO_R algorithm's efficiency for electromagnetic optimization benchmark problems. In *2019 11th International Symposium on Advanced Topics in Electrical Engineering (ATEE)* (pp. 1-5).

[9] Myers, Raymond H., Douglas C. Montgomery, and Christine M. Anderson-Cook. *Response surface methodology: process and product optimization using designed experiments*. John Wiley & Sons, 2016.

[10] Box, G.E. and Wilson, K.B., 1951. On the experimental attainment of optimum conditions. *Journal of the royal statistical society: Series b (Methodological)*, *13*(1), pp.1-38.

[11] Bezerra, M.A., Santelli, R.E., Oliveira, E.P., Villar, L.S. and Escaleira, L.A., 2008. Response surface methodology (RSM) as a tool for optimization in analytical chemistry. *Talanta*, *76*(5), pp.965-977.

[12] Leuca, T., Trip, N.D., Silaghi, H. and Burca, A.D.R.I.A.N., 2016. Design of experiments approach for induction heating optimization. *Revue roumaine des sciences techniques, Série Électrotechnique et Énergétique*, *61*(2), pp.169-172.

[13] Rong, Ruowen, David A. Lowther, Zahid Malik, Hua Su, J. Nelder, and R. Spence. "Applying response surface methodology in the design and optimization of electromagnetic devices." *IEEE Transactions on magnetics* 33, no. 2 (1997): 1916-1919.

[14] Gillon, Frederic, and Pascal Brochet. "Screening and response surface method applied to the numerical optimization of electromagnetic devices." *IEEE transactions on magnetics* 36, no. 4 (2000): 1163-1167.

[15] Box, G.E. and Behnken, D.W., 1960. Some new three level designs for the study of quantitative variables. *Technometrics*, *2*(4), pp.455-475.

[16] Doehlert, D.H., 1970. Uniform shell designs. *Journal of the Royal Statistical Society: Series C (Applied Statistics)*, *19*(3), pp.231-239.

[17] TEAM22 benchmark problem – international COMPUMAG society. http://www.compumag.org/wp/team.

[18] P. Di Barba, A. Gottvald, A. Savini, Global optimization of Loney's solenoid: A benchmark problem. *International Journal of Applied Electromagnetics and Mechanics*, 6(4), pp. 273–276, 1995.

[19] Duca, A., Duca, L., Ciuprina, G. and Ioan, D., 2016, November. Neighborhood Strategies for QPSO Algorithms to Solve Benchmark Electromagnetic Problems. In *International Conference on Evolutionary Computation Theory and Applications* (Vol. 2, pp. 148-155). SCITEPRESS.

[20] Ciuprina, G., Ioan, D. and Munteanu, I., 2002. Use of intelligent-particle swarm optimization in electromagnetics. *IEEE Transactions on Magnetics*, *38*(2), pp.1037-1040.

[21] Duca, A. RSM enhanced ACO_R algorithm for electromagnetic optimization. In2021 International Conference on Applied and Theoretical Electricity (ICATE) 2021 May 27 (pp. 1-5). IEEE.

Comparative Analysis of Two Methods of Calculating the Prescribed Current in a Shunt Active Filtering System

Mihăiță Daniel Constantinescu, Mihaela Popescu, Constantin Vlad Suru
University of Craiova, Faculty of Electrical Engineering, Craiova, Romania
mconstantinescu@em.ucv.ro, mpopescu@em.ucv.ro, vsuru@em.ucv.ro

DOI: 10.52846/AUCEE.2021.1.07

***Abstract* - In this paper, the performance of a three-phase shunt active power filter (APF) using the instantaneous power theory (p-q theory) has been compared with that corresponding to the use of the synchronous reference frame (SRF) based method. It is clear that, under balanced and sinusoidal voltage conditions, these two methods gives similar results. The entire system has been modeled using MATLAB-SIMULINK software. The simulation results demonstrate the applicability of both methods for the APF control.**

Cuvinte cheie: *filtru activ de putere, teoria p-q, semnal de referinţă sincron.*

Keywords: *Shunt Active Power Filter, p-q Theory, Synchronous Reference Frame* **.**

I. INTRODUCTION

Shunt active power filters (SAPFs) are voltage source inverter based static converters, bidirectional in current and voltage, which are connected in parallel with the nonlinear load and controlled so as to meet different compensation objectives (harmonics, reactive power and load unbalance).

Active power filters have many advantages over passive filters, which have established them as a competitive, modern and efficient filtering solution:

- they can reduce the total distortion factor (THD) to very low values, which fall within the limits imposed by regulations (the reduction is greater than 10:1);
- they cannot be overloaded due to the harmonic currents transmitted in the network by other distorting loads;
- the currents to be compensated can be selected;
- harmonic distortion and/or power factor can be compensated, simultaneously or independently (they can also suppress the reactive current, not only harmonic currents);
- the compensation accuracy is higher;
- they do not produce resonances with the power distribution systems;
- they have a great flexibility regarding the location and the connection schemes [1].

The first step in the SAPF control is the generation of the prescribed compensating current based on the sensed supply voltage and load current. There are many methods in the literature used for the calculation of the reference prescribed current, such as those based on the following theories: the instantaneous power (p-q) theory, the synchronous reference frame (SRF), the Conservative Power Theory (CPT), the Currents' Physical Components (CPC), the Fryze-Buchholz-Depenbrock (FBD) theory [1]-[13].

Then, the closed-loop control system must be able to handle the accurate tracking of this prescribed current.

In this paper, two methods of generation the prescribed current are analyzed, namely the p-q theory based method and synchronous reference frame (SRF) method.

II. COMPENSATING CURRENT COMPUTATION METHODS

In this part of study, the control scheme of APF system using p-q theory is discussed and compared with that using synchronous reference frame (SRF) method.

A. The p-q Theory Based Method

The specificity of the p-q theory lies in the use of so-called instantaneous active and reactive powers (p and q) in expressing the prescribed compensating current (iF).

$$\underline{i}_F = i_{F\alpha} + j i_{F\beta} = \frac{2}{3}\frac{1}{u_\alpha^2 + u_\beta^2}\underline{u}\cdot\underline{s}_F^*, \qquad (1)$$

where the SAPF apparent power (sF) is:

$\underline{s}_F = -p_\sim - jq_\sim$ for only the harmonic compensation ($p_\sim = p - P$; $q_\sim = q - Q$);

$\underline{s}_F = -p_\sim - jq$ for the total compensation.

P and p~ are the the average value and the AC component of the instantaneous active power p.

Q and q~ are the the average value and the AC component of the instantaneous reactive power q.

The components of voltage and current space vectors (u and i) in the (α, β) stationary reference frame (uα, uβ, iα, iβ) are used in the expressions of p and q [1].

The Simulink model in Figure 1 corresponds to the objective of total compensation of both current harmonics and reactive power.

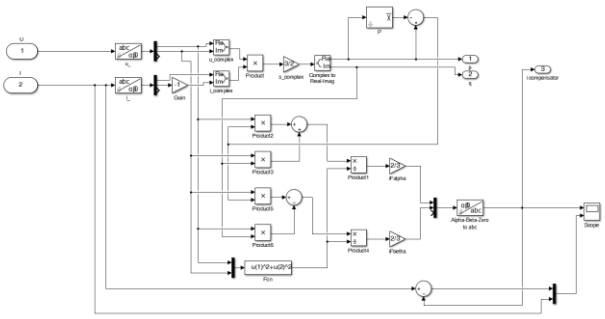

Fig. 1. Simulink model for the prescribed current generation by using the p-q theory in the case of total compensation.

The proper prescribed compensating current ensures a sinusoidal supply current after compensation in phase with the supply voltage.

B. *The SRF Based Method*

According to SRF method, the three-phase system of real currents is transformed into a two-phase rotating system d-q-0, whose speed is the fundamental pulsation when the identification of the fundamental component of load current is desired (Figure 2) [1]-[4], [14].

$$\begin{bmatrix} i_d \\ i_q \\ i_0 \end{bmatrix} = \frac{2}{3}\begin{bmatrix} \cos\theta & \cos(\theta-2\pi/3) & \cos(\theta+2\pi/3) \\ -\sin\theta & -\sin(\theta-2\pi/3) & -\sin(\theta+2\pi/3) \\ 1/2 & 1/2 & 1/2 \end{bmatrix}\cdot\begin{bmatrix} i_a \\ i_b \\ i_c \end{bmatrix} = \quad (2)$$

$$= [C]\cdot\begin{bmatrix} i_a \\ i_b \\ i_c \end{bmatrix}$$

θ is the angular position of the rotating reference system, which is determined by PLL circuits.

The currents obtained in the (d, q) coordinate system are formed by a direct current component (id-, iq-) and an alternating current component (id ~, iq~), which can be separated by a low-pass or high-pass filter.

If the rotating system is synchronous with the fundamental component of the current, to separate the compensating current, which corresponds to the alternative components of the current in the (d, q) coordinate system and constitutes the reference current for the active power filter, a high-pass filter is used. Then, the transition to the three-phase system is made by the inverse Park transformation, respectively:

$$\begin{bmatrix} i_{Fa} \\ i_{Fb} \\ i_{Fc} \end{bmatrix} = \begin{bmatrix} \cos\theta & \sin\theta & 1 \\ \cos(\theta-2\pi/3) & \sin(\theta-2\pi/3) & 1 \\ \cos(\theta+2\pi/3) & \sin(\theta+2\pi/3) & 1 \end{bmatrix}\cdot\begin{bmatrix} i_{d\sim} \\ i_{q\sim} \\ i_{0\sim} \end{bmatrix} = [D]\cdot\begin{bmatrix} i_{d\sim} \\ i_{q\sim} \\ i_{0\sim} \end{bmatrix} \quad (3)$$

The separation of the fundamental component of the current can also be considered, through the DC components of the current in the rotating system (d,q) through low-pass filters, followed by the passage in the three-phase system.

The performance of the SRF method are similar, but the p-q control method was more effective under transient conditions.

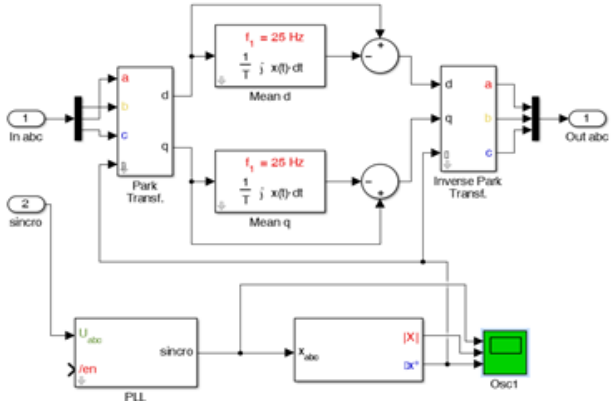

Fig. 2. Simulink model for the prescribed current generation by using the SRF method [2]-[4].

Like all time-frame reference current calculation methods, the SRF method is advantageous in terms of calculation volume, implementation speed, and control complexity compared to the methods in the frequency domain.

In practice, it is not only desired to eliminate a harmonic by active filtering and, therefore, the synchronous rotating system method is applied simultaneously for several harmonics, the reference current for the active filter being the sum of the reference currents on the harmonics.

Problems with the implementation of the synchronous rotating system method are mainly related to the correct detection of the angular position, especially when the three-phase power system is not balanced.

III. CURRENT CONTROL METHOD

The role of the active power filter control system is to generate signals for the control of semiconductor devices in the structure of the voltage inverter, so that the current injected into the power supply to follow its reference value. This function is conditioned by the need to control the voltage across the compensation capacitor.

The basic technique of current control by hysteresis, frequently adopted in the control of active filters, involves the generation of control signals for the semiconductor devices in the static converter by comparing the current error with a fixed hysteresis band (Figure 3). In this way, the hysteresis comparator also has the role of current regulator.

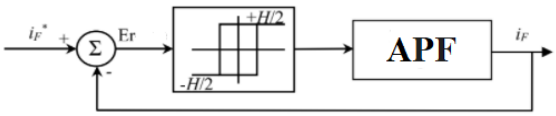

Fig. 3. Block diagram of the hysteresis control technique applied to the direct current control at the filter output.

As long as the error falls within the limits of the hysteresis band, no switching takes place. Switching occurs only when the error exceeds the hysteresis band. Thus, the hysteresis band (H) determines the maximum

and minimum limits of the current deviation from the reference value (Figure 4).

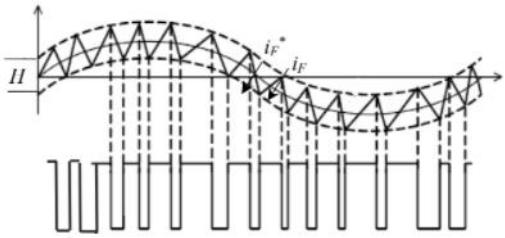

Fig. 4. Generation of the control signal in the case of control with hysteresis.

Therefore, in order to obtain the current compensation with small switching ripples, the value of H must be reduced, which determines the increase of the switching frequency. In the case of the active power filter, through this instant control, of the "bang-bang" type, the current to be controlled is forced to follow its reference value, without exceeding the tolerance imposed by the hysteresis band.

Although it is simple, robust and allows to obtain good dynamic performances, reasons for which it is frequently adopted in current control structures, the hysteresis control technique has a number of disadvantages, mainly due to the fact that the switching frequency of the converter is variable and is superiorly limited only by the width of the hysteresis band and the dynamics of the system. Thus, the losses in the power semiconductor devices increase, difficulties appear in the design of the interface filter of the active filter and the appearance of unwanted resonances in the network is favored. A negative influence of the filtering performances determined by the interaction of the phase currents was also noticed if the three-phase power system is with isolated zero [1], [5], [6].

The Simulink model of the hysteresis band based control is illustrated in Figure 5 and the generation of the control signals for the IGBTs is shown in Figure 6.

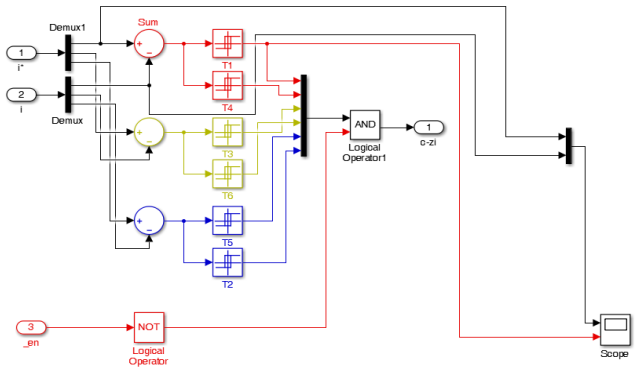

Fig. 5. Simulink model for the basic method of current control by hysteresis.

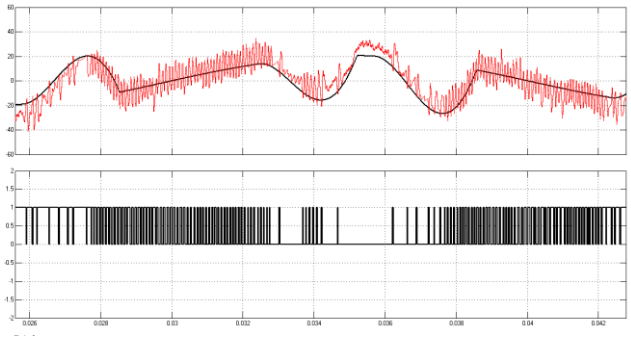

Fig. 6. Generation of the control signal in the case of hysteresis based control – Simulink.

IV. SIMULATION RESULTS

The study was done by simulation based on specific Simulink models, for both methods of calculating the reference current. It is specified that for the two calculation methods, the load is the same: a three-phase uncontrolled rectifier that feeds a passive load of RC type, which simulates a direct current motor. The current drawn from the power supply by the nonlinear load is shown in Figure 7.

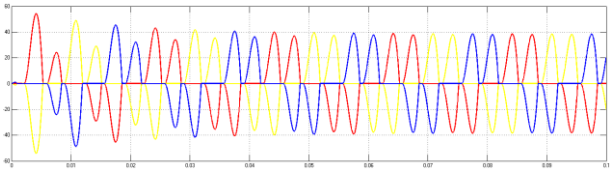

Figure 7. The waveform of the currents absorbed by the nonlinear load.

The rated values are:

Nominal voltage: 380 V;

Nominal current: 20 A;

Active power: 9.48 kW;

Apparent power: 12.55 kW.

For the current control, the hysteresis based method was used in both simulation systems.

A. The p-q Theory Based Method – Simulink results

The Simulink model conceived for the whole active filtering system based on the p-q theory based method is shown in Figure 8. All the components are illustrated (power supply, nonlinear load, active power filter with the compensation capacitor on the DC-side and the interface filter of L- type on the AC side, control blocks and calculation blocks).

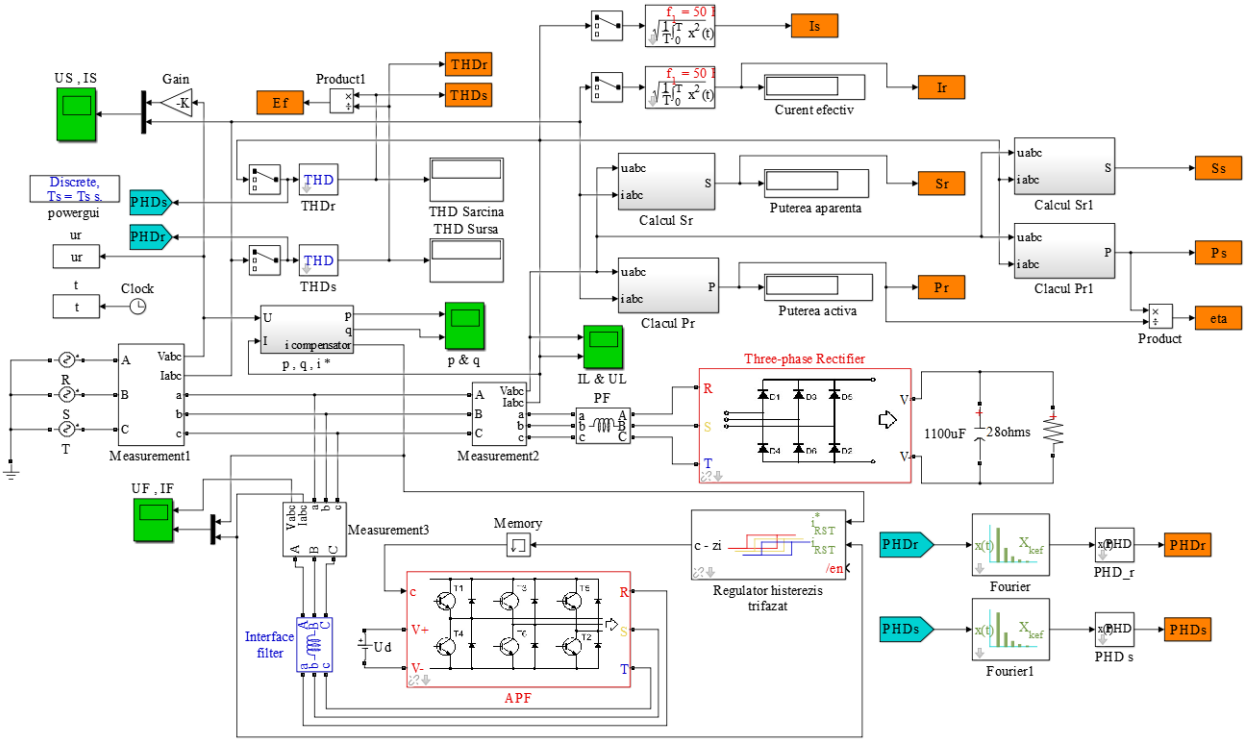

Fig. 8. Simulink model of the active filtering system in case of using the p-q theory based method.

The current waveforms in Figure 9 shows the performance of the active filtering system to perform the total compensation. The supply currents after compensation are very close to the sinusoidal shape, illustrating the switching influence of the inverter, whose effect is not completely eliminated by the inductive interface filter. The remaining distortion factor of the supply current is 5.42 %, leading to an active filtering efficiency of about 15.02 (Table I). The currents provided by the voltage source inverter to achieve the compensation are shown in Figure 10.

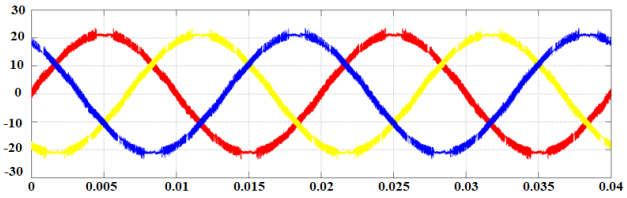

Fig. 9. Current waveforms at the supply side after compensation in case of using the p-q theory.

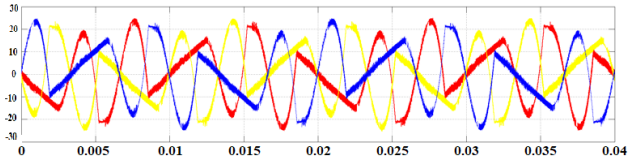

Fig.10. Waveforms of the currents at the inverter output in case of using the p-q theory

B. The SRF Based Method – Simulink results

In the Simulink model of the active filtering system in the case of the SRF based method (Figure 11), the specificity is given by the block "SRF" which provides the reference currents to the current controller.

As with the use of the p-q theory, the supply currents waveforms after compensation (Figure 12) are very close to sinusoids (THD ≈ 5.22 %). The resulting active filtering efficiency is of about 15.6 (Table I). Figure 13 illustrates the waveforms of the currents at the inverter output in case of using the SRF based method.

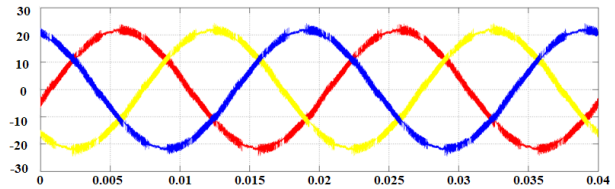

Fig. 12. Current waveforms at the supply side after compensation in case of using the SRF based method.

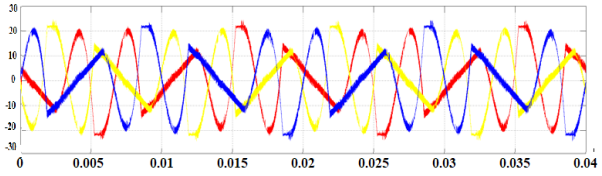

Fig.13. Waveforms of the currents at the inverter output in case of using the SRF based method.

TABLE I.
SUMMARY OF THE NUMERICAL RESULTS

p-q Method			
I (rms) [A]	THD_source [%]	THD_load [%]	Active filtering efficiency
19.02	5.42	81.41	15.0202

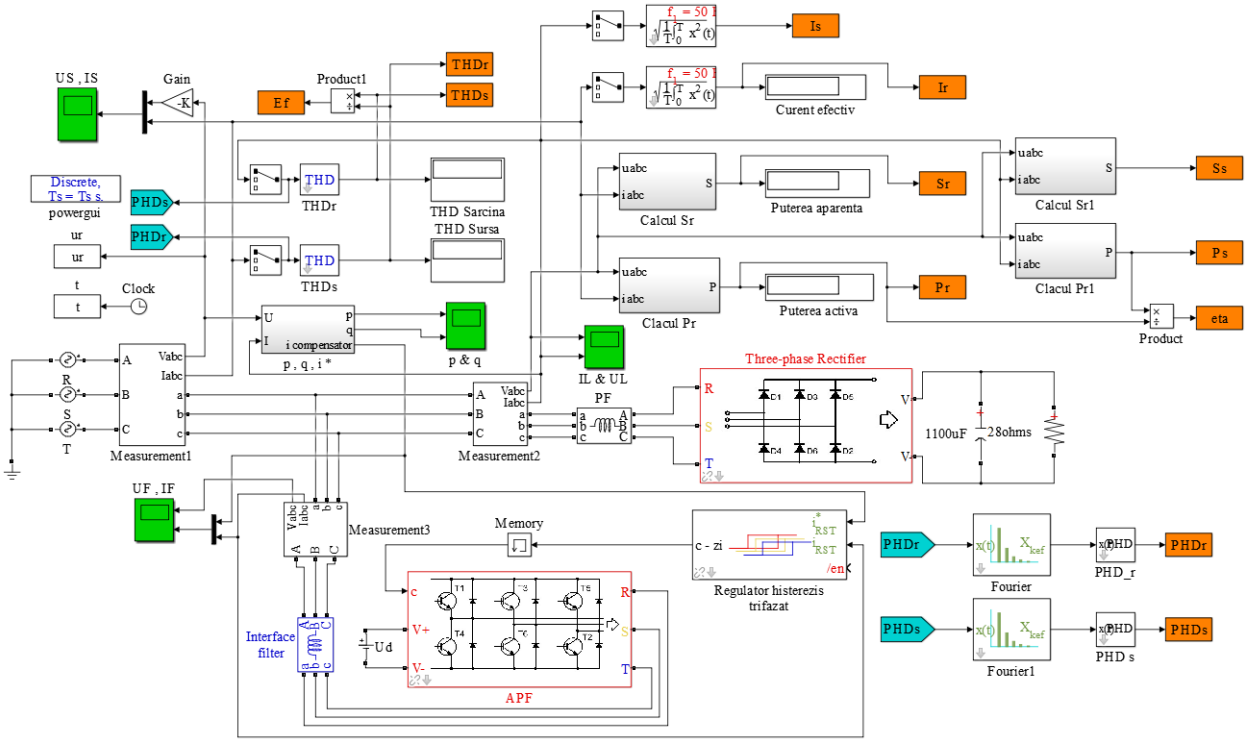

Fig.11. Simulink model of the active filtering system in case of using the SRF based method.

A summary of the numerical results obtained by simulation is presented in Table I and Table II. As shown, the THD values of the currents after compensation are very close to the value of 5% recommended by Std. IEEE 519 [15].

TABLE II.
SUMMARY OF THE NUMERICAL RESULTS

SRF Method			
I (rms) [A]	THD_source [%]	THD_load [%]	Active filtering efficiency
19.02	5.22	81.41	15.5957

V. CONCLUSION

Two methods for the reference current generation used in the control of a three-phase shunt active power filter, namely the p-q theory based method and the SRF based method, were investigated in this paper.

Under balanced and sinusoidal supply voltages these two methods gives similar results for total compensation.

Under nonideal voltage conditions, the synchronous reference frame method leads to better results. However, the p-q method allows the compensation of only the current harmonics, or of the reactive power, or the total compensation, being more flexible.

The SRF method is advantageous in terms of the volume of calculations, the execution speed associated with the implementation and the complexity of the control.

Both methods are frequently adopted in the control of active power filters.

ACKNOWLEDGMENT

This work was supported by the grant POCU380/6/13/123990, co-financed by the European Social Fund within the Sectorial Operational Program Human Capital 2014 – 2020.

Contribution of authors:
Mihăiță Daniel Constantinescu – 60%
Mihaela Popescu – 20%
Vlad Constantin Suru– 20%

Received on August 08,2021
Editorial Approval on November 29, 2021

REFERENCES

[1] Bitoleanu, A., Popescu, Mihaela, Suru V.C., *Filtre active de putere – Fundamente si aplicatii*, Bucuresti, Matrix, 2021.

[2] Popescu, Mihaela, Preda, Alexandra. Suru, V., "Synchronous reference frame method applied in the indirect current control for active DC traction substation", Athens: *ATINER'S Conference Paper Series*, No: TRA2015-1552, 2015, pp. 1-6, 8-11 June 2015.

[3] Suru, C.V., Patrascu, Alexandra, Linca M.. "The synchronous fundamental dq frame theory application for the active filtering", *Annals of the University of Craiova, Electrical Engineering series*, No. 38, pp. 92-97, 2014.

[4] Suru, C.V., Patrascu, Alexandra, Linca M., "The synchronous fundamental dq frame theory implementation and adaptation for the active filtering", *12th International Conference on Applied and Theoretical Electricity*, Craiova, Romania, 23-25 October 2014.

[5] Asiminoaei, L., Blaabjerg, F.. Hansen, S., "Detection is key. Harmonic detection methods for active power filter

applications", *IEEE Industry Applications Magazine, Vol. 13*, Issue 4, pp. 22-33, July/Aug. 2007.

[6] Asiminoaei, L., Blaabjerg. F., Hansen, S.. "Evaluation of harmonic detection methods for active power filter applications", *Applied Power Electronics Conference and Exposition*, pp. 635-641, 2005.

[7] Pătrașcu, Alexandra, Popescu, Mihaela, Suru, V.; "The conservative power theory and the active Filtering", *Bulletin AGIR No. 4*, pp. 179-182, 2012.

[8] Suru, V., Pătrașcu, Alexandra, Popescu, Mihaela, Bitoleanu, A., "Conservative, power theory application in shunt active power filtering under asymmetric voltage", *The 14th International Conference on Optimization of Electrical and Electronic Equipment (OPTIM 2014)*, , Brașov Cheile Grădiștei, Romania, pp. 647 – 654, 22-24 May 2014.

[9] Popescu, Mihaela, Bitoleanu, A., Suru, V., "Currents' Physical Components theory implementation in shunt active power filtering for unbalanced loads", *11th Conference-Seminar International School on Nonsinusoidal Currents and Compensation (ISNCC)*, , Zielona Gora, Poland, pp.1–6, 20-21 June 2013.

[10] Popescu, Mihaela, Bitoleanu, A., Dobriceanu, M., "FBD-based control in active dc-traction substations", *13th International Conference on Applied and Theoretical Electricity (ICATE), Craiova*, Romania, Oct. 6-8, 2016.

[11] Popescu, Mihaela, Pătrașcu, Alexandra, Dobriceanu, M., "Application of generalized instantaneous reactive/non-active power theories in the control of shunt active power line conditioners: Practical evaluation under nonideal voltage and unbalanced load", *Book Chapter: Nonlinear Dynamics of Electronic Systems, Series: Communications in Computer and Information Science, Vol. 438*, pp. 125-133, 2014.

[12] Popescu, Mihaela, Bitoleanu, A., Dobriceanu, M., Suru, V., "Optimum control strategy of three-phase shunt active filter system", *Proceedings of World Academy of Science, Engineering and Technology*, Vol. 58, pp. 245-250, October 2009.

[13] Popescu, Mihaela, Bitoleanu, A., Suru, V., Patrascu, Alexandra, "High performance shunt active power filter", *7th International Symposium on Advanced Topics in Electrical Engineering (ATEE)*, Bucharest, pp. 1-6, 12-14 May 2011.

[14] Teodorescu, R., Liserre, M.. Rodríguez, P., *Appendix A: Space vector transformations of three-phase systems, Grid Converters for Photovoltaic and Wind Power Systems*, 19 Dec. 2010.

[15] Hoevenaars, T., LeDoux, K., Colosino, M., *Interpreting IEEE STD 519 and meeting its harmonic limits in VFD applications*, Petroleum and Chemical Industry Conference, pp. 145-150, 2003.

Automatic Ventilation and Air Conditioning System for Educational Training

Ionel Laurentiu Alboteanu*, Andrei Cosmin Militaru†
* University of Craiova / Department of Electromechanical, Environmental and Applied Informatics, Craiova, Romania, e-mail: lalboteanu@em.ucv.ro
† SC ELPREST SRL/Technical-commercial department Craiova, Romania, e-mail: andreicosminmilitaru1@gmail.com

DOI: 10.52846/AUCEE.2021.1.08

Abstract **- The air quality from closed spaces is very important for people or for technological processes. The heating, ventilation and air conditioning installations ensure the maintenance of the air parameters in the rooms served within pre-established limits, throughout the year, regardless of the variation of meteorological factors, the degree of occupancy of the rooms or the development of production processes. The paper presents an automatic ventilation, heating and air conditioning system made on a small scale. Climatic parameters can be monitored and controlled in two ways: in local mode and also in remote mode. In local mode, the control of the installation is done with a Mega 2560 development system made around the Atmega 2560 microcontroller, which processes the information received from the DHT22 temperature and humidity sensor. Information about parameters and system status is displayed on the local screen. The WeMos D1 R2 WiFi development system based on an ESP8266 wireless microcontroller with Wi-Fi 802.11 compatible with the IDE-Arduino development environment was used for the remote control. All information is transmitted wirelessly to an online platform, called Cayene that allows their storage and control. The platform referred to offers a number of graphical features that do not involve costs for users. The system can be used both for educational purposes for engineering students, but can be adapted for real practical applications.**

Cuvinte cheie: *sistem de incalzire ventilare si climatizare, monitorizate, microcontroler, senzori, temperatura, umiditate.*

Keywords: *heating, ventilation and air conditioning system (HVAC), monitoring, microcontroller, sensor, temperature, humidity.*

I. Introduction

The room air may occur a number of pollutants from the occupants (carbon dioxide resulting from respiration, cigarette smoke, etc.), building materials (gases, vapors) or the process of manufacture (e.g. : solvents).

Air conditioning is the technique that consists in modifying, controlling and regulating the climatic conditions (temperature, humidity, etc.) of the room for various reasons: comfort (individual homes, small spaces), requirements imposed by various factors or for technical reasons (eg: electronic component production facilities, spaces for the production of automobiles, engines, medical laboratories, theaters of operations, rooms where computer servers are located, etc.) [1], [2]. Modern techniques and equipment are currently being used to increase the efficiency of HVAC systems [3].

II. Structure of Heating Ventilation and Air Conditioning System

The role of the ventilation system is to eliminate or dilute the harmful substances below the danger limit for the human body, by introducing fresh air and evacuating the contaminated air.

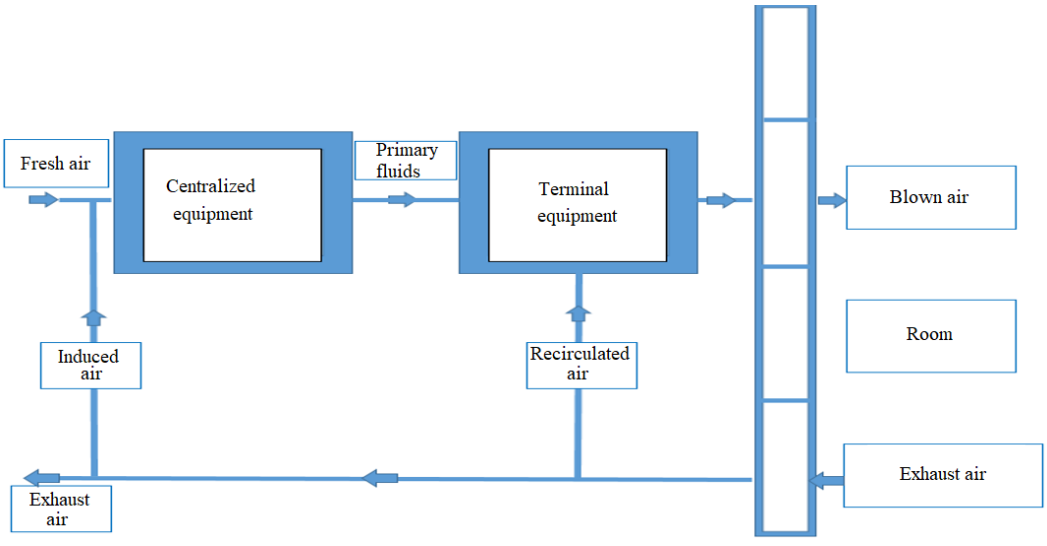

Fig.1. Block diagram of a heating, ventilation and air conditioning system

If, in addition to the requirements on air purity, it is necessary to ensure certain temperature and humidity parameters for the room air, the ventilation installation is transformed into an air conditioning installation (fig 1.) [4].

A heating, humidification and ventilation installation forms a central air conditioning installation and is made up of a set of equipment having the following functions [5] (fig.2):

- air preparation and distribution with well-defined thermal, aeraulic and acoustic characteristics;

- distribution of treated air in places with air conditioners through intermediate pipes and terminal devices

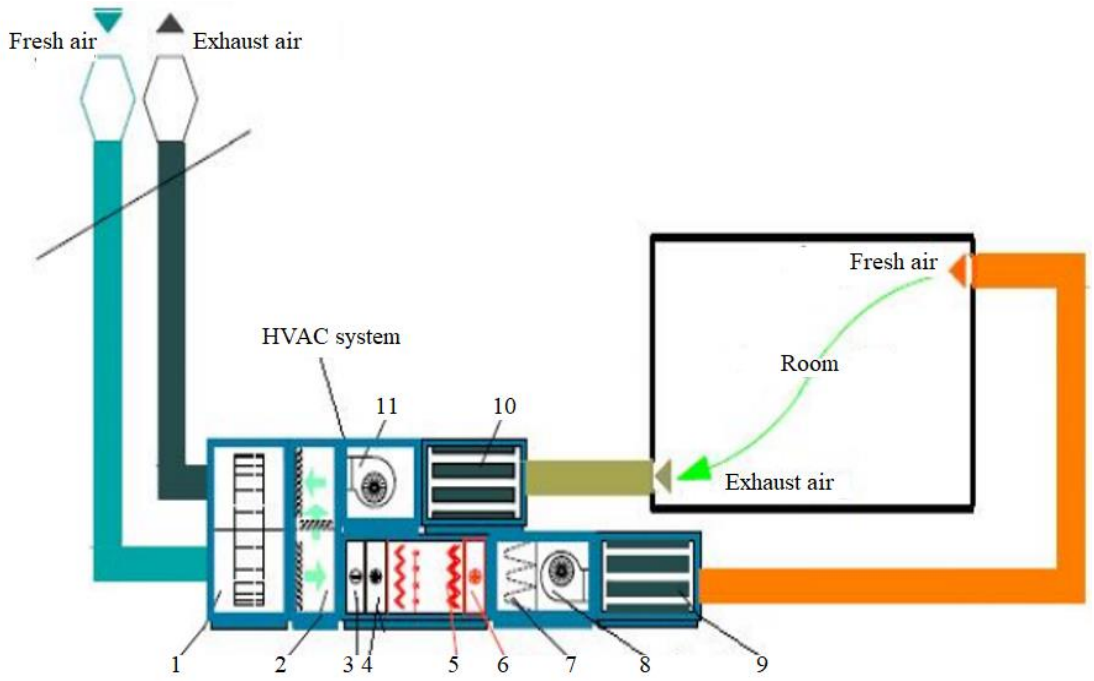

Fig. 2. Structure of a heating, ventilation and air conditioning system: 1- heat recuperated; 2- air recirculation module; 3- refrigeration module; 4, 6- heating module; 5- humidifier; 7- air filter; 8- suction fan; 9,10 - noise attenuators; 11- exhaust fan.

Primary fluids (such as air or water) are prepared in centralized equipment that is usually located in the engine room (in the case of large installations and large powers). The terminal equipment is always installed in the places / areas of occupation of the hall, receives the fluids (already prepared in centralized equipment) and uses them to discharge the treated air in the necessary areas [6], [7], (fig.1).

Between the centralized equipment and the terminal equipment, the primary fluids and the treated air are distributed through pipes that provide many accessories necessary for a good operation (dampers, filters, valves, etc.). In addition, the installations are equipped with control and safety devices (thermostat, pressure switches, fire detectors) that are controlled by centralized computing units (for example: high-performance control systems, which is in fact the object of this work) [8].

The central control unit –CCU takes the information from the sensor on the temperature and humidity in the air-conditioned enclosure and processes it (fig. 3). After processing this information, the control module receives a electrical signals and transmits the control of the execution elements of the air conditioning unit (compressor, heating element, humidifier pump, fan) [9].

The sensor reads the temperature and humidity in the air-conditioned enclosure in real time and transmits this information to the CCU.

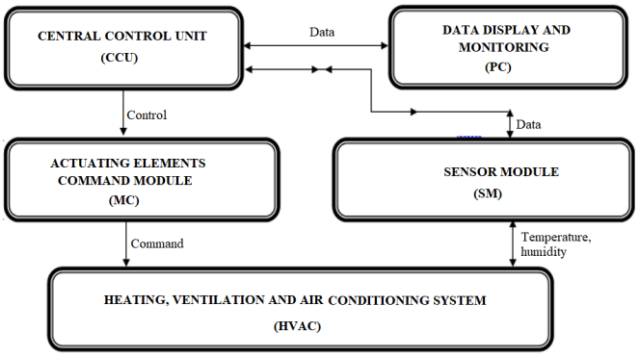

Fig. 3. Block diagram of a command and control system

The air conditioning unit has 3 operating modes: cooling, heating, humidification or dehumidification depending on the settings received from the command and control unit but also from the information transmitted by the sensor [10].

All collected data will be viewed in real time using a mobile device or a computer that constantly communicates with the control unit.

III. Implementation of Small Scale Model of Heating Ventilation And Air Conditioning System

Based on the real model system, a small-scale model was developed for the heating, ventilation and air conditioning system (HVAC) [4].

The whole air conditioning system is structured and composed of three subassemblies:

1) Air conditioning system (The power part of the system).

2) Electrical installation;

3) Control system.

Figure 4 shows the model of the HVAC system made.

According to figure 4, the realized physical model consists of:

- air conditioning unit - it contains: compressor, fan-condenser assembly, evaporator (cooling battery), fan for introducing air into the enclosure, heating elements;

- the enclosure where the air conditioning is performed: it was made of hobby glass (transparent material);

- the housing in which the cooling / heating battery is inserted: it was also made of a transparent material, in order to be able to observe the construction of the component elements;

- evaporator (cooling battery);

- electrical resistors used for the heating process;

- humidifier;

- piping for introducing air conditioning into the enclosure;

- piping for air recirculation;

- piping for introducing the air subjected to the humidification process;

- recirculation valve;

- temperature and humidity sensor;

- control panel;

- the electrical part of the installation (contactor, automatic fuses, connectors).

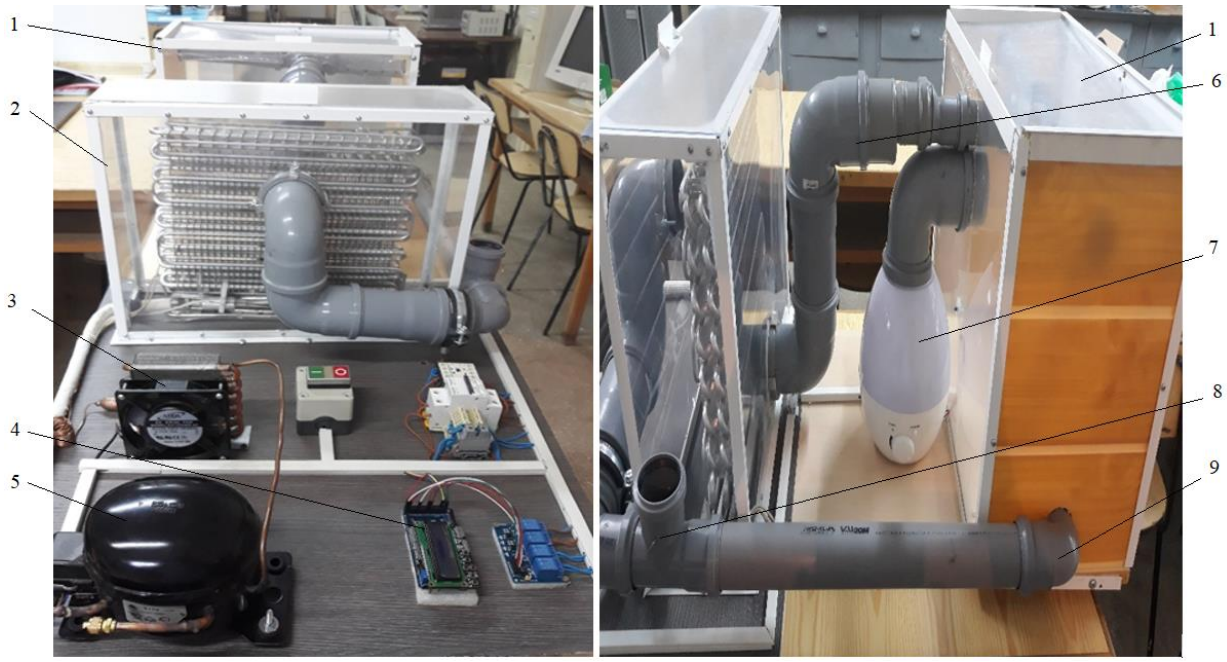

Fig. 4. HVAC system achieved:1- air-conditioned enclosure; 2- heating/refrigeration module ; 3- heat exchanger (condenser); 4-control module; 5-compressor; 6- supply air duct; 7- humidifier; 8- flap of air mixed ; 9- exhaust air duct

A. Achieved of local control system

In order to be brought to the parameters with which it can be introduced in the space where air conditioning is required, the air undergoes a succession of elementary transformations. These parameters are controlled by means of a Mega2560 development board, which processes the information received from the DHT22 temperature and humidity sensor. Then, the physical components of the command and control circuit of the installation are presented together with the electrical connection diagram [11].

Mega 2560 is a development system built around the Atmega2560 microcontroller which is provided with numerous communication pins, analog and PWM useful for connecting with various elements: monitoring, command, control, etc. (sensors, relays).

Technical specifications of the development system are presented in the product catalog sheet [12].

For the control of the actuating elements, a compact board with 4 relays was used, having the following characteristics:

Voltage: 250VAC or 30VDC

Current: 10A (Max)

Each relay is controlled by an optocoupler

Optocoupler supply voltage: 5V

Current required for control: 5mA

The DHT22 sensor was used to measure temperature and humidity, having the following characteristics:

Supply voltage: 3.3 - 6V DC

Operating plate: temperatures -40 and 80 ° C

Reading time: 2s

Humidity range: 0-100% RH

Accuracy: ± 0.5 ° C

Wiring diagram for connecting of control elements are shown in figure 5.

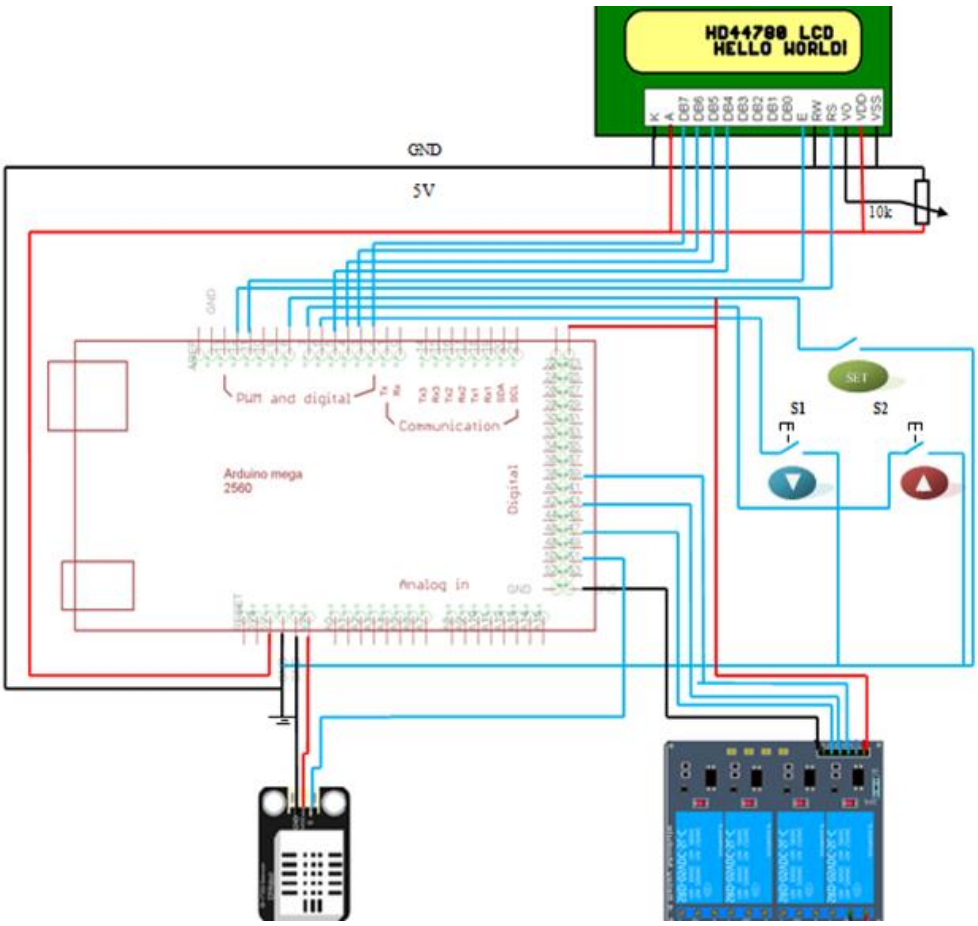

Fig. 5. Wiring diagram of local control system

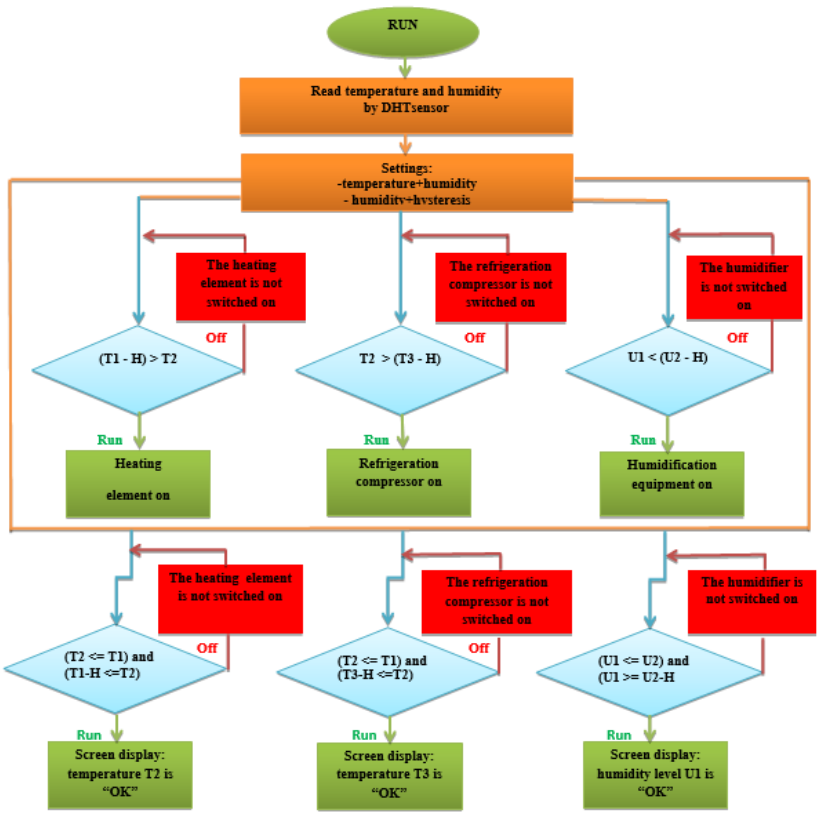

Fig. 6. Flowchart of control system

The software part of the platform is integrated in an IDE graphical interface, based on the Processing programming language. Programming the controller on the physical platform is done using the Arduino programming language.

The Arduino integrated development environment is designed to write programs that can be loaded onto physical Arduino platforms. The interface is written in Java and the programming environment uses open source programming languages such as Processing, AVR-GCC [13].

The mode of operation of the development board is presented in the form of a flowchart (Fig. 6) and the program code.

B. *Achieved of remote control system*

The WeMos D1 R2 WiFi development system based on an ESP8266 wireless microcontroller with Wi-Fi 802.11 compatible with the IDE-Arduino development environment is used for the remote control [14]. The structure of this board is based on a standard Arduino hardware design with similar proportions to Arduino Uno and Leonardo.

The CH340 USB interface allows it to be connected and programmed directly from the computer and requires only a micro USB communication and power cable.

The system can be accessed remotely via the Cayenne online platform based on a name, a user password and a customer ID [15]. The connection data on the platform together with the user data and password of the wireless router are added in the source program written in Arduino Ide.

Wiring diagram for connecting of control elements are shown in figure 7.

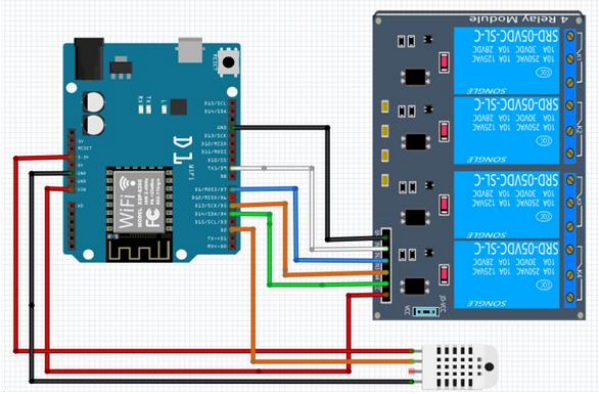

Fig. 7. Wiring diagram of remote control system

The main advantage of this system is given by the multitude of analog and digital outputs that are arranged on the same board but also by the technical characteristics.

IV. Testing Of HVAC System

A. *Testing of local control system*

In order to highlight the functionality of the experimental model, a series of tests were performed, in which all three modes of operation of the installation were captured in the form of images: cooling, heating, humidification.

Testing of HVAC system in cooling mode

In this case, when the system is started, the initial parameters are displayed on the screen: temperature and humidity (fig. 8. a). It can be seen from the figure that the temperature inside the enclosure at that moment is 25.2 °C.

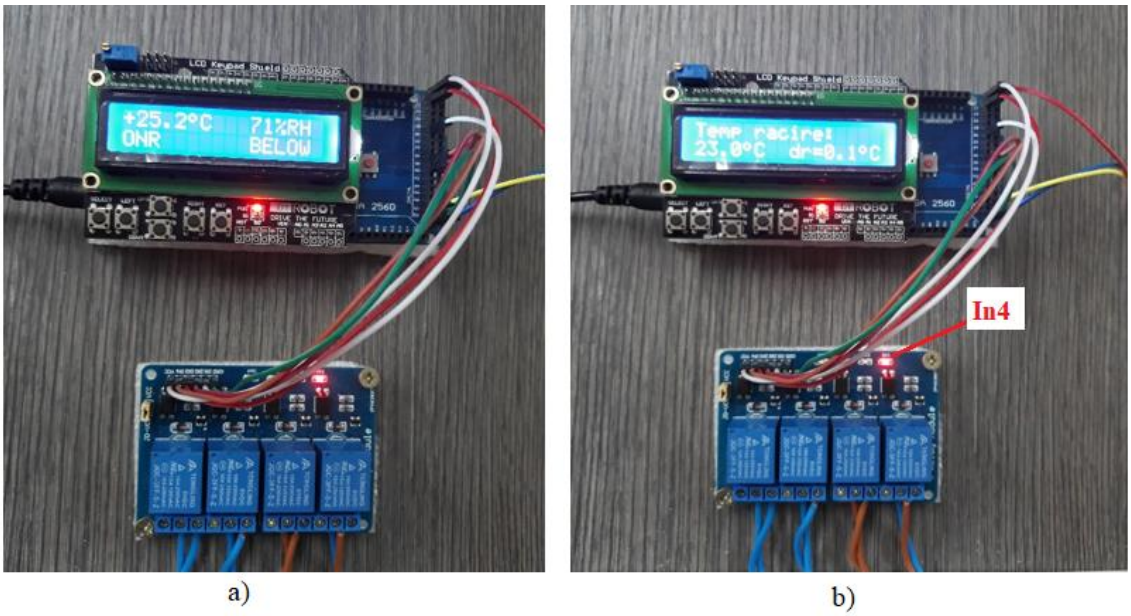

Fig. 8. Testing in cooling mode

For operation in cooling mode, the desired temperature is selected from the development system menu, for example: 23 °C. Then it is observed (fig. 8.b) the activation of the “In2” input of the relay that shows the operation of the compressor (red LED is OFF). The compressor will operate without interruption, until the desired temperature is reached, at which point the "In2" input of the relay will receive the compressor switch-off command (red LED is ON).

Testing of HVAC system in heating mode

Proceed identically to the case described above, namely:

- at the start of the system, the real parameters of the enclosure are displayed on the screen;

- it is observed from figure 9. a) that the temperature inside the enclosure at that moment is 24.6 ° C;

- for the selected operating mode, the indoor air heating mode, the temperature of 25.2 ° C is chosen from the system menu (fig. 9. b);

- the heating elements are controlled at this moment by activating the "In1" input of the relay (red LED is OFF);

- they operate without interruption until the desired temperature is reached (fig. 9 c), at which point the “In1” input of the relay will receive the command to disconnect the resistors (red LED is ON).

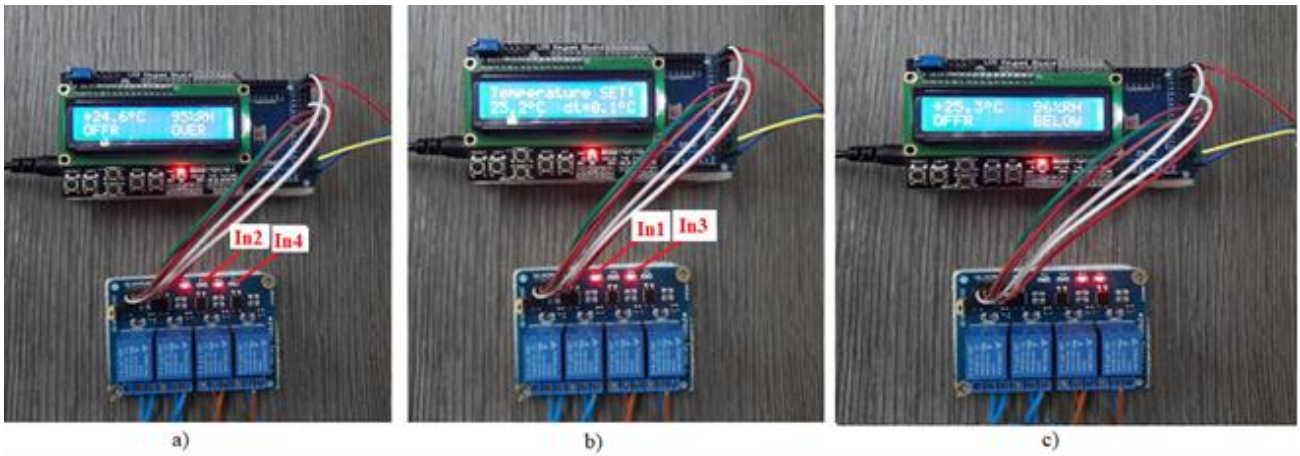

Fig. 9. Testing in heating mode

Testing of HVAC system in humidity mode

The same procedure is followed for this mode of operation of the installation:

- at the start of the system, the real parameters of the enclosure are displayed on the screen;

- it is observed from figure 10.a) that the humidity inside the enclosure at that moment is 95%;

- for the chosen operating mode, the humidification of the indoor air, the value for humidity of 99% is chosen from the system menu;

- the humidifier is currently controlled by activating the “In4” input of the relay (red LED is OFF), (fig 10 a);

- it works without interruption until the desired value is reached, at which point the “In4” input of the relay will receive the humidifier switch-off command (red LED is ON), (fig. 10 b).

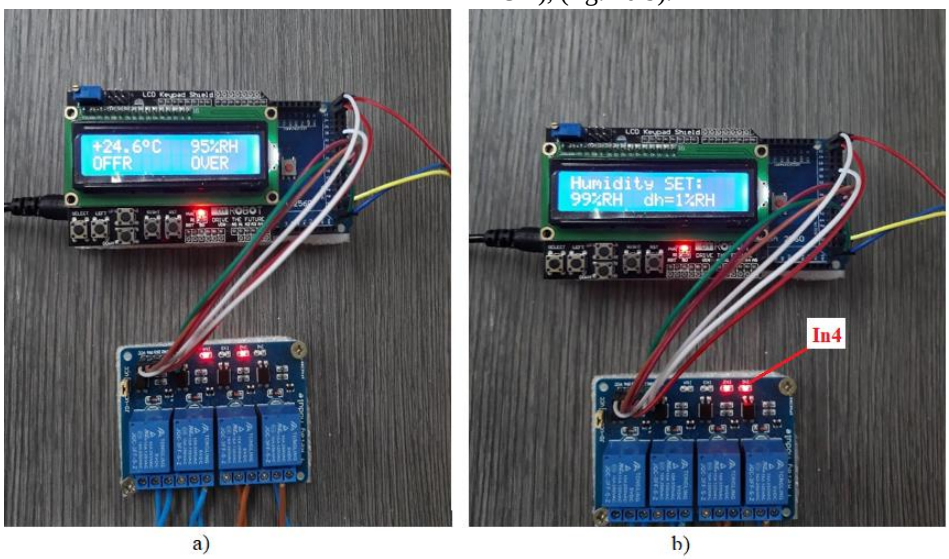

Fig. 10. Testing in humidity mode

B. Testing of remote control system

The verification of the operation of the system was performed through a series of tests, in which all the modes of operation of the installation were captured.

All information taken from the air-conditioned room is transmitted wirelessly to an online platform that allows their storage and control (figure 11). The platform referred to is called Cayenne and offers a number of graphical features that do not involve costs for users.

Fig. 11. Panel of remote control system

The simulation of the implemented system operation can be easily followed on the Cayenne platform, and the evolution of the parameters can be observed graphically over different periods of time or in real time, analyzing the operation graphs at the desired intervals.

According to those specified, simulations were performed for the 3 operating modes of the plant: cooling, heating, humidification.

Testing of remote control system in cooling mode

Figure 12 shows the operation of the HVAC system in cooling mode, when the compressor is controlled by the In1 input of the relay (red LED off), the temperature tends to gradually decrease to the prescribed value in the control panel of 22.0 °C.

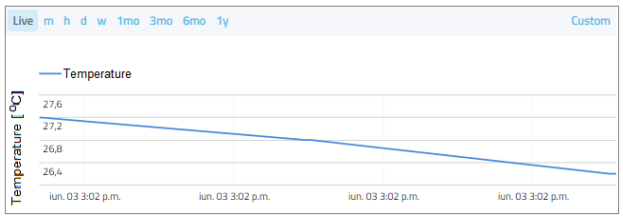

Fig.12 Evolution of the room temperature: mode of operation - cooling

Testing of remote control system in heating mode

After setting the desired temperature, the In2 input of the relay will be activated, which will control the heating elements and the system will start in heating mode. The graph in figure 13, shows the operation of the system and the ascending slope that tends to reach the value of the room temperature.

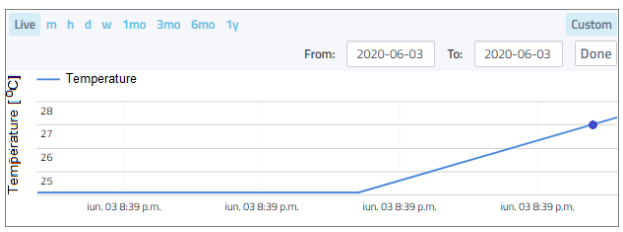

Fig.13. Evolution of the room temperature: mode of operation – heating

Testing of remote control system in humidity mode

The control principle of the installation in this mode of operation is similar to those presented above, except that the measured humidity will be compared with the set one. The set humidity value is 99%. With the entry into operation of the humidifier, the increase of humidity towards the maximum set value of 99% is observed (figure 14).

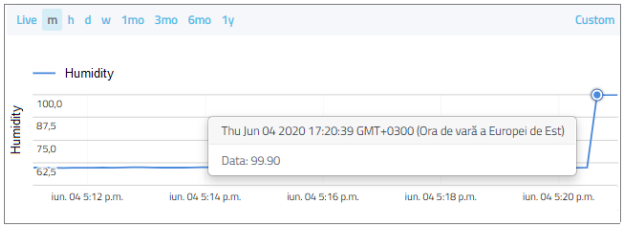

Fig.14. Evolution of the room humity: mode of operation – humidity

Having the same principle of operation, the installation also operates in this case without interruption until it reaches the prescribed value, at which point the microcontroller sends a pulse to the relay which is set to control the deactivation of the humidifier (In3 - red LED off).

V. Conclusion

The correct operation of the system in the three modes of operation (heating, cooling, and humidification) is highlighted in the experimental results.

Both the control part and the execution elements are different from those of a real HVAC system. The experimental model performs the same functions as a real system.

Considering these aspects and the low price of the system components, the possibility of use in civil or industrial applications can be analyzed.

The system designed, developed and tested can be used both in educational applications in electrical engineering and in industrial applications.

Acknowledgment

Source of research funding in this article: Research program of the Electrical Engineering Department financed by the University of Craiova.

Contribution of authors:

First author – 60%

First coauthor – 40%

Received on July 17, 2021

Editorial Approval on November 30, 2021

References

[1] *** Technical Encyclopedia of Installations, Installation Manual: Heating Installations, 2nd edition, Ed. Artecno Bucharest, 2010.

[2] *** Technical Encyclopedia of Installations, Installation Manual: Ventilation and Air Conditioning Installations 2nd Edition, Ed. Artecno Bucharest, 2010.

[3] S. Mahlangu, M. Sibanyoni; L. Ngoma, S. Chowdhury, "The Design of HVAC Network Control Panel For Battery Room", *2020 6th IEEE International Energy Conference (ENERGYCon*), 28 Sept.-1 Oct. 2020, Gammarth, Tunisia.

[4] L. Alboteanu, C. Militaru, "Small Scale Model of Heating, Ventilation and Air Conditioning System", *2021 International Conference on Applied and Theoretical Electricity (ICATE*), 27-29 May 2021, Craiova, Romania.

[5] L. Alboteanu, Air conditioning installations, Ed.Universitaria, Craiova, 2012.

[6] *** Norm for the design, execution and operation of ventilation and air conditioning installations, indicative I5 /2010.

[7] ANSI/AHRI Standard 210/240 with Addenda 1and 2 (Formerly ARI Standard 210/240), Performance Rating of Unitary Air-Conditioning & Air-Source Heat Pump Equipment.

[8] H. Jouhara, Y. Junjing, ″ Energy efficient HVAC systems″, *Energy and Buildings*, Volume 179, pp. 83-85, 15 November 2018.

[9] J. D. Kelso, Building Energy Data Book, 2012.

[10] F. Belic, Z. Hocenski, D. Sliskovic, ″HVAC Control Methods - A review″, *Procc. Of 19th International Conference on System Theory, Control and Computing (ICSTCC*), October 14-16, Cheile Gradistei, Romania, 2015.

[11] L. Alboteanu, Manolea Gh., Ravigan F., "Automatic sorting and handling station actuated by pneumatic drive" *Annals of the University of Craiova, Electrical Engineering Series*, no 1, 2018, ISSN 1842-4805, pp.1-8.

[12] *** http://www.atmel.com

[13] *** https://www.arduino.cc/

[14] ***https://www.instructables.com/Programming-the-WeMos-Using-Arduino-SoftwareIDE/

[15] *** https://developers.mydevices.com/cayenne/features/remote-monitoring/

Considerations on the Disturbances Occurred in the Operation of Medium Voltage Electrical Networks with Neutral Treated by Suppression Coil

Silvia-Maria Digă[*], Nicolae Digă[**], Paul-Mihai Mircea[*], Ion Marin[*]
[*] University of Craiova/ Department of Electrical, Energetic and Aerospace Engineering/ Doctoral School of Electrical and Energetic Engineering, Craiova, Romania, sdiga@elth.ucv.ro, mmircea@elth.ucv.ro, ion.marin@distributieoltenia.ro
[**] HELMKE/ Bureau Romania, Craiova, nicolae.diga@yahoo.ro

DOI: 10.52846/AUCEE.2021.1.09

***Abstract* – In this paper are analyzed the analytical models of theoretical calculation and analysis of the main consequences of neutral treatment by suppression coil on the operation of medium voltage electrical networks, both in normal regime and especially in single-phase fault regime. The size of stationary and transient overvoltages and fault currents is evaluated for a concrete case study. Also the authors present in this paper the results they obtained after the extension of their research and in the field of harmonic regime produced by the grounding of a power line. This type of fault occurs frequently in the case of medium voltage networks, with neutral treated with suppression coil. Thus, they managed to reconstruct the waveforms of currents and voltages during the fault period (grounding). Then, having these calculation elements available, a comparative analysis of similar incidents (earthing) from a 20 kV network with the neutral treated with classic suppression coil and modern Trench suppression coil, respectively, was made.**

Cuvinte cheie: *rețele electrice de medie tensiune, neutru tratat prin bobină de stingere, supratensiuni staționare și tranzitorii, curent de defect, regim armonic.*

Keywords: *medium voltage electrical networks, neutral treated by suppression coil, stationary and transient overvoltages, fault current, harmonic regime.*

I. INTRODUCTION

In the medium voltage networks in Romania it is most frequently used as "*neutral treatment modes*": neutral grounded by suppression (compensation) coil and respectively by low resistance or inductance.

The neutral treatment mode determines numerous consequences on the operation of the electrical networks both *in normal regime and especially in single-phase fault regime*. These consequences relate to: the size of transient and stationary overvoltages, the size of the fault current, the harmonic current emissions, the possibilities (methods and means) of separating single-phase faults, grounding potentials, transmitted disturbances in network, radiated disturbances in certain domains of standardized frequency, electromagnetic influences on low current lines (e.g. telecommunication lines) etc. [1], [2].

The objectives of this article consist in determining the value of transient and stationary overvoltages, fault current for different scenarios and the harmonic analysis of waveforms of these parameters in a 20 kV medium voltage electric network with the neutral treated through classical/modern suppression coil.

II. ANALYSIS OF THE MAIN CONSEQUENCES OF NEUTRAL TREATMENT BY SUPPRESSION COIL ON THE OPERATION OF MEDIUM VOLTAGE ELECTRICAL NETWORKS. CASE STUDY.

A. The size of stationary and transient overvoltages

It is considered as *a case study*, a medium voltage electrical network U_N = 20 kV with compensated neutral for which a series of **initial data** are known: maximum total network length l_{max} = 90 km; network capacities: C_A = 0,00485 μF/km; C_B = 0,0043 μF/km; C_C = 0,00485 μF/km; network (specific) conductance $G = 1/r = 0.5 \cdot 10^{-6}$ S/km; depreciation coefficient of the uncompensated network d' = 34,105 %. The compensation coil used is dimensioned to the entire capacitive current of the network, with an overcompensation of k = 15 % and to the phase voltage U_{f0}, having active losses p = 1.5 %.

In *the normal regime* of operation of the networks treated by the extinguishing coil, between the neutral point and the ground there is a voltage whose size depends on the degree of adjustment of the coil, the asymmetry of the network phase admittances to earth and the asymmetry of the phase voltages of power supply.

Because the authors systematized and customized, in their previous research [3], algorithms for the complete calculation of the parameters necessary for the choice and installation of suppression coils in medium voltage networks, they were able to select those system detailed mathematical models that give maximum values for calculated stresses.

Thus considering that the supply voltages form a direct succession system, that the insulation conductances on the three phases are equal (G) and that on phase A where the single-phase defect takes place, the capacity to earth differs by the coefficient m in relation to the other two phases ($m = C_A/C_B$), is obtained for *the modulus of the degree of neutral displacement* (the ratio between the neutral displacement voltage and the phase voltage), expression (1).

$$|\underline{u}| = \left|\frac{\underline{V_N}}{U_{f0}}\right| = \frac{m-1}{\sqrt{(3d)^2 + (2+m-3k)^2}} \quad (1)$$

where:
d = I_a/I_C is the depreciation coefficient of the network which operates by compensated neutral.
k = I_L/I_C is the degree of adjustment of the compensation coil.

Thus in Fig. 1 is presented the variation of the modulus of the neutral displacement degree related to the adjustment degree of the compensation coil.

Its size depends on the state of adjustment of the suppression coil, reaching the maximum value (u = 0.119) for k = (2 + m)/3 = 1.043, which corresponds to the perfect compensation of the capacitive current in a network with natural asymmetry of capacities to the ground expressed by the factor m (m = 1.128). In this case the maximum voltage of neutral displacement results V_N = 1374 V.

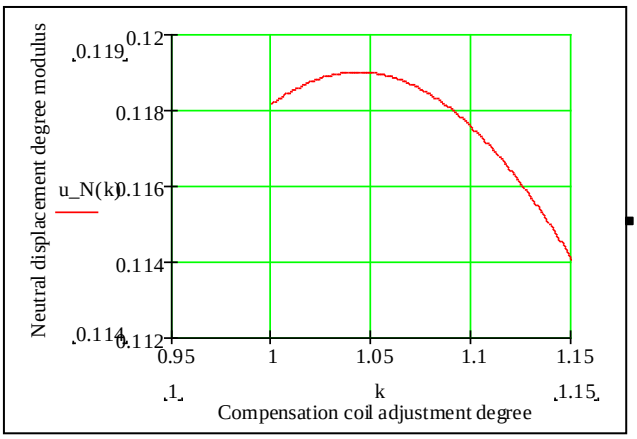

Fig. 1. Degree of displacement of the neutral depending on the degree of adjustment of the compensation coil.

The displacement voltage of the neutral V_N for the network with an overcompensation of k = 15 %, considering the net grounding results according to the graph in Fig. 1, V_N = 1316 V at a degree of neutral displacement of 0.114.

In the case of an artificial earthing, the voltage on the healthy phases with respect to the earth becomes equal to $\sqrt{3}U_{f0} = U_l$, which constitutes *the long-term overvoltage in fault stationary mode*.

In transient mode, the transient grounding overvoltage may be higher, depending on the mode of production of the defect: metallic or by intermittent electric arc. The duration of temporary overvoltages can be limited by the adjustment at resonating of the suppression coil, due to the self-elimination of defects that occur through electric arc [4], [5].

The overvoltage caused by the possible pulsation of the arc is calculated with the approximate relation (2):

$$U_{sup} = U_{f0}\sqrt{k} = 12.38\,\text{kV} \quad (2)$$

It is found that U_{sup} = 1.072·U_{f0} < 2.5·U_{f0} so it is not necessary to mount variable resistance dischargers in parallel with the compensation coil.

Consider the variation of the resetting voltage u in the production range of the electric arc (the total working time of the protection and the protection circuit breakers), according to the expression (3):

$$u(t) = U_N \cdot e^{j(\omega+\phi)}\left[1 - e^{\left(-\frac{d}{2} + j\frac{1-k}{2}\right)\omega t}\right] \quad (3)$$

where:
U_N = U_{f0} - is the rated voltage of the arc production interval, before the defect occurs.
φ = 0^0 - is the initial phase of the voltage at the time of connection, for which the overvoltage is maximum.

In the hypothesis of a perfect adjustment (1 - k = 0) an exponential dependence of the voltage is obtained that tends towards the value given by the expression (4):

$$u(t) = U_N\left(1 - e^{-\frac{\omega dt}{2}}\right) \quad (4)$$

It can be seen from Fig. 2 that the reset transient voltage (TTR) reaches the maximum value of $U_{TTR\ max}$ = 11.588 kV at t = 0.08398 s, i.e. there is an overvoltage $U_{TTR\ max}$ = 1.003·U_{f0}. The speed of increase of TTR after the current passes through zero is $(\Delta U/\Delta t)_{TTR\ max}$ = 138.579 kV/s which is higher than in the hypothesis of a perfect adjustment when it has the value $(\Delta U/\Delta t)_{TTR\ max\ perfect\ adjustment}$ = 63.312 kV/s (ΔU / Δt).

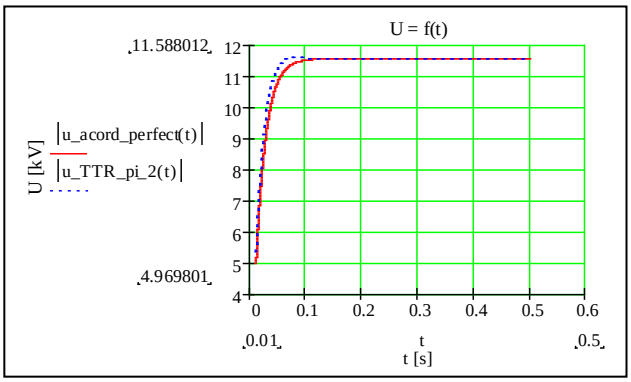

Fig. 2. Variation of the reset voltage in the interval of the electric arc production: for a perfect adjustment (red); TTR (blue).

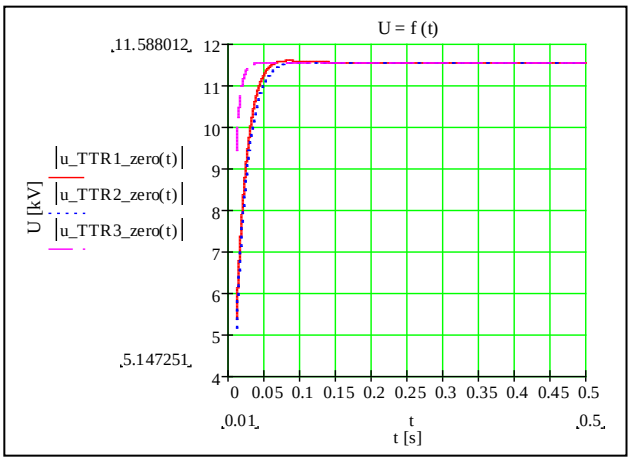

Fig. 3. Variation of the reset voltage in the interval of the electric arc production for different values of the adjustment degree: k1 = 1.15 (red); k2 = 1.1 (blue); k3 = 1.05 (magenta).

Regarding the variation of the reset voltage in the hypothesis of a perfect adjustment (1 - k = 0), it is found that it reaches the maximum amplitude equal to the phase voltage after t = 0.182 s.

From Fig. 3 it is found that the speed of increase of TTR after the current passes through zero, decreases with the decrease of the degree of disagreement and verifies the following inequalities:
$(\Delta U/\Delta t)_{TTR\ max\ k1}$ = 135.405 kV/s > $(\Delta U/\Delta t)_{TTR\ max\ k2}$ = 99.991 kV/s > $(\Delta U/\Delta t)_{TTR\ max\ k3}$ = 99.260 kV/s.

So *the compensation coil* used *ensures the extinction of the electric arc* on the one hand by reducing the grounding current I_{pp}, and on the other hand by reducing the speed of increase of the reset voltage, after the current passes through zero. In this respect, it is indicated that the degree of adjustment does not exceed (5-10) % (k = 1.05...1.1).

B. The size of fault current

The grounding current is calculated by the relation (5).

$$\underline{I}_{pp} = \underline{I}_C \sqrt{(1-k)^2 + d^2} \quad (5)$$

where:
I_C - is the capacitive current of the network which is calculated by the relation (6).

$$\underline{I}_C = 3j\omega C_p \cdot U_{f0} \quad (6)$$

where:
$C_p = l(C_A + C_B + C_C)/3$.
$1 - k$ = - 0.15 is the degree of non-adjustment of the compensation coil.

Consider that the studied network has a variable length l = (10 ... 90) km.

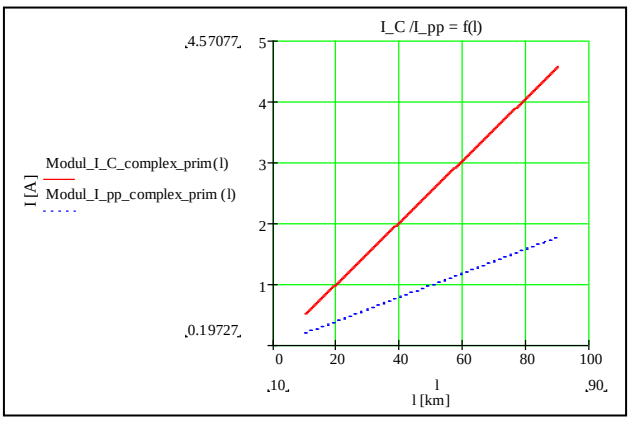

Fig. 4. Variation of the modulus of the grounding capacitive current (red) and of the grounding current (blue) depending on the line length.

From Fig. 4 it is found that, in absolute value, both the capacitive grounding current and the grounding current (at the grounding place), increase proportionally with the length of the line, but with different slopes:

- the capacitive grounding current:

$$m_{I_C} = \frac{C_A + C_B + C_C}{3}\left(3\omega \cdot \frac{U_N}{\sqrt{3}}\right) = 0.05\,\text{A/km}$$

- the grounding current (at the grounding place) (the right with a lower growth slope): $m_{I_{pp}} \approx 0.02\,\text{A/km}$.

It is also found that the current at the grounding place represents 0.388 of the capacitive grounding current, i.e. a little more than 1/3 of it and is of course inductive.

When **the grounding takes place through a resistance arc, R_{arc},** an additional depreciation coefficient denoted *dp* appears, so that the expression of the current passing in this case through the fault location I_{pp} will be:

$$I_{pp} = I_c \frac{\sqrt{(1-k)^2 + d^2}}{\sqrt{1 + \frac{2d}{dp} + \frac{(1-k)^2 + d^2}{dp^2}}} \quad (7)$$

It is found that **the residual grounding current is reduced** if the grounding takes place through a resistance arc R_{arc} = **5 Ω**, by 0.071 % compared to the case if the grounding is net.

III. Harmonic Analysis Of Waveforms Of Grounding Fault Currents And Voltages. Case Studies.

A. Fault in a 20 kV medium voltage electric network with the neutral treated through classical suppression coil without ancillary resistence and digital protections on the 20 kV cell. Case study 1.

The oscillogram of an incident (a ground fault **on the phase "A"**) that was downloaded from a numerical protection relay *SIPROTEC 4 - 7SA6* and viewed with the *SIGRA 4* software [6], [7], shows the evolution of the main analogue and binary quantities supervised by the digital protection relay, in a medium voltage electrical network, on a mixed 20 kV line (**O**ver**h**ead Power **L**ine (LEA) + **U**nder**g**round Power **L**ine (LES)) with neutral treated with + classic **S**uppression **C**oil (BS) without auxiliary resistance and digital protections on 20 kV cell. The yellow cursor is positioned on the oscillogram portion at the moment characterized by 360.5 ms (I circuit breaker connected) and the blue one at the moment characterized by 1384.8 ms (I circuit breaker disconnected).

All sizes that appear in tables or charts are reported at that time. The electrical quantities are displayed in secondary values (U, I, P, and so on). For a better analysis of the amplitude of the defect, it is useful to transform the targeted quantities into primary values.

Within the *SIGRA 4* software, a series of *visualization windows* are available, such as: **Time signals** (visualization of *analogue signals* on the time scale); **Digital signals (binary inputs)**; **Phasor diagrams**; **Viewing the harmonic content** of the circuit breaker disconnection period; **Size tables**. The harmonic content of the measured quantities can be displayed graphically as bars. In the case of the presented defect, the content of harmonics from the switching period of the circuit-breaker can be observed and also, the exact values of these harmonics that can be found in the size table presented in the viewing window from [3].

Regarding **the harmonics content of the currents in the circuit-breaker switching period** in the case of the presented fault, the following observations can be made according to [3], where Ia, Ib, Ic represent the phase currents in [A] secondary values (transformation ratio 200 A / 5 A = 40):

- These have a DC (continuous) component (≈ 52.8 A in primary value, which represents 28.2 % of the fundamental on the „A" phase on which the respective fault appeared (grounding), a value that is also found on the neutral conductor - the null of the network "G" namely ≈ 21.6 A which represents 45.4 % of the fundamental).
- Significant higher harmonics are the 2nd and 3rd order.

In Fig. 5 were graphically represented the fault currents (periodic component), in the same system of coordinate axes, using a calculation program of their own design, developed by the authors in the Mathcad programming environment.

The frequency spectra of the fault currents on the three phases and on the neutral conductor - "G" zero of the network, were synthesized during the switching period of the circuit breaker, knowing the effective values of the components from the size table provided by *SIGRA 4*.

Regarding **the harmonics content of the voltages in the circuit-breaker switching period** in the case of the presented fault, the following observations can be made according to Fig. 6, where Va,Vb,Vc represent the phase voltages in secondary values (transformation ratio 20000 V / 100 V = 200):

- The voltage on the fault phase (A) has a continuous component (≈ 14 V which represents 21.7 % of the fundamental on the phase „A" on which the respective fault appeared (grounding)), while on the healthy phases (B, C) and on the neutral "G" zero of the network, the proportions of the continuous components even if they are small, in absolute values are significant because the values of their fundamentals increase significantly).
- Significant higher harmonics are the 2nd and 3rd order.

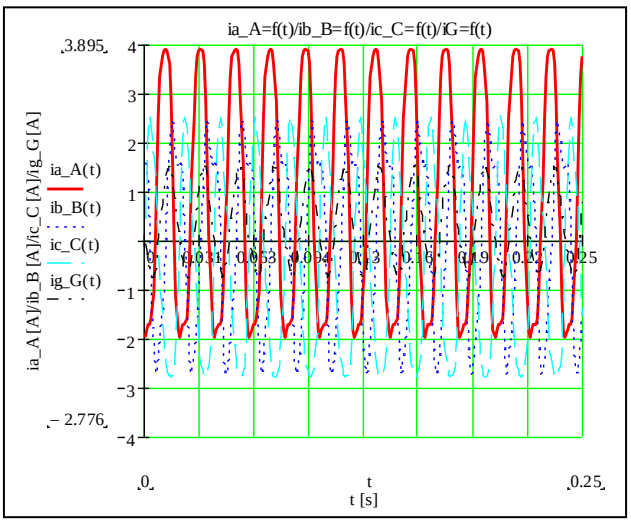

Fig. 5. The time variation of the fault currents on the three phases and on the neutral conductor - the null of the network "G", in secondary values, in the circuit-breaker switching period.

As in the case of fault currents, in Fig. 6 the fault voltages (the periodic component) were graphically represented in the same system of coordinate axes, using a similar calculation program of their own design, developed by the authors in the Mathcad programming environment.

The frequency spectra of the fault voltages on the three phases and on the neutral conductor - "G" zero of the network, were synthesized during the switching period of the circuit-breaker, knowing the effective values of the components from the size table provided by *SIGRA 4*.

It is noted that the variation of fault currents / voltages has been reconstituted over a time interval of 250 ms which represents the sum of the times required to the triggering circuit breaker of 20 kV (simultaneous opening time of the circuit breaker contacts, indicated in the catalogue, plus the breaking of the electric arc which is approximately 0.15 s for $U_N \leq 35$ kV), as well as of the intermediate relays or of the internal relays of the digital protection equipment.

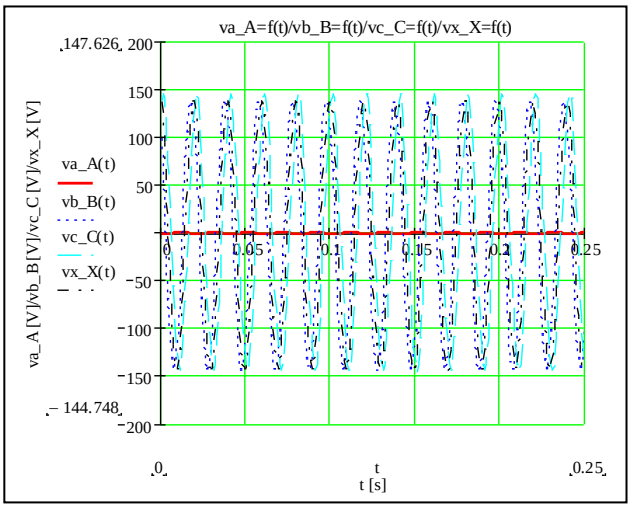

Fig. 6. The time variation of the fault voltages on the three phases and the neutral - the null of the network "G", in secondary values, in the circuit-breaker switching period.

According to [3], the first component represents the continuous component (average value of the function), then for each complex component *the amplitude - the effective (rms) value* and the argument (which represents *the phase angle (phase shift)*) *of the "k" order harmonics* were identified.

The corresponding Fourier series was written as:

$$y(t) = y_0 + \sum_{k=1}^{k=3} y_k \sin(k\omega t + \varphi_k) \qquad (8)$$

Thus, by making *a harmonic analysis* of the waveforms of the fault currents and voltages on the three phases and the neutral conductor - the "G" zero of the network, **the total harmonic distortion coefficient δ_I [%]** of the injected current in the power system and **the total harmonic distortion coefficient of the voltage δ_V [%]** were calculated, during the switching period of the circuit-breaker, using relation (9), [8], the results being centralized in TABLE I and TABLE II.

$$\delta_Y = \frac{Y_d}{Y_1} 100 = \frac{\sqrt{Y_0^2 + \sum_{n=2}^{3} Y_n^2}}{Y_1} 100 = \{\sqrt{\frac{1}{10^4}(\gamma_{y0}^2 + \sum_{n=2}^{3} \gamma_{yn}^2)}\} 100 [\%] \qquad (9)$$

where:

Y_1 - the rms value of the fault current / voltage fundamental harmonic;

Y_d - the rms value of the distortion residue of the current / voltage, obtained by suppressing the fundamental harmonic.

$\gamma_{yn} = Y_n/Y_1[\%]$ - the proportions of the *n*-order harmonics of the fault currents / voltages (the currents / voltages harmonic components on the phases and on the "G" zero of the network) and they are presented in [3].

$\gamma_{y0} = Y_0/Y_1[\%]$ it represents the proportions of the fault currents / voltages continuous components which are also presented in [3].

Regarding the fault currents, it is found that the proportions for the fundamental of the continuous com-

ponents are great, comparable in order of magnitude, with the proportions from the fundamental of the *n*-order harmonics of the fault currents.

TABLE I.
THE TOTAL HARMONIC DISTORTION COEFFICIENT OF THE CURRENT, COMPUTED ACCORDING OF THE RELATION (9).

	δ_I [%]
Phase A	**40.936**
Phase B	26.698
Phase C	36.387
The average value on the three phases, $\delta_{I\,av}$ [%]	34.673
The neutral conductor (the "G" zero of the network)	46.378

TABLE II.
THE TOTAL HARMONIC DISTORTION COEFFICIENT OF THE VOLTAGE, COMPUTED ACCORDING OF THE RELATION (9).

	δ_V [%]
Phase A	**73.529**
Phase B	3.164
Phase C	4.211
The average value on the three phases, $\delta_{V\,av}$ [%]	26.968
The neutral conductor (the "G" zero of the network)	3.943

Because of this, the harmonic distortion coefficients calculated with relation (9) have large values that also exceed the maximum allowable values imposed today by international standards.

Regarding the fault voltages, it is found that **only in the case of the fault phase (A)** the proportion relative to the fundamental of the continuous component is high, comparable in order of magnitude, with the proportions relative to the fundamental of the *n*-order harmonics of the fault voltages.

Because of this, the harmonic distortion coefficient of voltage on the fault phase A, calculated with relation (9) has a very large value that also exceeds the maximum allowable values imposed today by international standards.

It can be seen that **this fault (grounding of phase A of the 20 kV power line) can be assimilated with a strongly deforming (non-linear) consumer**.

B. Fault in a 20 kV medium voltage electric network with the neutral treated through Trench modern suppression coil and digital protections on the 20 kV cell. Case study 2.

This oscillogram shows the evolution of the main analogue and binary quantities monitored by the digital protection relay, in a medium voltage electrical network, on a 20 kV line (**O**ver**h**ead **P**ower **L**ine) with neutral treated with modern Trench Suppression Coil and digital protections on 20 kV cells, which had a grounding fault **on phase "B"**. This fault produced a grounding current whose maximum instantaneous primary value is approximate 75 A, taking into account that the transformation ratio of the measure current transformers is in this case 300 A / 5 A = 60.

In order to have a clearer view of the exact time when the power line was effectively disconnected, the cursors (sliders) can be moved on the graph at the end and beginning of the period when the current (I) is present, and the difference between the sliders is this time or the pause of RAR (**F**ast **A**utomatic **R**econnect).

Thus the yellow cursor is positioned on the oscillogram portion in the moment characterized by 1327.7 ms (Q0 circuit-breaker disconnected) and the blue one in the moment characterized by 2969.3 ms (Q0 circuit-breaker connected).

In this case, the actual time in which the power line was disconnected would result, resulting from the difference of the C2-C1 sliders calculated by the software, which means that the RAR pause set in the protection relay on this line is 2 seconds, a possible difference coming from of the time required for the switching of the 20 kV circuit-breaker, as well as for the tripping of the intermediate relays or of the internal relays of the digital protection equipment.

The triggering of the 20 kV cell took place through the cell's own protection, but through an external signal from the earthing modules related to the **Trench S**uppression **C**oil cabinet. The 20 kV **O**ver**h**ead Power **L**ine (OHL) is reconnected by RAR (**F**ast **A**utomatic **R**econnect) automation after the RAR break expires.

All data in the oscillogram are similar to those in the previous oscillogram (Section III *A*).

Regarding **the harmonics content of the currents in the circuit-breaker switching period** in the case of the presented fault, the following observations can be made according to harmonics content viewing window for: currents on the three phases - A, B, C; the current on the neutral conductor - the "G" zero of the network, provided by *SIGRA 4*:

- These have a DC (continuous) component (≈ 7.2 A which represents 6.6 % of the fundamental on the „B" phase on which the respective fault appeared (grounding), values that are also found on the neutral conductor - the null of the network "G" namely ≈ 10.2 A which represents 20.6 % of the fundamental).
- Significant higher harmonics are the 2nd and 3rd order.

In Fig. 7 were graphically represented the fault currents (periodic component), in the same system of coordinate axes, using a calculation program of their own design, developed by the authors in the Mathcad programming environment, similar to those mentioned above.

The frequency spectra of the fault currents on the three phases and on the neutral conductor - "G" zero of the network, were synthesized during the switching period of the circuit-breaker, knowing the effective values of the components from the size table presented in a viewing window similar to that presented in [3].

Regarding **the harmonics content of the voltages in the circuit-breaker switching period** in the case of the presented fault, the following observations can be made according to the harmonic content viewing window for:

voltages on the three phases - A, B, C; the voltage (potential) of the neutral conductor - the „Vx" zero of the network, similar to that presented in [3]:

- The voltage on the fault phase (B) has a continuous component in primary value (≈ 2918 V which represents 52.2 % of the fundamental on the phase „B" on which the respective fault appeared (grounding)), comparable in absolute value with the continuous components on the healthy phases (A, C). The continuous component of the neutral potential - the "G" zero of the network in absolute value has the highest value (≈ 5116 V).
- Significant higher harmonics are the 2nd and 3rd order.

In Fig. 8 the fault voltages (the periodic component) were graphically represented in the same system of coordinate axes, using a mentioned similar calculation program of their own design, developed by the authors in the Mathcad programming environment.

The frequency spectra of the fault voltages on the three phases and on the neutral conductor - "G" zero of the network, were synthesized during the switching period of the circuit-breaker, knowing the effective values of the components from the size table presented in a viewing window similar to that presented in [3].

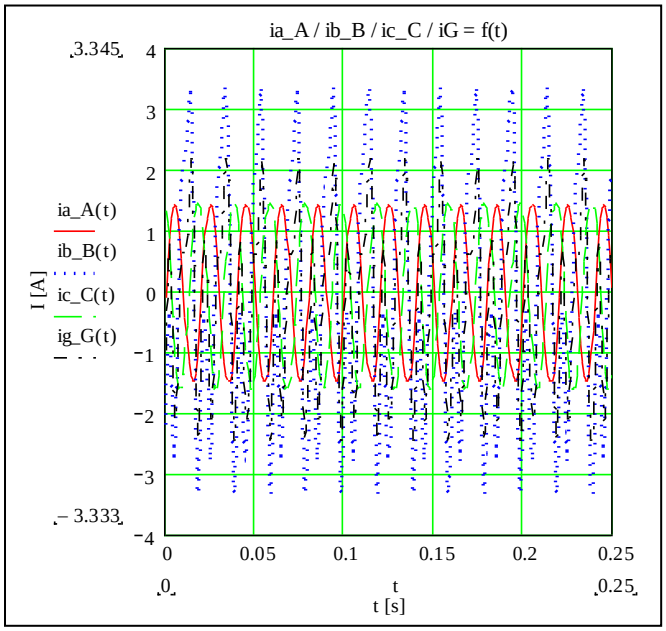

Fig. 7. The time variation of the fault currents on the three phases and on the neutral conductor - the null of the network "G", in secondary values, in the circuit-breaker switching period.

Thus, by making *a harmonic analysis* of the waveforms of the fault currents and voltages on the three phases and the neutral conductor - the "G" zero of the network, **the total harmonic distortion coefficient of the injected current δ_I [%]** in the power system and **the total harmonic distortion coefficient of the voltage δ_V [%]** were calculated, during the switching period of the circuit-breaker, using relation (9), [8], the results being centralized in TABLE III and TABLE IV.

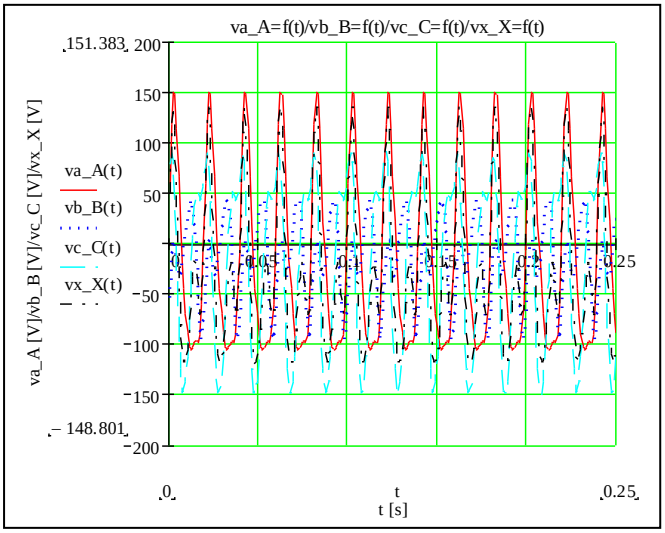

Fig. 8. The time variation of the fault voltages on the three phases and the neutral - the null of the network "G", in secondary values, in the circuit-breaker switching period.

TABLE III.
THE TOTAL HARMONIC DISTORTION COEFFICIENT OF THE CURRENT, COMPUTED ACCORDING OF THE RELATION (9).

	δ_I [%]
Phase A	5.213
Phase B	**68.067**
Phase C	6.22
The average value on the three phases, $\delta_{I\,av}$ [%]	26.5
The neutral conductor (the "G" zero of the network)	139.766

TABLE IV.
THE TOTAL HARMONIC DISTORTION COEFFICIENT OF THE VOLTAGE, COMPUTED ACCORDING OF THE RELATION (9).

	δ_V [%]
Phase A	38.236
Phase B	**115.666**
Phase C	42.508
The average value on the three phases, $\delta_{V\,av}$ [%]	65.47
The neutral conductor (the "G" zero of the network)	101.323

Regarding the fault currents on the phase B (fault) and on the neutral conductor (the "G" zero of the network), it is found that the proportions from the fundamental of the continuous component and these of the fault currents *n*-order harmonics are greater then these on the healthy phases (A, C).

Because of this, the harmonic distortion coefficients calculated with relation (9) **on the phase B (fault)** and on the neutral conductor (the "G" zero of the network) have very large values that exceed the maximum allowable values imposed today by international standards.

Regarding the fault voltages, it is found that **in the case of the fault phase (B)** and of the neutral conductor potential (the "G" zero of the network), the proportion relative to the fundamental of the continuous component is high, comparable in order of magnitude, with the proportions relative to the fundamental of the *n*-order harmonics of the fault voltages.

Because of this, the harmonic distortion coefficient of the voltage on the fault phase B and of the neutral conductor potential (the "G" zero of the network), calculated with relation (9) have a very large value that also exceed the maximum allowable values imposed today by international standards.

IV. CONCLUSIONS

We started from the importance of the way of treating the neutral that determines in certain conditions the appearance of overcurrents or overvoltages.

In this sense, *the authors used programs specially designed by them*, developed in the Mathcad programming environment, which allow the quantitative solution of the problem of neutral displacement, the calculation of grounding currents in the fault place for different scenarios such as net grounding or through an electric arc having a certain resistance.

From the comparative harmonic analysis of the waveforms of the fault currents and voltages from *the two case studies* presented above, namely faults in 20 kV medium voltage electrical networks with neutral treated with *conventional suppression coil without auxiliary resistance or Trench modern suppression coil* and digital protections on the 20 kV cell, the following conclusions can be drawn:

- For the *Case study 1*:

a) The total harmonic distortion coefficient of the fault current, according to TABLE I, records the highest value on the neutral conductor ("G" zero of the network) comparable to the value calculated for the fault phase A (by ≈ 11.7 % higher). The value of this coefficient for the fault phase A is higher than the values calculated for the healthy phases (than in phase B ≈ 1.5 times higher, than in phase C ≈ 1,125 times higher) so comparable to them, but all these values exceed the limits imposed by the specialized standards.

b) The total harmonic distortion coefficient of the fault voltage according to TABLE II, records the highest value on the fault phase A, while the values of this coefficient are at least an order of magnitude smaller for the healthy phases (on phase B - of ≈ 23.24 times lower, on phase C - ≈ 17.46 times lower) and for the neutral conductor ("G" zero of the network) ≈ 18.65 times lower, being just below the limits imposed by the specialized standards.

- For the *Case study 2*:

c) The total harmonic distortion coefficient of the fault current according to TABLE III, records the highest value on the neutral conductor ("G" zero of the network), higher than ≈ 2.05 times than the value calculated for the fault phase B. In the fault phase B the value of this coefficient is one order of magnitude higher than the values calculated for the healthy phases (≈ 13 times higher than in phase A, ≈ 10.9 times higher than in phase C), so that the values calculated for the healthy phases are just below the limits imposed by the specialized standards.

d) The total harmonic distortion coefficient of the fault voltage according to TABLE IV, records the highest value on the fault phase B, comparable to the value calculated for the neutral conductor ("G" zero of the network) - higher by 12.4 %, while the values of this coefficient are by an order of magnitude smaller for the healthy phases (on phase A - ≈ 3 times lower, on phase C - ≈ 2.7 times lower) but being above the limits imposed by the specialized standards.

ACKNOWLEDGMENT

This work was supported by Distributie Oltenia (https://www.distributieoltenia.ro/ https://www.cez.ro/ro).

We thank Distributie Oltenia - Craiova not only for the consistent support of this work, but also for providing data and generously making available their valuable expertise in the field of medium voltage electrical networks used for the distribution and supply of electricity to consumers in the national power system.

Source of research funding in this article: Research program of the Faculty of Electrical Engineering financed by the University of Craiova.

Contribution of authors:
First co-author – 40%
Second co-author – 20%
Third co-author – 20%
Fourth co-author – 20%
Received on July17, 2021
Editorial Approval on November 12, 2021

REFERENCES

[1] *** Neutral treatment of medium voltage electrical networks, The technique of high voltages - laboratory works, 2005 (in Romanian).

[2] M. Guşă, M. Istrate, N. Gavrilaş, and C. Asaftei, *The technique of high voltages - Overvoltages in electric power systems*, Romanian Renaissance Cultural Foundation Publishing House, 1997, pp. 186 - 221 (in Romanian).

[3] S. M. Digă, V. Năvrăpescu, N. Digă, C. Bratu, and P. M. Mircea, "Considerations on the Harmonic Regime Produced by the Faults Appeared in the Medium Voltage Networks with the Neutral Treated by Extinguishing Coil," *Proceedings of International Conference on Applied and Theoretical Electricity (ICATE 2021)*, May 27-29, 2021, Craiova, Romania, https://ieeexplore.ieee.org/document/9465063, ISSN Information: Electronic ISSN: 2688-0962, Print on Demand (PoD) ISSN: 2376-4163.

[4] *** Instruction manual EPSY Earthfault System Electronic Components – TRENCH.

[5] *** Methods for detecting homopolar faults in networks with compensated neutral, Protection, Automation & Control, PROTECTA Hungary, https://www.protecta.hu/, 09 November 2017.

[6] *** *SIPROTEC 4 - 7SA6 (SIEMENS) Remote Protection Relay Guide* (in Romanian).

[7] D. Dragomir, SIPROTEC 4 - 7SA6 - Remote Protection Relay for all voltage levels, C.E. 110 kV Craiova (in Romanian).

[8] M. Chindriş, A. Cziker, and D. D. Micu, *Power quality management applications*, MEDIAMIRA Publishing House, Cluj-Napoca, 2000 (in Romanian).

Experimental Study of HBC Fuses with Aluminum Fuse Element at Minimum Rated Breaking Current, Maximum Rated Breaking Current and Transfer Current of Fuse-Switch Combination

Cristian-Eugeniu SALCEANU[*], Marcel NICOLA[*], Daniel OCOLEANU[*], Daniela IOVAN[*], Sorin ENACHE[†]

[*]National Institute for Research, Development and Testing in Electrical Engineering - ICMET/Research Department, Craiova, Romania, csalceanu@icmet.ro, marcel_nicola@yahoo.com, pramlmp@icmet.ro, pdaniela@icmet.ro

[†]University of Craiova/Faculty of Electrical Engineering, Craiova, Romania, senache@em.ucv.ro

DOI: 10.52846/AUCEE.2021.1.10

Abstract **- The article presents an experimental study of high breaking capacity fuses with aluminum fusible element with and without a eutectic point, at minimum rated breaking current, preceded by experiments at maximum rated breaking current. The paper shows that in the construction with aluminum fusible element, the fuse has no problem breaking the maximum rated breaking current, but real difficulties appears when it comes to the minimum rated breaking current. The experiments were made on a homogeneous series 6-20 A, with a focus on the 36 kV, 25 kA, 16 A fuse. The fuses suffered multiple construction changes and tests with and without a eutectic point. After several tests was found an acceptable constructive solution was, but the obtained value for the minimum rated breaking current is not a commercially attractive value. It was also tested the capacity of the fuse to transfer the breaking duty to a load break switch.**

Cuvinte cheie: *siguranțe cu mare putere de rupere, current de rupere, fuzibil, arc intern, serie omogenă.*

Keywords: *high breaking capacity, breaking current, fuse, internal arc, homogeneous series.*

I. INTRODUCTION

Generally considered to be an elementary protection device, fuses are used to prevent disturbances caused by power currents in electrical circuits. Generally, an electrical fuse is an electrical conductor that melts under the action of power currents, cutting-out the electric current of the protected circuit. This article presents experiments performed on fuses belonging to the current-limiting fuses category. The fusible element of these high-breaking capacity fuses (HBC fuses) doesn't use silver, but 99% nickel-plated aluminum. The last set of experiments were conducted on fuses with fusible elements made of 99% nickel-plated aluminum, with a silver eutectic point. The paper shows that the HBC fuse is able to break the maximum rated breaking current, but difficulties appear at the minimum rated breaking current. Without the application of a eutectic point, an acceptable current cannot be broken. For the initial study of the phenomenon, a large number of reference fuses were made, considering previous research [1-3], each consisting simply in a length of silver fusible element housed in a ceramic tube that was filled with silica quartz and sealed at the ends. Silica quartz is the most frequently used filler material and its role has been comprehensively investigated. Granules of approximately equal size were used to fill the fuse cartridges. The inner and outer caps were made from aluminum and plated with tin. The end cap assembly sealed the fuse cartridge efficiently in order to prevent ingress of moisture and aid satisfactory operation of the fuse during short circuit and low over current fault conditions. The shape of the cartridge was tubular, this choice has an effect on the minimum fusing current and the mechanical strength of the fuse. The cartridges were checked to be sure they have good electrical insulating properties in addition to good thermal conducting properties. They were also non-porous and capable of withstanding significant thermal and mechanical shocks. Each component of the fuse assembly influences the overall performance of the high breaking capacity fuse. The properties of each component are carefully chosen to collectively control fuse operation for a particular application and can be subdivided and analyzed under the classifications of material, physical, objective and transient properties. Due to the numerous applications of fuses, their physical attributes such as size, shape and methods of constructions vary widely and are referred to as physical properties. The overall fuse-operating characteristic is derived from the individual component characteristics. Consequently, the operating response with respect to the time of a component may be referred to as its objective or transient properties [9]. All the samples were identical, only that a group contained a plain simple fusible and the other group had a globule of solder on the center of the fusible element.

Over time research has displayed in obtained current/operating time curves [4-5], that the minimum fusing current for the fuses with the solder globules was only about 60 per cent of that of the plain fuses. It turned out that the temperature rise necessary to melt the fusible with silver globule was only about 345°C, that is $(0.6)^2$ times the melting point of silver, being assumed that the heating effect was proportional to the square of the current. Further experiments in which the current was raised in small increments and steady temperatures being allowed to develop after each increment, shown a change when the globules melted.

The globules soon became red hot in spite of the fact that the wires adjacent to them remained unchanged in appearance. For a very short time, the globules glowed red and clearance was affected by the silver wires rupturing besides the globules. Subsequent examinations proved the brittleness of the silver wire in contact with solder, the wire broke immediately when touched.

Experiments resumed, but this time the currents were interrupted before the fusible melted. It was found that the resistances of the fusible passing through the globules increased by 100% per whereas the fusible without globule showed no measurable increase in resistance on cooling. The above researches were made by Metcalf; therefore, our research has focused on the rated minimum breaking current I_3, a limit value that cannot be exceeded in order to ensure that a high breaking capacity fuse will trip an electrical circuit.

In the event of an MV (medium voltage) short-circuit, the simple action of a high breaking capacity fuse blowing will not cut-out the current. For values of current less than the minimum rated breaking current, the fuse blows, but cannot break the current: the arc remains present until the current is cut by external intervention. Therefore, under no circumstances should a fuse assembly be used in the zone of I_N and I_3 [6-8]. The values of I_3 are generally between 2 and 8 I_N [9-15].

The presented article is based on [16]. The rest of the paper is organized as follows: Section II presents the construction of the experimental device (fuse) with versions for the homogeneous series 6-20 A, Section III presents the experiments made at the maximum breaking current, while Section IV presents the experiments made at the minimum breaking current. Conclusions are the final section.

II. Experimental Device and Test Conditions

A. *Experimental fuse*

The experimental fuse presented in Fig. 1 was designed to reproduce the phenomena occurring in high breaking capacity (HBC) industrial fuses. The fusible element is made of 99% nickel-plated aluminum, 1700 mm long and 0.08 mm thick, with various widths and design variants, presented in Fig. 2.

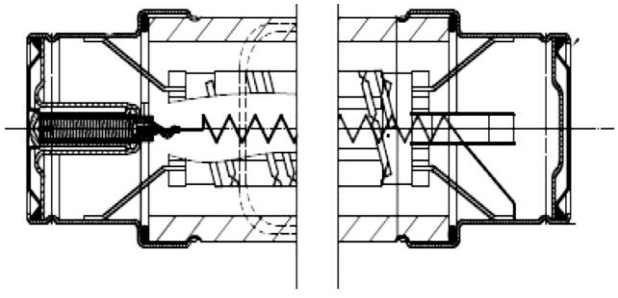

Fig. 1. Section drawing of experimental HBC fuse

High breaking capacity fuses may contain a single element or multiple elements connected in parallel. The elements most often have several areas of varying width referred to as “constrictions or notches”. A single element may have parallel notches or “bridges”. The objectives of the notches are to create areas of maximum current density and thus induce melting and subsequently arcing initially within the center location of the notch [9].

The ceramic envelope was filled with silica quartz (98% SiO_2 and 2% impurities Na_2O, K_2O, CaO) with a grit size of less than 300 µm. Particular attention was paid to sand granulation, drying and filling process, because the physical processes occurring during fuse operation are closely related to the morphometric properties of sand which influence temperature and electron density [9-13].

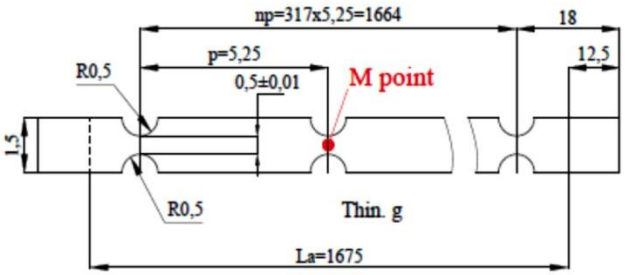

Fig. 2. Draft of the fuse element

Fig. 2 shows the variants of the design of the fusible element made for the experiments. Generally, the geometry of the fusible element is variable and may consist of wires or ribbons. HBC fuses may have a single or multiple fusible elements connected in parallel. In our experiments, we used a 2- parallel wire construction with constrictions or notches. Notches create areas of maximum current density and thus induce melting and subsequently arcing, initially within the central location of the notch.

For their execution were used precision molds to meet the imposed tolerances and to ensure the execution of any necessary quantity of identical elements. Table I presents four design variants for the homogeneous series 6-20 A. The monotonic equation imposed by IEC 60282-1; chapter 6.6.4.1 can be noted. The tested fuses have the same rated voltage U_r = 36 kV, breaking current I_1 = 25 kA, and the minimum breaking currents vary between 6 and 20 A. For experiments, fuse V03 was chosen with 2 fuse elements connected in parallel, 36 kV, 20 A, 25 kA.

TABLE I. Fuse Element Design Variants

Vers.	Thin g [*mm*]	n	p [mm]	R [mΩ]	I_n [A]	No. of elements
V01	0.04	317	5.25	884.42	6	2
V02	0.06	317	5.25	589.6	10	2
V03	0.1	317	5.25	353.76	16	2
V04	0.14	317	5.25	252.68	20	2

Fuse designs are closely related to applications. For new designs some parameters can be derived from mathematical models but, in general, prototype fuses have to be manufactured to enable precise characteristics to be determined by practical testing. Rapid fuse operation and current interruption are expected with this design.

The time period from the instant of fault current to the instant of element vaporization is minimized by using materials with low specific heat capacities, low melting and low vaporization temperatures. A key feature is that the energy let through to the protected circuit during this time period is minimized.

B. Experimental circuit and operations

Fig. 3 presents the circuit used for experiments. The circuit reproduces as closely as possible the most severe conditions encountered during operation. The represented G source is a 2500 MVA synchronous generator capable of supplying the current passing through the fuse under test, 2 step-up 80 MVA transformers (TF), with a magnetic circuit specially designed to reduce the capacitances, both on the primary and on the secondary. Z1 reactor whose proportion in the circuit calculation is of 15% and it is not susceptible to saturation, is inserted on the supply side. The reactance of the circuit, which may be the reactance of the transformer or the reactance of the transformer-reactance assembly must be shunted with a resistance R_p of a value sensibly equal to 40 times the reactance value. However, if this reactance value does not lead to at least critical damping, it must be reduced until critical damping is obtained. Critical damping is obtained when:

$$R = \frac{1}{2}\frac{f_0}{f_N} X \tag{1}$$

where: f_0 - is the inherent frequency of the circuit with no additional damping; f_N - is the power frequency; X - is the reactance of the circuit under power frequency.

MB1, MB2 and MM1 are high-precision switching pieces of equipment ensuring the desired connection, automatically programmed connection or, in case of failure, disconnection.

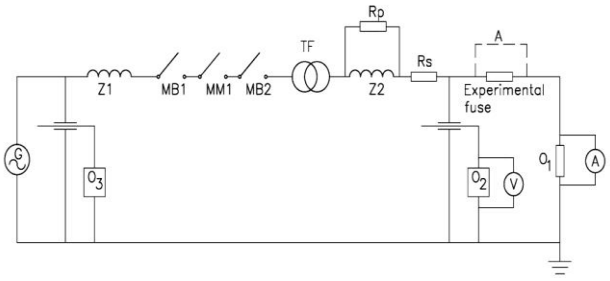

Fig. 3. The circuit used for experiments

The load side consists of resistive elements (R_s) and inductive elements (Z_2) for the adjustment of the power factor. The circuit allows a resistive load with values up to 189 Ω, and the inductive load consists of reactors with values between 5 and 2800 mH which cannot be saturated. A power factor between 0.1 and 0.9 can be obtained by adjusting the values of the resistors and reactors. The over-voltage protection has been chosen so that no ignition should occur during normal fuse operation. Each operation was performed with a phase angle of the electrical fault φ controlled and set by the operator and was achieved by using a high-precision sequential programmer that controls each switching device in the circuit; it is necessary to operate MM1 - Fig. 3, in order to ensure the phase angle of the current.

C. Calibration of the circuit

To check the feasibility of the testing parameters, the fuse was replaced by a dummy (copper rod) that was inserted in the fuse holder. The prospective value of the phase angle of the electrical fault φ was obtained by measuring the phase angle between the test voltage and the prospective current, corresponding to the fault current. The prospective value of the power factor is obtained from the equation:

$$\cos\phi = \frac{R}{\sqrt{R^2 + L^2\omega^2}} \tag{2}$$

Where R and L are the resistive and inductive components of the circuit load, and ω is the angular frequency at 50 Hz.

III. Validation of the Experimental Fuses at the Maximum Rated Breaking Current

I_1, or the maximum breaking capacity is the maximum prospective fault current that the fuse is capable to break. Therefore, it's essential to ensure that the line short-circuit current is at least equal to the current I_1 of the fuse. In real-life situations, in the event of a short-circuit current, the link blows within several milliseconds. A peak arc voltage immediately occurs and because it is higher and opposes the generator voltage, it reduces the current value. The fuse acts as a variable resistance is almost equal to zero when the fusible blow and then increases until it reaches the current zero point while modifying the value of the current and the lag between this value and the generator voltage [14].

The experiments were carried out for the following parameters: 0.87 x rated voltage (36 kV) with + 5% tolerance, power factor between 0.07 and 0.15 at the prospective current (r.m.s. value of the periodic component) of 25 kA. Making angle of short-circuit current is from 0° to 20° after the voltage crosses zero. The initiation of the arc after voltage crosses zero was performed for a test with an angle between 40° and 65°, and for two tests the angle was between 65° and 90°. The voltage was maintained after breaking for at least 15 seconds.

During the operation, a wide variety of fuse stresses can occur and these experiments were aimed at reproducing the strictest requirements, especially in terms of the energy of the arc.

The circuit in Fig. 3 was used, with no load, zero value of R_p, Z_z and R_s. The value of the reactance Z_1 was < 100 mΩ. To adjust the transient recovery voltage, connected capacitors were inserted into the circuit to obtain 0.8 μF and a resistance of 40 Ω.

After modelling the circuit to obtain the parameters of the transient recovery voltage, the graphic record in Fig. 4 was obtained.

It has been taken into account the fact that the current limiting fuses are not sensitive to the characteristics of the TRV (transient recovery voltage) unless a very high arc voltage is reached immediately after arc initiation, the circuit characteristics and the time of arc initiation between 65° and 90° being intended to simulate the most severe situation encountered in operation. During the tests, within a time interval less than or equal to 2 x t_3 after arc initiation, the arc voltage did not reach the highest peak value, so the tests were considered adequate.

Fig. 5 shows the waveform of the current during calibration, with the overlapped waveform of the maximum rated breaking current.

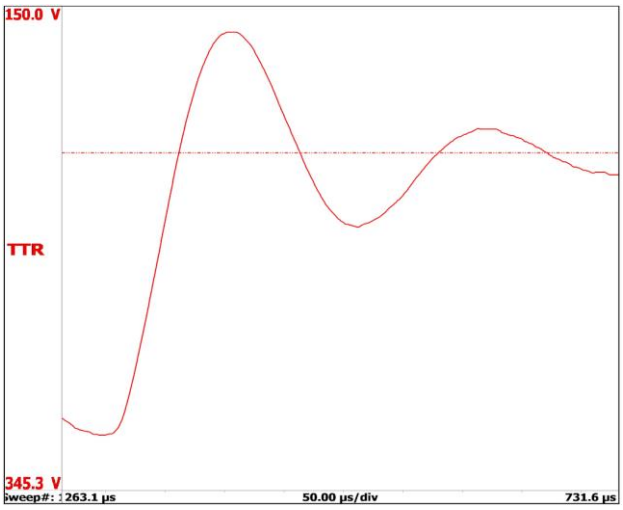

Fig. 4. Prospective transient recovery voltage with two parameters envelope, which corresponds to the imposed parameters (rate of rise Uc/t_3=0.59 kV/µs)

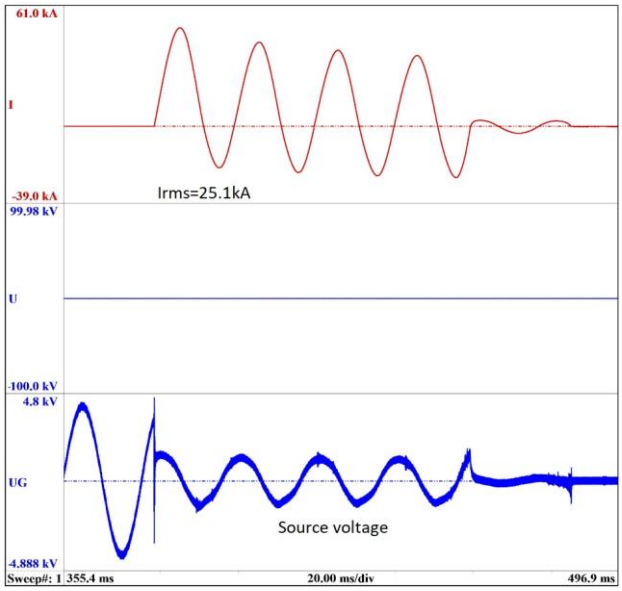

Fig. 5. Graphic record of the prospective current during calibration

In Fig. 5 the U_G voltage represents the source voltage before the step-up transformers with a value of 4.41 kV. The U voltage with zero value during calibration measured with O_2 voltage divider as presented in Fig. 3.

Three fuses were tested at various phase angles of the current, and Fig. 6 presents the waveforms obtained for a 16 A fuse with a resistance of 269 mΩ. The values obtained for this high breaking capacity fuse are: applied voltage 32.7 kV; phase angles of the current: 77.9° el; phase angles of the arc: 80.9° el; limited current: 2.1 kA; recovery voltage: 32.5 kV; total energy - Joule integral: 1.6 kA^2s.

For I^2t high-precision calculation under the curve in Fig. 6, the following formula was used:

$$I^2t = \left[\left(\sum_{n=n_1}^{n_2} y^2(n)\right) - \frac{y^2(n_1)+y^2(n_2)}{2}\right]\cdot \Delta x \quad (3)$$

In equation (3), n_1=first sample, n_2=last sample, and Δx=difference between two samples, y(n) represents the value of y function in each n sample. The numerical integration is performed by assuming the linear interpolation of the squared curve between the samples.

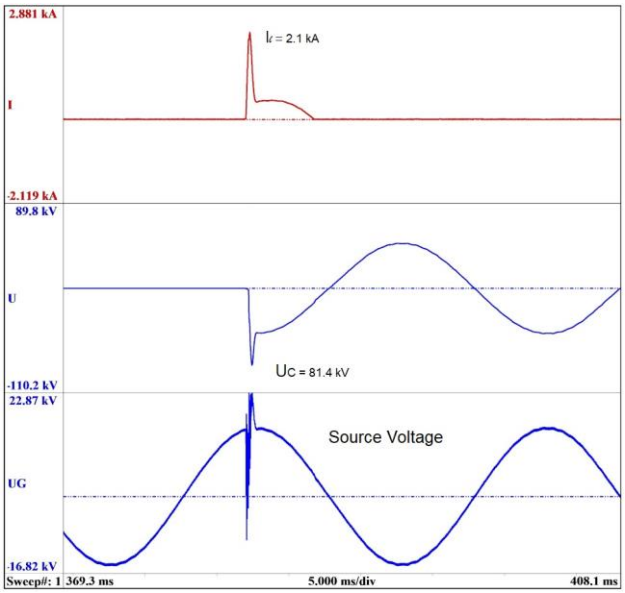

Fig. 6. Graphic record of the maximum rated breaking current

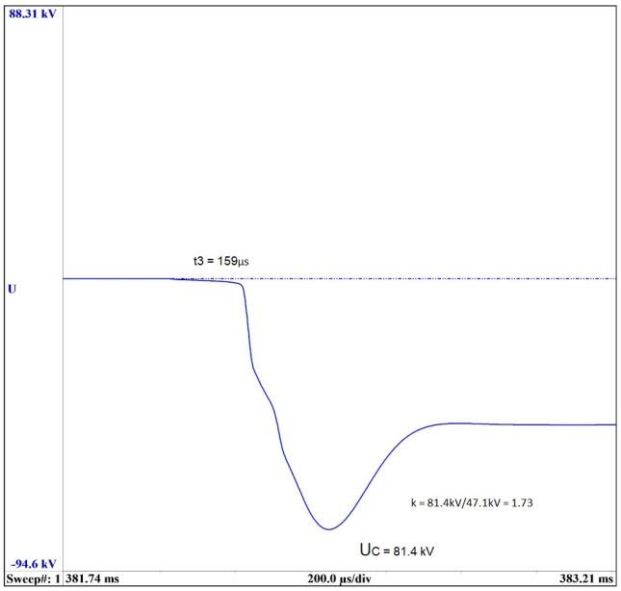

Fig. 7. Graphic record of the transient recovery voltage

Fig. 7 shows the detail of the TRV in Fig. 6. The value of the peak of voltage U_c= 81.4 kV, compared to the prospective value of 62 kV and t_3 (rate of rise) of 150 µs. The hot particles resulting under the action of the arc in the first milliseconds after the current zero passing are still in a conductive state and this conductivity results in additional damping of the transient phenomena of the recovery voltage.

The values obtained in this experiment are higher than expected, but the fuse behaved accordingly. The value of the damping is proportional to the impedance of the circuit:

$$\sqrt{\frac{L}{C}} = 2\pi f_0 L \quad (4)$$

The limited current is 2.1 kA as stated in Figure 5. The obtained peak recovery voltage U_C is 81.4 kV compared with a minimum of 63 kV imposed by IEC 60282-1 standard. The circuit was calculated for a value of 62 kV.

The transient phenomena at high inherent frequency f_0 are much more damped than those at a lower inherent frequency. These transient low-frequency phenomena are maintained for a longer time and, because they overlap the recovery voltage at power frequency, subject the melted element to additional voltage stress.

According to the results obtained above, it is concluded that the fuse is capable of breaking the current under the most severe operating conditions.

IV. Experiments at the Minimum Rated Breaking Current

The experimental tests at rated breaking current were performed at the rated fuse voltage with a margin of +5% and a power factor between 0.4 and 0.6 [15]. The breaking current shall be the r.m.s. value of the periodic component of the current, measured at the time of arc initiation during the breaking test. The experiments were performed on high breaking capacity fuses with the highest rated current because this test is not required in the standards if the I3/s ratio of any fuse in the homogeneous series is smaller than that of the tested fuse.

For the tests presented below was used the circuit in Figure 3. Its parameters were calculated to obtain a prospective current between 100 and 200 A. The reactance used for the supply side is Z1= 1200 mΩ and Z2= 330 mH series connected with Rs= 60 Ω are used on the load side. For the presented graphic record, in the parameters of the circuit calculation cos φ = 0.5 was used, while the values at the source are 9 kV and 50 A, and the transformation ratio used is k = 4.28.

The fuse has to be capable of breaking any current between the minimum value of the breaking current and the maximum short-circuit current. One of the qualities of fuses, commercial appealing, is that the value of the minimum breaking current is close to the value of the rated current.

Usually, the minimum breaking current is between 4 and 8 rated current, and this value must be validated by tests. There is no maximum value of the maximum breaking current imposed in the standards however, a small value is appealing and can be a criterion in the specification. At the beginning of the experiments, we started from a current value resulting from the calculation: 6 x IN, while the calibration current is 100 A. The obtained graphic record is presented in Fig. 8.

In any switching device after the arc occurrence, for the arc extinguishing operation to be successful, is necessary that the curve of the dielectric strength does not intersect with the curve of the supply voltage. Any intersection of the two curves involves the re-ignition of the arc and often the increasing of its duration beyond the limits withstood by the fuse leads to fuse breaking and blowing out.

In Fig. 8 it can be noted that the arc occurs after 3100 ms from the initiation of the current, the arc voltage increases with the tendency to become the power frequency recovery voltage, but the dielectric strength of the fuse does not increase fast enough, so the arc re-ignites countless times, causing high arc energy and thus the blow-out of the fuse.

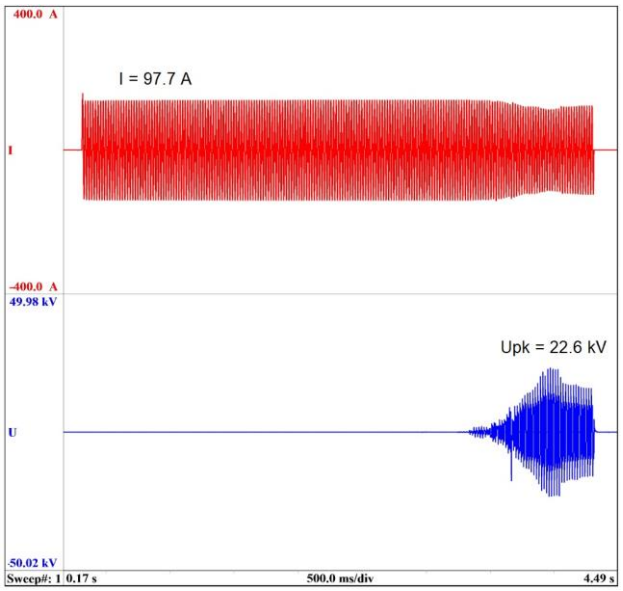

Fig. 8. Graphic record of the test 36 kV, 100 A

An important part is also played by the pre-arcing time (elongation), for its entire duration the fuse is heated and the conditions for arc extinguishing change, the longer it lasts, the more difficult the breaking becomes. By analyzing the scraps of the fuse, it was concluded that one of the fusible wires of the fuse broke (according to the graphic record at 3200 ms), but this was not enough for the fuse to break the current.

The next step consisted in modifying the test circuit to ensure a prospective current of 130 A, and the resulting graphic record is shown in Fig. 9. The pre-arcing duration decreased to 1900 ms, but the internal processes in the fuse body were repeated, and the fuse blew out.

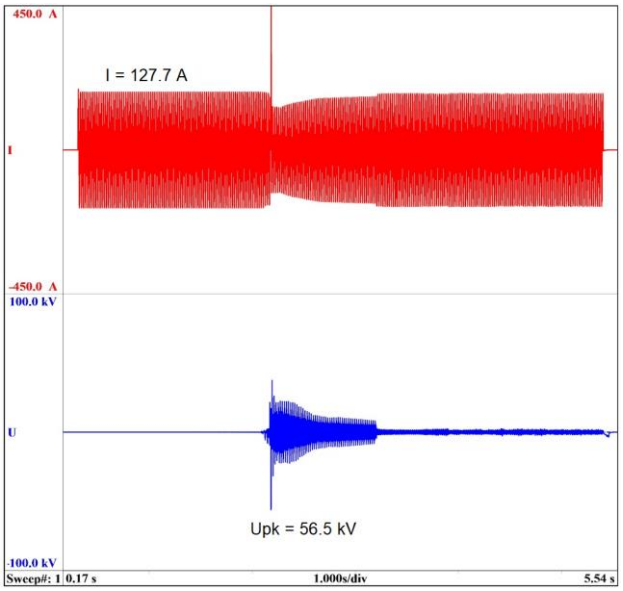

Fig. 9. Graphic record of the test 36 kV, 130 A

A conclusion for the exact cause could not be taken, many phenomena are associated with the disintegration of electrical conductors. Consequently, the disintegration of electrical conductors and significantly the disintegration of fuse elements need to be categorized relative to criteria of specific phenomena to clarify the arcing behavior.

There are three categories associated with fuse element explosions: slow, fast and super-fast [9].

After analyzing the fuse element disintegration, based on the magnitude of current density, in the range 10^1~10^4A/mm^2, we can categorize it as fast. Super-fast explosions of electrical conductors in practice are not feasible due to the inherent inductance of practical circuits [3]. Further, the test current was not increased, because its value had already exceeded 8 x I_N = 128 A. The fusible element was modified, by adding a eutectic point M in the middle (Fig. 2).

This solution was not initially used, because the fuse becomes sensitive to temperature rise tests and to the maximum breaking current. This technique, named after AW Metcalf [5] adds a point from another alloy on the fuse element, in a sensitive spot. The eutectic temperature is lower than the melting temperature of the fuse element, which leads to a cut-off at lower currents.

Tests were performed starting with 2 x I_N = 32 A, and, although the times obtained were shorter than those preceding the addition of the eutectic point M, the tested fuses failed to break the applied current.

The first successful test was obtained at a prospective current of 150 A, and is shown in Fig. 10.

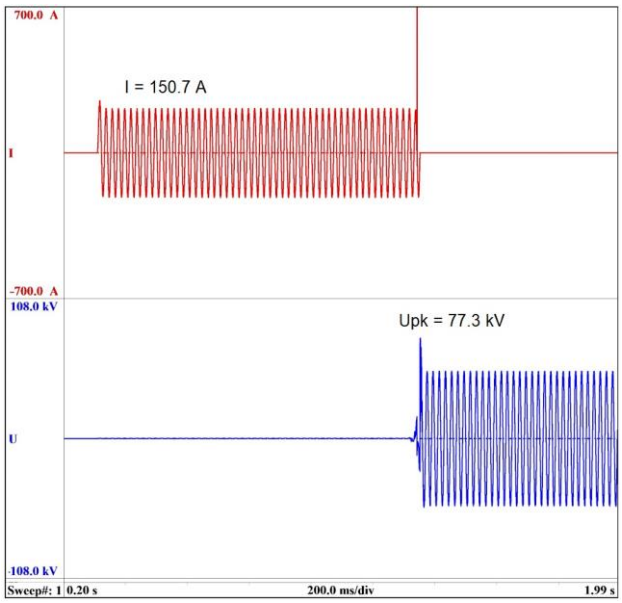

Fig. 10. Graphic record of the test 36 kV, 150 A

As seen in Fig. 10, after 1000 ms of pre-arcing, the current is successfully broken and the power frequency voltage is restored. When the arc current passes zero a surge occurs, however, due to the dielectric strength created inside, the fuse withstands this surge successfully.

The values obtained are the following: I=150.7 A; Joule integral on pre-arcing I^2t_{pa}=23.11 kA^{2}s, Joule integral on arc period I^2t = 23.99 kA^{2}s, operating time t=1.04 s; arcing time t_{to}=0.027 s.

V. Experiment on an Assembly of Switches and High Breaking Capacity Fuses

Fig. 11 presents a simplified circuit of an assembly of switches and HBC fuses capable of breaking at rated voltage (36kV) any current up to and including the rated short-circuit current. It is also capable of making but this was not verified during this experiment.

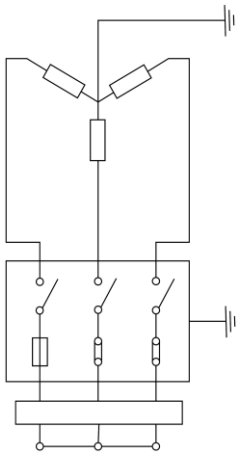

Fig. 11. Arrangement of the test circuit

The fuses are incorporated in this assembly in order to extend short-circuit breaking rating beyond that of the switch alone. The HBC fuses are fitted with strikers in order both to open automatically all three poles of the switch on the operation of a fuse and to achieve a correct operation at values of fault current above the minimum melting current, but below the minimum breaking current of the fuses. The purpose of the experiment is to check if the values obtained in previous experiments are enough for a safe operation of the load break switch in case of fault. For this, the specific mechanism of the load break switch was disabled. The load break switch could only be operated by the action of the fuse's strikers.

The earthing switches were in the open position and a Ø 1 mm copper wire was tied across all three phases downstream the fuses to simulate a fault and to produce an internal arc. The link between the HBC fuse strikers and the switch release must be such that the switch operates satisfactorily under both three-phase and single-phase conditions at the minimum and maximum requirements of the striker, no matter of the method of striker operation.

The assembly in Fig. 12 was designed so that the combination of fuse-switch will perform satisfactorily at all values of breaking current from the rated maximum breaking current of the switch down to the minimum melting current under low over-current conditions. To prove the time coordination between the switch and fuse, the fuse initiated opening time must be shorter than the maximum arcing time the fuse can withstand, values obtained in previous experiments [16].

The experiment should have been connected in a circuit having the neutral point of the supply isolated and the neutral point of the three-phase short-circuit earthed. Given the capacity of the test site, this condition could not be done so, the supply was earthed and the three-phase short circuit was isolated, as shown in Fig. 11.

Fig. 12. Assembly of HBC fuses and in the upper part LBS

For the first test, with the circuit from Fig. 11, the high breaking capacity fuses from two poles were replaced by solid links of negligible impedance, having the same shape, dimension and mass of the high breaking capacity fuses they replace. The circuit consisted of a three-phase supply and load circuit (L-R series). The supply circuit had a power factor lower than 0,2, the impedance of ~15% of the total impedance of the circuit. The prospective TRV of the supply circuit under shorts-circuit condition was in concordance with the one used in Chapter III.

The fuse worked properly, as can be observed in Fig. 13, the fuse managed to open the LBS. Values obtained $I_{1,2,3}$=620A, where I_2 is the current limited by the fuse, the fuse cut the current after 16,2 ms and after 77,7 ms the LBS also break the current, which is near the no-load opening time of the LBS. The recovery voltage was the rated voltage divided by 2. The TRV peak voltage U_C=60kV with a rate of U_C/t_3=0,3kV/µs. Next, three new fuses were inserted and short-circuit made with Ø 1mm copper wire downstream the fuses. The prospective applied voltage is 36 kV with 20 kA, for 1 s. To obtain a peak current the closing of the master maker was delayed for 2.7 ms (Fig. 14).

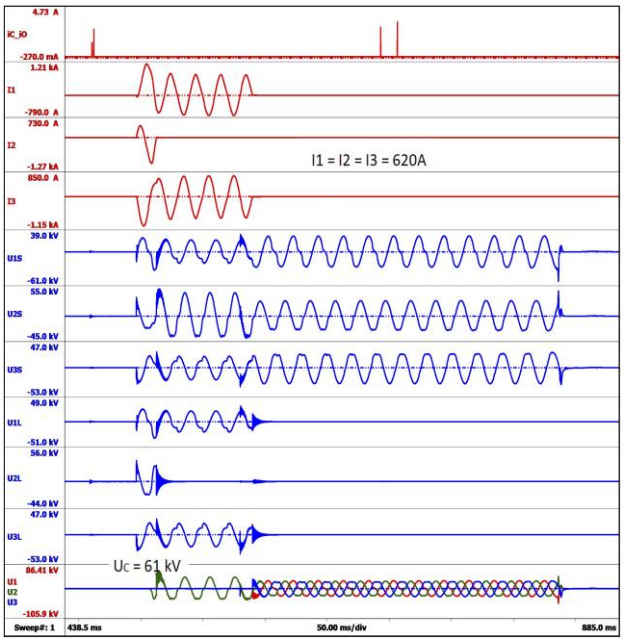

Fig. 13. Graphic record of the test with prospective values 36 kV, 630 A

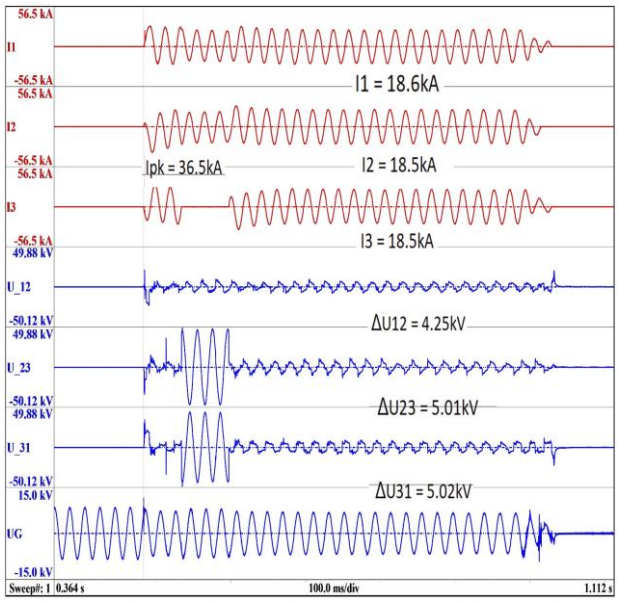

Fig. 14. Graphic record of the test with marker on the 2.7 ms delay

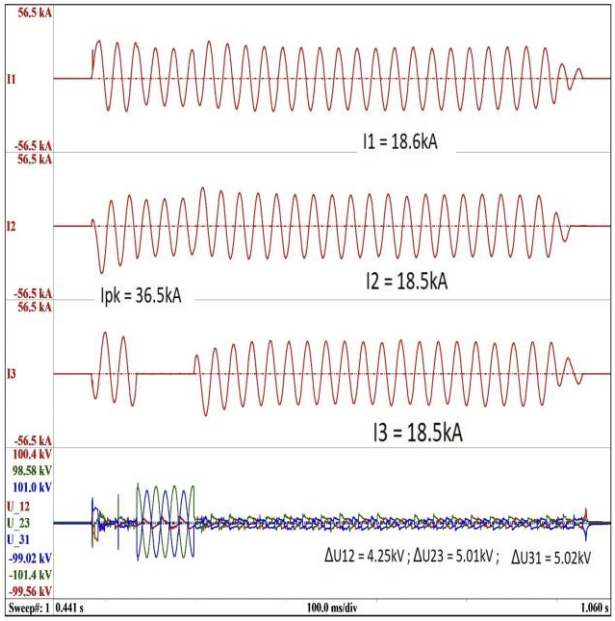

Fig. 15. Graphic record of the test 36 kV, 20 kA

After 50 ms on L_3 phase, the fuse worked but it wasn't able to break the current or to transmit the breaking operation to the LBS (Fig. 15). The result can be seen in Fig. 16. The result was not adequate. Because the assembly was destroyed during the test, it is required to be made further experiments, in order to make any conclusion for this.

Values obtained:

I_{pk}=29.1/-36.5/31.9 kA;

I_{rms}=18.6/ 18.5/18.5 kA;

Connection: 2.7ms after zero of the supply;

$U_{12,_23,_31}$_rms_drop_arcing_voltage=4.25/5.01/5.02kV;

$U_{\_23,\_31}$=33.6/31.2 kV - line voltage measured between the phase that opened L3 and one of the remaining closed phases.

Fig. 16. Aspect of the assembly after the experiment

In summary, after analyzing the remaining of the HBC fuses, the phenomena of unduloid formation on the fusible element have been observed, which propose that the mechanism of disintegration is dependent on the instability of the liquefied cylinder [17-24] and the evolution of the cylinder into stable spheres. Cylinder instability due to electromagnetic forces is questionable since in separate cases unduloids have been observed to form due to stored thermal energy. Alternatively, it assumed uneven temperature distribution would induce disintegration, which would occur at the hottest point, usually at the center of the conductor.

VI. CONCLUSIONS

The experiments were performed in a high-power laboratory that allowed the adjustment of the values needed to obtain the required parameters. The measurements were acquired using TRAS (Genesis optically isolated digitizer): 100 Ms/s, 16-bit, 1 GB Memory Channel, 24 channels. The first experimental results were obtained for the most severe operating conditions 0.87X36 kV and 25 kA, at different phase angles of the current. They checked the experimental solution for the maximum rated breaking current; the experiments were performed without applying a eutectic point M on the fuse element. The next set of experiments was performed in order to demonstrate the capacity of the fuse to break the nominal minimum breaking current, without applying a eutectic point M. Although one or more fusible elements in the structure of the fuse broke, the fuse as a whole was not capable to break these currents. In the final experiments, fuses of the same design were used, but a eutectic point was applied to their fusible element. When a current of $9xI_N$ was applied, the fuse broke the current after 1000 ms in satisfactory conditions. However, this value of the current does not make this type of fuse an actual competitor for fuses with silver fusible elements. The project includes the execution of other design types of fuse elements, to verify whether the results obtained can be improved.

ACKNOWLEDGMENT

The paper was developed with funds from the Ministry of Education and Scientific Research - Romania as part of the NUCLEU Program: PN 19 38 02 04.

Contribution of authors:

First author – 60% ; First coauthor – 10%;
Second coauthor – 10%; Third coauthor – 10%
Fourth coauthor – 10%

Received on August 4, 2021
Editorial Approval on November 10, 2021

REFERENCES

[1] Y. Kawase, T. Mivatake, S. Ito, “Heat analysis of a fuse for semiconductor devices protection using a 3-D finite element method,” in IEEE Trans. Magn., vol. 36, no. 4, pp. 1377-1380, July 2000.

[2] D. Rochette and W. Bussiere, “Pressure evolution during HBC fuse working,” in Plasma Sources Science and Technology, vol. 13, no. 2, pp. 293-302, April 2004.

[3] A. Wright and P.G. Newbery, Electric Fuses 3rd Edition, Power and Energy Series 49.

[4] M. Young, The Technical Writer's Handbook. Mill Valley, CA: University Science, 1989.

[5] A. W. Metcalf, “A new fuse Phenomena”, BEAMA Journal 44, p.109, 151, 1939.

[6] A. L.Wilkins, “Use of semiconductor - protection fuses on DC Drives/ Motors/Controls”, UK, 1987

[7] A. Wright and P. G. Newbery, 2004 Electric Fuses (IEEE Power and Energy Series 49) 3rd ed. (London: The Institution of Electrical Engineers).

[8] O. Bouilliez and J. C. P. Quesada, “Design and use of MV current-limiting fuses”, Cahier technique no.128.

[9] Brown, Robert Ernest, “Investigation of disintegration and arcing in electric fuses”, Doctoral, Sheffield Hallam University

[10] T. Reichelt, “Numerical and Analytical Solution of the Transient Adiabatic Joulean Heat Equation of Common Electrical Conductors”, Diplomarbeit, Technische Universitat Ilmenau, 1997.

[11] W. Bussiere, “Influence of sand granulometry on electrical characteristics, temperature and electron density during high-voltage fuse arc,” J. Phys. D: Appl.Phys, 2001.

[12] M. Lindmayer, “3D simulation of fusing characteristics using the M-effect,” The 6th international conference on Electric fuses and their applications, Instituto Elettrotecnico Nazionale Gailieo, Ferraris, Torino, Italy, 1999, pp. 13-20.

[13] T. Yorozu, M. Hirano, K. Oka, Y. Tagawa, “Electron Spectroscopy Studies on Magneto-Optical Media and Plastic Substrate Interface,” in IEEE Translation Journal on Magnetics in Japan, vol. 2, no. 8, pp. 740-741, Aug. 1987.

[14] L. A. Kojovic, S. P. Hassler, H. Singh, C. W. Williams, “Current-limiting fuses improve power quality,” in IEEE/PES Transmission and Distribution Conference and Exposition. Developing New Perspectives (Cat. No.01CH37294), vol.1, pp. 281-286, April 2001.

[15] IEC 60282-1:2002 High-voltage fuses – Part 1: Current-limiting fuses

[16] C. -E. Salceanu, M. Nicola, D. Ocoleanu, D. Iovan, S. Enache, “Experimental Study of HBC Fuses with Aluminum Fuse Element at Minimum Rated Breaking Current,” International Conference on Applied and Theoretical Electricity (ICATE), Craiova, Romania, 2021, pp. 1-6.

[17] Baxter, H.W., “Arcing Characteristics of Fuses with Small Over Currents (DC and AC),” The British Electrical and Allied Industries Association, Report G/T 228, 24 March 1950

[18] Aslak Ofte, Rondeel, W., “Test Procedures and Arcing Phenomena in HV Fuse Links near the Minimum Breaking Current,” in Conference Proceedings, *International Conference on Electrical Fuses and their Applications*, Trondheim, Norway 13-15 June 1984, pp. 190-195.

[19] Mr. Edward Nairne FRS – Discoverer of the Electrical Fuse

[20] Mc. Ewan, P.M., “Prospects of Developments of Current Breaking Techniques,” PTWPiS, Gdansk, 1996

[21] Carne, E.B., “A Mechanism for the Fuse Pre-Arcing Period,” A.I.E.E. Transactions, Vol. 72, 2 March 1953, pp. 593-599

[22] Lipsky, T., “Why Unduloids Do Not Always Appear,” Conference Proceedings, 3rd International Sumposium on Switching Arc Phenomena, Lodz, Poland. 1977, pp. 305-309

[23] Bisaria, A.K., “Appearance of Unnuloids in Exploding Wire Phenomenon,” Indian Journal of Pure Applied Physics, Vol. 11, September 1973.

[24] Meyer, E., Rinderer, L., “Use of Capillary and Pinch Instability for Dendritic Crystal Growing”, Journal of Crystal Growth, Vol. 28, 1975, pp. 199-208.

Simulation of Multi-Motor Propulsion System for Energy Efficiency in Electric Vehicles

Cristian-Liviu Popescu*, Laureţiu Marius Dumitran* and Alexandru Stănescu*
* University POLITEHNICA of Bucharest/Electrical Engineering Faculty, Bucharest, Romania,
liviu_p@yahoo.com, laurentiu.dumitran@upb.ro, alexandru.stanescu@upb.ro

DOI: 10.52846/AUCEE.2021.1.11

***Abstract* - For a vehicle, the knowledge of components, characteristics, performances, and behaviors are some base elements for a successful simulation. Today's tools are offering instruments able to cover a such request and new possibilities appear. Choosing the right ones, representing the entire vehicle as a system of subsystems, integrating as much as possible the parameters of different components, are also few additional elements. For internal combustion engine vehicles, the generation and the transmission of the mechanical power to the wheels imply the usage of specific mechanic parts. From a single engine, the mechanical power is controlled to offer the requested torque and speed simultaneously to the vehicle wheels, passing by clutches and gearboxes. An electric propulsion, generating high torque at zero speed, and covering large speed area, implies less components for the mechanical transmissions. One single gear, a reducer, could cover the entire speed area request of the vehicle. On the other hand, it is possible to approach the generation of the mechanical power to the wheels, by using not only one electric motor, but one for each axle, or, even more, one electric motor for each wheel of the vehicle. This paper presents the usage of numerical simulation in such situations, emphasizing opportunities for onboard energy efficiency improvement, and opening new possibilities for optimization in multiple motor solutions.**

Cuvinte cheie: *vehicule electrice, motoare electrice, grup motopropulsor electric, soluţii multimotor, modelare şi simulare..*

Keywords: *electric vehicles, electric motors, electric powertrain, multi-motor solutions, modelling and simulation.*

I. INTRODUCTION

Modeling and simulation of Electric Vehicles (EV) requires good knowledge of the vehicle on technical and regulatory aspects, appropriate mathematical models for different components and especially a valuable contribution of researchers who have been working and works in the field [1]. The advantages of electric motors as high instant power, fast torque response, fast power density, low cost and high acceleration [2] are good premises for mobility usage. But even if electric vehicles present high energetic performance, the optimization remains an important feature [3] for providing higher operational range and continuing costs reduction. From the vehicle characteristics, the resistant forces can be calculated as presented in [4] and represent input data for the powertrain calculation, based on the e-drive knowledge [5]. Different architectures have been already studied, as mentioned in [6] and the improvements continue for different components of the EV.

An important attention is dedicated to the control aspects in order to generate the necessary torque and speed for the vehicle [7]-[20]. From [21] results that the torque balance between motors on the same vehicle represents a source of energy efficiency, of course preserving the vehicle stability. Energetic aspects are also studied, as presented in [22], design aspects for robot solutions [23] to high power systems [24]-[25]. And an important attention is accorded to in-wheel solutions [26]-[32]. Physical aspects are also emphasized in several studies, as for example in [33]-[35]. In [36] a simulation with interior permanent magnet synchronous motor (IPMSM) shows some advantages of a multi-motor solution. Such solution could be adapted for low autonomy needs as presented in [37]. Of course, the capability of controlling a such system could be also applied to different mobility solutions, as for example presented in [38]. From a testing cycle as input data, for the simulated system, the operating points in terms of speed and torque of the powertrain could be calculated [39]. The result is confirmed by performing a testing cycle. In this paper the simulation of an EV with two IPMSM is presented, with future possible extension to four motors. Comparisons between the results of an architecture with a single motor, and respectively two identical and different motors are possible. The involvement of each motor is seen during the testing cycles. At the end of the tests, the influence of different solutions for energy efficiency is seen on the onboard energy state.

The present paper is structured in multiple sections. Elements regarding the vehicle model as vehicle fundamentals are detailed first, with tractive effort calculation and specific considerations. A next section integrates a short description of the testing cycle used as input data and the resulted torque request for the propulsion system. It follows the studied vehicle configuration with two motors, one motor per axle with a complementary torque strategy between motors, and the possible extension to four motors, versus an initial single-motor configuration. The dedicated modules for the simulation are described in the same section, with an example of a diagram. Before the conclusion, a dedicated section presents the results obtained by the simulation, for the studied torque allocation strategies. The respective energy consuption for each case is determined at the end of each testing cycle. The Conclusion section ilustrates the improvment possibilities and general directions for physical implementation.

II. VEHICLE FUNDAMENTALS FOR THE MODEL

Following the description in [36], the vehicle has more than 100 years of history. The forces distribution during different usage (starting, braking, cornering) and different aspects related to maintenance and usage had been studied in the past [40]-[43]. The general behavior of the vehicle did not change, but the modeling and simulation capabilities have given a new dimension for researchers, but also for development time. In vehicle performance modeling, establishing the physical model is fundamental. It relates to the forces transmitted through the wheels to the ground, the force received directly on the body of vehicle and also through the wheels [1].

A. Vehicle Dynamics and Modeling

Considering M, the mass of the vehicle and g, the gravitational acceleration, the gravitational force acting on the vehicle

$$G = Mg, \tag{1}$$

gives a normal component on the road,

$$G_n = Mg\cos\alpha, \tag{2}$$

where α is the grade angle.

The classic case of forces on a vehicle is illustrated in Fig. 1.

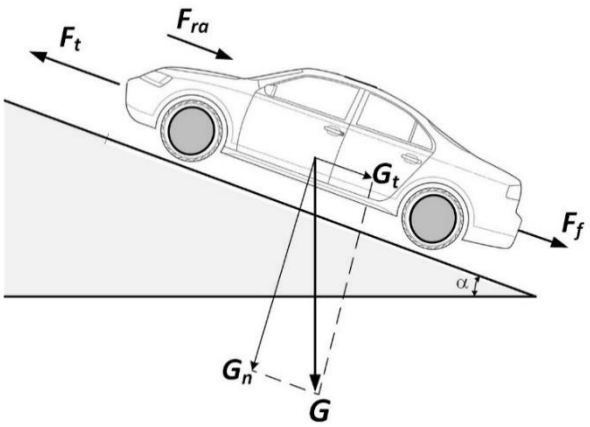

Fig. 1. Forces on the vehicle moving uphill ($\alpha > 0$).

The rolling resistance force is

$$F_f = fMg\cos\alpha, \tag{3}$$

where f represents the rolling resistance coefficient, as a linear function of the vehicle speed V.

The next formula could be used for most common range of tires inflation [1]:

$$f = 0.01\left(1+\frac{V}{160}\right). \tag{4}$$

The grading resistance force is

$$G_t = Mg\sin\alpha. \tag{5}$$

In order to simplify the calculation, $\sin\alpha$, is replaced by the grade value α, when the road angel is small.

The air pressure creates a force resisting the vehicle motion, depending linearly on the air density, ρ, the vehicle frontal area, S, the shape of the vehicle characterized by the aerodynamic drag coefficient C_x and the square of the speed:

$$F_{ra} = \frac{1}{2}\rho S C_x (V - V_w)^2, \tag{6}$$

where V is the vehicle speed and V_w the wind speed on the vehicle moving direction.

B. Specific Behavior During Vehicle Movement

On the road, possible disturbing effects appears and, of course, additional solicitations on the vehicle. In front of changes in its external environment, the vehicle reacts. Its response represents the characteristic behavior of the vehicle in such situations.

The normal forces applied on each wheel change during driving. The Fig. 2 represents the air flow around the vehicle.

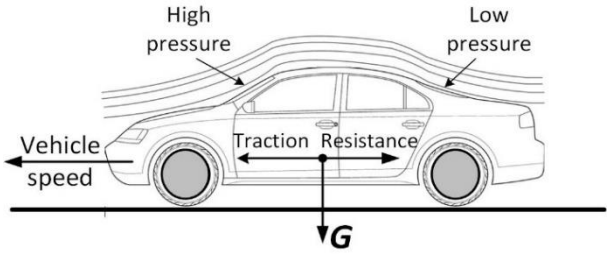

Fig. 2. Shape drags.

At speed, the higher frontal pressure is "charging" more front wheels and discharging the rear ones. A similar situation appears when the vehicle is braking. For the electric motors powering the front of the vehicle is the moment to provide an increased traction force, or make a better energy recuperation on braking.

During the vehicle start and acceleration phases, the inertia is "charging" more the rear part of the vehicle. The increased traction forces have to be on this side. Such considerations push not only to control better the electric motors on the vehicle, but also to design and implement different motor types for rear and front side of the vehicle. For improved performances of the vehicle, it is also possible to design for example two electric motor types acting in parallel on the font side (or rear side) of the vehicle, one acting more for low speed and another for high speed.

Similar situations appear between lateral sides of the vehicle on lateral wind conditions or, left or right road inclination (often met in off-road conditions).

The vehicle's stability has to be controlled during precedent situations. Differences between rotational speed and torque from one wheel to the other could result in uncontrollable vehicle, especially at high-speed values.

The complexity of the model increases by integrating the cornering aspects. The angles of steering wheels are not identical, and the rotational speed has to increase on the exterior side. A mechanical differential simplifies the control when an electric motor is dedicated to each axle. A more complex situation includes a dedicated motor for each wheel.

To exemplify the trajectories of the wheels when cornering, a schematic view is illustrated in Fig. 3.

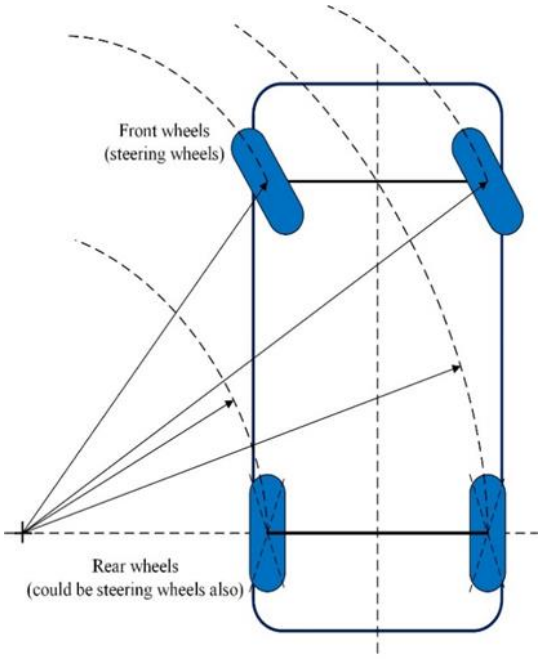

Fig. 3. Schematic view of wheels trajectories in the case of cornering.

For better cornering, the rear wheels could receive inclination angles (not identical to the correspondent frontal ones) adding supplementary constraints to the model.

C. *Wheel Sleep and Tractive Effort Considerations*

The tractive effort

$$F_t \geq F_{ra} + F_f \,, \tag{7}$$

for acceleration and constant speed movement.

F_t is limited by the tire-ground adhesion. The maximum tractive effort is calculated similarly to (3) but using this time a tractive effort coefficient instead of the rolling resistance one. When the adhesive capabilities between the tire and the ground are not enough to support the tractive effort, the respective wheel will spin on the ground. The tractive effort will depend on the type of ground. The elasticity of the tire will generate a good adhesive capability on dry asphalt road, but much less adhesive capability on ice. Following measurements in real conditions, the maximum tractive effort relates to the slipping of the wheel, s:

$$s = \left(1 - \frac{V_t}{V_r}\right) \times 100 \,, \tag{8}$$

where, V_t is the speed of the wheel (measured in the center of the wheel), and

$$V_r = \omega \times r \,, \tag{9}$$

where ω and r represents the angular speed and the radius of the wheel.

For braking, the slip can be expressed similarly:

$$s = \left(1 - \frac{V_r}{V_t}\right) \times 100 \,. \tag{10}$$

The maximum tractive effort will depend on the vertical load of the tire, N and a function of the tire slip, $a(s)$:

$$F_t = a(s) \times N \,. \tag{11}$$

The dependence is approximatively linear, due to the elasticity of the tire. As specified in [1], the peak tractive effort is reached at a slip of 15-20%. After that the relation becomes non-linear and for normal driving, the precedent values are to be considered as a superior limit.

III. Preparation of the Study

A. *Input Data*

A set of data has to be generated to perform the simulation. Usually, it represents requests in terms of speed evolution during a period of time. The vehicle has to follow the requests, aspect confirmed by specific measurements.

The test has to be the same for all situations, allowing at the end the possibility to compare the results obtained for each one. For the present simulation, a normalized testing cycle is used to run different configurations of the vehicle.

Fig. 4 presents the speed evolution for the FTP75 test.

Fig. 4. Speed request during the testing cycle (FTP75).

From the speed evolution results the acceleration request. Using the vehicle data, a classic sedan type, and following the calculation model presented in section II, it is possible to obtain the torque request.

B. *Vehicle Configurations and Sepcific Data*

A mono-motor EV with a full traction system is considered as reference. The configuration is shown in Fig. 5, and on the Fig. 6 is presented the requested torque for the electric motor as a result of the vehicle configuration, input data and resistant forces calculation.

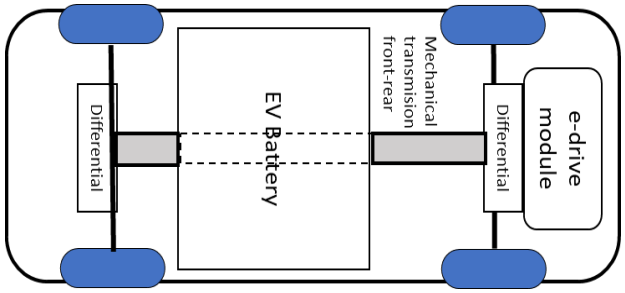

Fig. 5. Reference vehicle configuration.

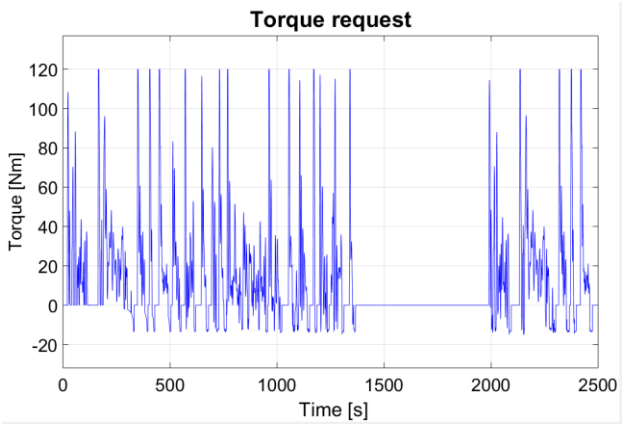

Fig. 6. Torque request in initial configuration.

In order to cover the request, for the present study, two different IPMSM motors will be involved. The most powerful motor is attached to the rear axle. Fig. 7 shows the correspondent configuration for the vehicle.

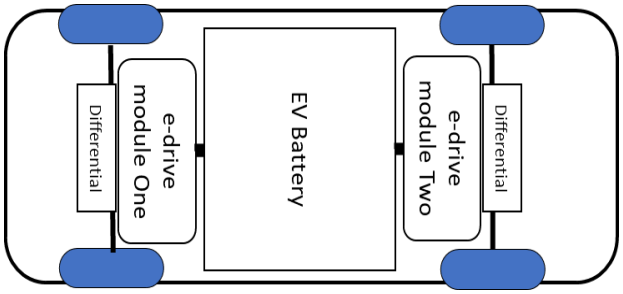

Fig. 7. Vehicles configuration for the study.

A dedicated mechanical differential is kept on each axle of the vehicle, but there is no more any mechanical link between axles as in the configuration with a single motor. A same battery is used for both motors, but each motor controller receives dedicated torque command. The total torque request for the powertrain is covered by adding the contribution of each motor.

A future possible extension to four motors is presented in Fig. 8.

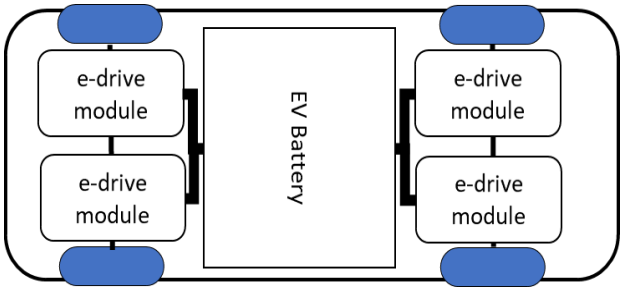

Fig. 8. Future configuration with four motors.

Each wheel receives a dedicated e-drive module including the electric motor. The wheels on the same axle have to receive identical motors in order to reduce the complexity of the control. A dedicated control for each wheel has to act under all driving wheels supervision. In the case of a modular extension form one single-motor to two motors, and, respectively, four motors a dedicated battery could integrate each module. For physical implementation reasons, also a single battery could deserve all modules.

C. *Main Modules for the Simulation*

For the simulation, the MATLAB environment has been chosen, as multiple functions and facilities are already available. Once the model is implemented, it offers several possibilities to analyze different configurations for different input data, compare the results, and improve it.

A general view on simulation modules is represented in the next figure.

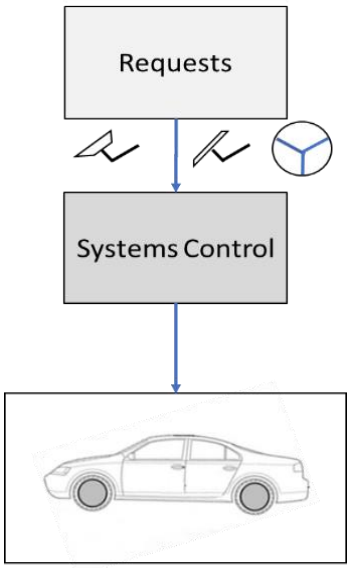

Fig. 9. Main modules for the simulation.

In the Fig. 9 the vehicle box represents the systems that an EV integrates. Behind it, on one side, there are the EV battery model, motors models and their control with their specific characteristics. On the other side, there are the mechanical systems ensuring the link from the motor axles to the ground, with their inertia and other characteristics. The model of the vehicle body has the characteristics mentioned in section II.

The “Systems Control” box presents the models for energy management and powertrain control.

The “Requests” box integrates the input data. As input data, the testing cycle is transformed in requests for the vehicle by modeling this transformation in data for the vehicle control.

Usual characteristics of a classic vehicle are kept, as for steering system and mechanical braking. The capabilities are improved by the usage of the electric motors. For example, the brake command is resulted from the torque request when the reduction of the torque implies an additional resistant force than the resistant forces acting on the vehicle at the moment. A negative torque is created by transforming the motors in electric generators. Limitations related to electric motors capabilities and batterry charging aspects require the intervention of the mechanical braking system. It could work in parallel with the electric motors acting as generators.

A more structured look into the modules is shown in the next figure.

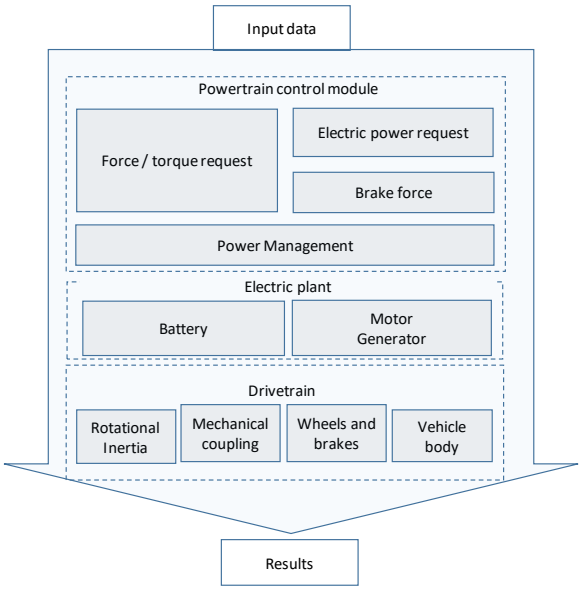

Fig. 10. Modules main components [36].

Inside the electric plant, the torque allocation between the two motors follows a complementary strategy. An implementation with visible thresholds is presented in Fig. 11.

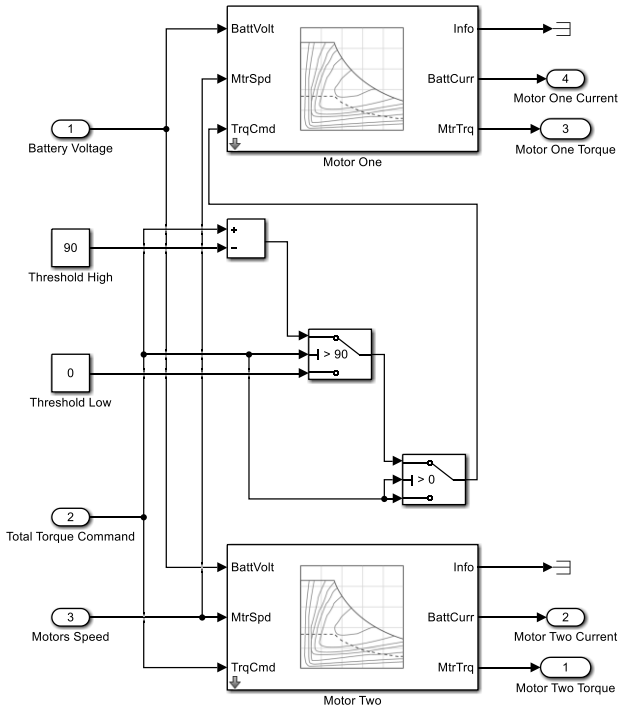

Fig. 11. Complementary torque allocation diagram with two motors.

Motor One and Motor Two integrate specific characteristics, covering together the request in terms of power, torque, and speed for the propulsion system of the vehicle.

In this case, the „threshold high" represents the torque capabilities of the biggest motor.

IV. Results and Discussions

The torque request values result from the Fig. 6. Maximum, minimum and mean values are integrated in the Table I.

TABLE I.
Torque Data

Minimum torque request	-15.05 Nm
Maximum torque request	120 Nm
Mean torque during the cycle	11.72 Nm

Applying the testing cycle with a single motor, at the end it results the evolution of the state of charge of the battery (SOC) in this vehicle configuration, as presented in Fig. 12.

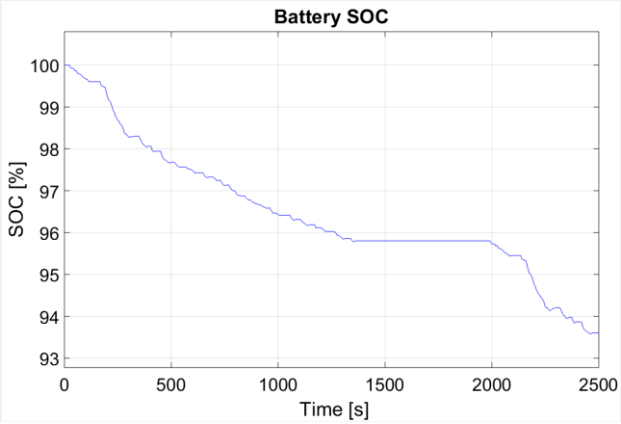

Fig. 12. Battery SOC with a single motor.

At the end of the test, it can be observed that the SOC value is 93.58 %.

The configuration of the vehicle with two different motors is considered, in two cases. For the first case, the charge is affected starting with the biggest motor and after that the smallest one. In the second case, the smallest motor is charged first. It means that the two motors will produce torque in the same time, only if the capacity of the first charged motor is exceeded.

During the simulation for the first case, the resulted torque on Motor One, which is the biggest motor, is presented in Fig. 13.

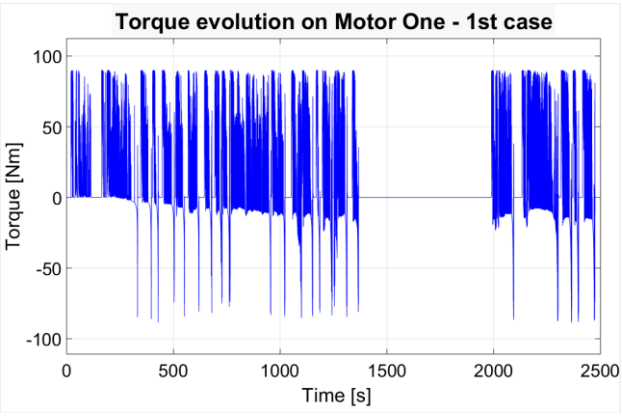

Fig. 13. Torque on the biggest motor in the first case.

The torque evolution for the Motor Two in the 1st case is presented in Fig. 14.

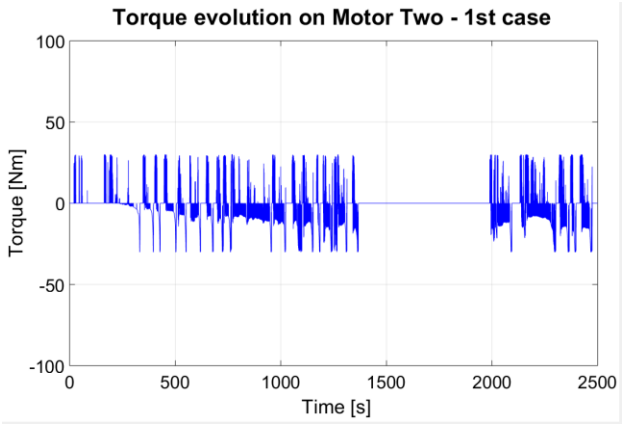

Fig. 14. Torque on the smallest motor in the first case.

The energy of the battery is monitored during the test. Fig. 15 presents the SOC evolution for this case.

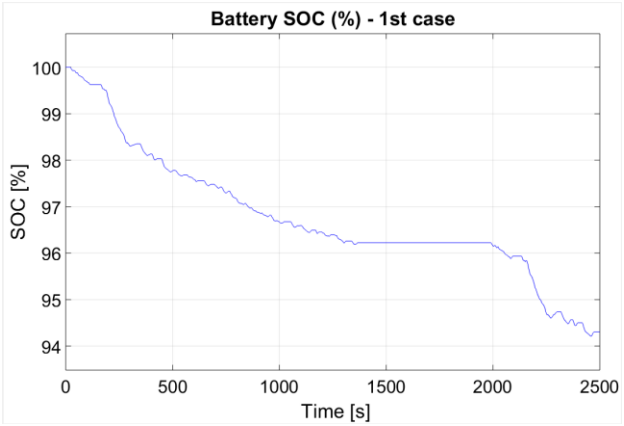

Fig. 15. Battery SOC with two motors in the first case.

At the end of the testing cycle the available electric energy in the battery reported to the energy at the beginning of the cycle is 94.21%.

As mentioned before, during the second case, the smallest motor is charged first. On Motor One, the torque is presented in Fig. 16.

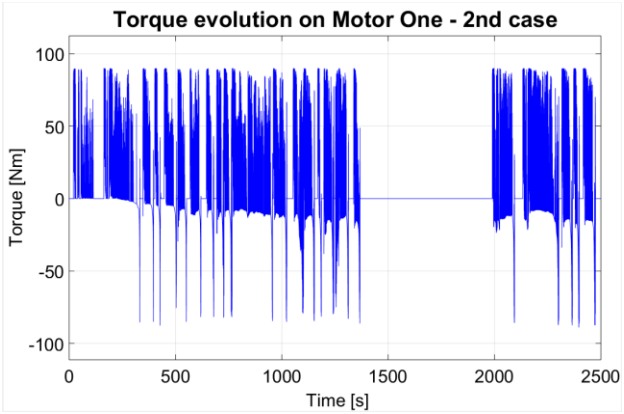

Fig. 16. Torque on the biggest motor in the second case.

The torque evolution of the Motor Two for 2nd case is presented in Fig. 17.

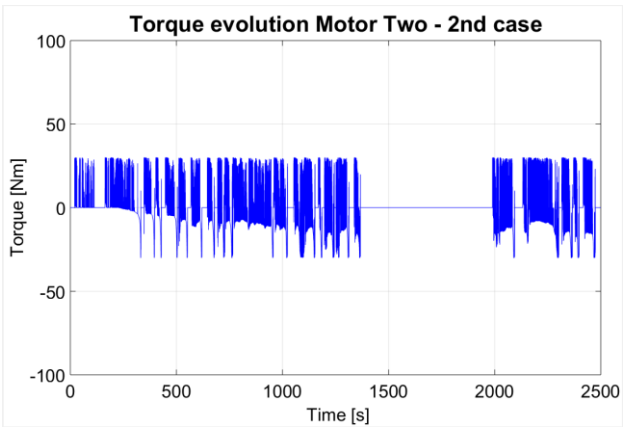

Fig. 17. Torque on the smallest motor in the second case.

It is visible that the Motor Two is much more involved than in the first case.

The battery SOC for the 2nd case is presented in Fig. 18.

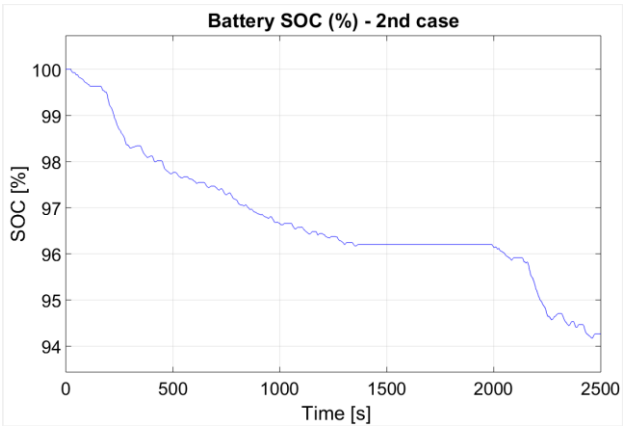

Fig. 18. Battery SOC with two motors in the second case.

For this second case, at the end of the testing cycle, the available electric energy in the battery reported to the energy at the beginning of the cycle is 94.17%.

Each simulation started with the same electric energy stored in the battery. It can be observed that during the same testing cycle, the vehicle with one single motor would consume 10.88% more energy than the bi-motor vehicle in the first case, and 10.12% more energy than the bi-motor vehicle in the second case.

In [36] the tested multi-motor vehicle had two identical motors and also generated improvement on energy usage than the same vehicle with a single motor. Passing to four motor solution would mean to replace each motor studied in the present paper with two smaller and identical motors. From this point of view, this will be similar to [36], and new possibility for improving energy efficiency appears.

For a smaller vehicle, the two-motor solution has been studied in [21] using the criterion of the optimal load reparation between the two motors. Also, in [39] different percentual repartition criteria have been analyzed. The present paper comes with simulation based on a new criterion for the bi-motor solution, analyzed in two cases.

V. CONCLUSION

A bi-motor solution has been simulated and analyzed in this paper using a new charging repartition criterion based on the different capabilities of each motor. The simultaneous functioning of the motors has been reduced to the situations when the capabilities of the first charged motor are exceeded. The results confirm improvement in the energy efficiency usage compared to the equivalent solution with a single motor.

For real situations, the application of different torque allocation criteria in a multi-motor solution, is first of all conditioned by safety. Additional optimizations for more performance in terms of speed, acceleration, deceleration and improvements in electric energy consumption, have to perform under stability control of the vehicle.

Also, the vehicle configuration represents an important element for generating improvement on onboard energy efficiency. For the same configuration, different optimization scenarios can be applied. There are no general criteria to cover all real situations. The optimization process can include diverse techniques to involve the electric motors, depending on the state of the vehicle as accelerating, decelerating, cornering, running at constant speed etc.

In parallel with the optimization studies, new electric motors are analyzed. The results of such research activities are influenced by the capabilities of the motors. More performant motors will generate better results for multi-motor solutions in EV.

ACKNOWLEDGMENT

Special thanks are accorded to Prof. Aurelian Crăciunescu for his guidance, precious indications, and dedicated documentation for electric vehicles design and optimization.

R.B.G tanks goes to Prof. Leonard Melcescu for special help concerning IPMSM, simulation, motors controlling and optimization processes

Source of research funding in this article: Research program of the Electrical Engineering Department financed by the University Politehnica of Bucharest.

Contribution of authors:

First author – 50%

First coauthor – 30%

Second coauthor – 20%

Received on July 17,2021

Editorial Approval on November 15, 2021

REFERENCES

[1] S. Soylu (ed.), "Electric Vehicles – Modelling and Simulations", InTech, 2011.

[2] L. Popescu, "Electric vehicles entering a new decade", *SME 2020 Conference*, University POLITEHNICA of Bucharest, Bucharest, 20 Nov. 2020.

[3] E. K. P. Chong și S. H. Zak, "An Introduction to Optimization", Wiley, 2001.

[4] M. Ehsani, Y. Gao and A. Emadi, "Fundamentals of Vehicle Propulsion and Brake" in *Modern Electric, Hybrid Electric, and Fuel Cell Vehicles. Fundamentals Theory, and Design*, second edition, CRC Press, 2010, pp. 19-65.

[5] I.F. Soran, "E-drive systems" ("Sisteme de actionare electrica"), Matrix Rom 2010.

[6] Chris Mi, M. Abdul Masrur and David Wenzhong Gao, "Hybrid Electric Vehicles – Principles and Applications with Practical", Perspectives, Wiley, 2011.

[7] R. Pusca, Y. Ait-Amirat, A. Berthon , J M. Kauffmann, "Modelling and Simulation of a Traction Control Algorithm for an Electric Vehicle with Four Separate Wheel Drives", *Proceedings IEEE 56th Vehicular Technology Conference*, Vancouver, 24-28 Sept. 2002.

[8] S. J. Hallowell, L. R. Ray, "All-wheel driving using independent torque control of each wheel", *Proceedings of the American Control Conference Denver*, Colorado, June 4-6, 2003.

[9] Li Zhai, Sh. Dong, "Electronic Differential Speed Steering Control for four in-wheel motors independent drive vehicle", *2011 9th World Congress on Intelligent Control and Automation*, Taipei, 21-25 June 2011.

[10] Nobuyoshi Mutoh, "Driving and Braking Torque Distribution Methods for Front- and Rear-Wheel-Independent Drive-Type Electric Vehicles on Roads", *IEEE Transactions on Industrial Electronics* (Volume: 59, Issue: 10, Oct. 2012).

[11] A. Stern, Z. Shiller, "Control Allocation of All-Wheel Drive Vehicles: a Longitudinal Model", *2013 IEEE/RSJ International Conference on Intelligent Robots and Systems*, Tokyo, 3-7 Nov. 2013.

[12] Yue Ma;Xiaohong Li;Jinning Zhi, "The Research of Torque Distribute Strategy for 6-Wheel-Independent-Driving (6WID) Electric Vehicle", *2014 IEEE Conference and Expo Transportation Electrification Asia-Pacific* (ITEC Asia-Pacific), Beijing, 31 Aug.-3 Sept. 2014.

[13] S. Kulkarni, S. Junghare, A. Sapkal, "PWM Controlled Independent Six Wheel Drive for an All-Terrain Robotic Vehicle", *2014 IEEE International Conference on Power Electronics*, Drives and Energy *Systems* (PEDES), Mumbai, 16-19 Dec. 2014.

[14] C. Bian, G. Yin, M. Hu, N. Zhang and N. Chen, "Fault Tolerant Control Design for All Wheels Independent Drive and Steering Electric Vehicle with Singular Effective Drive Wheel", *2016 IEEE Vehicle Power and Propulsion Conference (VPPC)*, Hangzhou, 17-20 Oct. 2016.

[15] B. Guo, Y Chen, "Robust Adaptive Fault-Tolerant Control of Four-Wheel Independently Actuated Electric Vehicles", *IEEE Transactions on Industrial Informatics* (Volume: 16, Issue: 5, May 2020), p. 2882 – 2894.

[16] "Optimal Traction Forces for Four-Wheel Rovers on Rough Terrain", *Canadian Journal of Electrical and Computer Engineering* (Volume: 42, Issue: 4, Fall 2019), p. 215 – 224.

[17] K. Cao, M. Hu, D. Wang, S. Qiao, C. Guo, C. Fu and A. Zhou, "All-Wheel-Drive Torque Distribution Strategy for Electric Vehicle Optimal Efficiency Considering Tire Slip", *IEEE Access*, 18 January 2021, p. 1-1.

[18] C. Chatzikomisa, M. Zanchettab, P. Gruberb, A. Sorniottib, B. Modicc, T. Motalnc, L. Blagotinsekc, G. Gotovacc, "An-energy efficient-torquevectoring-algorithm-for-electric-vehicles-with-multiple-motors", *Mechanical-Systems-and-Signal-Processing* Volume 128, 1 August 2019, p. 655-673.

[19] F. Dongsheng, W. Ye, "Study on Vehicle Driving State Estimation for Four-Wheel Independent Drive and Steering Electric Vehicle", Proceedings of China SAE Congress 2019: Selected Papers, 05 November 2020.

[20] R. Wang, J. Wang, "Fault-Tolerant Control With Active Fault Diagnosis for Four-Wheel Independently Driven Electric Ground Vehicles", *IEEE Transactions on Vehicular Technology* (Volume: 60, Issue: 9, Nov. 2011).

[21] L. Popescu, L. Melcescu, L. Dumitran, and A. Crăciunescu, " Analysis of the influence of wheel torque distribution on energy efficiency in the case of an electric vehicle with two motors", *1st International Conference on Applıed Engıneerıng and Natural Scıences (ICAENS)*, 2021, in press for Journal of Applied Engineering and Natural Sciences.

[22] R. Buchta, X. Liu-Henke, "Energetic aspects for an integrated vehicle dynamic control for E-vehicles with decentral drives and all-wheel steering", *2013 International Symposium on Electrodynamic and Mechatronic Systems (SELM)*, Opole-Zawiercie, 15-18 May 2013.

[23] HJ. Li, W. Jiang, Y. Yan, A. Zhang, "Operation Motion Planning and Principle Prototype Design of Four Wheel Driven Mobile Robot for High Voltage Double Split Transmission Lines" *Mathematical-Problems-in-Engineering*, March 2020.

[24] S-Y. Baek, Y-S. Kim, W-S Kim, S-M Baek and Y-J. Kim, "Development and Verification of a Simulation Model for 120 kW Class Electric AWD (All-Wheel-Drive) Tractor during Driving Operation", *Energies*, May 2020.

[25] F. Verbruggen, E. Silvas and Th. Hofman, "Electric-powertrain-topology-analysis-and-design-for-heavyduty-trucks", *Energies*, May 2020

[26] Y. Ki Kim, J. Woo Lee, Y. Kyu Lee, Y. Young Choe, H. Soo Mok, "Drive system of 25kW in wheel type IPMSM for electric vehicle", *2010 International Conference on Electrical Machines and Systems*, Incheon, 10-13 Oct. 2010.

[27] R. Nejat Tuncay, O. Ustun, M. Yilmaz, C. Gokce, "Design and implementation of an electric drive system for in-wheel motor electric vehicle applications", *2011 IEEE Vehicle Power and Propulsion Conference*, Chicago, 6-9 Sept. 2011.

[28] S. Ren, H. Qiu, Z. Dong, Z. Qi, "An Inverse kinematics analysis for a four in-wheel-motor drive and all-wheel independent steering electric vehicle", *2012 19th International Conference on Mechatronics and Machine Vision in Practice (M2VIP)*, Auckland, 28-30 Nov. 2012.

[29] Ziming Qi, Xu Zhao, Kuang Ma, Matthew King, Wei-Chen Lee, Ji-Wei Lin, Shao-Min Lee, "4-wheel Independent In-wheel-motor Drive and Independent Steering Electric Vehicle Safety Analysis Method Based on Mass Re-distribution Experiment", *2015 6th International Conference on Automation, Robotics and Applications (ICARA)*, Queenstown, 17-19 Feb. 2015.

[30] M.H. Rasul, H. Zamzuri, A.M.A Mustafa, and M.H.M Ariff, "Development of 4WIS SBW In-Wheel Drive Compact Electric Vehicle Platform", *2015 10th Asian Control Conference (ASCC)*, Kota Kinabalu, 31 May-3 June 2015.

[31] Y. Wang, X. Zhao, Sh. Li, B. Su and J. Gao, "Path tracking of eight in-wheel-driving autonomous vehicle - controller design and experimental results", *2019 IEEE International Conference on Unmanned Systems (ICUS)*, Beijing, 17-19 Oct. 2019.

[32] Z. Zhang, C. Liu, X. Ma, Y. Zhang and L. Chen, "Driving-force-coordinated-control-of-an-8x8-inwheel-motor-drive-vehicle-with-tireroad-friction-coefficient-identification", *Defence-Technology*, Elsevier, 17 June 2020.

[33] N. Mutoh, Y. Nakano, "Dynamic Characteristic Analyses of the Front-and Rear-Wheel Independent-Drive-Type Electric Vehicle (FRID EV) When the Drive System Failed during Running under Various Road Conditions", *2009 IEEE Vehicle Power and Propulsion Conference*, Dearborn, Michigan, 7-10 Sept. 2009.

[34] N. Mutoh, Y. Takahashi, "Front-and-rear-wheel-independent-drive type electric vehicle (FRID EV) with the outstanding driving performance suitable for next-generation advanced EVs", *2009 IEEE Vehicle Power and Propulsion Conference*, Dearborn, Michigan, 7-10 Sept. 2009.

[35] N. Mutoh, S. Manaka, "Driving Performance on Low Friction Coefficient Roads Which the Front-and-Rear-Wheel Independent-Drive-Type-Electric Vehicle (FRID EV) Has", *2009 35th Annual Conference of IEEE Industrial Electronics*, Porto, 3-5 Nov. 2009.

[36] L. Popescu, L. Dumitran and A. Stanescu, "Multi-motor solutions for electric vehicles," *2021 International Conference on Applied and Theoretical Electricity (ICATE)*, 2021, pp. 1-6, doi: 10.1109/ICATE49685.2021.9465016.

[37] A. Stanescu, N. Mocioi and A. Dimitrescu, "Sulina — Environmentally friendly transport based on renewable sources", *2017 Electric Vehicles International Conference (EV)*, IEEE, Bucharest, 5-6 Oct. 2017.

[38] A. Stanescu, N. Mocioi and A. Dimitrescu, "Hybrid Propulsion Train with Energy Storage in Metal Hydrides", *2019 Electric Vehicles International Conference (EV)*, IEEE, Bucharest, 3-4 Oct. 2019

[39] L. Popescu, L. Melcescu, L. Dumitran, A. Crăciunescu and A. Stanescu, "Control analysis of a bi-motor electric traction system for energy and performance optimization", *International Scientific Conference on Communications, Information, Electronic and Energy Systems (CIEES)*, 2021, in press for AIP Conference Proceedings.

[40] C. Arama, A. Mihai, "Automobile from A to Z" (Automobilul de la A la Z), Ed. Militara, Bucuresti 1985.

[41] A. Brebenel, D. Vochin, "Passengers car and performances" (Autoturisme si performante), Ed. Sport Turism, Bucuresti, 1983.

[42] A. Brebenel, C. Mondiru, "Der personenkraftwagen DACIA 1300", Ed. Tehnica, Bucuresti, 1983.

[43] "Vehicle technician's memorandum" (Memoratorul tehnicianului de autovehicule), Ed. Tehnica, Bucuresti, 1959.

Ways to Determine the Structural Resource of Highly Maneuverable Aircraft

Nicolae-Alin Niculescu[1], Jenica-Ileana Corcău[2], Nicuşor Cătălin Stancu[1]
[1]Research, Innovation and Flight Test Center Military Equipment and Technologies Research Agency Craiova, Romania, niculescu.alin88@gmail.com, nicusorcatalinstancu@yahoo.com
[2]Department of Electrical, Energetic and Aerospace Engineering, University of Craiova, Craiova, Romania
jcorcau@elth.ucv.ro

DOI: 10.52846/AUCEE.2021.1.12

***Abstract* — This paper emphasizes the importance of monitoring aircraft structural fatigue and proposes as paramount the analysis of military aircraft structural constitutive materials aging process, during flight. Aircraft structural health monitoring is defined as an evaluation process for the integrity of key structural components with the sole purpose of enhancing flight safety and mitigating maintenance risks and loses. Nowadays, aircraft are predominantly built from composite materials with at least two layers with different mechanical properties, which combined, result in a new composite material with highly superior resilience and elastic properties. Even though there are great advantages of using composite materials, when it comes to operating military aircraft, a mere visual inspection cannot be sufficient for observing or identifying structural damages within the composite layers of the aircraft. The focus of this study is on improving the process of monitoring the structural condition of highly maneuverable military jet aircraft by using the strain gauge marks methods. Monitoring aircraft structural condition can be easily implemented, both during maintenance and flight missions, by using a wide array of sensors that can generate specific sets of instructions for all processes involved in enhancing flight and maintenance safety. The main concern of implementing a structural evaluation, within aircraft maintenance processes, sits on preventing and not ameliorating incidents and accidents during flight. As a result of the continuous research and testing, it has been proved that the operational resource of the aircraft structure, provided by the manufacturer, can be easily reached in a lot lesser flight hours than initially anticipated, by engaging the aircraft in specific operational missions and, therefore, inflicting pronounced fatigue on the aircraft structure.**

Cuvinte cheie*: monitorizarea aeronavei, structural, metoda mărcilor*.

Keywords: *monitoring aircraft, structural, marks method*.

I EVOLUTION OF AIRCRAFT BUILDING AND MAINTENANCE PROCESS

Aircraft building, in the last decade, has known a significant improvement, from both navigation and flight control systems and the material used for structure building stand points. All these technological advances have had the main purpose of increasing the flight safety level and, therefore, statistically, airborne transportation has become, nowadays, the safest and the most reliant way of reaching different locations.

Composite materials offer a series of advantages in comparison with the conventional materials as fatigue resilience, corrosion resilience, advantageous specific resistance and resilience (according to weight ratio). The most important aspect regarding composite materials is that its chemical and mechanical proprieties can be altered in order to reach maximum resilience for the known types and directions of strains within the aircraft structure [1].

Although composite materials come with lots of upsides, whether it is low weight, superior chemical and mechanical proprieties or facile structure building, it is important to mention that the composite layers present a great risk in having trouble to timely identify structural deteriorations.

The most important deteriorations that can occur within the composite structure are: fibre detachment from its matrix, cracks in the matrix, gap expansions within the matrix, delamination and fibre breakings; these alterations are, actually, stages within the progressive cracking process of the composite structures. The main concern is that, in the case of composite structures, a mere visual inspection does not qualify as a tool for identifying structural deteriorations and, consequently, using composite materials in the aviation industry could represent a safety issue [11].

Shifting the paradigm in what regards the environmental preservation is yet another reason for which composite materials are prone to be used in the aviation industry. ACARE (Advisory Council for Aviation Research and innovation, Europe), has set environmental goals as reducing carbon dioxide (CO2) emissions by 50%, reducing acoustic emissions by 50% and reducing oxide nitrate by 80% [2].

Even though, by using composite materials, the cost of developing and certifying a new type of technology for aircraft maintenance and aircraft structural monitoring has considerably risen, the benefits are deducted from the time reduction for the aircraft maintenance process and from decreasing the added risks of aviation accidents. It can be estimated that by implementing a method of continuously monitoring the aircraft structural condition, even though it increases the costs of aircraft maintenance processes by 20%, the affected time for aircraft maintenance will drop by 40% - which is the main concern and cost generator for an airline company [3].

Since the first time composite materials were used in the aviation industry, in 1957, the interest in these materials has met a great expansion, mostly in the military aviation industry. The use of these materials has increased

not only due to the obvious advantages as mass reduction, high resilience or increased resistance, but also because of the continuous maturing process of this technology and its applications.

An annual report of Lufthansa has recorded a number of 1648 events on a fleet of 243 monitored aircraft and the statistics showed that the average repair costs reached 33 million euros per year. The average repair time was 3.5 days which led to a loss of 200.000 euros for airplane in the fleet. Since 1996 a special form has been implemented in order to record maintenance problems and between 1999 and 2007, a number of 104 relevant ground incidents have been studied [12].

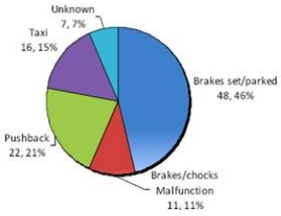

Chart 1. Position of aircraft during incident

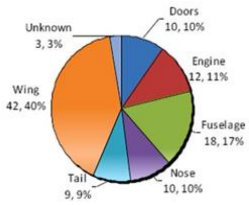

Chart 2.Damaged structural area

The survey specified that most incidents were produced due to ground operations and by the impact with ground vehicles, the wing being the area with the highest probability of being damaged [12].

Due to these reasons, aircraft structural condition monitoring becomes a primordial necessity and of utmost importance in the aircraft maintenance field, both civilian and military, this being the first step for increasing the safe use of aircraft and increasing aircraft availability, by reducing time and costs for aircraft maintenance and repair [4].

II. Different Methods of Monitoring the Structural Condition

The most important step in the full analysis of structural damages is their identification. There are many techniques of detecting structural damages and the costs rise in accordance with the technology used for the process.

The most widespread and also the cheapest one is visual inspection through which damages can be discovered by observing different surface deformations or paint cracks.

The second method is called the tap-test or coin-test and it consists of using special electronic hammers having an accelerometer at one end that can measure the response time between impulses. An internal structural damage will reduce the structural rigidity and the transmitted signal will have lower amplitude and bigger response time interval [16].

Other way of identifying propose the use of thermal images based on emitting energy waves (ultrasounds, microwaves, UV) towards the surface of the structure. The periodic waves penetrate the fabric of the structure, where they are absorbed, until a discontinuity is met and then the waves are partially reflected backwards. The reflected wave interferes with the initially emitted wave, thus, generating a thermic pattern over the local surface. The internal structure can finally be analysed by observing the thermic patterns across the airplane surface.

A different and more expensive direction proposed for monitoring the structural condition is the use of repairing technologies, which, in the case of composite materials, have not reached at full maturity in what concerns their development and, therefore, they were not unanimously accepted. Repairing technologies suggest the use of different materials imbedded within the structure of the aircraft that can be activated to repair small deformations, cracks or damages, even during flight [15].

Structural Health Monitoring is the name of most widespread safety programme used by the aircraft users and manufacturers for the maintenance process. Structural Health Management is defined as an evaluation of key structural elements` integrity with the sole purpose of mitigating risks and reducing losses of any kind. There are two approaches for monitoring structural integrity: degradation monitoring and operational monitoring.

Degradation monitoring can be obtained through more direct methods such as evaluating the fatigue level of the structure, observing a relation between damages and implications of weather elements and identifying damages rendered by accidents and mechanic shocks.

Operational monitoring consists of using indirect ways of measuring the structural fatigue with the help of sensors mounted on the soft spots of aircraft. Operational monitoring is a continuous process of evaluating and preventing serious structural damages and deformations in accordance with data available. The data used for calculating and analysing the structural fatigue can be time since last repair, the strain forces applied to the structure during flight, temperature during flight and other operational data.

The costs of developing new repairing process and maintenance technology are very high but the benefits surpass them. It is estimated that, by implementing such a technology on aircraft, can rise the maintenance costs by 20% but could also reduce inspection time intervals by 40%, which is the main source of money drain for an airline operator.

It can be stated that implementing a structural monitoring technology is a necessity if the goal is to reduce the stationing time of airplanes and mitigate safety risks during flight.

III. Strain Gauge Marks Method

Strain gauge marks represent the most widespread type of sensors used for monitoring structural condition as it presents great advantages. They both are used in the analysis of aircraft structure, within the aviation incidents, that result in structural damages of external causality and in monitoring the structural fatigue during flight maneuvers, by measuring the strain resistive voltage effect. The strain resistive voltage effect represents the resistive proprieties modification of a conductor by applying a strain effort that determines a certain elongation or suppression. The strain resistive voltage effect has been more widely used after roughly 75 years

since it was discovered, in 1856, by Lord Kelvin, once the first strain gauge marks started being used.

Since then, strain gauge marks have known a rapid development, due to both its constructive simplicity and the relative simplicity of converting the resistive voltage variation into usable signal (the circuit is usually a Wheatstone bridge) [5].

Operating principle

The force and moment convertors are mainly useful for monitoring dynamic structures which are subject to variable strain loading regimes (e.g. tool apparatus, robots, conveyor gauges, etc.); in these situations, the strain takes the form of a force vector and determining its direction is the most important step for completing the structural deformation calculus.

A particular case in which only the absolute value of the force vector is important, vector direction not being important, is the action of calculating the weight of a mass. In this case the value of the force vector can be determined by using the acceleration of the dynamic structure:

$$F = k\, m\, a \tag{1}$$

Where F is the force vector that presses on the mass m, a represents the acceleration, and k represents a coefficient dependent of the measuring unit. The IS for [m] = 1 kg and $[a] = 1\ m/s^2$, $k = 1$ and $[F] = 1$ N.

The torque M is generated by the relation between the vector and the distance between the vector direction and the rotation (center) axis:

$$M = F\, l \text{ or } M = J\, a_u \tag{2}$$

where l is the lever arm, J – inertia moment, a_u – angular acceleration; the torque could take the form of bending, torsion or sectioning; the usual measurement that takes place as a part of the industrial processes is measuring torsion moments.

The IS measuring unit for torque is [N m]. Strongly connected to measuring the stretch and compression forces is the calculus of the relative elongation (measured through the unit effort), which represents the deformation rendered by the force acting on the surface unit within a solid form:

$$\varepsilon = \sigma / E \tag{3}$$

where: ε is the deformation; σ – unit effort; E – elasticity module. Usually ε measuring unit is expressed as [mm/m] or [μm/m].

Considering a fixed conductor with a section A, length l and resistivity ρ, its resistivity variation due to dimension variation produced by the Δl elongation is going to be:

$$\Delta R = (\rho / A)\, \Delta l - \rho\, (l / A^2)\, \Delta A + (l / A)\, \Delta\rho \tag{4}$$

And by dividing the relation to R, the relative variation is going to be:

$$\Delta R / R = (\Delta l / l) - (1/l)*(\Delta A / A) + (1/l)*(\Delta\rho / \rho) \tag{5}$$

Since relative variation of its area can be expressed as:

$$\Delta A / A = -2\mu\, (\Delta l / l) \tag{6}$$

where μ represents the Poisson coefficient (the division of transversal contraction by its elongation); it can be determined, for its resistivity, a linear variation with the volume V, having the form:

$$\Delta\rho/\rho = k(\Delta V/V) = k(\Delta l A + l\Delta A)/V = k\,(1-2\mu)\,(\Delta l / l) \tag{7}$$

Results the expression:

$$\Delta R/R = (\Delta l/ l)\,[1-2\mu + k\,(1-2\mu)] = K\,(\Delta l /l) = K_\varepsilon \tag{8}$$

In practice the strain resistive voltage elements are known as strain gauge marks, where the K coefficient from the last relation is called the mark factor. It is dependent on the nature of the material (k coefficient) and on the production technology of the mark, representing the sensibility of the sensor (the relation between the relative variation of its resistance and the relative elongation).

IV. Case Study: Structural Condition Analysis of the IAR-99 Aircraft

Structural condition monitoring of aircraft, during a life cycle, represents the most important step in determining the real structural resource consumption with the purpose of:

- Increasing safety within the flying activities;
- Reconsidering the aircraft technical resource;
- Updating the maintenance technical documentation;
- Maintenance cost reduction during the aircraft life span;

This paper proposes to use the in-flight practical testing and evaluating in order to validate the theoretical model used for monitoring the structural condition of the IAR-99 aircraft, equipped with strain gauge marks. The evaluation of IAR-99 aircraft structural condition will be done by using the data recorded by the SAIMS on-board recording system, counting the loading cycles according to the G-strain levels and finally comparing results between the data collected from both strain gauge marks and SAIMS on-board recording system.

Based on the results of the analysis and centralizing the real aircraft strain loading data, important decisions can be made in what regards the maintenance process of the entire fleet of aircraft. The purpose is to monitor the fatigue condition of the aircraft, based on the mission profiles and according to the loading spectre, determined by measuring structural linear specific deformations of the structure and flight parameters. Using data from the in-flight testing, estimations can be made for the structural components' life span, by determining the tensions resulted from the specific linear deformations, provided by the strain gauge marks and by calibrating the theoretical calculus model of the finite structural elements specified by the manufacturer [6].

General testing conception

Calculating the aircraft life span is being made by taking into consideration different subparts of the structure, by facilitating the initial building process of the aircraft. Data analysis, after in-flight testing, allows the comparison of recorded data with the initial fabrication data of the aircraft. A number of 12 specific areas of the aircraft have been chosen as representative for monitoring the structural fatigue condition. In figure 1 it is represented the IAR-99 aircraft and the specific areas in which strain gauge marks have been placed.

The areas on which strain gauge marks have been mounted next to high tensions zones and are specific for calculating the real structural life span of the aircraft. According with the studies conducted by the manufacturer, the areas with the maximum strain pressure are the ones where the wings meet the main body of the aircraft. In-flight testing and creating a relation between deformation and resistive tensions lead to calculating the theoretical model for the aircraft structure and updating the real life span resource of the aircraft structure [7]. This latter calculus should not be very different from its original theoretical model because there have been applied safety coefficients and, thus, covering the strain loading factors for the aircraft.

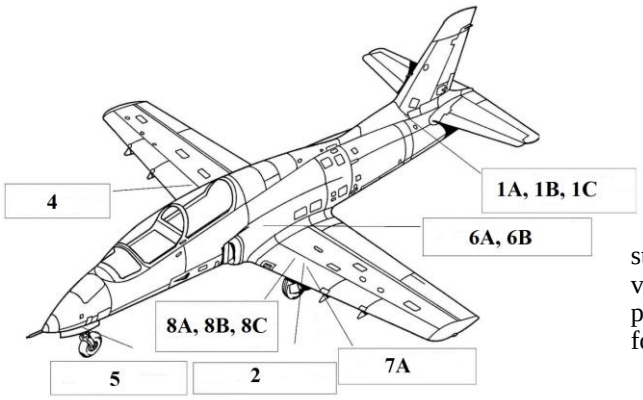

Fig.1. Areas where strain gauge marks have been placed.

Technical data representative for mounting the strain gauge marks:

- the strain gauge marks have been mounted near the maximum tension areas and, therefore, only after the theoretical model had been calibrated, the real life span calculus could be made, according to specific deformation data recorded from the flight testing.
- the strain gauge marks mounted on the aircraft have a correct indication area between -10^{o}C ... +45^{o}C, reason for which the flight testing had to be made under temperature restrictions.
- establishing the loading/unloading strain model during flight testing led to an asymmetric alternant cycle where $S\ max > |S\ min|$ and to an asymmetric coefficient (tension relation $R = S\ min/S\ max$) for the negative cycle.
- the surfaces susceptible for fatigue breakings are the bolted structural elements, surfaces with screws and bolts, these being areas with high strain tension that can transmit the axial cutting forces to the bolting elements.

The testing and evaluation activities have been conducted through the means of recording a big amount of flight data and creating a sufficient database to show the repeatability of the correct results. Altogether, different tension values can be set for the strain gauge marks areas in accordance to the acceleration levels 5 different types of validation sorties have been conducted, which led to verifying data rendered by a 2 year period of flight training with the same aircraft. Model testing, implemented on the analysis ground station for monitoring the structural condition of IAR-99 aircraft, has been made through recording parameters by SAIMS system for all sorties and creating a database for the measurement of fatigue loading cycles.

V. Testing Activities

The general testing and evaluation concept of producing the theoretical model used for monitoring IAR-99 aircraft structure, equipped with strain gauge marks, is structured as follows.:

- Stage 1: - Executing flight testing for the purpose of extracting data from strain gauge marks;
- Stage 2: - Extracting data rendered by the strain gauge marks and creating a database with the newly available data;
- Stage 3: - Analysing the database and creating a function (relation) between the specific linear deformations and the normal Nz accelerations;
- Stage 4: - Executing flight testing in order to validate the function (relation);
- Stage 5: - Gathering the strain loading cycles data in accordance to the normal Nz acceleration for the flight sorties that used the SAIMS system.

In order to confirm results from previous sorties and structural condition data correctness, the specific function validation has been obtained through specialized flight procedures and specific manoeuvres, predominantly used for 5 types of profiles specific for military missions:

1) Stable maneouvers and Navigation;
2) Air-to-air attacks;
3) Air-to-ground attacks;
4) Aerobatic manoeuvres;
5) Demo flight.

Flight testing sorties have been done between heights of 200 m÷5000 m, clean profile of aircraft, with a crew of 2 pilots, take-off weight of 4910 kg, total fuel quantity of 1300 l and play-time between 10 min - 45 min.

In order not to apply any correction, the temperature interval, during all 5 types of sorties, has been kept within the strain gauge marks temperature restrictions -10^{o}C ... +45^{o}C, at any given altitude.

Using strain gauge marks, different strain tensions have been recorded for every flight manoeuver, in correspondence with the specific strain loading cycles, suffered by the IAR-99 aircraft, used for flight tests. Thus, a relation between different types of flight missions and the equivalent strain loading cycles has been established, which can be very useful in determining the real structural fatigue level for each flight manoeuver.

It has been concluded that, mostly, the resulted strain tensions are within the limitations provided by the manufacturer, actually being lower in the case of calculated limits for elastic fatigue. It can be observed that the recorded values, transformed into strain tensions, are

very close to the ones provided by the manufacturer as technical resource for IAR-99 aircraft structure.

Next, a database has been created using the results recorded by the SAIMS system. The analysis of this database can lead to obtaining a theoretical model to correlate the strain loading cycles and normal G-strain acceleration levels. The purpose is to measure and analyse strain loading cycles for every aircraft in the fleet and impose safety measures when the technical resource provided by the manufacturer is depleted, in order to anticipate the right time to conduct more intricate and complex structural verification and maintenance [14]. Composite materials represent a much bigger part in the building process of structural components and elements of aircraft. Although the cost is bigger than the conventional materials, aeronautical industry has appreciated composite materials' mechanical proprieties as being the best solution for building airplanes and also reducing weight. Introducing composite materials in the aviation industry comes with the burden of developing new types of maintenance technology that can also be applied to isotropic materials [8].

Knowing the way materials behave is paramount for anticipating its response to different types of strains in order to considerably reduce the maintenance costs. A crack within the aircraft structure does not necessarily mean that the structure is damaged beyond repair. Continuously monitoring the structure allows further using of damaged components until the anticipation of the right time to change it, by predicting the critical length of the crack. Identifying the deformation of a structure is fundamental. Materials, mostly the composite ones, can present internal deteriorations that cannot be observed with the naked eye. Even though there is multiple detection technics, the visual inspection is still the most widespread. Only when more dangerous deformations are identified, more precise, but more expensive detection technics are applied [9].

New materials rely on new technics for exploiting them, characterized by high costs. Starting with the main idea for which the use of composite materials has been adopted, reducing costs on the long run, it is considered mandatory to implement new technologies of using these new materials in order to efficiently apply the entire industrial process, from both economical and operational stand points.

By using the data recorded during a 2 years period and for an amount of, roughly, 300 flight hours, with the help of the SAIMS system, a database has been created and the available data for comparison are presented in table 1.

Therefore, by comparing strain loading cycles, provided by the manufacturer as technical resource, with the strain loading cycles resulted from the relation between data recorded by SAIMS system and data taken from the strain gauge marks, a correct fatigue level of the aircraft structure can be established, for each aircraft, according to its flight history.

It can be observed that within 300 real flight hours, the aircraft has already consumed its technical resource provided by the manufacturer for 1000 theoretical flight hour, according to the strain loading/unloading cycles:

TABLE 1. STRAIN LOADING CYCLE COMPARISON

1	2	3	4	5	6
G-factor level	Strain loading cycles provided by manufacturer (per 1000 flight hours resource)	Number of strain loading cycles for 300 flight hours (SAIMS)	Number of real strain loading cycles available after 300 flight hours	Theoretical number of real strain loading cycles for 3000 flight hours	Theoretical number of real strain loading cycles available after 3000 flight hours
(1)	(2)	(3)	(4)=(2)-(3)	(5)=(3)x10	(6)=(2)x3-(5)
2,45	17.000	4769	12.231	47690	3310
3,15	9.500	4021	5.479	40210	-11710
3,85	6.500	2594	3.906	25940	-6440
4,55	4.500	1263	3.237	12630	870
5,25	2.500	458	2.042	4580	2920
5,95	1.500	54	1.446	540	3960
6,65	300	5	295	50	850
7,35	150	1	149	10	440
0	500	1343	-843	13430	-11930
-0,36	200	958	-758	9580	-8980
-0,72	100	489	-389	4890	-4590
-1,08	60	235	-175	2350	-2170
-1,44	35	86	-51	860	-755
-1,8	30	34	-4	340	-250
-2,16	25	12	13	120	-45
-2,52	20	4	16	40	20
-2,88	15	1	14	10	35

- positive cycles for 2,45 N z - 28,05%;
- positive cycles for 3,15 N z - 42,32%;
- positive cycles for 3,85 N z - 39,90%;
- positive cycles for 4,55 N z - 28,06%;
- positive cycles for 5,25 N z - 18,32%;
- positive cycles for 5,95 N z - 3,6%;
- positive cycles for 6,65 N z - 1,66%;
- positive cycles for 7,35 N z - 0,66%.

(*Column 3 cycles* as compared to *Column* 2 cycles)

Regarding the negative cycles specter, the resource given for 1000 theoretical flight hours has been completely depleted in just 300 real flight hours, for G-Force values between 0 and -1,8 g. Thus, the number of strain loading cycles is bigger than it was initially calculated for 3000 theoretical flight hours. As a side note, the low number of negative strain loading cycles provided initially by the manufacturer has been calculated this way in order to keep the aircraft weight as low as possible.

The highlighted red-colored loading cycles, in table 1, represent the number of cycles that are not covered by the theoretical cycles/resource provided by the manufacturer.

Data show that for the G-force intervals of (+3,15… +3,85) and (0 … -2,16), the real loading cycles are bigger than the ones provided by the manufacturer. Therefore, more thorough and more often investigations are required, in order to prevent in-flight safety issues.

It is obvious that the theoretical resource provided by the producer is to be met way before it was foreseen. Therefore, by utilizing the proposed method of monitoring the structural condition, the real remaining technical resource can be determined for each airplane, according to

the way it was used, and also it would increase the safety level for both flight procedures and maintenance processes.

At the end of this analysis a set of rules could emerge in what concerns the flight missions and specific use, for every airplane, by calculating the remaining number of strain loading cycles, taking into consideration data recorded from all previous sorties.

A new emerging direction is represented by the use of intelligent materials with self-repairing capabilities. Although this concept is very interesting, it is not mature enough in order to be adopted by big aviation manufacturers. Another problem identified for this type of materials is the high production costs. There are numerous efforts from civilian airliners to reduce costs with stationed airplanes due to maintenance or incident-related activities. The development of a voluntary system using guidance from anonymous declarations regarding incidents, implemented by the American Agency ASRS, has allowed the reduction of incident on the ground, mainly by improving all operational and maintenance procedures. A system of sensors, for monitoring the structural condition of an aircraft, would reduce stationing time periods, affected by mandatory inspections and, thus, reduce general costs of operating any type of aircraft. [10].

The problems of the newly proposed maintenance technology are connected to limitations given by the implementation and certification of the new monitoring system. The next step into this area is to include the structural monitoring system in the initial processes of airplane building. Flight data have highlighted the possibility of directly monitoring the structural strains of an aircraft with implications in identifying the difference between the real technical resource and the theoretical resource specified by the manufacturer.

Monitoring the structural condition allows the current fatigue state of the tested aircraft and, by interpolating data, it can be determined how the entire fleet is currently affected. This leads to the optimization of maintenance planning and processes for all airplanes in the fleet. Direct structural monitoring and the determination of the remaining technical resource cannot replace planned maintenance specified by the manufacturer but can represent the basis for future safety recommendations and measures for improving the general use of airplanes. The results of the recorded linear specific deformations can be compared with the theoretical calculus and it can offer important data for calibrating the theoretical model.

With the help of this model, a precise estimation of the remaining technical resource can be made and, by knowing the total flight hours of an aircraft, the structural fatigue condition can be determined.

The results obtained from the validation of the theoretical model of calculus, presented in this project, can be used in order to analyse the structural condition with no strain gauge marks mounted on. If the total flight history of the fleet is not available, an approximation can be made using the 5 types of flight missions, previously recorded, each type of mission corresponding to a certain number of strain loading cycles for every G-factor level obtained.

In this way, possible measures can be identified when theoretical technical resource, given by the manufacturer, is depleted before its time, as rescheduling the planned period for capital revision specified by the producer, respectively 800±50 functioning hours or/and 8±0,5 years for IAR-99 aircraft.

The process of monitoring the structural condition of aircraft is rapidly becoming a necessary method for determining technical resource for airplanes, thus, reducing safety problems, related to flight activities, and eliminating different technical errors. Most aircraft manufacturers, both military and civilian, are investing in different methods of anticipating technical problems in order to reduce maintenance cost and aeronautical safety incidents.

Of course, there are more efficient methods of monitoring and repairing aircraft than the one using strain gauge marks, as making use of intelligent materials ASRC type (Active Sensing Repair Composite), characterized by implementing of self-repairing materials while the structural damages are being produced. Although this advanced system could offer better results, it implies very big costs due to the fact that this technology hasn't yet been developed to be mature enough to offer a decent safety level for practical utilization of it [11].

There are two approaches regarding structural integrity monitoring: structural degradation monitoring and operational monitoring. In general, structural degradation monitoring can be made only after structural damages, as cracks, appear and are already visible. Operational monitoring implies evaluation of material fatigue level, extreme strains suffered by the material and effects of environmental factors on the structure, even before cracks or stress marks become visible [12].

In what concerns operational monitoring, the most efficient method, from cost and safety stand points, has been proved to be the one using strain gauge marks. The proposition of this method is applied mostly to military aircraft, used for flying in all types of missions.

VI. CONCLUSIONS

Even though aviation is a very standardized area, the usage of military aircraft in all types of mission and pushing its structure to the limit, make it very hard to implement a standardization of the way we determine the real structural technical resource.

The main goal of this paper was to efficiently monitor the structural condition of a highly maneuverable aircraft using strain gauge marks and it has been demonstrated that the operational resource given by the manufacturer can easily be depleted within a smaller number of flight hours than initially anticipated, by executing a number of specific sorties, that can stress the aircraft structure way above the normal use of it. The calculated model for every type of mission can enhance the maintenance process by measuring the structural strain loading cycles and, consequently, the operational resource of aircraft structure, by producing a database containing information such as the types of sorties, play-time and the results recorded by the strain gauge marks.

The role of this study is to equip every aircraft with strain gauge marks, in order to improve structural condition monitoring or at least to use the calculated

theoretical model. By utilizing the strain gauge marks method for monitoring the structure of highly maneuverable aircraft, a database can be created using strain loading/unloading cycles for every type of flight mission and, therefore, structural damages of any kind can be anticipated for every aircraft, according to its previous utilization, in different operational types of missions.

The theoretical model, validated through flight testing activities, corroborated with the database for every aircraft and type of mission, represent an effective way to reduce maintenance costs and improve aeronautical safety, by anticipating and preventing technical incidents or even aviation accidents.

Source of research funding in this article: Research, Innovation and Flight Test Center Military Equipment and Technologies Research Agency Craiova and Department of Electrical, Energetic and Aerospace Engineering financed by the University of Craiova.

Contribution of authors:

First author – 40%

First coauthor – 30%

Second coauthor – 30%

Received on July 10, 2021

Editorial approval on October 25, 2021

REFERENCES

[1] E. F. Bhrun, B. S., M. S., C.E., "Analysis and Design of Flight Vehicle Structures" - , Tri-State Offset Co., 1973.

[2] F. Smith - Advisory Council for Aviation Research and Innovation, Avalon Consultancy Services Ltd, 2013.

[3] "Structural Health Monitoring System Implementation on Civil Aircraft", SMART MATERIALS, STRUCTURES & NDT in AEROSPACE. Montreal, Quebec, Canada, 2011.

[4] Alwyn and J Topham – "Boeing Dreamliner Incidents Raise Safety Concerns", *Aviation Week*, 2013.

[5] RD3 WichiTech Industries. Digital Electronic Tap Hammer. Operations and Maintenance Manual;

[6] G. Georgeson, S. Lea, and J. Hansen, "Electronic Tap Hammer for Composite Damage Assessment", SPIE - The International Society for Optical Engineering, 1996.

[7] H. Kim, "Impact Damage Formation on Composite Aircraft Structures", *JAMS 2014 Technical Review*, 2014, March 25-26.

[8] H. Massengill, "Applied Aerodynamics" – Commercial Flight. Aerospace America, p. 7. 97, 2005

[9] S. Mancini, G. Tumino, and P. Gaudenzi, "Structural Health Monitoring for Future Space Vehicles", *Journal of Intelligent Material Systems and Structures*, 2005.

[10] M. Kaden & R. Keck, "Repair Concept Supported by Laser Removal and Inductive Heating", *The 28th Intern. Congress of the Aeronautical Sciences.* Brisbane, Australia, 2012.

[11] G. Marsh, "The challenge of composite fuselage repair", Reinforced Plastics, 2012.

[12] B.G. Kanki and C.L. Brasil, "Analysis of Ramp Damage Incidents and Implications for Future Composite Aircraft Structure", *Proceedings of the 15th International Symposium on Aviation Psychology*. Dayton, OH: Proceedings of the 15th International Symposium on Aviation Psychology, Dayton, OH, 2009.

[13] MILHDBK5H –Military Handbook – Metallic Materials and Elements for Aerospace Vehicle Structures, 1998.

[14] ASTM E 1049-85 - Standard Practices for Cycle Counting in Fatigue Analysis, 1997.

[15] E.F. Bhrun et al., "Analysis and Design of Flight Vehicle Structures", Tri-State Offset Co., 1973.

[16] Niculescu N.A., Corcau J., Gavril A. "Integrated System for Monitoring Aircraft Structural Condition by Using the Strain Gauge Marks Method", *International Conference on Applied and Theoretical Electricity (ICATE) 2021*, 27-28 May, IEEE conference; 10.1109/ICATE49685.2021.9465010; ISBN:978-1-7281-8036-6.

[17] RD3, WichiTech Industries. Digital Electronic Tap Hammer. Operations and Maintenance Manual.

Two Numerical Studies for Longitudinal Movement of a Canard UAV with Vectored Thrust

*Liviu Dincă, *Jenica-Ileana Corcău and **Dionis Cumpan
*Department of Electrical, Energetic and Aerospace Engineering,University of Craiova, Romania
** AEROSTAR S.A. Bacău, Bacău, Romania
ldinca@elth.ucv.ro, jcorcau@elth.ucv.ro. , deniscumpan@gmail.com

10.52846/AUCEE.2021.1.13

***Abstract* — This work presents a study concerning the possibilities to improve the longitudinal dynamic of a canard UAV using vectored thrust. It is followed to harness the advantages of canard configuration of UAV and to obtain further a better longitudinal dynamic, able to fulfil more complex missions than canard UAV without vectored thrust. There are tested two methods. The first uses the UAV polars obtained in XFLR 5 and extended, using literature experience, a little bit over the stall angle. By this method is determined the necessary gain between the elevator steering angle and thrust deflection angle in order to maintain the UAV in landing configuration (flaps down) to the optimum angle of attack for landing. Using this method is studied also the effect of vectored thrust in maneuver, in cruise configuration. Step signal on the elevator, thrust and both commands simultaneously are applied on the UAV without and with vectored thrust and are identified the advantages of vectored thrust in this situation. The second method uses the polars of the UAV components obtained in XFLR5, extended independently up to a little bit above each stall angle. By this way is studied the effect of the vectored thrust on the atack angle in horizontal flight for the UAV in cruise configuration. There are obtained horizontal flight parameters (speed, elevator steering, angle of attack and thrust), when vectored thrust is used. It is followed to obtain results for attack angle as high as possible. Both methods are limited by the results obtained in XFLR 5, that can't determine polars at atttack angles near stall, and for the second method, by the aerodynamic interferences between UAV components.**

Cuvinte cheie: *metode numerice, mişcare logitudinală, configuraţie UAV, propulsie vectorizată.*

Keywords: *numerical methods, longitudinal movement, canard UAV, vectored thrust.*

I. Evolution Of Aircraft Building And Maintenance Process

UAVs have known a very fast development in the last period, due to technological progress, their applications reaching a wide variety. UAV configurations are very divers and they folds each time to the mission they were designed. For relative short distance and relative small flight speed (a few dozen of km/h) are used frequently in present multi-rotor UAVs with net superior maneuverability than airplane type UAVs [4]. By the other hand, airplane type UAVs have the advantage of a superior aerodynamic efficiency than multi-rotors, so they are better for long range missions with higher speeds and larger payload [1],[7].

An airplane type configuration with a very high aerodynamic efficiency is the canard [2]. By the way, excepting the glider configuration, with a very large span, canard UAVs can reach the higher aerodynamic efficiency for a given mission. This fact is due to lift obtained both on the wing and the horizontal tail, so the aerodynamic efficiency is higher. Nevertheless, canard configuration has some disadvantages [3]. One disadvantage concerns this configuration can't reach high angle of attack. This fact limits both maneuverability performances and take-off and landing performances. Low angle of attack means low load factor, high take-off and landing speeds and further, longer runways.

This load factor limitation is produced by the higher angle of attack for the horizontal tail than for the wing. In these conditions, horizontal tail reaches first the stall angle and can't produce enough pitch moment to maintain the airplane and as result, the wing, at high angle of attack. In landing configurations, with flaps at maximum steering angle, the problem is more difficult because the horizontal tail, even with a maximum elevator steering, can't compensate the wing dive moment. A solution to substantially increase the pitch moment is to use vectored thrust [6], [11]. By deflecting the thrust, it is possible to obtain larger pitching moment and further to reach higher angle of attack and to perform manoeuvres with higher load factor.

II. Configuration Of Studied Uav

In this study is considered a configuration similar to other studies, but with some modifications. This configuration is presented in figure 1. UAV constructive parameters are presented in table 1.

Table 1. Uav Constructive Parameters

Entire UAV	
Length [m]	2.25
Span [m]	2
Height [m]	0.4
Weight [kg]	7
Wing	
Aerodynamic profile	NACA 64A-212
Span [m]	2
Chord in symmetry plane [m]	0.25
External chord [m]	0.125

Mean aerodynamic chord [m]	0.194
Sweep angle [°]	-20
Dihedral angle [°]	0
Setting angle [°]	0
Ampenaj horizontal	
Aerodynamic profile	NACA 64A-212
Span [m]	1
Chord in symmetry plane [m]	0.22
External chord [m]	0.11
Mean aerodynamic chord [m]	5
Sweep angle [°]	0
Dihedral angle [°]	2
Ampenaj vertical	
Aerodynamic profile	NACA 0012
Span [m]	0.25
Chord in symmetry plane [m]	0.22
External chord [m]	0.11
Mean aerodynamic chord [m]	0

Wing aerodynamic profile was choose NACA 64A-212, with a relative high thickness, good aerodynamic qualities and ensures a good wing rigidity. In order to improve aerodynamic efficiency a negative sweep angle was used. A negative sweep angle also avoids flutter danger. Wing setting angle is 0^o.

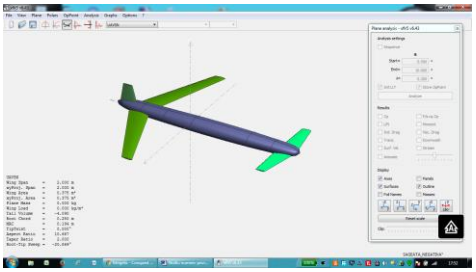

Fig. 1. Studied UAV configuration.

Because the horizontal tail has to produce a big enough pitching moment in order to maintain the longitudinal equilibrium we gave up the practice to use symmetric aerodynamic airfoil and it is adopted also NACA 64A-212 with a setting angle 2^o. In these conditions, horizontal tail offers enough lift to maintain longitudinal equilibrium. For the vertical tail it is used the symmetric profile NACA 0012, suited for this application. Using XFLR5 the following polar curves are obtained for this configuration.

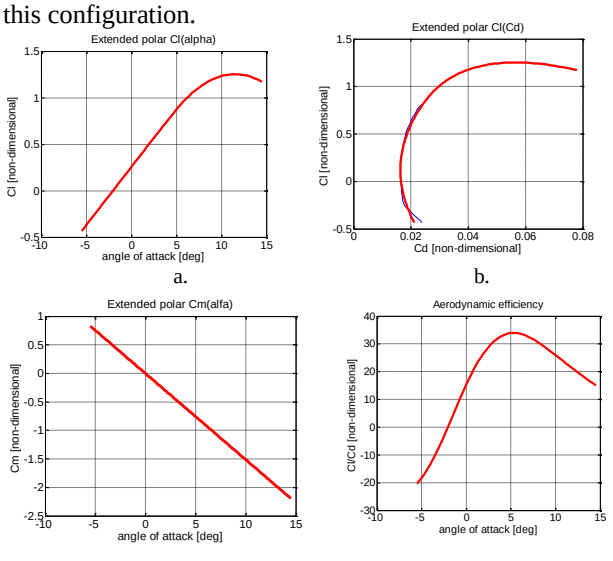

Fig. 2. Polar curves for the studied configuration.

XFLR5 can't determine polar curves at high angle of attack, near the stall angle. For these angle of attack values the polar curves were extrapolated and approximated using profiles data and indications in literature.

We can observe a high aerodynamic efficiency, above 30, that is a very good value for airplane configuration. Aerodynamic studies were performed neglecting the fuselage, because XFLR5 has a better behavior in these conditions.

From $C_m(\alpha)$ dependence it is obtained equilibrium attack angle 0^o, with elevator in neutral position. This attack angle offers a lift coefficient 0.278, useful at high speed.

Take-off and landing conditions were studied also. For take-off it is considered a 20^o flaps steering and for landing 30^o. Elevator was considered with a 20^o steering angle both for take off and landing in order to reach the most convenient attack angle. Take-off and landing polars in comparison with cruise polars are presented in figure 3.

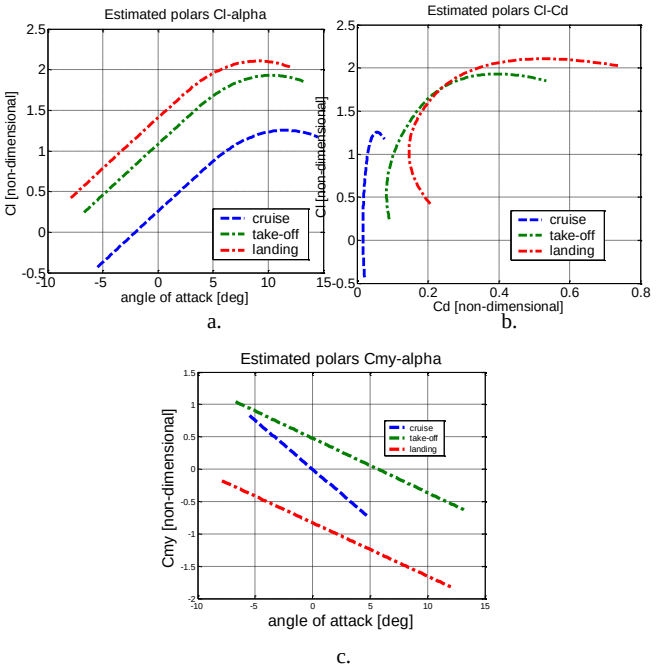

Fig. 3. Take-off and landing polars.

In $C_z(\alpha)$ polar (figure 3.a) we observe a convenient angle of attack both for take-off and for landing about 5^o. It is not a high attack angle, but we have to take into account in take-off and landing configuration flaps produces a high dive moment. This angle of attack can be maintained in take-off configuration with a maximum elevator steering angle about 20^o, as it results in $C_m(\alpha)$ dependence (figure 3.c). For landing configuration, in order to maintain the 5^o angle of attack, it is necessary an extra pitching moment coefficient $\Delta C_m = 1.24$. This moment can be obtained with vectored thrust.

III. Improving Longitudinal Behaviour With Vectored Thrust

The aim of this study is to obtain with vectored thrust a pitching moment to maintain the UAV at 5° angle of attack, considered optimum for landing. A simple hypothesis concerning vectored thrust is to consider the thrust deflection angle proportional with the elevator steering angle. It is produced by this way the extra pitch moment with UAV behavior similar with a UAV with higher elevator efficiency. So, we consider the thrust deflection proportional with the elevator steering and we will follow to reach a 5° attack angle in landing configuration.

UAV equilibrium with vectored thrust is presented in figure 4 and is described by equations (1) [2],[5].

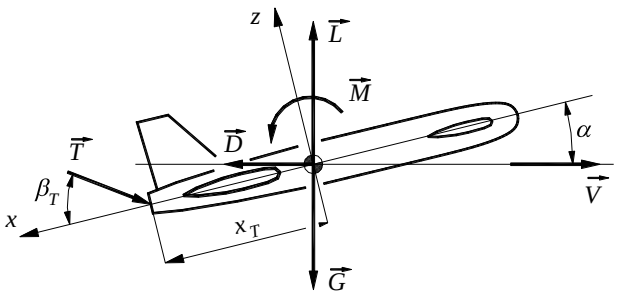

Fig. 4. Longitudinal equilibrium of UAV with vectored thrust.

$$\begin{cases} L - G - T\,sin(\beta_T - \alpha) = 0 \\ D - T\,cos(\beta_T - \alpha) = 0 \\ M + T \cdot x_T\,sin\,\beta_T = 0 \end{cases} \quad (1)$$

From the second equation results

$$T = \frac{\frac{\rho}{2}V^2 S C_d}{cos(\beta_T - \alpha)} \quad (2)$$

that substituted in the third leads to

$$\frac{\rho}{2}V^2 S c_{ma} C_m - \frac{\rho}{2}V^2 S C_d x_T \frac{sin\,\beta_T}{cos(\beta_T - \alpha)} = 0 \quad (3)$$

Supposing attack angle α small (5°) it is possible to approximate $cos(\beta_T - \alpha) \approx cos\,\beta_T$ and results

$$tg\beta_T = \frac{c_{ma} \cdot C_m}{x_T C_d} \quad (4)$$

Relation (4) is very simple and allows determining the thrust deflection to obtain the desired angle of attack. In relation (4) C_m and C_d are the aerodynamic coefficients for the optimum landing attack angle in landing configuration.

Considering proportionality between thrust deflection and elevator steering

$$\beta_T = K_T \cdot \beta_e \quad (5)$$

and elevator steering in landing $\beta_e = 20^o$, proportionality coefficient K_T can be found.

With the polars considered before results C_{mland}= -1.24, C_{xland}=0.313 C_{zland}=1.955. From UAV configuration it is obtained x_T=1.05 m and so, β_T =36.5°, with $K_T = 1.82$.

Equilibrium angles of attack, without vectored thrust, in cruise configuration can be found from $C_m(\alpha)$ dependences for different elevator steering angles, using XFLR5. These are shown in figure 5.a and dependence between elevator steering and equilibrium angle of attack is in figure 5.b. Elevator steering angles were considered between 0° and 20° with 5° step.

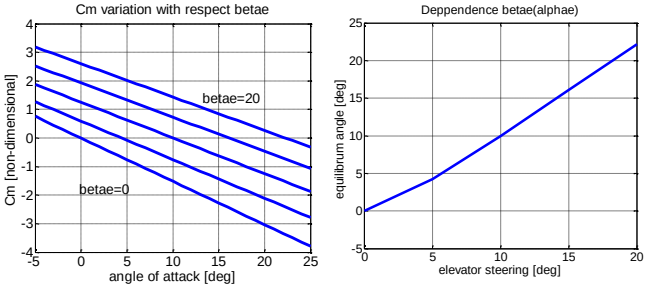

Fig. 5. Equilibrium angle of attack without vectored thrust, cruise configuration.

A convenient dependence between angle of attack and elevator steering is obtained in cruise configuration, so the UAV could be well controlled in cruise configuration.

The same study is performed for landing configuration. Results are in figure 6. Obtained results show high module and negative values for the equilibrium angle of attack. These values were obtained by extrapolation of $C_m(\alpha)$ dependences in XFLR5. By consequence, these values have not to be considered accurate, but we can conclude the flaps pitch moment in landing configuration is too large and optimum angle of attack for landing can't be maintained with an acceptable elevator steering.

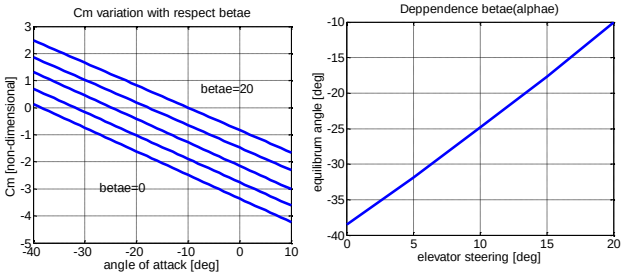

Fig. 6. Equilibrium angle of attack without vectored thrust, landing configuration.

We tried to obtain the optimum landing angle of attack using vectored thrust, with a thrust deflection described by relation (5), with K_T values around 1.82, as it resulted from previous estimations.

For this situation, aerodynamic coefficients have to satisfy relation

$$c_{ma} \cdot C_m(\alpha, \beta_e) - x_T C_d(\alpha, \beta_e) \frac{sin(K_T \beta_e)}{cos(K_T \beta_e - \alpha)} = 0 \quad (6)$$

that is in fact relation (3) detailed for equilibrium angle of attack in landing configuration. Equation (6) is solved for elevator steering between 5^o and 20^o with step 5^o using dependences $C_m(\alpha,\beta_p)$ and $C_d(\alpha,\beta_p)$ estimated using XFLR 5.

Using these dependences we represented function *F* in the left hand term in equation (6) and found the equilibrium angles of attack.

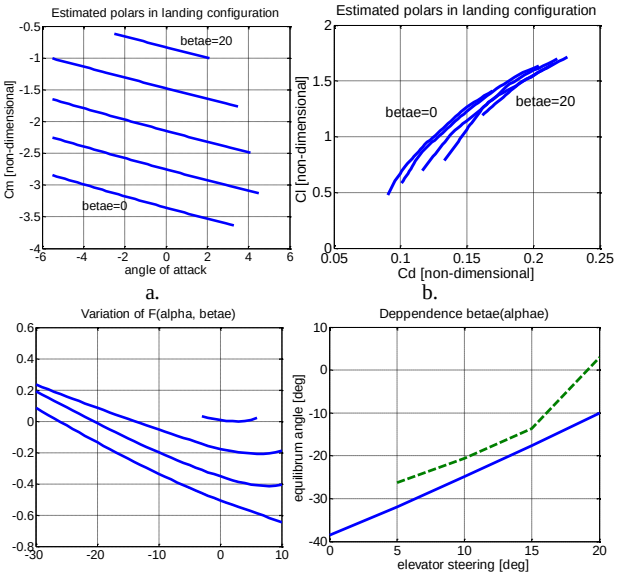

Fig. 7. F function variation and equilibrium angle of attack in landing configuration (dashed line in figure 7.d).

In figure 7.d we observe elevator steering around 20^o can maintain angle of attack around optimum value in landing configuration. Nevertheless, a very rapid decrease of equilibrium angle of attack produces when elevator steering decrease. Again, equilibrium angle of attack lower than -10^o can not be considered accurate, but we have to notice it is possible to maintain optimum landing angle of attack at maximum elevator steering using vectored thrust.

IV. Vectored Thrust Effects Upon Longitudinal Command Response

In the following is studied the effect of vectored thrust upon the elevator command response, around a flying regime characterized by zero elevator steering and zero thrust deflection, as it assumed in relation (5). In this purpose we used the longitudinal movement equations [5],[8], [9]

$$\begin{cases} m\dfrac{dv_x}{dt} = T\cos(\beta_T) - D\cos\alpha - G\sin\alpha \\ m\dfrac{dv_z}{dt} = T\sin(\beta_T) + G\cos\alpha - L\cos\alpha \\ J_y\dfrac{d\omega_y}{dt} = M + T\cdot x_T\sin\beta_T \end{cases} \quad (7)$$

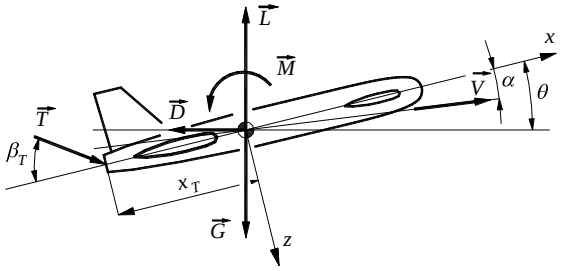

Fig. 8. Reference frame for command response study.

Equations (7) were deduced using the flight dynamics reference frame, as is presented in figure 8.

These equations linearized leads to the same system as the system for UAV without vectored thrust, but with some extra terms in the command matrix.

We considered as command variable the elevator steering and thrust, that is accompanied now by the thrust deflection according relation (5) and thrust variation.

Command matrix without vectored thrust is [10],

$$B = \begin{bmatrix} \frac{\partial F_x}{\partial \beta_e} & \frac{\partial F_x}{\partial T} \\ \frac{\partial F_z}{\partial \beta_e} & \frac{\partial F_z}{\partial T} \\ \frac{\partial J_y}{\partial \beta_e} & \frac{\partial F_z}{\partial T} \\ 0 & 0 \end{bmatrix} \quad (8)$$

and when vectored thrust is used, it becomes

$$B = \begin{bmatrix} \frac{\partial F_x}{\partial \beta_e} - \frac{T}{m}K_T\, sin(K_T\beta_e) & \frac{\partial F_x}{\partial T} \\ \frac{\partial F_z}{\partial \beta_e} - \frac{T}{m}K_T\, cos(K_T\beta_e) & \frac{\partial F_z}{\partial T} \\ \frac{\partial J_y}{\partial \beta_e} + \frac{T}{J_y}x_T K_T\, cos(K_T\beta_e) & \frac{\partial M_y}{\partial T} \\ 0 & 0 \end{bmatrix} \quad (9)$$

Stability and command matrices can be obtained using XFLR5 for airplane without vectored thrust, and for data considered in this study are.

$$A = \begin{bmatrix} -0.00022 & 0.1601 & 0 & -9.81 \\ -0.3555 & -12.478 & 46.560 & 0 \\ 3.287\cdot 10^{-11} & -1.207 & -1.9087 & 0 \\ 0 & 0 & 1 & 0 \end{bmatrix}$$

$$B = \begin{bmatrix} 0.214 & 9.9\cdot 10^{-3} \\ -142.15 & 0 \\ 10.278 & 0 \\ 0 & 0 \end{bmatrix} \quad (10)$$

(11)

We considered a flying regime in cruise configuration with 0^o elevator steering, with parameters V=55.204m/s, $\beta_{e0} = 0^o$, $\alpha_0 = -1.172^o$, $C_{z0} = 0.098$, $C_{x0} = 0.016$. Inertial parameters are m=7kg, $J_y = 44.72$ kgm2 and gravity center position XCG=-0.7 m. A SIMULINK study produced results in figure 9.

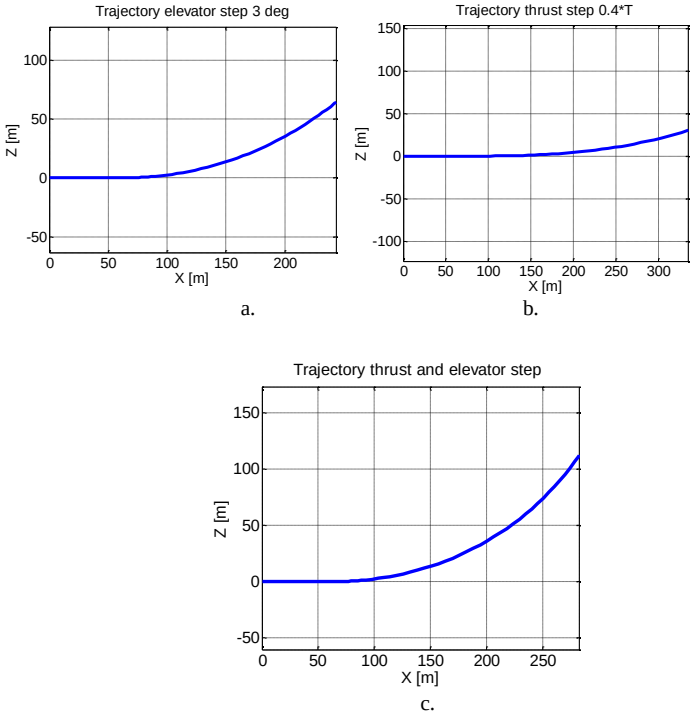

a. b. c.

Fig. 9. Command response without vectored thrust.

In the case with vectored thrust, command matrix is (12) and the command response is presented in figure (10).

$$B = \begin{bmatrix} -6.108 & 9.901^{-3} \\ -4.517 \cdot 10^2 & 0 \\ 3.354 \cdot 10^2 & 0 \\ 0 & 0 \end{bmatrix} \quad (12)$$

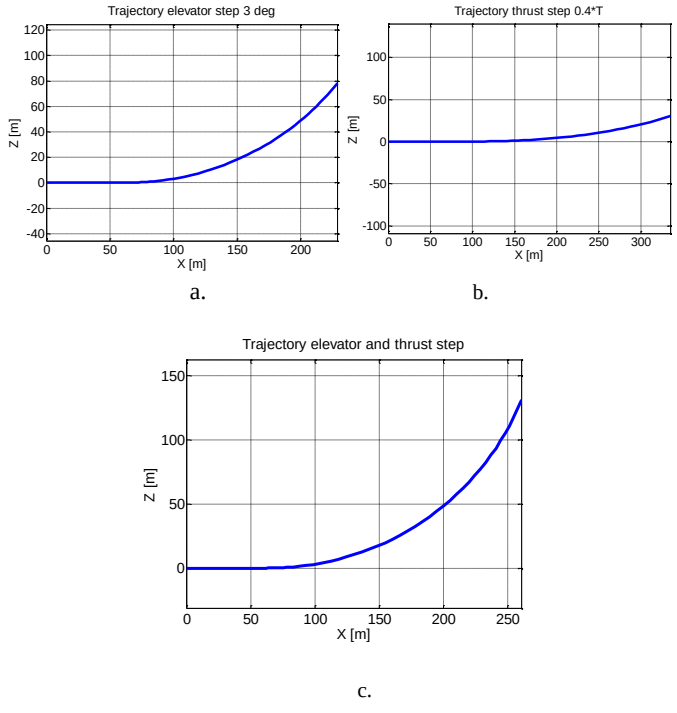

a. b. c.

Fig. 10. Command response with vectored thrust.

We can observe about 25 m extra altitude after 5 second from the step command, when vectored thrust is used. It correspond an extra climbing slope about 5 deg when the elevator steering step is 3° and thrust deflection is about 6 deg. A more edifying evaluation of the vectored thrust effect can be obtained if is estimated parameter $\partial\beta_e/\partial n_z$ [7] that is often used for airplane maneuverability estimation.

V. Study Of The Longitudinal Movement Using UAV Components Polars

Previous study based on the UAV polars obtained in XFLR 5 has an important limit using the UAV angle of attack. XFLR 5 can not compute the polars at high angle of attack. We intent to determine in the following the vectored thrust UAV behavior at high attack angles, near the take-off and landing angles of attack. In this purpose we studied first the polars for each UAV component – wing, stabilizer, fin – in XFLR 5. For each component the polars are determined for higher attack angles, even not for attack angles near stall angle. After that, based on the literature experience we performed an estimation of these polars until the stall attack angle and a little bit higher. We assumed the forces upon the UAV as the sum of the forces upon each component. This approach has also limits due to aerodynamic interferences between the UAV components, but we accept this approach in this study.

This study is performed for the cruise configuration. Components polars obtained by the specified method are presented in figures 11, 12 and 13.

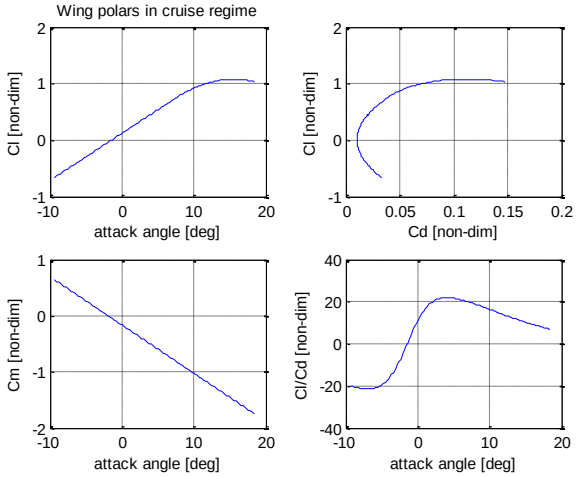

Fig. 11. Wing polars in cruise regime.

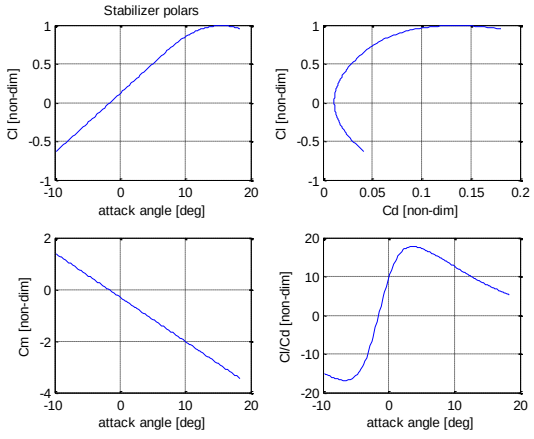

Fig. 12. Stabilizer polars.

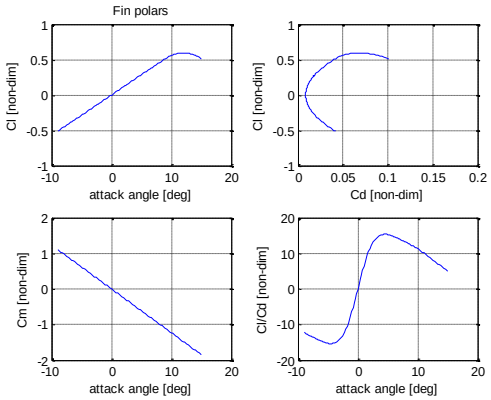

Fig. 13. Fin polars.

We studied the horizontal flight at different angles of attack, considering the vectored thrust effects. In this purpose we took into account the following forces and moments upon the UAV: weight; lift, drag and pitching moment due to the wing in translation movement, lift, drag and pitching moment due to the stabilizer in translation movement; forces and moments due to the engine; forces and moments due to the elevator steering. We considered the forces along x and z axis and the pitching moment.

VI. Flight Parameters Estimation For Equilibrium Conditions

In order to determine the equilibrium flight parameters we considered the non-linear system

$$\begin{bmatrix} F_x \\ F_z \\ M_y \end{bmatrix} = \begin{bmatrix} F_x(\alpha, \beta_p, T) \\ F_z(\alpha, \beta_p, T) \\ M_y(\alpha, \beta_p, T) \end{bmatrix} \quad (12)$$

with the parameters attack angle α, elevator steering β_p and engine thrust T. Between the thrust deflection angle and the elevator steering angle we considered a linear dependence with different proportionality factors with respect the gravity center position. For each flight speed we solved the system (12) using Newton method with a relaxation factor 0.4. By this way we determined for each horizontal speed the angle of attack, elevator steering and thrust. For four center of gravity positions X_{cg} = -0,6 , -0,4, -0,2 and 0 m we obtained the results in figure 14.

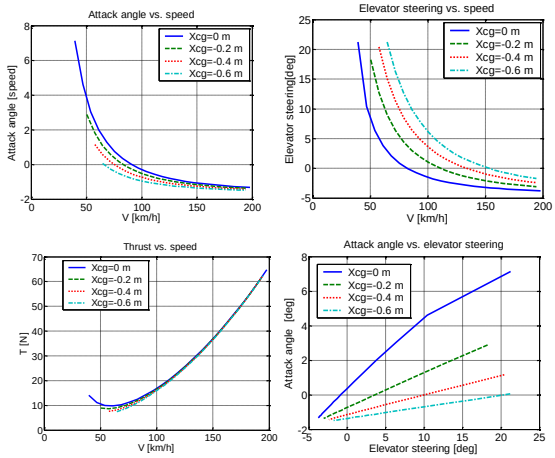

Fig. 14. Flight parameters for each gravity center positing.

As consequence of attack angle limitation once the gravity center moves forward, minimum speed increase for the considered UAV. Thrust variations are negligible.

Further we studied the vectored thrust effect upon the horizontal flight regime. We considered a thrust deflection proportional with the elevator steering. Proportionality factor was considered K_T =2 for X_{cg} = -0.2 and 0 m and K_T =2 for X_{cg} =-0.6 and -0.4 m. Engine exhaust was considered first placed rear the airplane as is shown in figure 8. Results for the considered gravity center positions are presented in fgure 15, 16, 17 and 18.

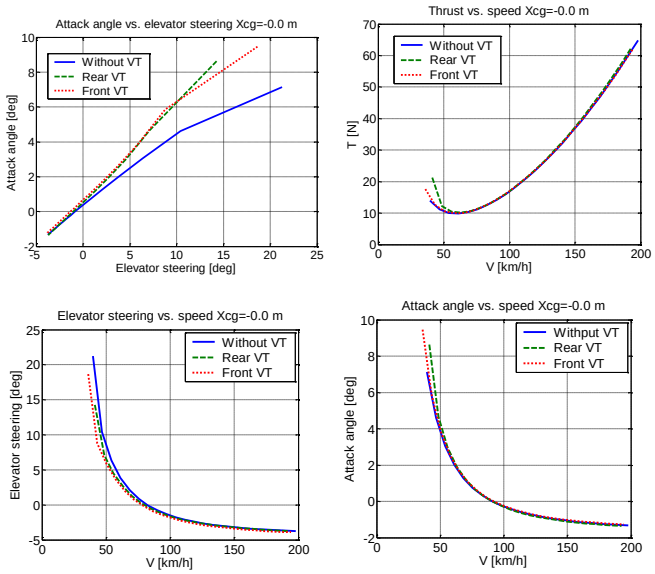

Fig. 15. Flight parameters using vectored thrust for Xcg = 0 m.

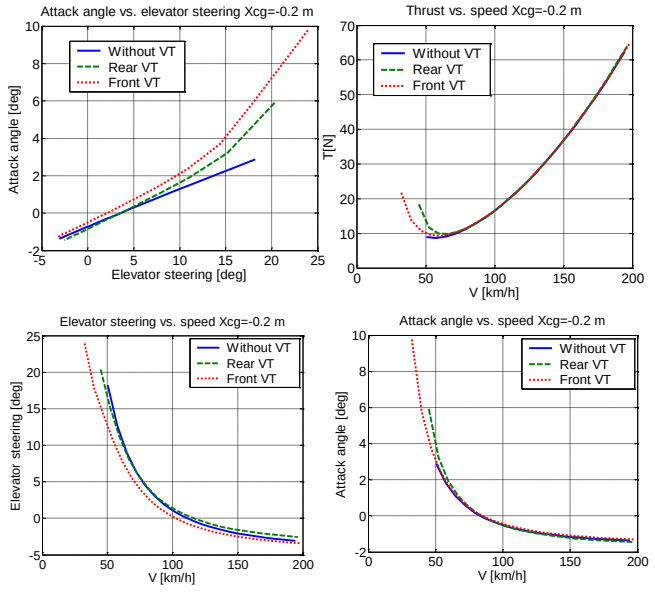

Fig. 16. Flight parameters using vectored thrust for Xcg = -0.2 m.

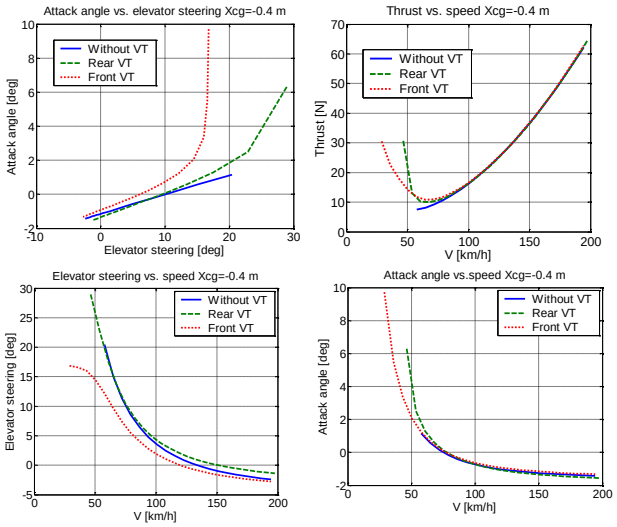

Fig. 17. Flight parameters using vectored thrust for Xcg = -0.4 m.

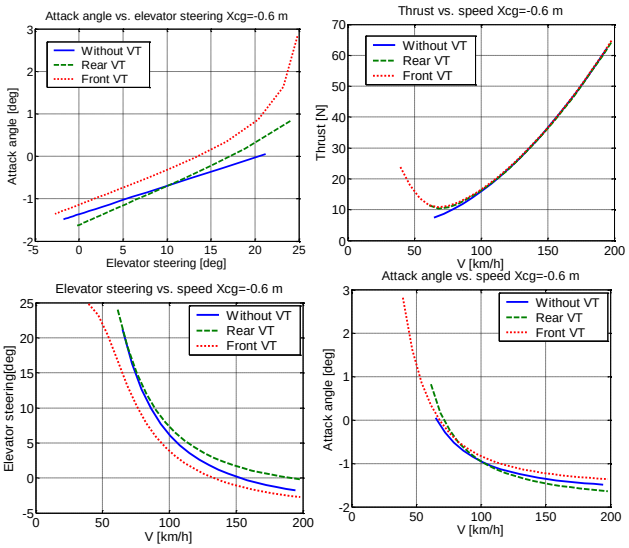

Fig. 18. Flight parameters using vectored thrust for Xcg = -0.6 m.

Results in figures 15, 16, 17, 18 show that for the rear placed vectored thrust, efects upos the horizontal flight are negligible concerning the benefits. In order to obtain a pitching moment to help the elevator steering in angle of attack increase and to decrease the minimum speed, thrust has to be deflected downward (see figure 8) and by this way a descending component appears. Even the angle of attack increases and aerodynamic lift increases, the gain is canceled by the descending component of the thrust. Necessary thrust for small speeds increases substantially, but the minimum speed does not decrease significative, even a slight increase in minimal speed appears for a gravity center position Xcg = 0 m.

As consequence of this aspect, we can propose a new solution, with two smaller engines placed in front of the UAV, on the stabilizer, that is big enough in this case. For an attack angle increase, now the engines nozzles will be deflected in the opposite direction, so an ascendent component of the thrust will appear and will improve the entire lift of the UAV (see figure 19).

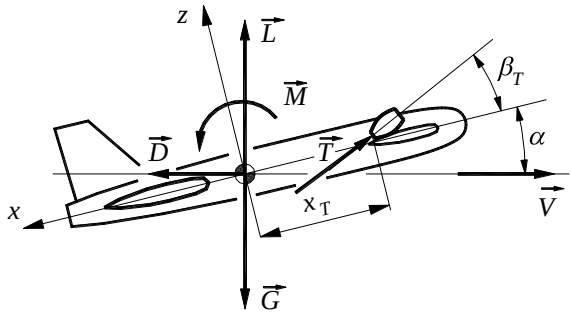

Fig. 19 - Front placed vectored thrust.

We considered in this case also thrust deflections proportional with elevator steering, but gain factors were K_T =1 for Xcg = 0 m, K_T =2 for Xcg = -0,2 m and K_T =3 for Xcg = -0.4 and -0.6 m. Results are presented in comparison with rear placed vectored thrust in figures 15, 16, 17 and 18. This solution offers an increase of attack angle along a semnificative decrease of the minimum speed. For gravity center position Xcg = 0 m, minimum speed decrease is small. Here the gain coefficient is small K_T = 1), because here the UAV can reach high angles of attack any by elevator steering. Significative decreases of the minimum speed are obtained for the others gravity center positions, where high angles of attack are not accessible without vectored thrust.

For gravity center positions Xcg = -0.4 and -0.6, we obtained about a half minimum speed comparing when vectored thrust is not used. So, we combine the advantages of a good static stability with a smaller minimum speed and a better maneuverability, even the gravity center is place far forward.

VII. Conclusions

Vectored thrust improves canard UAV maneuverability in all flight phases. It can be useful in take-off and landing configurations in order to obtain optimum angles of attack when flaps are down. Without vectored thrust it is not possible to maintain that angles of attack.

In the paper is presented a simple but efficient method to find the gain coefficient between elevator steering and thrust deflection, when such command law is used. Nevertheless, taking into account results in figure 7, for landing regime this control law is not very convenient because parameter $\partial\alpha/\partial\beta_e$ has a very large value and so is difficult to be control the UAV.

Taking into account initially we followed to improve UAV behavior in landing configuration, it is expected to obtain better results in the control low for thrust deflection angle is considered also the flaps steering angle. In these conditions we could obtain a smaller slope and a more convenient UAV control. In future works it is intended to test control laws with a component proportional with flaps angle and a component proportional with elevator angle. By this way will be improved the behavior in take-off and

landing configurations, but the effect in the other flying regimes will decrease.

This behavior will be convenient for missions don't need high maneuverability, but only improve take-off and landing qualities to operate on shorter runways. For high maneuverability missions other control laws will be necessary for thrust deflection control, to improve UAV behavior both at take off and in the mission.

Rear positioned vectored thrust has small effects on the horizontal flight performances. Thrust component along oz axis is opposite the airplane lift and even the maximum angle of attack increases, lift increase is canceled by the vertical component of thrust. Minimum horizontal speed does not decrease significative. Vectored thrust advantages maintains in medium and high-speed maneuvers. Torgues produced by the vectored thrust increase the angle of attack and we can obtain higher load factor maneuvers.

A solution to improve the vectored thrust efficiency at small flight speeds is to place the vectored thrust system in front the UAV, in this case two EDF motors placed on the front stabilizer that is large enough in this case. Engines nozzles will be deflected is that way they will produce an ascending component of the thrust, and the gain concerning the minimum speed is significative, mainly for advanced positions of the gravity center.

ACKNOWLEDGMENT

Source of research funding in this article: Research, program of Electrical, Energetic and Aerospace Engineering Department financed by the University of Craiova.

Contribution of authors:

First author – 40%

Second coauthor – 30%

Third coauthor – 30%

Received on August 05,2021
Editorial Approval on November 30, 2021

REFERENCES

[1] Dinca, L., Corcau, J.I. - *Mechanic and dynamic of airplane flight*. Editure Universitaria, Craiova, 2018;

[2] Nita, M. M., Patraulea, R., Sarbu, A., *Aircraft mechanic*, Reprography IPB, Bucharest, 1985;

[3] Napolitano,M. - *Aircraft Dynamics – from modeling to simulation*. John Wiley and Sons, 2012;

[4] Marques, P., Da Ronch, A. (editors) - *Advanced UAV aerodynamics, flight stability and control: novel concepts, theory and applications*. Wiley, 2017;

[5] Hull, D. - *Fundamentals of airplane flight mechanics*, - Springer Verlag, Berlin, Heidelberg, , 2007;

[6] Vingh, N. - *Flight mechanics of high performance aircraft*. Cambridge University Press 1993;

[7] Grigore, I. - *Airplane flight mechanic* – Technical Military Academy, Bucharest 1987;

[8] Kermode, T., *Mechanics of flight 11th edition*, Pearson Education 2011;

[9] Kolk, R., Besserer, C., - *Modern flight dynamcs* –Literary Licensing LLC 2012;

[10] Stengel, R. - *Flight Dynamics* – Princeton University Press, 2004;

[11] Dinca L., Corcau J., *Numerical Study Concerning Longitudinal Dynamic of a Canard UAV with Vectored Thrust*. International Conference on Applied and Theoretical Electricity (ICATE) 2021, 27-28 May, IEEE conference; 10.1109/ICATE49685.2021.9464988; ISBN:978-1-7281-8036-6

[12] Raymer, D. - "Aircraft Design: A Conceptual Approach" – AIAA 2012.

Pentru comenzi și informații, contactați:
Editura Universitaria
Departamentul vânzări
Str. A.I. Cuza, nr. 13, cod poștal 200585
Tel. 0251598054, 0746088836
Email: editurauniversitaria@yahoo.com
marian.manolea@gmail.com
Magazin virtual: www.editurauniversitaria.ro